



Rowan University

From the Selected Works of Francis (Mac) Haas

November, 2016

Studies of small molecule reactions foundational to combustion chemistry

Francis M. Haas, *Princeton University*



Available at: <https://works.bepress.com/francis-haas/8/>

In meditatione

mea exardescet ignis

In meditatione mea exardescet ignis
In my meditation a fire shall flame out
Psalms 38:4 *Clementine Vulgate*/Douay-Rheims Bibles
Image of Charcoal Rubbing
From an inscription above Pyne Tower fireplace,
The Graduate College, Princeton University

**Studies of Small Molecule Reactions
Foundational to Combustion Chemistry,
Including Experimental Measurements from a
Novel High Pressure Flow Reactor**

Francis M. Haas

A DISSERTATION
PRESENTED TO THE FACULTY
OF PRINCETON UNIVERSITY
IN CANDIDACY FOR THE DEGREE OF
DOCTOR OF PHILOSOPHY

RECOMMENDED FOR ACCEPTANCE
BY THE DEPARTMENT OF
MECHANICAL AND AEROSPACE ENGINEERING

Advisor: Frederick L. Dryer

November 2016

Copyright © Francis M. Haas, 2016.

All rights reserved.

Abstract

A high pressure laminar flow reactor facility (HPLFR) was designed and constructed to serve as a platform for the experimental study of the gas phase chemistry of small molecule species. This facility accommodates pressures from slightly above atmospheric to ~30 atm, temperatures from ambient to ~1000 K, and plug flow residence times on the order of 100 milliseconds to 10 seconds. Quasi-steady state NO_x plateau (QSSP) experiments were conducted in the newly-constructed HPLFR to determine rate coefficients for the reaction $\text{H}+\text{O}_2(+\text{M})\leftrightarrow\text{HO}_2(+\text{M})$ (H.9.M) relative to the reasonably well-known rate coefficient for $\text{H}+\text{NO}_2\leftrightarrow\text{OH}+\text{NO}$. Initial experiments for $\text{M} = \text{Ar}$ and N_2 , for which a considerable $k_{\text{H.9.M}}(\text{T,P})$ database already exists, returned $k_{\text{H.9.M}}(\text{T,P})$ determinations in generally good agreement with literature $k_{\text{H.9.M}}$ expressions. For the present purpose, these results serve to validate the utility of the HPLFR facility for determining $k_{\text{H.9.M}}$ for various bath gases. However, the primary focus of these HPLFR QSSP experiments was to develop recommendations for $k_{\text{H.9.CO}_2}$, which is comparatively less well characterized despite its potential importance in high CO₂-content combustion applications. QSSP experiments were performed at temperatures of ~800 K and pressures between ~2-8 atm to yield values of $k_{\text{H.9.CO}_2}(\text{T,P})$, which were then extrapolated to the low pressure limit (LPL) for ease of fusion with other literature results. Other H.9.CO₂-sensitive literature experiments were critically reinterpreted to expand the range of conditions considered for $k_{\text{H.9.CO}_2\text{LPL}}(\text{T})$. A final un-weighted least-squares regression fitting to the compilation of all of these experimentally-derived $k_{\text{H.9.CO}_2\text{LPL}}$ determinations yields an absolute, uncertainty-bounded (95% CI) rate coefficient recommendation of

$$k_{\text{H.9.CO}_2\text{LPL}} = (6.1 +1.2/-1.0)\times 10^{15} \exp((+1164\pm 306 \text{ kcal/mol})/\text{RT}) [\text{cm}^6/\text{mol}^2/\text{s}]$$

valid over the 633-1305 K range of included data. The present $k_{\text{H.9.CO}_2\text{LPL}}$ recommendation was incorporated into an update of a CO oxidation chemistry submodel also addressed in this work. This update favors the use of available theory-based rate coefficient expressions to avoid the influence of hydrogenous impurities (via $\text{CO}+\text{OH}\leftrightarrow\text{CO}_2+\text{H}$, C.1) that tend to skew experimentally-derived rate coefficients for secondary CO oxidation reactions. Additionally, the influence of including HOCO chemistry submodel variants on model predictions was assessed; however, such chemistry appears to contribute little to the predictive abilities of the present CO submodel.

Acknowledgements

I am immensely grateful to the many people who have, in one way or another, supported me up to and throughout my Princeton career. This humble recognition no more explains how these people have shared their encouragement, opportunity, friendship, perspectives, enthusiasm, scholarship, and time with me than does it explain the significance and interconnectedness of our respective relationships. I leave the memoir explaining this to be written some other day – such a story would easily occupy a volume much greater than what is contained here.

Nevertheless, this occasion does permit me an opportunity to express a heartfelt “thank you” to so many who have invested so much in me – in approximately alphabetical order: Fahd Alam; Eitan August; Rich Baliban and Jen Vondran; Tim Bennett; Lauren Biernacki; Michael Brear; Debbie Brown; Garry Brown; Mike Burke; Eduardo Cadava; Eric Cady; Regina Cagle; Valerie Carroll; Nick Cernansky; Marcos Chaos; Mun Choi; Matt Cramer; Steve Dooley; Tanvir Farouk; Fiona Gillespie; Meghan Gottschall; John Gray; Tyler Groff; Ben Gross; Selcuk Gucer; Alex Gutsol; Chuck Haas; Gail Hearn; Josh Heyne; Jeff Hollinger; Saeed Jahangirian; Yiguang Ju; Will Kain; Marcia Kuonen; Harvey Lam; Ed Law; Joe Lefkowitz; Clark Lennon; Mike Littman; Jo Ann Love; Coskun Manchuan; Andrew Mandelbaum; Anthony Marchese; Gigi Martinelli; Joe Michael; Paul Michniewicz; Michael Mueller; Fred Northcutt; Glenn Northey; Jessica O’Leary; Tim Ombrello; Manish Paliwal; Cassandra Pinkney; Joanna Pope and Mark Weir; Allen Qin; Amanda Ramcharan; Jill Ray; Candy Reed; Suzanne Rocheleau; Sylvia San Pedro; Jeff Santner; Dmitry Savransky; Adam Schelhammer; Bridget Schmal; Nanette Schultz; Bijan Sepahpour; Zeynep Serinyel; Keith Sevcik; Lucia and Don Sevcik; Jennifer Shim; Jeff Siegell; Raghu Sivaramakrishnan; Joe Sivo; Lex Smits; Alena Sudholdt; Wenting Sun; Selen Tanner; Eric and Celia Tazelaar; Melissa Thiessen; Joan Thomason; Peter Veloo; Mike Vocaturo; Paul and Vera Wojtowicz; Sang Hee Won; my friends, co-authors, and collaborators too numerous to list here; and my parents Fran and Diane Haas, my in-laws John and Anne Wodnick, and the rest of my family.

Fred Dryer, my advisor, merits special recognition – from him I have gained so much more than could ever be inferred from reading this thesis.

In many ways my biggest supporter has been my wife, Beth. It is to her and our daughter, Stella, that I dedicate this thesis as a small token of appreciation for the time they have permitted me to finish its writing.

This dissertation carries the number T-3290 in the records of the Department of Mechanical and Aerospace Engineering.

Contents

Abstract	iii
Acknowledgements	iv
Contents	vi
List of Figures	ix
List of Tables	xiii
Chapter 1: Introduction	1
1.1 A General Structure Describing Combustion Chemistry	3
1.2 Thesis Objectives and Organization.....	5
1.3 Additional Research Conducted during Degree Candidacy	7
PART I	14
Chapter 2: A High Pressure Laminar Flow Reactor for Chemical Kinetic Studies	15
2.1 HPLFR Facility Overview.....	15
2.2 Feed/Calibration Subsystem	19
2.2.1 Gas Reactant Metering.....	19
2.2.2 Liquid Reactant Metering.....	20
2.2.3 Uncertainties in Flow Rate and Composition.....	21
2.3 Reactor Subsystem	24
2.3.1 Pressure Vessel.....	24
2.3.2 Reactor Duct/Duct Sealing System	26
2.3.3 Sample Probe	30
2.4 Sample Analysis Subsystem	32
2.5 Experimental Design Considerations in Use of the HPLFR Facility.....	34
2.5.1 Ideal Plug Flow Operation of Laminar Reactor.....	36
2.5.2 Axial Diffusion-Affected Plug Flow Operation of Laminar Reactor	37

2.5.3 2-Dimensional Operation of Laminar Reactor	37
2.5.4 An Important Caveat: Experimental Designs and Interpretation of HPLFR Data.....	37
Chapter 3: HPLFR Design Validation by Rate Coefficient Measurement for	
H+O₂(+M)→HO₂(+M), M = Ar and N₂	47
3.1 Description of the Quasi-Steady State Plateau (QSSP) Condition	48
3.1.1 The Simplified QSSP Reaction System.....	49
3.1.2 Departures from the QSSP Condition (Extended QSSP Conditions).....	52
3.2 Validation of HPLFR for QSSP Measurements of kH.9.M	54
3.2.1 Plug Flow Assumption Consideration for QSSP Experiments	55
3.2.2 Validation Experiments Using M = Ar	56
3.2.3 Validation Experiments Using M = N ₂	62
3.3 Alternative Validation of HPLFR with QSSP Measurements of kN.1	65
Chapter 4: Rate Coefficient Determination for H+O₂(+CO₂)→HO₂(+CO₂)	92
4.1 HPLFR Measurement of kH.9.CO ₂ Using QSSP Conditions	92
4.1.1 Low Pressure Limit Determinations of kH.9.CO ₂ from HPLFR Data	94
4.2 Reassessment of kH.9.CO ₂ from Literature Sources	95
4.2.1 Static Reactor Experiments of Ashmore & Tyler	96
4.2.2 Atmospheric Pressure Flow Reactor Experiments of Ashman & Haynes	98
4.2.3 Static Reactor Experiments of von Elbe & Lewis, Willbourn & Hinshelwood, and Linnett & Selley	105
4.2.4 Atmospheric Pressure Flow Reactor Experiments of Dryer	106
4.2.5 Shock Tube OH Time Histories of Vasu <i>et al.</i>	107
4.3 Recommended kH.9.CO ₂ LPL Expressions Based on HPLFR Measurements and Literature Reinterpretations	123
PART II	155

Chapter 5: An Updated Combustion Kinetic Model for Syngas Fuels Based on Recent Theory and Experiment	156
5.1 Kinetic Model Development Overview.....	157
5.2 Thermochemistry Parameters	159
5.3 Transport Parameters.....	161
5.4 Reaction Rate Coefficient Parameters	162
5.4.1 H.9.M: $H + O_2 (+ M) \leftrightarrow HO_2 (+ M)$, $M = H_2O, CO_2, O_2$	163
5.4.2 C.1: $CO + OH \leftrightarrow CO_2 + H$	168
5.4.3 C.2: $CO + O_2 \leftrightarrow CO_2 + O$	172
5.4.4 C.3: $CO + HO_2 \leftrightarrow CO_2 + OH$	174
5.4.5 C.4.M: $CO + O (+ M) \leftrightarrow CO_2 (+ M)$	176
5.4.6 C5.M-C7: Reactions of HCO	183
5.4.7 Consideration of HOCO Chemistry.....	186
5.5 Chapter Summary	188
Chapter 6: Concluding Remarks and Perspectives on Related and Future Work.....	201
References	205
Appendix: CO/Syngas Combustion Kinetic Model	217
Thermochemistry and Elementary Reaction Parameters (chem.inp)	217
Transport Parameters (tran.dat)	221

List of Figures

Figure 1.1 – Depiction of a hierarchical scheme for combustion chemistry.	10
Figure 2.1 – High Pressure Laminar Flow Reactor (HPLFR) overview schematic.	40
Figure 2.2 – Simplified Feed/Calibration Subsystem schematic.	41
Figure 2.3 – Simplified Reactor Subsystem schematic.	42
Figure 2.4 – Comparison of maximum allowable and representative applied stresses for the HPLFR pressure vessel.	43
Figure 2.5 – Example sketches of duct geometries that can be accommodated by the pressure shell.	44
Figure 2.6 – HPLFR Sample Probe schematic.	45
Figure 2.7 – Simplified Sample Analysis Subsystem schematic.	46
Figure 3.1 – Illustration of quasi-steady state plateau (QSSP) features: Base Case conditions.	70
Figure 3.2 – Response of P_s to initial NO_2 level.	71
Figure 3.3 – Scaling of P_s with both initial O_2 pressure and initial total reactor pressure.	72
Figure 3.4 – Response of P_s to $\text{NO}+\text{NO}_2$ sensitizer composition.	73
Figure 3.5 – Response of QSSP condition to complete H_2 consumption.	74
Figure 3.6 – Sensitivity of P_s to rates of key reactions, Base Case conditions.	75
Figure 3.7 – QSSP features and P_s sensitivity to rates of key reactions at conditions representative of HPLFR experiments.	76
Figure 3.8 – Illustration of departures from QSSP condition estimated by $\sigma_{H.9.M}$	77
Figure 3.9 – Correction of simulated $\text{kH.9.M}^{\text{QSSP}}$ measurement using $\sigma_{H.9.M}$	78
Figure 3.10 – Measured species and temperature profiles for HPLFR QSSP Experiment 3/I.	79
Figure 3.11 – Measured species and temperature profiles for HPLFR QSSP Experiment 3/II.	80

Figure 3.12 – Measured species profiles for HPLFR QSSP Experiments 3/IIIa and 3/IIIb.	81
Figure 3.13 – Area-averaged, wall, and centerline axial species profile results from two-dimensional simulation of M = Ar experiment 3/II.	82
Figure 3.14 – Comparison of literature experimental determinations and several expressions for $k_{N.1}$ ($H + NO_2 \rightarrow OH + NO$) for $200 \leq T \leq 2000$ K.	83
Figure 3.15 – Comparison of presently determined $k_{H.9.Ar^{QSSP}}$ rate coefficients to several literature-based pressure-dependent rate coefficients for M = Ar at 752 K.	84
Figure 3.16 – Measured species and temperature profiles for HPLFR QSSP Experiment 3/IV.	85
Figure 3.17 – Measured species profiles for HPLFR QSSP Experiments 3/Va and 3/Vb.	86
Figure 3.18 – Comparison of presently determined $k_{H.9.N_2^{QSSP}}$ rate coefficients to several literature-based pressure-dependent rate coefficients for M = N ₂ at 739 K.	87
Figure 3.19 – Measured species and temperature profiles for HPLFR QSSP Experiment 3/VI.	88
Figure 3.20 – Measured species and temperature profiles for HPLFR QSSP Experiment 3/VII.	89
Figure 3.21 – Comparison of presently determined $k_{H.9.N_2^{QSSP}}$ rate coefficients to several literature-based pressure-dependent rate coefficients for M = N ₂ at 825 K.	90
Figure 3.22 – Comparison of presently determined $k_{N1^{QSSP}}$ rate coefficients to literature $k_{N.1}$ expressions and experimental determinations.	91
Figure 4.1 – Measured species and temperature profiles for HPLFR QSSP Experiment 4/I.	140
Figure 4.2 – Measured species and temperature profiles for HPLFR QSSP Experiment 4/II.	141
Figure 4.3 – Measured species and temperature profiles for HPLFR QSSP Experiment 4/IVa.	142
Figure 4.4 – Measured species and temperature profiles for HPLFR QSSP Experiments 4/Va and 4/Vb.	143
Figure 4.5 – Measured species profiles for HPLFR QSSP Experiment 4/III.	144
Figure 4.6 – Measured temperature profile for HPLFR QSSP Experiment 4/III.	145
Figure 4.7 – Simulated NO ₂ profiles for HPLFR QSSP Experiment 4/III.	146

Figure 4.8 – Measured species profiles for HPLFR QSSP Experiment 4/IVb.	147
Figure 4.9 – Results from Ashman’s (1999) M = CO ₂ laminar flow reactor experiments.	148
Figure 4.10 – Comparison of simulated OH profiles from GRI-VDH, present GRI-VDH reconstruction, and GRI-Mech 3.0 kinetic models	149
Figure 4.11 – Li-C ₁ model-predicted OH profile and OH sensitivity for the 1277 K experiment of Vasu <i>et al.</i>	150
Figure 4.12 – Kéromnès <i>et al.</i> model-predicted OH profile and OH sensitivity for the 1277 K experiment of Vasu <i>et al.</i>	151
Figure 4.13 – Predicted OH profiles from iteration of kH.9.CO ₂ values after kH.9.M swapping from GRI-Mech 3.0 into GRI-VDH, 1277 K experiment of Vasu <i>et al.</i>	152
Figure 4.14 – Predicted OH profiles for several entire literature kinetic models with kH.9.CO ₂ -optimized to match the experimental OH profile from the 1277 K experiment of Vasu <i>et al.</i>	153
Figure 4.15 – Comparison of final kH.9.CO ₂ LPL rate coefficient expression recommendations with literature expressions and present determinations/reinterpretations of experimental measurements.	154
Figure 5.1 – Scheme for present H ₂ /CO kinetic model development.	190
Figure 5.2 – Comparison of model predictions and Santner <i>et al.</i> (2013) experimental laminar mass burning rate measurements for H ₂ O-diluted a) H ₂ flames and b) syngas flames.	191
Figure 5.3 – Comparison of model predictions and Qiao <i>et al.</i> (2007) experimental laminar burning velocity measurements for CO ₂ -diluted H ₂ -air flames.....	192
Figure 5.4 – Comparison of model predictions and experimental measurements for which high levels of CO ₂ have been included in the reactants.	193
Figure 5.5 – Pressure-temperature relationship delineating conditions for which stabilized HOCO radical may form at non-negligible rates, based on Joshi & Wang (2006).	194
Figure 5.6 – Comparison of rate coefficient expressions for C.1 (CO + OH → CO ₂ + H) for temperatures between 500 and 2500 K.	195

Figure 5.7 – Comparison of rate coefficient expressions for C.2 ($\text{CO} + \text{O}_2 \rightarrow \text{CO}_2 + \text{O}$) for temperatures between 1000 and 2500 K. 196

Figure 5.8 – Comparison of rate coefficient expressions for C.3 ($\text{CO} + \text{HO}_2 \rightarrow \text{CO}_2 + \text{OH}$) for temperatures between 500 and 2500 K. 197

Figure 5.9 – Comparison of rate coefficient determinations for C.4.HPL ($\text{CO} + \text{O} \rightarrow \text{CO}_2$) for $300 \leq T \leq 3700$ K. 198

Figure 5.10 – Comparison of rate coefficient determinations for C.4.Ar_{LPL} for $1000 \leq T \leq 3300$ K. 199

Figure 5.11 – Comparison among predictions of several kinetic model variants and experimental 435 nm CO flame band emission decay measurements of Hardy *et al.* (1978). 200

List of Tables

Table 1.1 – H ₂ chemistry subset used in this thesis	11
Table 1.2 – CO chemistry subset used in this thesis	12
Table 1.3 – NO _x chemistry subset discussed in this thesis	13
Table 3.1 – Nominal initial conditions for HPLFR kH.9.M validation experiments in Ar, N ₂ bath gases.....	67
Table 3.2 – Measured profile-averaged ratio of O ₂ and NO ₂ mole fractions from HPLFR-QSSP validation experiments.....	68
Table 3.3 – Model-derived estimates of $\sigma_{H.9.M}$ for Experiment 3/VI	69
Table 4.1 – Nominal initial conditions for HPLFR kH.9.CO ₂ determination experiments.....	126
Table 4.2 – Measured profile-averaged ratio of O ₂ and NO ₂ mole fractions from HPLFR CO ₂ bath gas experiments.....	127
Table 4.3 – Measured ratio of O ₂ and NO ₂ mole fractions from HPLFR pressure-varying M = CO ₂ experiments.....	128
Table 4.4 – Summary of falloff corrections for HPLFR kH.9.CO ₂ _{LPL} determinations	129
Table 4.5 – Summary of kH.9.CO ₂ reinterpretations of 633 K Ashmore & Tyler (1962) experiments	130
Table 4.6 – Reinterpretation of Ashman & Haynes (1998) kH.9.CO ₂ experiments by apparent collisional efficiency	131
Table 4.7 – Reinterpretation of Ashman (1999) kH.9.CO ₂ experiments by QSSP analysis	132
Table 4.8 – Reinterpretation of static reactor kH.9.CO ₂ experiments by apparent relative collisional efficiency	133
Table 4.9 – Reinterpretation of Dryer (1987) kH.9.CO ₂ experiments by apparent collisional efficiency..	134
Table 4.10 – Low pressure limit corrections to nominal kH.9.CO ₂ values from Vasu <i>et al.</i> (2011)	135
Table 4.11 – Alternative “swap” model kH.9.CO ₂ interpretations of Vasu <i>et al.</i> (2011) values	136

Table 4.12 – Vasu *et al.* (2011) $kH.9.CO_2$ determinations based on Consensus $kH.9.Ar$ expressions... 137

Table 4.13 – Alternative whole-model determinations of $kH.9.CO_2$ from the Vasu *et al.* (2011) 1277 K experiment..... 138

Table 4.14 – Summary of $kH.9.CO_2$ determinations for the Vasu *et al.* (2011) 1277 K experiment..... 139

Chapter 1: Introduction

There appears to be no strong consensus among the approaches of governmental, NGO, industrial, or academic institutions towards addressing global climate and energy challenges that will persist into future generations. However, projections generally agree that, short of disruptive technology intervention, *combustion technology will remain the principal source of energy conversion for decades to come* (e.g., Committee on America's Energy Future *et al.*, 2009; International Energy Agency, 2011; ExxonMobil, 2013). Although the relative share of combustion-derived energy may decline amid increased contributions from wind, non-biomass solar, hydro, geothermal, and nuclear fission primary energy sources, absolute combustion energy output will continue to increase. A more detailed discussion of the energy outlook including uncertain but significant associated social, environmental, economic, and policy issues is beyond the scope of this thesis; however, the present work is contributed with the perspective that energy accessed from combustion will remain the chief energy supply for some time.

Some may consider combustion a relatively mature discipline, yet the scale, growth, and diversity of its application warrant ongoing study, especially in the context of a varying and insecure global energy supply, emerging alternative- and bio-fuel technologies, and ever tightening restrictions on emissions from energy conversion. The perennial challenge of increasing the efficiency of energy conversion while reducing emissions of conventional and greenhouse pollutants and operating within application-specific performance constraints drives continued fundamental and applied research on combustion-related topics.

For example, recent Corporate Average Fuel Economy (CAFE) regulations (Federal Register, 2012) seek to more than double the 2010 mandated light-duty vehicle effective fuel economy to 54.5 miles per gallon (mpg) by 2025. This is an aggressive rate of fuel economy increase without precedent in the history of the CAFE program. Government-estimated cumulative impacts of this program for light-duty vehicles produced in model years 2017-2025, if realized, include reduced fuel consumption by ~4 billion barrels of oil and net social benefits valued at hundreds of billions of dollars for the United States economy. The overall fuel economy gains mandated by this ambitious regulation require continued improvement of combustion technologies, as well as synergistic improvements in vehicle weight

reduction, advanced vehicle aerodynamics, and fuel-conscious driving behavior, among other aspects of automotive socio-technical systems.

Even considering only combustion-related processes, it still follows that seemingly marginal increases in efficiency can result in significant aggregate fuel savings and avoided emissions when integrated over the large scales of energy utilization. Based on 2010 figures for the US passenger car fleet (Davis *et al.*, 2012), a modest 1.0 mile per gallon (~4.3%) improvement in aggregate fuel economy from 23.0 to 24.0 mpg would result an annual offset of ~2.8 billion gallons of fuel consumed and ~28 million fewer tons of CO₂ emitted. Such efficiency gains are obtainable by applying *existing* combustion technologies to the 2010 fleet (EPA & NHTSA, 2012), and further gains due to future advances in combustion technology can be reasonably expected.

The present examples, though general, are of admittedly narrow scope compared to the ubiquitous application of combustion processes for transportation, manufacturing, electric power generation, heating and cooking, *etc.* Nevertheless, they demonstrate the potential magnitude of fuel use and emissions reductions resulting from improvements in combustion processes. Clearly, significant social and economic gains remain to be realized through context-considered development and optimization of combustion processes across many diverse facets of the global energy economy.

This thesis concerns itself with gas phase chemistry of small molecules relevant to combustion, which is a topic that may appear significantly removed from applied subjects such as the fuel economy examples discussed above. However, this chemistry ultimately governs important mesoscale processes such as multistage ignition, flame propagation and extinction, heat release rate, and pollutant formation. These processes, in turn, contribute to a diversity of systems-level consequences of combustion such as automotive fuel economy, high altitude reflight of jet aircraft engines, wildfire propagation, and regional air quality deterioration.

Considered in the context of mathematical physics, gas phase chemistry contributes significant, highly-coupled, non-linear source terms to the governing equations generally used to describe combustion and related reacting flow phenomena. Studies such as this one remain necessary to unravel the dynamics encoded by these chemical source terms, which ultimately control macroscopic phenomena bearing directly on energy conversion and the broader socio-technical complex.

1.1 A General Structure Describing Combustion Chemistry

The chemical source terms used to model combustion phenomena are themselves commonly modeled by consistent sets of chemical species interacting with each other through elementary chemical reactions. These source term models involve reaction rate coefficient, thermochemistry, and transport property parameterizations for the individual chemical species and reactions thought to adequately describe chemical contributions to overall system behavior. This type of complex model description for the chemical source term represents a dominant paradigm in the combustion chemistry community. Schofield (2012) offers an interesting and somewhat contrapuntal viewpoint on the structure, uniqueness, uncertainty, and utility of such models. This dissenting perspective merits further contemplation; however, any specific consideration is beyond the scope of the present thesis, which adopts the mainstream model framework for hierarchically constructed, detailed chemical kinetic models described in more detail below.

A seminal review by Westbrook & Dryer (1981) discusses dividing the combustion chemical source term model into generalized hierarchically-structured species/reaction submodels. This organization technique is in widespread use today, and it reflects a rational description of the chemical processes leading to reactant conversion into products. Further, such description is consistent with decades of empirical studies. Hierarchical kinetic model descriptions hold generally for systems such as those involving conventional hydrocarbon fuels; oxygenated, nitrogen-containing, or halogenated hydrocarbons; synthesis gas; fuel blends; electronically- and/or vibrationally-excited species; and even relatively exotic systems for which hydrogen- or carbon-containing species are not found.

In these hierarchical schemes, chemical species and their reactions appearing at superior (closer to the root) ranks in the hierarchy continue to participate in overall chemical behavior at subordinate (albeit more complex) ranks. Hierarchical descriptions of hydrocarbon/oxygenate combustion (Figure 1.1) generally begin at the root with a fairly small set of reactive species (~8) and reactions (~19) describing gas-phase oxidation of H_2 to form product H_2O . These reactions are presented in Table 1.1. Addition of a second rank describes CO oxidation to product CO_2 and involves few (~3) additional species and few (~7) additional reactions (Table 1.2). Since species from the H_2 rank participate in CO oxidation and therefore may react among each other as described by the H_2 rank, *both* ranks must be included to

describe CO oxidation. This thesis is devoted to chemistry encompassed by these two foundational ranks of the combustion chemistry hierarchy, and detailed discussion of the H₂/CO system follows in later chapters.

Hierarchical ranks commonly progress beyond the H₂/CO foundation to include CH₂O; followed by CH₃OH; CH₄; the C₂ hydrocarbons C₂H₆, C₂H₄, and C₂H₂; and so on to more complex molecules that may better represent some practical fuels such as gasoline, diesel, or bio-derived fuel. The underlying logic for specifying species and reactions in a particular rank often considers fragments that may be formed from the nominal fuel assigned to that rank. For example, fragments of CH₃OH not already included at the H₂/CO/CH₂O ranks include CH₂OH and CH₃O. These species, their mutual reactions, and their reactions with H₂/CO/CH₂O species belong to the CH₃OH rank of the hierarchy and are further necessary to describe chemistry of CH₄, C₂ species, and larger molecules (Figure 1.1).

Hierarchical model descriptions are non-unique and are often defined heuristically based on insight sought about a particular fundamental or applied system – a point that appears to be a general feature of most lower-order model descriptions of complex systems. In general practice as well as in this particular study, the ambiguity associated with delineation of a hierarchy is primarily semantic and often depends on the intended system to be modeled. This in no way detracts from the rational structure of hierarchical chemistry schemes.

For example, the chemistry of nitrogen oxides (NO_x) – which are important conventional/greenhouse gas pollutant, explosives, and rocket propellant species – has been excluded in the hierarchical scheme discussed above since many fundamental and applied combustion processes can be modeled with very high fidelity by an approximate chemical source term excluding NO_x chemistry. However, addition of NO_x chemistry to the chemical source terms is critical to predict emissions of these pollutants from, *e.g.*, gas turbines used for stationary power generation or automotive fuels with added nitrogen-containing ignition enhancers. Several experiments described in this thesis depend on direct reactions of NO_x species with H₂-rank species; however, there is negligible direct interaction of CO and NO_x reaction subsets at these experimental conditions. Accordingly, the present hierarchical chemical source term model presented schematically in Figure 1.1 treats CO and NO_x chemistry as peers in the

rank immediately subordinate to the root H₂ chemistry rank. Under this assumption, these subsets interact only indirectly through common reactions in the H₂ chemistry rank.

One final point pertaining to general hierarchical descriptions of combustion chemistry involves uncertainty. Each elementary reaction rate coefficient, thermochemistry, and transport property parameterization contributes an element of uncertainty to the chemical source term model. The choice of included species and elementary reactions used in the hierarchical description further contributes uncertainty to the source term model. These combined uncertainties propagate and grow as the hierarchy itself grows from superior (*i.e.*, H₂) to subordinate ranks. To minimize uncertainty propagation in chemical source term models for combustion in general, it is therefore important to reduce uncertainty in the chemistry description of the superior ranks involving H₂, CO, and other small molecules.

Formal uncertainty analysis is an emerging topic in the combustion chemistry community, even as minimization of uncertainty in combustion kinetics appears to be of critical importance to the ongoing development of combustion science in general (see *e.g.*, the relatively recent review of Tomlin (2013) and more focused studies of Burke *et al.* (2013) and Mueller *et al.* (2013)). Large uncertainties associated with the chemical source term may mask other important uncertain phenomena – either those associated with non-chemical terms in the governing equations of combustion or those associated with the assumptions and boundary conditions employed in theoretical, computational, and experimental combustion studies (*e.g.*, Dryer *et al.*, 2014 and Santner *et al.*, 2014). Later chapters discuss existing literature data that have been subjected to re-analysis, resulting in revised uncertainty recommendations for several reaction rate coefficient measurements. Although beyond the scope of this thesis, further critical evaluation of existing literature data appears necessary to more accurately characterize and further reduce uncertainties in H₂/CO core chemistry models and, thereby, propagated uncertainty in chemistry models of more complex fuels.

1.2 Thesis Objectives and Organization

This thesis is divided into two main Parts, both directed at improving the hierarchical description of combustion chemistry outlined above. Part I discusses a novel high pressure laminar flow reactor facility (HPLFR) developed as a general platform to study combustion chemistry of small molecules.

Based partly on measurements made using the HPLFR, new uncertainty-quantified recommendations are made for the elementary reaction rate coefficient for the reaction



for $\text{M} = \text{CO}_2$, which – despite the ubiquity of CO_2 formed from hydrocarbon combustion – is comparatively less well characterized than for $\text{M} = \text{Ar}$ or N_2 , for example. Part II discusses construction and validation of an updated H_2/CO core chemistry model towards a more general update of existing combustion chemistry models applicable to a wide variety of fuels and applications.

As a matter of nomenclature, elementary reactions referenced throughout this thesis are associated with a unique number and a specific letter such as H, C, or N, which respectively correspond to the H_2 , CO, or NO_x chemistry subsets discussed above and indicated schematically in Figure 1.1. The H, C, and N reaction subsets are listed in Tables 1.1-1.3. The additional parameter M associated with, for example, the reaction reference H.9.M indicates an unspecified molecule “M” acting as a third-body collision partner in the termolecular reaction among H, O_2 , and M to form HO_2 . When referring to particular collision partners such as CO_2 and H_2O , this M parameter is specifically enumerated (*e.g.*, H.9.CO2 and H.9.H2O). Also, because the identity of collider M does not affect reaction rates in the high pressure limit (HPL), discussions of pressure-dependent reactions at the HPL are similarly referenced (*i.e.*, H.9.HPL). This particular nomenclature is specific to maintaining clear discourse in this thesis and differs from the convention used by much of the gas phase chemistry community. For example, $k_{\text{H.9.HPL}}$ used in present context would correspond to $k_{\text{H9},\infty}$ under more conventional treatment. This should be no cause for confusion.

Parts I and II listed above both relate in a way to the preceding introductory material describing the overall importance of chemistry to combustion, its hierarchical structure, and the need for well-characterized and reduced uncertainty for inputs to chemical source term models. Additionally, topically-focused introductions accompany each chapter, permitting each to be considered somewhat independently of the others. A final chapter summarizes the contents of this thesis and offers some additional perspective on future avenues of research for combustion chemistry.

1.3 Additional Research Conducted during Degree Candidacy

The scope of this thesis is confined to the two coherently connected topics listed in the preceding section; however, the present work has been conducted as part of a broader arc of inquiry developed over the course of this degree candidacy. These additional combustion-related investigations involve critical evaluation of or design modifications to experimental facilities other than the HPLFR as well as consideration of a more extensive variety of fuels/fuel blends, each having relatively unique chemical behavior. Topics considered are relevant to a large range of fundamental and applied problems in the combustion field. Many of the techniques and analytical tools employed in these other projects have informed material covered in this thesis.

The following lists of peer-reviewed literature and archival conference proceedings indicates the author's contributions to additional research aims not principally discussed in this thesis. Though the content of later chapters references or duplicates elements of publications (4) and (9) (in particular), the objectives of these studies are not fully developed herein. The interested reader is instead referred to these publications for a more thorough treatment of this shared material.

Peer-reviewed Literature

1. C.-W. Zhou, Y. Li, E. O'Connor, K.P. Somers, S. Thion, C. Keesee, O. Mathieu, E.L. Petersen, T.A. DeVerter, M.A. Oehlschlaeger, G. Kukkadapu; C.-J. Sung, M. Alrefae, F. Khaled, A. Farooq, P. Dirrenberger; P.-A. Glaude, F. Battin-Leclerc, J. Santner, Y. Ju, T. Held; **F.M. Haas**, F.L. Dryer, and H.J. Curran. "A comprehensive experimental and modeling study of isobutene oxidation." *Combust. Flame*, 167, 353 (2016). <http://dx.doi.org/10.1016/j.combustflame.2016.01.021>
2. S.H. Won, P.S. Veloo, S. Dooley, J. Santner, **F.M. Haas**, Y. Ju, and F.L. Dryer. "Predicting the global combustion behaviors of petroleum-derived and alternative jet fuels by simple fuel property measurements." *Fuel*, 168, 34 (2016). <http://dx.doi.org/10.1016/j.fuel.2015.11.026>
3. S.H. Won, **F.M. Haas**, A. Tekawade, G. Kosiba, M.A. Oehlschlaeger, S. Dooley, and F.L. Dryer. "Combustion characteristics of C4 iso-alkane oligomers: experimental characterization of iso-dodecane as a jet fuel surrogate." *Combust. Flame*, 165, 137 (2016). <http://dx.doi.org/10.1016/j.combustflame.2015.11.006>
4. **F.M. Haas** and F.L. Dryer. "Rate coefficient determinations for $\text{H}+\text{NO}_2\rightarrow\text{OH}+\text{NO}$ from high pressure flow reactor measurements." *J. Phys. Chem. A*, 119, 7792 (2015). <http://dx.doi.org/10.1021/acs.jpca.5b01231>
5. A. Sudholdt, L. Cai, J. Heyne, **F.M. Haas**, H. Pitsch, and F.L. Dryer. "Ignition characteristics of a bio-derived class of saturated and unsaturated furans for engine applications." *Proc. Combust. Inst.*, 35, 2957 (2015). <http://dx.doi.org/10.1016/j.proci.2014.06.147>

6. J. Santner, **F.M. Haas**, F.L. Dryer, and Y. Ju. "High temperature oxidation of formaldehyde and formyl radical: A study of 1,3,5-trioxane laminar burning velocities." *Proc. Combust. Inst.*, 35, 687 (2015). <http://dx.doi.org/10.1016/j.proci.2014.05.014>
7. S.M. Burke, U. Burke, R. Mc Donagh, O. Mathieu, I. Osorio, C. Keesee, A. Morones, E.L. Petersen, W. Wang, T.A. DeVerter, M.A. Oehlschlaeger, B. Rhodes, R.K. Hanson, D.F. Davidson, B.W. Weber, C.-J. Sung, J. Santner, Y. Ju, **F.M. Haas**, F.L. Dryer, E.N. Volkov, E.J.K. Nilsson, A.A. Konnov, M. Alrefae, F. Khaled, A. Farooq, P. Dirrenberger, P.-A. Glaude, F. Battin-Leclerc, H.J. Curran. "An experimental and modeling study of propene oxidation. Part 2: Ignition delay times and flame speeds." *Combust. Flame*, 162, 296 (2015). <http://dx.doi.org/10.1016/j.combustflame.2014.07.032>
8. S.M. Burke, W. Metcalfe, O. Herbinet, F. Battin-Leclerc, **F.M. Haas**, J. Santner, F.L. Dryer, H.J. Curran. "An experimental and modeling study of propene oxidation. Part 1: Speciation measurements in jet-stirred and flow reactors." *Combust. Flame*, 161, 2765 (2014). <http://dx.doi.org/10.1016/j.combustflame.2014.05.010>
9. F.L. Dryer, **F.M. Haas**, J. Santner, T. Farouk, and M. Chaos. "Interpreting chemical kinetics from complex reaction-advection-diffusion systems: Modeling of flow reactors and related kinetics experiments." *Prog. Energy Combust. Sci.*, 44, 19 (2014). <http://dx.doi.org/10.1016/j.pecs.2014.04.002>
10. **F.M. Haas** and F.L. Dryer. "Application of blending rules for ignition quality metrics: A comment on 'A linear-by-mole blending rule for octane numbers of n-heptane/iso-octane/toluene mixtures.'" *Fuel*, 120, 240 (2014). <http://dx.doi.org/10.1016/j.fuel.2013.10.025>
11. J. Santner, **F.M. Haas**, Y. Ju, and F.L. Dryer. "Uncertainties in interpretation of high pressure spherical flame propagation rates due to thermal radiation." *Combust. Flame*, 161, 147 (2014). <http://dx.doi.org/10.1016/j.combustflame.2013.08.008>
12. H. Guo, W. Sun, **F.M. Haas**, T.I. Farouk, F.L. Dryer, and Y. Ju. "Measurements of H₂O₂ in low temperature dimethyl ether oxidation." *Proc. Combust. Inst.*, 34, 573 (2013). <http://dx.doi.org/10.1016/j.proci.2012.05.056>
13. J.K. Lefkowitz, J.S. Heyne, S.H. Won, S. Dooley, H.H. Kim, **F.M. Haas**, S. Jahangirian, F.L. Dryer, and Y. Ju. "A chemical kinetic study of tertiary-butanol in a flow reactor and counterflow diffusion flame." *Combust. Flame*, 159, 968 (2012). <http://dx.doi.org/10.1016/j.combustflame.2011.10.004>
14. S. Jahangirian, S. Dooley, **F.M. Haas**, and F.L. Dryer. "A detailed experimental and kinetic modeling study of n-decane oxidation at elevated pressures." *Combust. Flame*, 159, 30 (2012). <http://dx.doi.org/10.1016/j.combustflame.2011.07.002>
15. **F.M. Haas**, A. Ramcharan, and F.L. Dryer. "Relative reactivities of the isomeric butanols and ethanol in an Ignition Quality Tester." *Energy & Fuels*, 25, 3909 (2011). <http://dx.doi.org/10.1021/ef2008024>
16. **F.M. Haas**, M. Chaos, and F.L. Dryer. "Low and intermediate temperature oxidation of ethanol and ethanol-PRF blends: An experimental and modeling study." *Combust. Flame*, 156, 771 (2009). <http://dx.doi.org/10.1016/j.combustflame.2009.08.012>

Archival Conference Proceedings

17. **F.M. Haas**, A. Qin, and F.L. Dryer. "'Virtual' smoke point determination of alternative aviation kerosenes by Threshold Sooting Index (TSI) methods" AIAA Propulsion and Energy Forum and Exposition 2014: 50th AIAA/ASME/SAE/ASEE Joint Propulsion Conference, Cleveland, Ohio, July 28-30, 2014. [AIAA-2014-3468](http://dx.doi.org/10.2514/6.2014-3468)
18. S. Dooley, S.H. Won, **F.M. Haas**, J. Santner, Y. Ju, F.L. Dryer, and T. Farouk. "Development of reduced kinetic models for petroleum-derived and alternative jet fuels" AIAA Propulsion and Energy Forum and Exposition 2014: 50th AIAA/ASME/SAE/ASEE Joint Propulsion Conference, Cleveland, Ohio, July 28-30, 2014. [AIAA-2014-3661](http://dx.doi.org/10.2514/6.2014-3661)

19. J.-P. Tessonier, **F.M. Haas**, D.M. Dabbs, F.L. Dryer, R.A. Yetter, and M.A. Barteau. "Polyoxometalate clusters supported on functionalized graphene sheets as nanohybrids for the catalytic combustion of liquid fuels." *Mat. Res. Soc. Symp. Proc.*, 1451, mrss12-1451-dd18-04, 2012. <http://dx.doi.org/10.1557/opl.2012.1457>
20. J.K. Lefkowitz, J.S. Heyne, S.H. Won, S. Dooley, H.H. Kim, **F.M. Haas**, S. Jahangirian, F.L. Dryer, and Y. Ju. "A chemical kinetic study of the alternative transportation fuel, tertiary-butanol." 49th AIAA Aerospace Sciences Meeting including the New Horizons Forum and Aerospace Exposition, Orlando, Florida, January 4-7, 2011. [AIAA-2011-698](#)

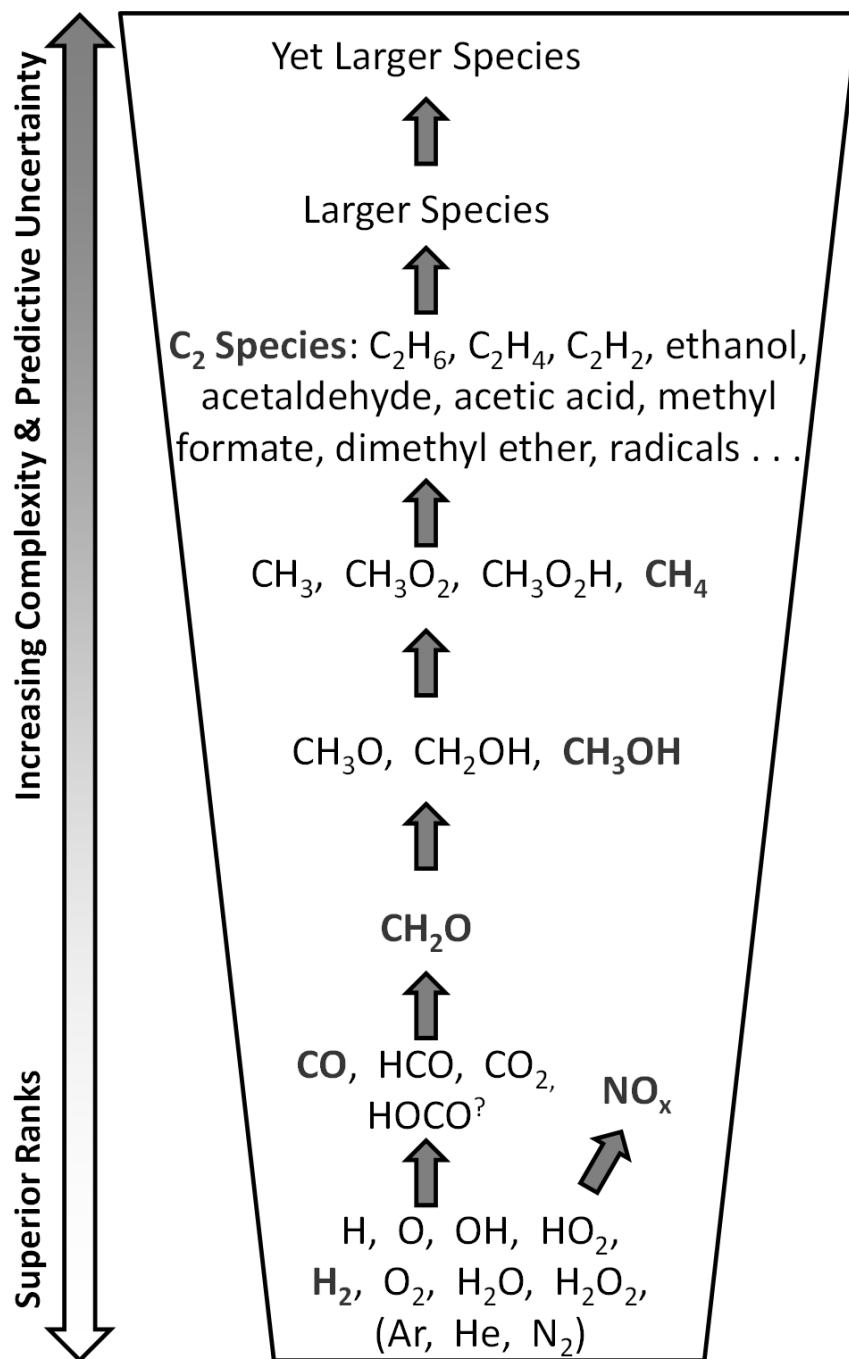


Figure 1.1 – Depiction of a hierarchical scheme for combustion chemistry.

Uni-directional arrows inside the trapezoidal structure indicate non-reciprocal participation of species below the arrow (those belonging to higher rank) in reactions with lower rank species above the arrow. The expanding trapezoid itself represents the increasing number of species and elementary reactions necessary to describe chemical behavior as parent fuel complexity increases.

[?]HOCO-related chemistry is briefly addressed in Chapter 5.

Table 1.1 – H₂ chemistry subset used in this thesis

Elementary Reaction	Reaction Reference
$\text{H} + \text{O}_2 \leftrightarrow \text{O} + \text{OH}$	H.1
$\text{O} + \text{H}_2 \leftrightarrow \text{H} + \text{OH}$	H.2
$\text{H}_2 + \text{OH} \leftrightarrow \text{H}_2\text{O} + \text{H}$	H.3
$\text{OH} + \text{OH} \leftrightarrow \text{O} + \text{H}_2\text{O}$	H.4
$\text{H}_2 + \text{M} \leftrightarrow \text{H} + \text{H} + \text{M}$	H.5.M
$\text{O} + \text{O} + \text{M} \leftrightarrow \text{O}_2 + \text{M}$	H.6.M
$\text{O} + \text{H} + \text{M} \leftrightarrow \text{OH} + \text{M}$	H.7.M
$\text{H}_2\text{O} + \text{M} \leftrightarrow \text{H} + \text{OH} + \text{M}$	H.8.M
$\text{H} + \text{O}_2 (+ \text{M}) \leftrightarrow \text{HO}_2 (+ \text{M})$	H.9.M
$\text{HO}_2 + \text{H} \leftrightarrow \text{H}_2 + \text{O}_2$	H.10
$\text{HO}_2 + \text{H} \leftrightarrow \text{OH} + \text{OH}$	H.11
$\text{HO}_2 + \text{O} \leftrightarrow \text{O}_2 + \text{OH}$	H.12
$\text{HO}_2 + \text{OH} \leftrightarrow \text{H}_2\text{O} + \text{O}_2$	H.13
$\text{HO}_2 + \text{HO}_2 \leftrightarrow \text{H}_2\text{O}_2 + \text{O}_2$	H.14
$\text{H}_2\text{O}_2 (+ \text{M}) \leftrightarrow \text{OH} + \text{OH} (+ \text{M})$	H.15.M
$\text{H}_2\text{O}_2 + \text{H} \leftrightarrow \text{H}_2\text{O} + \text{OH}$	H.16
$\text{H}_2\text{O}_2 + \text{H} \leftrightarrow \text{HO}_2 + \text{H}_2$	H.17
$\text{H}_2\text{O}_2 + \text{O} \leftrightarrow \text{OH} + \text{HO}_2$	H.18
$\text{H}_2\text{O}_2 + \text{OH} \leftrightarrow \text{HO}_2 + \text{H}_2\text{O}$	H.19

Reactions among species H, O, OH, HO₂, H₂, O₂, H₂O, and H₂O₂. Species Ar, He, and N₂ are also included as otherwise non-reactive participants in three-body reactions.

This reaction list follows a modified listing from the study of Burke *et al.* (2012); additional, excluded reactions among the enumerated species are discussed therein. Double-headed arrows indicate reactions are considered to proceed in either direction. Reactions involving third-body collider M may proceed with rates that are linearly dependent on the concentration of M (*e.g.*, in the low pressure limit) and dependent on the identity of M. Reactions additionally indicated with parentheses around M are considered to proceed at rates with complex dependencies on both the identity and concentration of M. Species commonly specified for M include Ar, He, N₂, H₂, H₂O, O₂, CO, and CO₂. Under strict hierarchical construction, these latter two species correspond to CO-rank chemistry as developed above. However, their association with three-body reactions in the H₂ chemistry subset is a matter of organizational clarity and shall be no cause for confusion.

Table 1.2 – CO chemistry subset used in this thesis

Elementary Reaction	Reaction Reference
$\text{CO} + \text{OH} \leftrightarrow \text{CO}_2 + \text{H}$	C.1
$\text{CO} + \text{O}_2 \leftrightarrow \text{CO}_2 + \text{O}$	C.2
$\text{CO} + \text{HO}_2 \leftrightarrow \text{CO}_2 + \text{OH}$	C.3
$\text{CO} + \text{O} (+ \text{M}) \leftrightarrow \text{CO}_2 (+ \text{M})$	C.4.M
$\text{HCO} + \text{M} \leftrightarrow \text{H} + \text{CO} + \text{M}$	C.5.M
$\text{HCO} + \text{O}_2 \leftrightarrow \text{CO} + \text{HO}_2$	C.6
$\text{HCO} + \text{H} \leftrightarrow \text{CO} + \text{H}_2$	C.7

Reactions among CO, HCO, CO₂ and several species from the H₂ chemistry subset, which are indicated in bold to indicate the strong hierarchical overlap between CO and H₂ chemistry submodels.

This reaction list follows a modified scheme from the study of Li *et al.* (2007). Several reactions involving HCO reacting with HCO, HO₂, OH, and O radicals do not appear necessary to predict observed ignition, burning, or species evolution behavior across the wide parameter space of H₂/CO systems considered in this thesis. Under the present hierarchical construction, these reactions effectively belong to CH₂O rank chemistry and are not explicitly considered further. Chapter 5 discusses the reaction of CO + OH to form HOCO, as well as subsequent reactions involving the HOCO molecule and species from the H₂/CO chemistry subsets.

Table 1.3 – NO_x chemistry subset discussed in this thesis

Elementary Reaction	Reaction Reference
H + NO ₂ ↔ OH + NO	N.1
HO ₂ + NO ↔ OH + NO ₂	N.2
H + NO (+ M) ↔ HNO (+ M)	N.3.M
OH + HONO ↔ H ₂ O + NO ₂	N.4
O + NO ₂ ↔ O ₂ + NO	N.5

Species from the H₂ chemistry subset are indicated in bold to highlight the hierarchical overlap between NO_x and H₂ chemistry submodels.

Dozens of reactions describe interactions of NO_x species with either other NO_x species or species participating in the H₂/CO chemistry subsets (*e.g.*, Mueller *et al.*, 1999b). Consequently, only those reactions relevant to later discussion in this thesis are tabulated here.

Part I

Chapter 2: A High Pressure Laminar Flow Reactor for Chemical Kinetic Studies

A high pressure laminar flow reactor facility (HPLFR) has been developed as part of this thesis work to study combustion-relevant chemistry of small molecules. Experiments in the HPLFR generate stable reactant/intermediate/product species concentration profiles as a function of axial position in the reactor test section and can access temperatures up to 1000 K, pressures from ~1-30 atm, and residence times spanning tens of milliseconds to several seconds. Under appropriate operating conditions, species-position profiles can be interpreted as species-time profiles, which can be used to extract fundamental rate coefficient information (e.g., Haas & Dryer, 2015) or provide overall reaction progress validation data for combustion chemistry modeling (e.g., Burke *et al.*, 2014). There are dozens of flow reactor/flow tube facilities described in the kinetics literature, and it is impractical to compare the HPLFR to each of these. Some comparisons to similar high pressure (≥ 1 atm), steady-flow, species-resolving flow reactor facilities will be discussed below to illustrate important or unique features distinguishing the HPLFR from among other flow reactor facilities.

Other canonical experimental configurations, such as shock tubes, rapid compression machines, static and well-stirred reactors, and laminar flames, are also used to study combustion chemistry under (presumably) well-defined conditions. These general reactor configurations are reviewed elsewhere (e.g., Held, 1993) and so will not be discussed in detail here. However, it is important to recognize that each of these reactor configurations may permit access to unique measurements or reaction conditions that the other configurations cannot readily achieve. As such, this ensemble of reactor types can provide complimentary measurements to improve understanding of combustion chemistry.

2.1 HPLFR Facility Overview

The HPLFR is the latest in a series of flow reactor facilities developed for combustion chemistry studies at Princeton, beginning with the atmospheric pressure turbulent flow reactor facility initially described by Crocco *et al.* (1959). This original reactor has evolved through several iterations into the variable pressure flow reactor facility (VPFR), a turbulent flow system initially described in the thesis of Vermeersch (1991) and which is the immediate predecessor to the HPLFR.

The design of the HPLFR takes some inspiration from features of both the VPFR as well as the Technical University of Denmark (DTU) laminar flow reactor described by Rasmussen *et al.* (2008). The HPLFR borrows the approximate size and premixed laminar flow conditions of the DTU facility but departs significantly in design of both the reactor duct (described in Section 2.3) as well as the flow sampling technique, which is similar to the VPFR convective quench probe design. Though there are some additional similarities between the VPFR and HPLFR, the list below highlights several key *differences* in design aspects of the HPLFR and its VPFR predecessor:

- Size – relative to the VPFR and earlier Princeton flow reactors, the HPLFR is of significantly smaller geometric scale.
- Reactant Resources – the HPLFR has been designed to operate under a laminar flow regime and consume total reactant flow rates on the order of 1-25 standard liters per minute (slpm), whereas the VPFR consumes several hundred slpm of total flow to support turbulent mixing of reactants and nearly uniform radial species and temperature profiles.
- Species/Thermal Mixing – reactant feed to the HPLFR is premixed well upstream of the test section at temperatures significantly below the nominal reaction temperature. Well-mixed HPLFR reactants share the same thermal history as they approach the test section entrance. In the VPFR, reactants of dissimilar temperatures meet at the test section entrance, where species and thermal mixing is facilitated through turbulent transport (local $Re > 10^4$). At the mixing point in the VPFR, fuel concentrations may be an order of magnitude higher than the well-mixed average, and local temperature gradients may be hundreds of kelvin over the span of a few centimeters.
- Reactor Walls – the HPLFR has been designed to accommodate ducts of varying materials, sizes, and shapes to contain the reacting flow. The VPFR uses a permanent cylindrical quartz duct of ~10 cm inner diameter.
- Bath Gas – the relatively low flow rates and indirect wall heat transfer design employed by the HPLFR permit experiments using a variety of bath gases, including species containing oxygen or carbon (*e.g.*, CO, CO₂, and CH₄). Flow rate, pressure, and heater constraints of the VPFR design practically limit experiments to use of N₂, though Mueller *et al.* (1998) report some experiments in Ar.

These particular design attributes have been specifically considered in the development of the HPLFR in order to realize certain advantages over the earlier VPFR design:

- Smaller geometric and flow scales associated with the HPLFR permit experiments with certified gas mixtures or rare/expensive reactants, neither of which would be feasible in the VPFR. Overall operation and maintenance costs are also significantly lower.
- The thermal and species mixing gradients in the VPFR may confound definition of the initial reaction conditions in this system. For example, oxygenated fuels have been shown to be particularly susceptible to accelerated reaction in the VPFR mixing section (e.g., Haas *et al.*, 2009 and Lefkowitz *et al.*, 2012). The HPLFR mixing concept aims both to avoid the gradients inherent in the VPFR mixing process as well as to control effects of surface reaction through choice of wall material, duct diameter, *etc.*
- Flexibility in the specification of the HPLFR reactor duct and bath gas also permits a greater variety of experiments than are accessible in the VPFR. Experiments involving variation of the duct may include those considering *intentional* surface reactions on the duct wall.

Despite these apparent advantages, there are tradeoffs inherent in the HPLFR design. The most important of these is the additional potential complexity in interpreting the coupling between the laminar flow field and the chemical source term, discussed further in Section 2.5 and in Dryer *et al.* (2014). This coupling itself depends on several factors including the duct size and bath gas and so it is apparent that the advantage of added experimental flexibility may result in a disadvantage of increased complexity for experimental interpretation.

Well-designed experiments can capitalize on the advantages of the HPLFR facility design while minimizing impact of non-idealities. Towards informing the design of future experiments in the HPLFR, the following sections describe the HPLFR facility in more detail, and the rest of this section provides a general summary of the facility.

NOTE: The HPLFR accesses high pressures and temperatures, and handles a variety of reactants that may be potentially hazardous either alone or in mixtures with other reactants. Accordingly, safety considerations are indicated bold script in the descriptions provided throughout the rest of this chapter.

Figure 2.1 presents a general schematic of the HPLFR with major subsystems indicated. A PID-thermostatted three-zone tube furnace encloses a 1.5 in. OD stainless steel pressure shell, which in turn encloses the reactor duct. This duct is fed by a steady flow of premixed, preheated gaseous reactants from the Feed/Calibration Subsystem. Reactants that are normally liquid at ambient conditions can be evaporated and also incorporated into the gaseous reactant feed. Under conditions favoring reaction, this premixed gas feed converts into products in the duct and subsequently exhausts from the reactor. A back pressure regulator at the exhaust controls pressure in the duct, and some pressurized exhaust bleeds into the annular space between duct and pressure shell to maintain pressure equilibrium across the duct wall. This bleed feature is particularly important when the duct is made of relatively fragile materials and cannot sustain a large pressure difference across its wall.

A hot water-cooled, convection quench probe with integrated thermocouple extracts a small, quenched, continuous sample flow from a fixed axial coordinate in the duct test section. This flow passes through heated transfer lines to the Sample Analysis Subsystem. This presently consists of a pressure-regulated online FTIR spectrometer/micro gas chromatograph (micro GC) analytical system, which permits identification and quantification of stable species of interest. However, the modular nature of the HPLFR facility may permit other diagnostics to be used singly or in combination with the current FTIR/micro GC setup. A screw drive translates the probe axially through the duct, enabling sample collection along the duct axis. The relatively higher pressure inside of the HPLFR drives sample flow through the probe into the Sample Analysis Subsystem, which is held slightly above atmospheric pressure to prevent contamination from the ambient atmosphere.

2.2 Feed/Calibration Subsystem

A high pressure syringe pump and four thermal mass flow controllers provide up to five independently controlled reactant feeds for HPLFR experiments or analytical equipment calibrations. A sixth flow, regulated and metered by systems external to the HPLFR facility, may also be employed for HPLFR experiments/calibrations. These flows premix in the feed/calibration panel, and the product mixture is conveyed to the Reactor Subsystem through an insulated, high-pressure rated heated transfer line. The product flow may also be diverted directly to the Sample Analysis Subsystem for calibration purposes. This Feed/Calibration Subsystem enables substantial flexibility in experiments accessible to the HPLFR, especially when using precision-mixed specialty gas feeds. Figure 2.2 shows a schematic of this subsystem. **Specific health, flammability, and reactivity hazards of each individual reactant and its anticipated behavior upon mixing with other reactants under high pressure, elevated temperature conditions must be considered when designing and operating HPLFR experiments.** Certain reactants such as silane (SiH_4) or concentrated NO_x species may not be appropriate for use in the HPLFR without additional modifications to the facility.

2.2.1 Gas Reactant Metering

Four Swagelok model SS-4BHT-36 Teflon-lined, stainless steel braid-encased hoses connect high pressure gas reservoirs to the feed/calibration panel. Gas flows first pass through normally-open Swagelok model SS-43GS4 manual quarter-turn isolation valves. **These isolation valves separate the gas reservoirs from the rest of the HPLFR facility and can be rapidly closed to cut off gas supply in case of emergency.** From these isolation valves, individual gas flows pass to one of four Scott model 318E two-stage high purity gas regulators with a maximum nominal service pressures of 3000/500 psig input/output, enabling reactant flows up to the ~425 psig (30 atm) HPLFR design pressure. Each regulator supplies a Brooks model 5850 thermal mass flow controller (MFC) configured for an input pressure of up to 500 psig. Use at lower input pressures may limit the maximum flow that can be provided by an individual MFC to values below the device rating. However, a low input pressure may be desirable for extending useable gas bottle contents when reactants are provided at lower pressure (*i.e.*, CO_2 gas bottles limited to maximum sub-critical pressures of ~600 psig). The MFCs are powered and controlled through a Brooks model 0254 interface with RS-232 control capability presently unrealized in

the HPLFR system. Manual control at the interface device has been adequate for all experiments described later; although (semi)automated operation is envisioned as a further enhancement of the facility.

The MFCs are nominally sized at 20, 4, 0.5, and 0.5 slpm maximum flow rates for N₂, O₂, H₂, and CH₄ flows, respectively. In practice, gas identity assigned to the MFCs is not particularly important since, prior to each experiment, flows of actual reactant gases (pure or multi-component) are calibrated to standard conditions (273 K, 1.00 atm) using a Bios DryCal model DC-2 volumetric flow calibration cell or an Agilent Optiflow 650 bubble flow meter. Flow rate ranges for gases other than specified can be estimated based on widely available K-factors tabulated for thermal MFCs and subsequently verified by calibration.

The nominal turndown ratio for total gas flow rate produced from this MFC ensemble is 250:1, taking the sum of the MFC nominal flows as an upper accurate operational bound and 100 sccm as the lower accurate operational bound associated with the operation of a single 0.5 slpm MFC. This turndown ratio complements the ~30:1 and ~2:1 turndown ratios in reaction pressure and temperature, respectively, enabling a large range of plug flow residence times to be accessed by the HPLFR. However, practical residence times are limited by a host of additional considerations such as the chemical timescales of the reacting system of interest, provision of adequate sample flow to the gas analyzers, maintenance of a desirable flow velocity/thermal profile in the HPLFR duct, delivery of sufficient enthalpy to the evaporator module, and ability to create accurate gas mixtures using the MFCs. This latter consideration has been successfully addressed by using accurate, commercially available reactant premixtures, which have become relatively inexpensive to use due to the significantly lower flow rate requirements of the HPLFR compared to the VPFR.

2.2.2 Liquid Reactant Metering

A gas-blast evaporator, custom-built with the same essential hardware as the liquid evaporator used in the VPFR, couples with a Harvard Apparatus model PHD 22/2200 high pressure syringe pump and the 20 slpm MFC flow stream to deliver to the HPLFR vaporized reactants that are liquid at ambient conditions. **While the gas-only feed system is rated in excess of 500 psig, this evaporator is rated to only 100 psig (~7.5 atm), which must not be exceeded when the evaporator is connected to the**

rest of the gas feed system. The evaporator must be isolated from such high pressure streams using built-in isolation valves. All lines downstream of the evaporator up to the heated transfer line are heat-traced with PID-thermostatted heat tape to prevent vapor condensation.

The syringe pump feeding the evaporator is equipped with a set of 200, 50, 20, 8, and 2 mL stainless steel syringes, permitting precise volumetric dosing of liquid reactants to the evaporator system with several orders of magnitude isolated flow rate turndown ratio. Similar to the MFC-only subsystem discussed above, several practical considerations limit turndown in the built system and so a new evaporator is under development towards expanding the operability limits afforded by the present one.

Reactants from the gas streams and evaporator premix in the line volumes of the feed/calibration system and exit the panel through a Swagelok model SS-43GXS4 three-way valve. This valve selects a flow path either to the Reactor Subsystem through a high pressure Conrad Company series CH67 insulated, heated, Teflon-lined transfer line or directly to the Sample Analysis Subsystem via temporary lines used for device calibration.

2.2.3 Uncertainties in Flow Rate and Composition

This and following discussions of uncertainty assume normally-distributed, unbiased, independent measurement errors, permitting summation of uncertainties in quadrature. The uncertainty of sensitive parameter measurements due to systematic bias has been addressed by repeating measurements using independent sources and/or measurement devices.

Flows from the Feed/Calibration Subsystem MFCs are calibrated using either of the subsequently described DryCal or Optiflow gas flow rate calibration devices. Both of these devices measure volumetric flow rate at near-ambient conditions, permitting ideal gas law correction of actual volumetric flows to standard volumetric/mass/molar units. Respective accuracies for these devices are 1.4 and 2% of reading, according to the manufacturers.

The DryCal unit, used for flows of 0.5-30 slpm, automatically compensates actual volumetric flow readings to standard temperature and pressure, while the Optiflow unit does not. The Optiflow requires additional manual flow rate correction for temperature and pressure variations, although corrections from on-site mercury barometer and thermocouple measurements contribute negligible additional uncertainty to the compensated Optiflow gas flow measurements. This device nominally measures flows from 5.0

sccm to 5.0 slpm, but the upper range is practically limited to ~2.0 slpm, beyond which regular bubble formation was found to be unreliable.

To rule out significant bias in flow calibration accuracy, nitrogen flow measurements using the same MFC to control flow were made with both the Optiflow and DryCal units for their overlapping flow rate range (*i.e.*, 0.5-2.0 slpm). For the same nominal MFC flow rate, Optiflow measurements deviated on average ~1.3%, and no greater than ~2.3%, from DryCal measurements. These values are well within joint flow rate uncertainties ascribed to the calibration devices and the MFC suggesting that both calibration devices provide accurate flow rate measurements.

Each MFC is typically used at or above 20% of nominal full scale and at these conditions contributes approximately 1% uncertainty to the flow rate set point, according to the manufacturer. Since MFCs are calibrated *for each experiment* using actual reactant gases, negligible uncertainty due to calibration drift or gas composition is expected. If uncertainties due to individual flow rate calibration (2%) and individual MFC set point precision (1%) are summed in quadrature, the relative uncertainty $\Delta Q/Q$ in flow rate Q of an individual gas flow j is ~2.25% of reading. This figure permits computation of uncertainty attributable to total gas flow rate as well as mixture composition. In practice, this will depend on the flow rates and compositions of individual gas streams. For four gas streams with MFC-controlled flow rates, the relative uncertainty $\Delta Q/Q$ in total volumetric gas flow rate will be

$$\Delta Q/Q = 0.0225 \sqrt{Q_1^2 + Q_2^2 + Q_3^2 + Q_4^2}/Q, \quad (2.1)$$

where Q is the total gas flow rate and some of the Q_j may be zero. By the triangle inequality, $\Delta Q/Q$ will not exceed 2.25%.

The relative uncertainty $\Delta X_i/X_i$ in mole fraction of species i in the *combined reactant feed flow* Q can likewise be computed as the quadrature-summed relative uncertainties of x_i , Q_j , and Q .

$$X_i = (x_i Q_j)/Q \quad (2.2)$$

$$\Delta X_i/X_i = \sqrt{(\Delta x_i/x_i)^2 + (\Delta Q_j/Q_j)^2 + (\Delta Q/Q)^2}. \quad (2.3)$$

Here species i is initially associated with gas stream j , in which it appears with mole fraction x_i . When pure component gases are used for species i , the first term of the radicand in Equation 2.3 contributes negligible uncertainty; however, 1-2% uncertainties are usually associated with this term for species i present in specialty gas blends. Given maximal relative uncertainties of 2.25% each in the latter radicand terms, representative *maximal* uncertainties in the species i mole fraction X_i are ~3.25 and 3.75% for the cases of pure component and specialty gas blends, respectively. Further manipulations are possible, for example, to determine ΔX_i if species i appears in multiple gas streams.

Uncertainty results computed by Equation 2.3 are conservative since the second and third terms in the radicand are not actually independent. In particular, for the case when a pure component carrier gas stream j is used such that flow $Q_j \approx Q$, only the third term under the radicand is relevant and uncertainty in X_i is essentially maximally bounded by the same 2.25% that bounds individual flows.

The syringe pump/evaporator system introduces into the combined feed flow any reactants that are liquid at room temperature and pressure. This situation little affects the formal flow rate and mole fraction uncertainty analysis presented above, although issues such as condensation or presence of bubbles in the liquid could drastically affect this assessment. For this reason, great care is taken to de-bubble liquid reactant charges as well as prevent condensation in any of the HPLFR subsystems.

Since the syringe pump meters flow on a volumetric basis, liquid density (mass or molar) is used to convert the volumetric flow into conserved units. Most liquid densities tend to be relatively insensitive to small variations in temperature and generally remain within 1% of room temperature density even for large excursions (~10°C) from nominal 298 K “room” temperature. These liquids likewise have low bulk moduli and may be considered ideally incompressible with regard to computing mass/molar flow rate. Overall uncertainty in pure component liquid reactant flows due to both density variation and the pump system itself is estimated at 2%, leading to a ~3.75% uncertainty in overall mole fraction X_i in the combined reactant feed flow similar to the case for specialty gas blends. However, there exist notable exceptions to the assumed idealities for liquid reactant handling, including cases for liquids approaching their freezing or boiling points at the handling temperature, such as tertiary-butanol (e.g., Lefkowitz *et al.*, 2012) or methyl formate. Liquids such as these were not used in the present work but may be considered in future work.

2.3 Reactor Subsystem

Figure 2.3 shows a schematic of the Reactor Subsystem. This is comprised of a custom-built reaction vessel mostly contained inside wall-mounted, vertically-oriented Thermcraft model XST-3-0-36-3C three-zone tube furnace. An Aramid-insulated heat tape (**maximum temperature ~300°C**) wrapped around the lower (input) head of the pressure vessel serves as an additional zone for flow preheating. The oven zones and preheater are controlled to set point temperatures by separate PID temperature controllers, enabling some measure of spatial temperature profile tuning along the reactor axis.

The vertically-mounted oven contains a type 347 stainless steel pressure shell, which itself contains the reactor duct. The duct contains the reacting flow to be studied and is supplied reactant feed by the heated transfer line from the Feed/Calibration Subsystem. Flow direction in the duct is from bottom to top, which aligns buoyant and forced convection components of the flow. A hot water-cooled sample probe penetrates the reactor through an on-axis seal at the top of the pressure shell and can translate axially through the reacting flow. It directs a continuous, quenched sample of the flow to the Sample Analysis Subsystem. Unsampled flow both exhausts the reactor through the upper head and fills the annular volume between pressure shell and duct, maintaining essentially equal pressure across the duct wall. Since the pressure shell, duct, and sample probe have been custom-engineered for the HPLFR facility, each of these is described in detail below.

2.3.1 Pressure Vessel

The pressure vessel assembly essentially consists of a 43.5 in. long, 1.50 in. OD, 1.31 in. ID seamless SS347 tube welded to SS347 ANSI B16.5 class 1500 weld neck flanges. Ends of the pressure vessel are sealed using size R-20 metal ring type joint (RTJ) seals, bolted between the weld neck flanges and corresponding class 1500 blind flanges. These blind flanges are modified to accommodate the duct, internal seals, and flow pathways for reactants, exhaust, *etc.* Relative to the VPFR design, this pressure vessel permits easy disassembly and cleaning, and facile replacement of different reactor ducts (geometries and/or materials). The ability of the HPLFR to intentionally accommodate ducts of different diameters, flow geometries, and material construction makes this facility unique among existing flow reactor facilities.

Type 347 stainless steel was selected as the principal pressure vessel construction material for both its high temperature mechanical properties and availability. Compared to more common SS304 and SS316 stainless steel alloys, niobium-stabilized SS347 resists intergranular chromium carbide precipitation to temperatures several hundred degrees higher – up to 1089 K (816 °C). According to the tube stress equations for the HPLFR geometry and SS347 material specified, the relatively thin tube walls (0.095 in.) of the pressure vessel assembly can withstand pressures well in excess of the 30 atm (~425 psig) nominal reactor rating over most of the 500-1000 K HPLFR operating temperature range. However, at temperatures above 866 K (593 °C), maximum allowable stress in the metal decreases in an Arrhenius-like manner (ASME, 2007), substantially de-rating the maximum pressure for the pressure vessel.

Maximum allowable HPLFR pressure is temperature-dependent and should not be exceeded upon peril of catastrophic vessel failure! Figure 2.4 contains additional details for recommended pressure-temperature operating conditions.

Based on ASME temperature-stress relationships for SS347, the maximum allowable pressure-temperature relationship for the HPLFR pressure vessel above 866 K is given by the empirical, dimensional equation

$$P_{max} [\text{psig}] = ((1.82 \times 10^6) / T[\text{K}]) - 1735 \quad (2.4)$$

for a minimum design factor of safety of 2.5. Here P_{max} is the maximum allowable pressure in the pressure vessel and T is the maximum pressure vessel temperature. **Maximum allowable pressure at 1000 K (the highest HPLFR design temperature) is ~85 psig ≈ 6.75 atm (absolute).** A cautionary sign has been added to the HPLFR furnace temperature controller module as an explicit warning for users to carefully consider operating at temperatures in excess of 866 K (593 °C).

To extend the temperature-pressure operating range, future iterations of the HPLFR reactor vessel might include either thicker walls for SS347 or tube replacement with a superalloy such as Inconel or Hastelloy. Neither thicker-walled SS347 nor these specialty alloys were available options at the time of present pressure vessel construction. However, tube replacement with either of these options is a

straightforward process involving removal of the weld-neck flanges from the present tube. These reclaimed flanges can be re-welded to the replacement tubing.

The fabricated pressure vessel assembly passed an ambient-temperature hydrostatic pressure test (hydrotest) conducted by Marshall Industrial Technologies (Trenton, NJ) to 2200 psig (~151 atm, absolute pressure). Since the hydrotest occurred near room temperature, this specific hydrotest pressure was targeted to correspond to pressures well above those given by Equation 2.4 after temperature adjustment. After hydrotesting, the pressure vessel was installed inside the tube furnace, filled with N₂, and temperature-pressure cycled within its T-P_{max} limits to determine both high temperature leak-fastness and thermal expansion effects. Negligible leaking was detected during temperature-pressure cycling. However, 12-16 mm axial lengthening was measured at a nominal furnace temperature 1000 K, indicating that thermal expansion is an important consideration for HPLFR design. The duct sealing system discussed below further considers thermal expansion effects since differential thermal expansion between pressure vessel and duct may lead to duct failure.

2.3.1.1 Pressure Relief Hardware

The installed pressure vessel assembly has additional safety features, which are indicated in Figure 2.3 and described in this subsection. The annular space between the pressure vessel and duct communicates directly through the lower (input) reactor head to a pressure relief manifold, comprised of a 500 psig rupture disc, adjustable relief valve currently set at ~450 psig, and fixed pressure relief valves set to relieve at 175 and 80 psig. In the event of pressure regulator failure or other unforeseen high pressure excursion, vessel overpressure is limited by the 450 psig relief valve and burst disc, which are sized for flows well in excess of those provided by the Feed/Calibration Subsystem. **The additional relief valves are intended for use as pressure limiters when the pressure shell is operated at high temperatures and can be engaged/isolated by manual block valves for experiments between 866-950 K (175 psig) and 950-1000 K (80 psig).** These temperature-pressure pairings are further discussed in the details of Figure 2.4.

2.3.2 Reactor Duct/Duct Sealing System

2.3.2.1 Duct Seals and Consideration of Thermal Expansion

A specially-designed internal sealing system enables the pressure vessel to be outfitted with ducts of different materials and geometries, according to intended research objective. Axial pockets

machined into the blind flanges sealing either end of the pressure vessel accommodate ducts with end diameters of up to ~18 mm OD, while ID is determined by duct material robustness (quartz versus stainless steel, *etc.*) or the 6.4 mm (0.25 in.) OD sampling probe. Seal designs for the upper and lower pockets are duct-specific and not elaborated on here, though it is important to note that seals for the exhaust (top) end of the reactor must permit (1) penetration by the moving sample probe, (2) exhaust flow to the back pressure regulator that sets the reactor pressure, and (3) flow communication with the annular space to equalize pressure differences across the duct wall.

Differential thermal expansion of the pressure shell relative to the duct, particularly for dissimilar materials such as SS347 and quartz, may lead to failure of the Reactor Subsystem and therefore must be accommodated. By design, the lower seal is intended to act as a fixed point from which thermal expansion occurs, with the upper seal additionally providing an additional feature: (4) minimal restriction of axial differential thermal expansion. However, empirical tests show that friction in the upper seal presently used in the HPLFR does not permit the free axial expansion specified by the design. Until this design issue is resolved, **the HPLFR cannot be used for experiments involving on-the-fly temperature changes. To avoid excessive stresses imposed by thermal expansion, the nominal reactor temperature must be varied according to the HPLFR Temperature Change Procedure described immediately below.** Future improvement to the HPLFR facility includes developing an upper seal with demonstrated ability to simultaneously satisfy requirements (1)-(4) described above, thereby permitting on-the-fly temperature changes during HPLFR experiments. Despite the present limitation, the current upper seal design is still quite versatile as it does permit on-the-fly changes for reactor pressure, axial sampling position, flow rate, and initial reactant composition.

HPLFR Temperature Change Procedure

To change the nominal reactor temperature, the reactor is first depressurized and flow is stopped and then the *bottom seal* is disengaged. The tube furnace temperatures are modified to the desired set points, and the Reactor Subsystem is allowed to differentially expand to the new equilibrated temperature set point (generally for several hours) before the bottom seal is replaced and experiments can proceed.

2.3.2.2 Duct Design

The internal diameter of the pressure vessel limits maximum duct diameter to ~32 mm between the 18 mm OD pocket/seal constraints. This sealing system permits experimental flexibility for HPLFR experiments that is essentially inaccessible to the DTU and VPFR designs, among other existing flow reactor facilities. Modifying the duct enables studies of the effects of wall-reaction coupling and flow profile, among others. Moreover, duct geometries are not restricted to simple tubes; a jet-stirred reactor (JSR) similar in design to the prolific CNRS JSRs (Dagaut *et al.*, 1986) can be accommodated by the pressure vessel and seals. Figure 2.5 suggests some additional examples of duct geometries accommodated by the pressure vessel duct sealing system. At present, two duct geometries and two duct materials have been considered in depth for HPLFR implementation.

A simple constant-area circular tube was initially proposed for the HPLFR duct geometry, following the DTU flow reactor design. Though mechanically simple, this straight duct geometry poses a thermalization problem for the premixed reactant flow similar to the problem discussed in Dryer *et al.* (2014). Both this problem and the present solution employed in the HPLFR are explained semi-quantitatively below. General quantitative analysis of such thermalizing flows is context-specific and beyond the scope of the present thesis. Such analysis itself merits further experimental and numerical study across a large parameter space of internal flow geometries, heat transfer environments, reactant mixtures, and flow regimes. Nonetheless, the present scaling arguments reveal leading-order considerations in the present reactor duct design.

Assuming an initially plug flow profile developing in a simple circular duct under laminar flow conditions, the thermal entry length $L_{e,th}$ and mean residence time $\tau_{e,th}$ for the flow to achieve nominal reaction temperature T_f from the initial preheat temperature T_0 are approximately

$$L_{e,th} = 0.05 D Re_D Pr \quad (2.5)$$

$$\tau_{e,th} = 0.05 D^2 Pr/\nu \quad (2.6)$$

where D is the duct diameter, Re_D is the diameter-based Reynolds number commonly used for pipe flows, Pr is the Prandtl number of the premixed gas, and ν is the kinematic viscosity of the flow. The temperature difference $T_f - T_0$ may be several hundred kelvin, over which characteristic chemical reaction

times may vary by several orders of magnitude with either Arrhenius-like or non-monotonic (*i.e.*, with negative temperature coefficient) dependencies.

The plug flow residence time $\tau_{e,th}$ in this heat-up region can be a significant fraction of the total reaction time at the nominal reaction temperature T_f . Consider a representative HPLFR flow with Re_D of 300 and Pr of 0.7 passing through a 1.0 cm ID duct of uniform wall temperature T_f . By Equation 2.5 the thermal entry length is 10.5 cm, or about 20% of the ~50 cm long HPLFR test section. The plug flow residence time spent in heat-up is then ~20% of the total plug flow reaction time, during which significant reaction of the premixed reactants may occur in the entry length zone. Although the plug flow assumption employed here is an expedient idealization for a 2-dimensional steady flow process, it still highlights the potentially severe non-ideality in initialization of the reactions to be studied at T_f . Accurate characterization of this potentially reacting entry length flow is complicated by the highly non-linear coupling of the 2-dimensional flow, temperature, and reaction fields, and interpretation of observables measured in the entry length or at downstream locations may be especially confounded. The recent review of Dryer *et al.* (2014) discusses such thermalization issues at length.

To overcome complications of thermalization processes in the straight duct, a tapered design like the one suggested by Figure 2.3 was developed for use in the HPLFR. For constant mass flow rate and fluid properties, the thermalization residence time $\tau_{e,th}$ scales quadratically in duct diameter while the entry length $L_{e,th}$ remains constant. Hence a reduction in the diameter of the entry length section of the duct relative to the diameter of the test section can be used to quickly bring the reactant premixture up to the nominal reaction temperature T_f while remaining inside the spatial $L_{e,th}$ constrained by the HPLFR pressure shell and tube furnace. The present duct design employs a 1.0 mm ID preheat duct joined by a 5° half-angle conical diffuser to a 1.0 cm ID test section duct. Under the assumptions of the scaling argument employed above, this reduces $\tau_{e,th}$ to much less than 1% of the total test time, with an additional short residence time in the conical diffuser section. As demonstrated by experimental results in Chapter 3, this small overall heat-up time is often substantially exceeded by the chemical induction time of the reacting flow, in which case no measurable depletion of reactants occurs. For these cases, the initial flow conditions are reasonably taken to be the nominal reaction temperature, duct pressure, and reactant mole

fractions with appropriate allowance for time shift or initialization as detailed in the Supplement to the study of Zhao *et al.* (2008) or the review of Dryer *et al.* (2014).

The HPLFR duct initially tested was of this tapered geometry and constructed from SS347, the same material used for the HPLFR pressure shell. For a reactant mixture of 1.0/2.0/97.0% H₂/O₂/N₂, preliminary experiments at nominal initial conditions of 830 K and 10 atm showed up to ~30% conversion of H₂ to H₂O at seconds-long timescales for which no measureable reaction was expected. Moreover, the measured water profile was constant (within ±3%) along the duct axis, indicating no gas phase reaction beyond the diffuser section of the duct. These combined observations strongly suggest that the hot stainless steel duct acted as a surface catalyst for the H₂+O₂ reaction and that the catalysis was exacerbated by the very high surface to volume ratio of the preheat tube. Based on the results of this experiment, a tapered quartz duct was fabricated to replace the SS347 duct. Subsequent experiments made over the course of several years using diverse reactants (*e.g.*, H₂+O₂ in several bath gases with or without NO_x species, C₃H₆, *n*-C₃H₅OH) and a variety of reactor temperatures and pressures indicate no catalytic effects using quartz ducts. All HPLFR experiments later described employed tapered quartz ducts.

2.3.3 Sample Probe

A stainless steel hot water-cooled, wall convection quench sampling probe extracts a small, continuous flow from the duct test section to the downstream sample analysis system. As indicated in Figure 2.6, much of the probe is jacketed in a ¼" OD SS321 sheath (1), which serves to resist heat transfer between the hot duct walls and relatively colder internal surfaces, to act as a sealing surface for an O-ring in the top reactor head to separate the reactor environment and ambient atmosphere, and to provide mechanical rigidity to the probe during screw-driven insertion and withdrawal from the reactor. A coaxial 4 mm OD tube (2) extends 5 cm beyond the end of the sheath. This tube itself contains a bundle of three parallel 1.5/1.1 mm OD/ID tubes: a cooling water injection tube (3), a thermowell tube (4), and a sample/thermocouple tube (5). The sample/thermocouple tube penetrates the sealed end of the 4 mm tube tip, while the others remain inside the sealed end of the water cooling jacket.

Hot deionized water is pumped at ~7.5 psig into the water injection tube (3) by a thermostatted Excal EX-200DD circulating bath. Water exiting this internal tube impinges onto the inside of the sealed

probe end, where it passes across a fine gauge type-K thermocouple inserted through the thermowell tube (4) while returning to the circulation bath in the annular spaces between the internal tubes (3)-(5) and the inner wall of the outer tube (2). Due to phase change, water/steam flow in the annular space does not exceed ~ 112 °C as measured by the thermocouple in tube (4). This boiling temperature is consistent with the water injection pressure.

Sample flow passes through the sample port into tube (5), where it quickly quenches through heat transfer to the $\leq \sim 112$ °C walls imposed by the return water/steam flow in tube (4). Following Equation 2.6 above, a conservative quench time for a gas viscosity of $\nu \approx 20$ mm²/s (typical of HPLFR carrier gases near 400 K) is on the order of a few milliseconds, which is negligible compared to the uncertainty in flow residence time for all experiments described in this thesis. This sample flow quench is necessary to effectively stop chemical reaction at the local reactor temperature; for example, Arrhenius-type reactions with global activation energies of 20 and 40 kcal/mol slow by factors of $\sim 3 \times 10^5$ and $\sim 8 \times 10^{10}$ respectively when temperature decreases from 800 K to 400 K. The latter activation energy is close to that reported by Vermeersch (1991) for 1 atm H₂ oxidation around 900 K and is therefore relevant to experiments discussed in following chapters. Quenched sample flow is conveyed out of the probe, through a heated sample line, and to the Sample Analysis Subsystem described in more detail in the following section.

Temperature in the test section is monitored by a 0.010 in. OD Inconel-sheathed type-K thermocouple that passes through the end of the sample/thermocouple tube (5) and extends 5 cm beyond the probe tip. Extension of this thermocouple beyond the gas sampling port is intended to minimize conductive losses from the thermocouple bead to the relatively cold probe body. Analytical heat transfer analysis for a 1-dimensional cylindrical fin suggests that the $\sim 200:1$ length-to-diameter ratio precludes any conductive heat loss from the thermocouple junction to the probe body. Following the energy balance analysis adopted by Dryer (1972), radiative heating of the thermocouple bead is estimated to contribute around 6 K uncertainty to measured temperatures at the most extreme (~ 1000 K) conditions in the HPLFR assuming a radiative (wall) environment differing from the local gas temperature by 20 K and a conservative limiting emissivity of unity.

Additionally, diagnostic experiments at 530-663 K with non-dilute mixtures of N₂ and O₂ with each of H₂, CH₄, or CO were conducted to assess catalytic activity of the thermocouple. No gas phase reaction/heat release was expected at these conditions, and thermocouple measurements also showed no temperature rise due to catalytic activity of the Inconel thermocouple sheath. The apparent inertness of Inconel found in these diagnostic tests agrees with thermocouple catalysis experiments of Olsen (1962).

The sample probe assembly passes through the high pressure seal in the top head of the reactor shell and connects to a custom-built screw drive controlled by a precision stepper motor. This arrangement permits the probe to travel through a ~75 cm stroke along the duct axis and sample both flow and temperature, albeit offset by 5 cm. To establish a baseline experimental temperature profile before each experiment, temperatures along the duct axis are measured at the experimental pressure using a non-reacting flow with similar properties as the reactant mixture. In practice, this flow is usually the premixed carrier and fuel gas, from which the small O₂ flow (on the order of 1-2% of the total flow) has been subtracted to preclude reaction. This non-reacting flow essentially captures the hydrodynamic and heat transfer coupling of the O₂-included flow without imposing additional influences of chemical heat release, if any, on the baseline temperature profile measurement. Moreover, species mole fraction measurements of the non-reacting flow provide an end-to-end check of the HPLFR facility to rule out some catalytic effects when compared to mole fraction measurements of the same mixture taken from reactor-bypassed cold flow samples.

2.4 Sample Analysis Subsystem

Quenched sample flow passes from the sample probe through a heated (100 °C) 1/16" OD Teflon transfer line into the Sample Analysis Subsystem (Figure 2.7). Use of small diameter tubing reduces line volume, thereby reducing the overall response time of sample analysis. A needle valve upstream of the diagnostic instrumentation regulates the sample flow, enabling a steady sample flow rate and sample system pressure downstream of the valve for consistent analytical results. The sample flow rate is essentially governed by pressure drop through the sampling system such that the nominal sample system pressure measured at the outlet of the FTIR cell determines the flow rate through the sampling system.

Great care is taken during experiments to maintain analysis system temperatures and pressures well away from sample condensation limits, which is a particularly important consideration upstream of the needle valve where pressures may significantly exceed atmospheric pressure (Burke *et al.*, 2014).

Beyond the needle valve, sample flow first enters a Nicolet 550 Magna-IR FTIR spectrometer (henceforth, FTIR) outfitted with a 2 m pathlength gas analysis cell thermostatted to 100 °C and liquid N₂-cooled MCT/A detector suitable for quantitative analysis over 650-4000 cm⁻¹ with 0.241 cm⁻¹ resolution. The cell volume is ~200 cm³, which if modeled as a perfectly mixed volume, requires at least 1000 cm³ of steady sample flow purge to effectively achieve steady state. Hence, the time to acquire a sample depends on the sample flow rate as monitored by an installed downstream flow meter. The cell pressure is regulated by the needle valve to ensure tightly controlled number density in the gas cell and limit FTIR quantitation uncertainty due to overall gas concentration to under 1%. To ensure that NO_x species central to the HPLFR experiments described later do not react with FTIR cell windows and confound measurements, the KBr windows originally supplied with the gas analysis cell have been replaced with NO₂-compatible ZnSe windows.

From the FTIR spectrometer, sample flow passes through another 1/16" OD Teflon transfer line to a tee branching to either the sample flow exhaust or an Inficon series 3000 micro gas chromatograph (henceforth, micro GC) equipped with a heated sample inlet, heated backflush injectors, and Molsieve 5A, Plot U, and OV-1 columns. A pump internal to the micro GC draws only a small, intermittent quantity of the primary sample flow into the micro GC. In practice, this leads to a small perturbation in FTIR cell pressure for low sample flow rates. Effects of this perturbation are easily overcome by first taking FTIR measurements and then taking micro GC measurements.

FTIR spectrometry is capable of identifying and quantifying numerous stable infrared-active species relevant to small molecule combustion chemistry, including NO, NO₂, N₂O, H₂O, CO₂, CO, CH₄, and CH₂O, among others. However, two important factors limit the usage of the FTIR as the sole sample analysis tool: 1) several key species such as H₂ and O₂ are not IR-active and cannot be detected using this diagnostic, and 2) spectral bands of complex sample mixtures may overlap across the range of accessible wavenumbers. Overlap reduces detection sensitivity and accuracy for species having low mole fraction, weak absorptivity, or narrow absorption limits. This may be especially significant under

presence of high H₂O and CO₂ concentrations, where detector saturation or line broadening interferences may altogether obscure detection of other species. Uncertainties associated with quantitative FTIR measurements are therefore specific to species, calibration method, mole fraction, and experimental conditions, and are not prescribed here for the HPLFR facility in general.

The micro GC is employed to complement the FTIR for quantitative analysis. The backflush-equipped Molsieve columns separate H₂, O₂, CO and CH₄, while the other columns separate H₂O, CO₂, CH₂O, and N₂O, among other species. Both NO and NO₂ react on the columns and cannot be reliably detected by the micro GC. Species are quantified using thermal conductivity detection and gas mixture calibrations blended in the Feed/Calibration Subsystem or taken directly from premixtures certified by specialty gas vendors. For experiments described in the following chapter, tandem FTIR/micro GC species quantification from a single extracted HPLFR sample is conducted in less than 3 minutes, resulting in relatively fast data acquisition for the C₀-C₁ and NO_x species previously discussed.

2.5 Experimental Design Considerations in Use of the HPLFR Facility

The present section intends to illuminate the design of flow reactor experiments in very general terms and does not attempt to consider many of the condition-dependent departures from ideality that may arise in these experiments. More thorough treatment of such flow reactor non-idealities and interpretation of departure-affected flow reactor results may be found in the review of Dryer *et al.* (2014). Nevertheless, the following discussion still highlights the need for in-depth consideration of flow reactor operating conditions when interpreting experimental and simulation results.

Not all conceivable experiments conducted in the HPLFR will lead to straightforward interpretation of observed species versus axial position profiles, as is the case with other facilities which access a large parameter space of flow rates, reactant compositions, temperatures, pressures, time scales, flow regimes, *etc.* Each experiment therefore merits specific consideration of these factors and their coupling. In particular, the laminar conditions under which the HPLFR is intended to operate may present complications to the steady plug flow assumptions generally used to interpret isobaric axisymmetric turbulent flow reactor (*i.e.*, VPFR) results. The governing equations for species mole fraction and temperature scalars \mathbf{Y} under the idealized steady plug flow assumption take the form

$$U_{pl} \frac{d\mathbf{Y}}{dz} = \widehat{\boldsymbol{\omega}}(\mathbf{Y}). \quad (2.7)$$

This idealization assumes no axial diffusion and infinitely fast radial mixing such that at any axial location z , the velocity, species, and temperature fields are radially uniform. The axial location is related to flow time through a simple plug flow velocity transformation $z/U_{pl} = t$ such that

$$d\mathbf{Y}/dt = \widehat{\boldsymbol{\omega}}(\mathbf{Y}), \quad (2.8)$$

which enables zero-dimensional interpretation of spatially-resolved steady plug flow reactor data as an autonomous initial value problem (IVP) in \mathbf{Y} governed solely by the chemical kinetic source term $\widehat{\boldsymbol{\omega}}$ and corresponding initial conditions. The circumflex on $\boldsymbol{\omega}$ here indicates dimensional transformation consistent with the dimensions of $d\mathbf{Y}/dt$.

The purely axial plug flow velocity U_{pl} serves as the key assumption on which the relatively simple IVP of Equation 2.8 rests. For either developing or developed laminar flow, viscous effects impart a radial profile in the axial velocity such that additional terms must be added to those considered in Equation 2.7. Assuming fully developed laminar flow with constant transport properties and no radial velocity and following the perturbation analysis of Lee (1996) and qualifications therein, the dimensionless governing equation for mole fraction of species i (or, similarly, temperature) can be derived from an axisymmetric governing equation for conservation of scalars \mathbf{Y}

$$\rho U(r) \frac{\partial Y_i}{\partial z} - \rho D_i \left(\frac{1}{r} \frac{\partial}{\partial r} \left(r \frac{\partial Y_i}{\partial r} \right) + \frac{\partial^2 Y_i}{\partial z^2} \right) = MW_{avg} \boldsymbol{\omega}(\mathbf{Y}) \quad (2.9a)$$

to yield

$$\varepsilon u(R) \frac{\partial Y_i}{\partial Z} - \frac{1}{Pe_i} \left(\frac{1}{R} \frac{\partial}{\partial R} \left(R \frac{\partial Y_i}{\partial R} \right) + \varepsilon^2 \frac{\partial^2 Y_i}{\partial Z^2} \right) = \varepsilon \mathbf{D}\boldsymbol{\alpha}(\mathbf{Y}). \quad (2.9b)$$

Here ε is a small value (≤ 0.1) defined to be the inverse of the reactor aspect ratio defined by its inner diameter d divided by reactor length L ; $u = u(R)$ is the axial velocity relative to the mean U_{pl} ; R is the radial coordinate scaled by d ; Z is the axial coordinate z scaled by L ; D_i is the average diffusivity of species i relative to the rest of the flow; Pe_i is the Péclet number for species i defined as the product of the flow Reynolds number and species Schmidt number such that $Pe_i = U_{pl}d/D_i$; and Da is the Damköhler number

for the reacting system defined by the ratio of advective timescale L/U_{pl} to the characteristic reaction time based on the flow mass density ρ , mean molecular weight MW_{avg} , and relevant reaction rates embodied in the chemical source term $\omega(\mathbf{Y})$.

For the fully developed laminar flow assumed, several general operating regimes exist depending on the relative magnitudes of ε , Pe_i , and Da and their concerted influences on the axial advection, radial diffusion, axial diffusion, and reaction terms in Equation 2.9b. These three dimensionless parameters are defined by the reactor geometry and advection-diffusion-reaction properties for a given set of experimental conditions.

The small value assumption on ε is the important premise on which further illustrative perturbation analysis rests. The $\varepsilon \leq 0.1$ assumption underlying application of Equation 2.9b should be satisfied for the tubular geometries that can be accommodated by the HPLFR pressure shell as discussed above in Section 2.3. For the particular HPLFR experiments described in the following chapter, $\varepsilon \approx 0.02$ for the duct diameter and test section length employed.

To maximize the resolution of spatial/temporal sampling of a reacting system, well-designed flow reactor experiments typically operate at conditions for which the Damköhler number for major species is near unity. This condition effectively stretches the length of the reaction zone to be on the order of L . For the assumed $O(1)$ Damköhler number typical of flow reactor experiments, three operating regimes can be defined based on the relative ratios of ε and Pe_i , as discussed below.

2.5.1 Ideal Plug Flow Operation of Laminar Reactor

For $Pe_i \approx O(1)$ and $\varepsilon \ll 1$, radial diffusion dominates (to order ε^0) the other transport and reaction terms on the left and right sides of Equation 2.9b and admits a solution of $Y_i(r) = \text{constant}$. The mole fraction of species i follows a plug profile to leading order. The $O(\varepsilon^1)$ solution degenerates to

$$u(R) \frac{\partial \mathbf{Y}}{\partial Z} = \mathbf{Da}(\mathbf{Y}), \quad (2.10)$$

which can be integrated in R using the parabolic velocity profile of developed laminar tube flow to yield the zero-dimensional plug flow Equation 2.8 after appropriate dimensional transformation among mean flow velocity, axial distance, and time. Axial diffusion is of $O(\varepsilon^2)$ and can be neglected.

2.5.2 Axial Diffusion-Affected Plug Flow Operation of Laminar Reactor

For $Pe_i \approx O(\varepsilon)$ and $\varepsilon \ll 1$, radial diffusion also dominates (to order ε^{-1}) the other transport and reaction terms on the left and right sides of Equation 2.9b and admits a solution of $Y_i(r) = \text{constant}$. The mole fraction of species i follows a plug profile to leading order. After integration in R , the $O(\varepsilon^1)$ solution becomes

$$\frac{\partial \mathbf{Y}}{\partial Z} - \frac{\varepsilon}{Pe_i} \left(\frac{\partial^2 \mathbf{Y}}{\partial Z^2} \right) = \mathbf{D}\mathbf{a}(\mathbf{Y}), \quad (2.11)$$

in which axial diffusion appears as an additional term modifying the simple plug flow results described by Equations 2.8 and 2.10. Importantly, this solution retains the radial uniformity and IVP characteristics of the plug flow solutions. Measurements of $Y_i(z)$ can constrain the chemical source term, but the simple Eulerian-Lagrangian transformation $z/U_{pl} = t$ requires modification to account for axial diffusion effects that would tend to smooth out the ideal plug flow gradients of \mathbf{Y} .

2.5.3 2-Dimensional Operation of Laminar Reactor

For $Pe_i \approx O(\varepsilon^{-1})$ and $\varepsilon \ll 1$, the leading order solution no longer supports the plug flow solution $Y_i(r) = \text{constant}$. The magnitudes of radial diffusion, axial advection, and reaction are similar and are governed by the equation (to $O(\varepsilon)$)

$$u(R) \frac{\partial Y_i}{\partial Z} - \frac{1}{\varepsilon Pe_i} \left(\frac{1}{R} \frac{\partial}{\partial R} \left(R \frac{\partial Y_i}{\partial R} \right) \right) = \mathbf{D}\mathbf{a}(\mathbf{Y}). \quad (2.12)$$

Species mole fractions are governed by this partial differential equation in R and Z , which significantly complicates interpretations of experimentally measured $Y_i(z)$ data as it bears on illuminating the chemical source term. In general, such an experiment requires full 2-dimensional axisymmetric modeling to interpret measured species mole fraction results (e.g., Guo *et al.* (2013)). Due to associated computational costs and interpretive complexities, this operating regime is the least desirable of the three modes discussed.

2.5.4 An Important Caveat: Experimental Designs and Interpretation of HPLFR Data

As discussed throughout this chapter, the HPLFR can operate in a broad parameter space of temperature, pressure, flow rate, duct geometry, and reactant composition. The three operating modes described above are included for some intuitive generality in describing reactor operation; however, they

are neither rigorously derived nor do they completely describe the space of operating modes available when using the HPLFR. This latter point is elaborated upon in the following chapter in discussions of the Quasi-Steady State Plateau (QSSP) condition employed for measurement of certain elementary reaction rate coefficients.

In any case, design of future experiments to be conducted in this facility will benefit from consideration of the particular laminar reactor operating mode that may be accessed under planned experimental conditions as well as constraints imposed by experimental hardware, sample collection times, *etc.* In practice, experimental design can be advised through either or both of 1) iteration around conditions of prior successful experimental design and 2) chemical/physical model-advised conditions for experiments.

Prior consideration of experimental conditions may be helpful for the successful execution of experiments; however, posterior consideration of experiments is necessary to properly interpret measurements from the HPLFR facility. *The value of measurements taken from the HPLFR relies heavily on their careful interpretation.* Though this statement is true of any experimental measurements, the highly non-linear, coupled nature of the advection-diffusion-reaction systems that can be studied in the HPLFR may yield results that deviate significantly from the intended experimental design and/or simplified interpretive model. This is particularly true as most HPLFR experiments are, by design, operated under uncertain chemical forcing in order to further constrain this selfsame uncertain chemical source term. Anticipated reaction conditions may therefore deviate significantly from those encountered during the experiment.

For example, the $O(1)$ Damköhler number assumed in the analysis above is violated as mixtures of H_2+O_2 transition from slow-reacting to explosive chemistry. Small uncertainties in the chemistry model used for experimental design may lead to choice of experimental conditions which exhibit this transition. Experiments near the explosion limit may obey ideal plug flow assumptions given by Equation 2.8 for upstream axial locations/early times and then transition to significantly faster chemistry downstream; this transition further induces strong axial gradients in species mole fraction and temperature. In this case upstream flow/slow reaction can be treated as ideal plug flow, while downstream/explosive reaction flow may be described by another reactor operating mode. Similar transitional behavior is evident in the

temperature profiles associated with laminar flow reactor dimethyl ether oxidation experiments of Herrmann *et al.* (2014), and this may confound interpretation of the results by plug flow assumptions (Dryer *et al.*, 2014). Clearly, proper post-experiment interpretation in such cases is crucial in properly applying the data to inform the chemical source term.

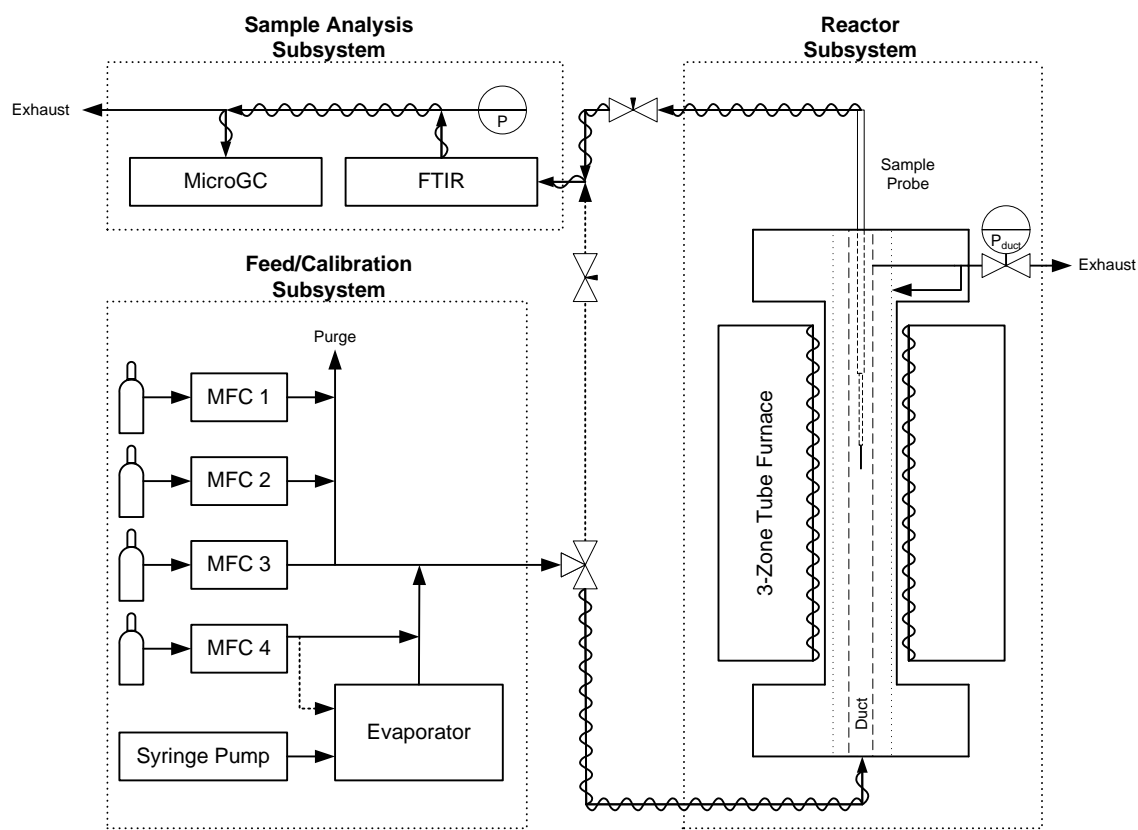


Figure 2.1 – High Pressure Laminar Flow Reactor (HPLFR) overview schematic.

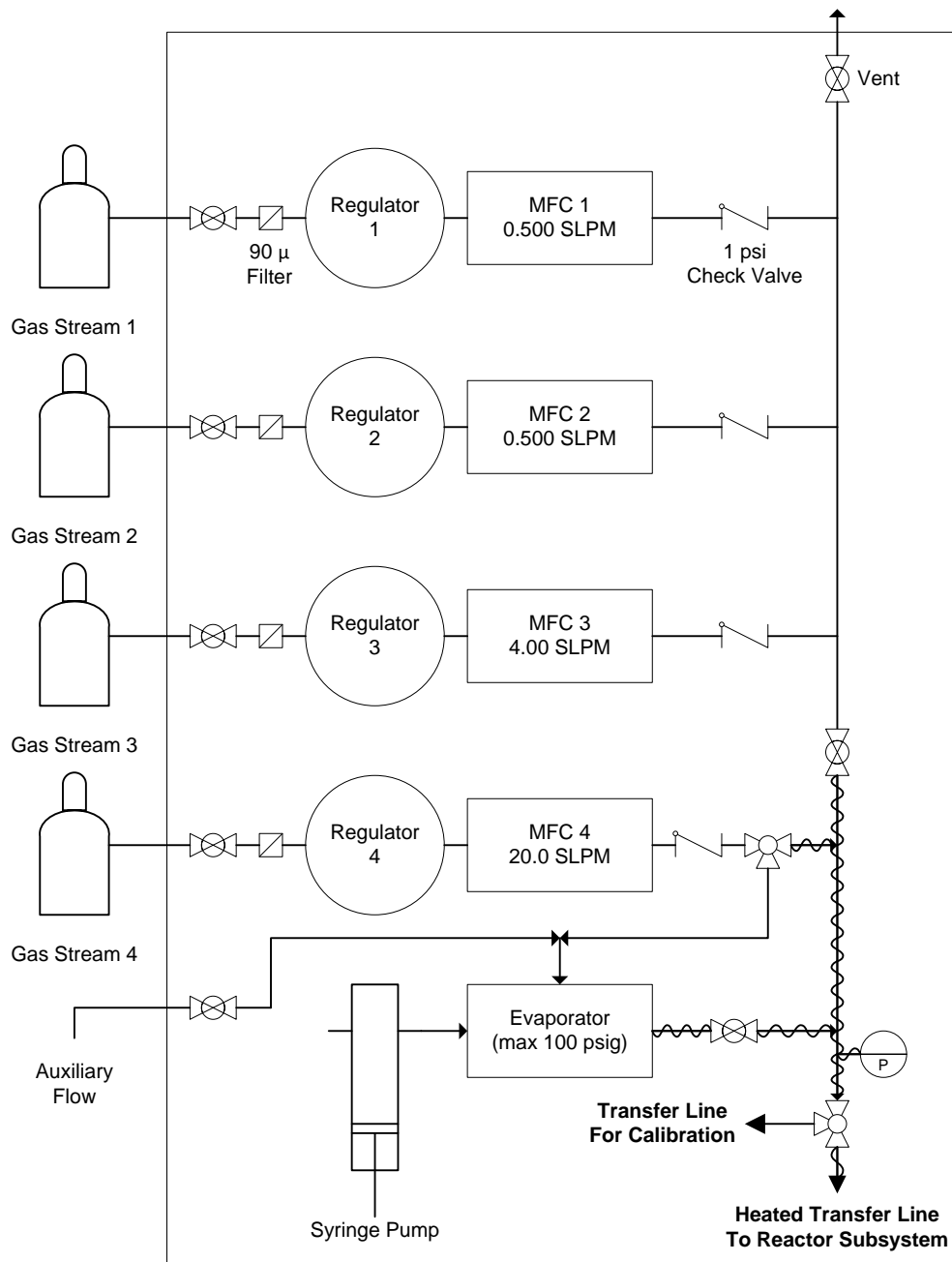


Figure 2.2 – Simplified Feed/Calibration Subsystem schematic.

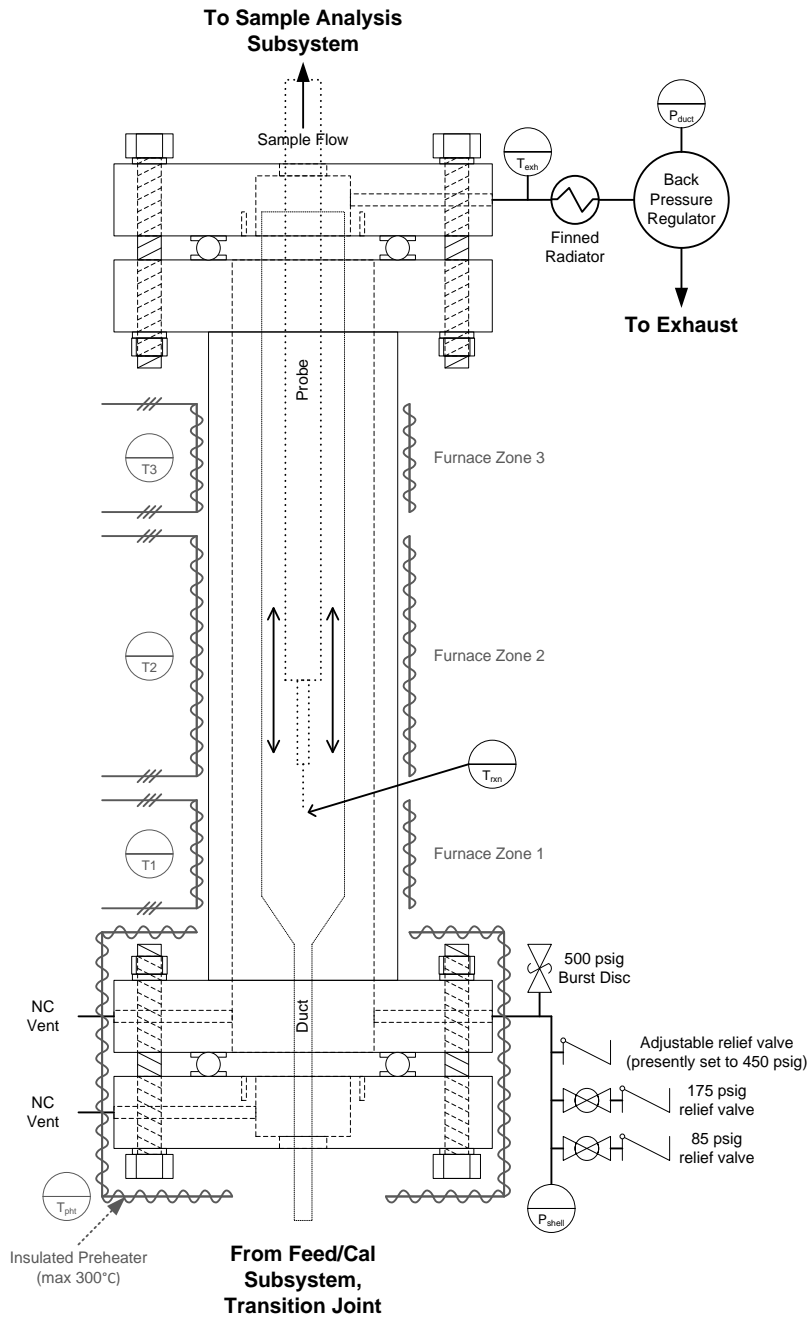


Figure 2.3 – Simplified Reactor Subsystem schematic.

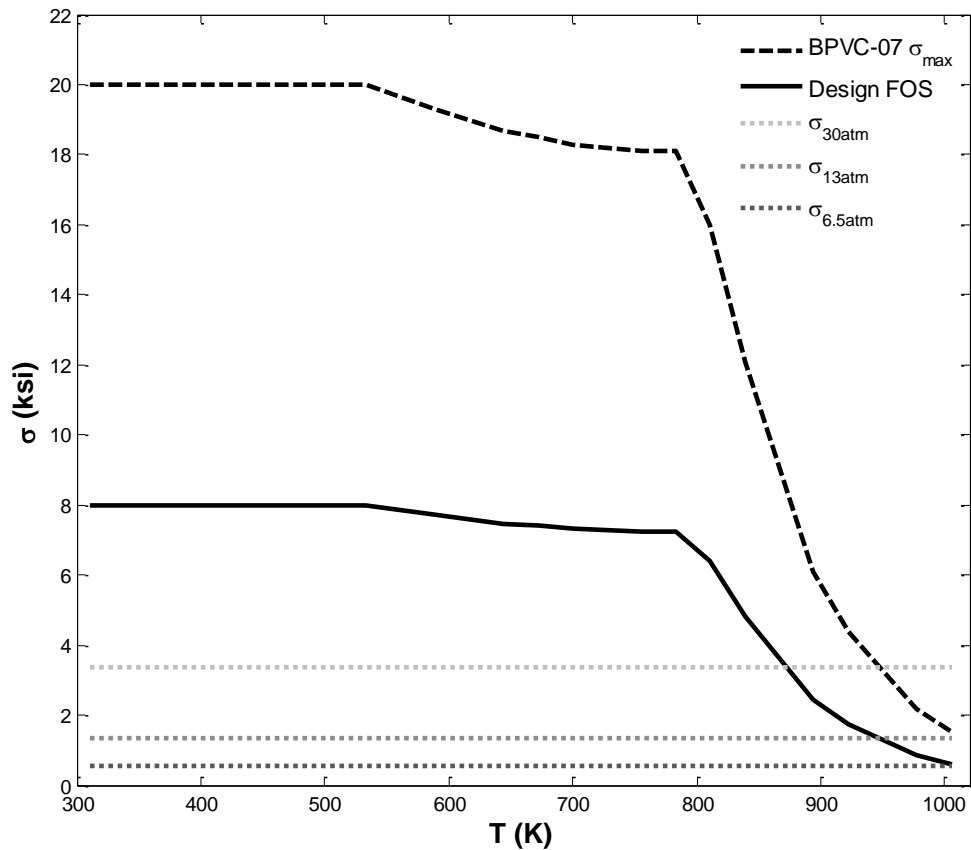


Figure 2.4 – Comparison of maximum allowable and representative applied stresses for the HPLFR pressure vessel.

ASME 2007 Boiler and Pressure Vessel Code (BVPC) recommends that temperature-dependent stress for seamless SS347 tubing not exceed the dashed black line (ASME, 2007). For the present pressure vessel design, a factor of safety (FOS) of 2.5 has been applied above any implicitly included in BVPC to derive maximum allowable applied stresses in the HPLFR pressure shell defined by the solid black line. Computed stresses applied by pressurized gas contained in the pressure shell are denoted by dotted lines corresponding to representative pressures of 30, 13, and 6.5 atm (absolute). **Crossing points of these computed stress curves with the FOS-adjusted maximum stress curve identifies recommended temperature-pressure operating ranges for the HPLFR facility:**

- 1) below 866 K, $P_{max} = 30$ atm (~425 psig), which is the nominal facility design pressure;
- 2) $866 \leq T \leq 950$ K, P_{max} falls from 30 atm to 13 atm (~425 psig to ~175 psig) and recommended operation is to limit P_{max} to 13 atm (~175 psig, using the provided manual block valve);
- 3) $950 \leq T \leq 1000$ K, P_{max} falls from 13 atm to 6.75 atm (~175 psig to ~85 psig) and recommended operation is to limit P_{max} to 6.5 atm (~80 psig, using the provided manual block valve).

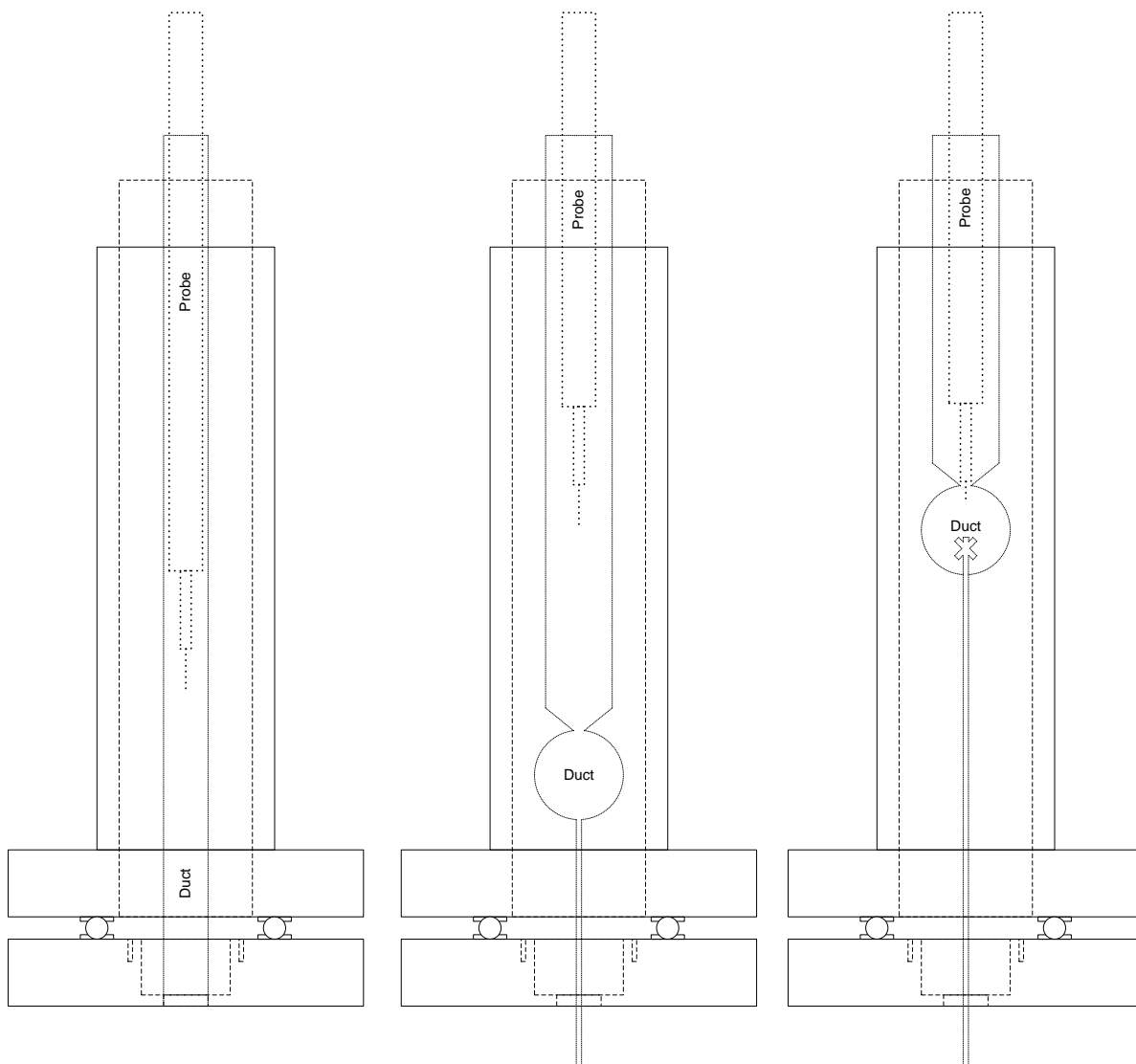


Figure 2.5 – Example sketches of duct geometries that can be accommodated by the pressure shell.

From left to right: a straight tubular duct suitable for laminar or plug flow reactor; a duct approximating a well-stirred reactor in series with a tubular flow reactor; a well-stirred reactor similar to the CNRS JSRs (Dagaut *et al.*, 1986). Figure 2.3 shows an example of a tapered duct.

Seal designs for each of these geometries require custom combinations of bushings, spacers, O-rings, gaskets, and ferrules to fit the seal pocket and/or transition joint.

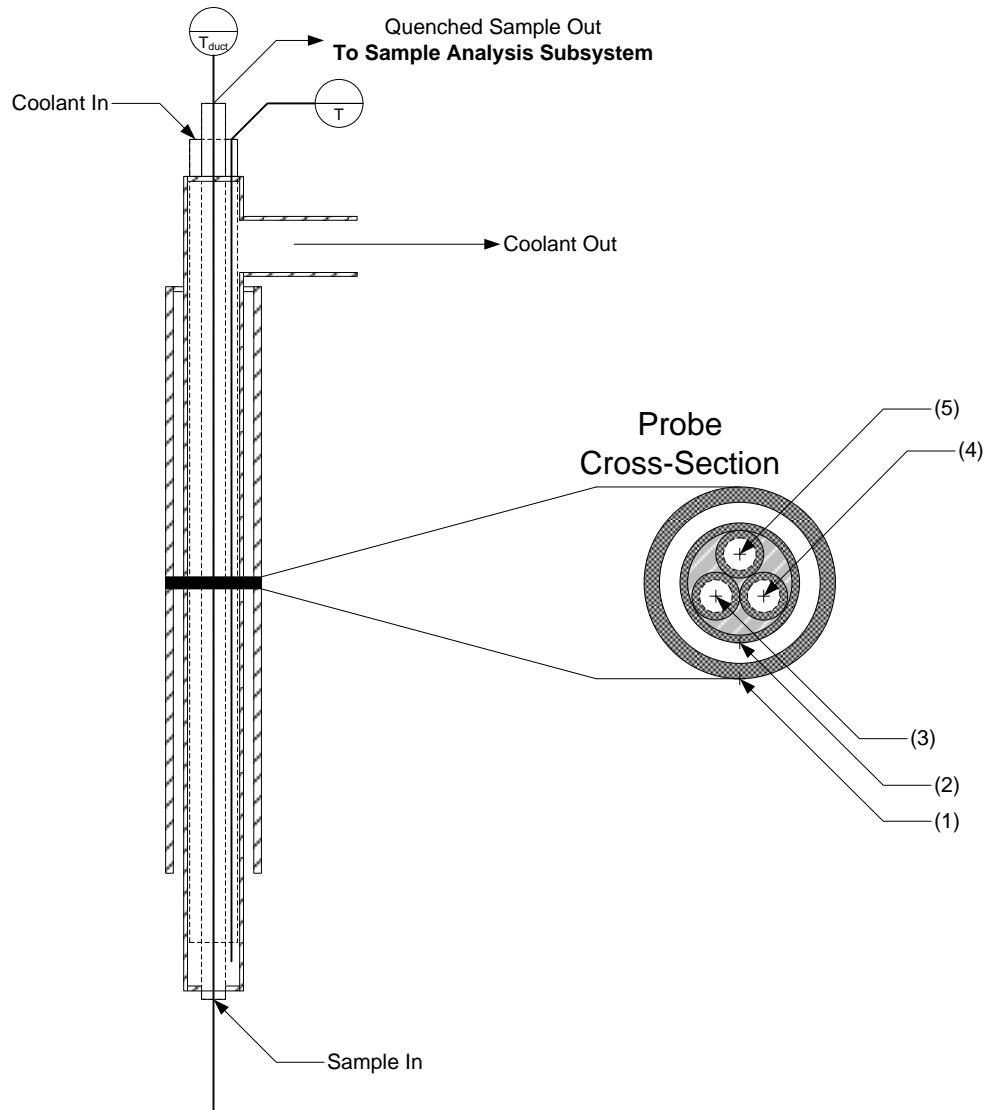


Figure 2.6 – HPLFR Sample Probe schematic.

Components discussed in the text and indicated in the figure include (1) – Heat Shield/Mechanical Shell; (2) – Coolant Return Jacket; 3) Coolant Injection Tube; 4) Thermowell; 5) Sample/Thermocouple Tube. The thermocouple used for duct temperature measurements runs coaxially down tube (5) and extends 5 cm beyond the Sample In port.

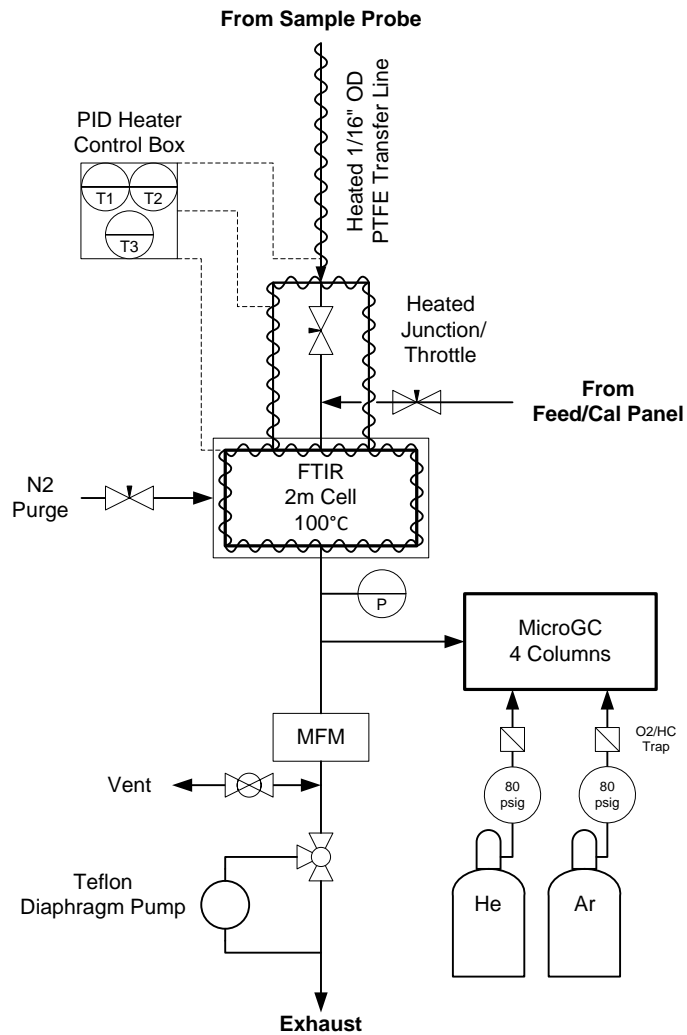


Figure 2.7 – Simplified Sample Analysis Subsystem schematic.

Chapter 3: HPLFR Design Validation by Rate Coefficient Measurement for $\text{H} + \text{O}_2(+\text{M}) \rightarrow \text{HO}_2(+\text{M})$, $\text{M} = \text{Ar}$ and N_2

The temperature-, pressure- and bath gas-dependent HO_2 -forming reaction



is among the most important in combustion chemistry since it converts reactive H atoms into relatively less reactive HO_2 radicals. Reactions of HO_2 typically occur on significantly longer timescales than reactions of the H, O, and OH radicals that also participate in the foundational H_2/O_2 oxidation system (Figure 1.1), so HO_2 formed by H.9.M may be considered to effectively terminate reactivity in many cases. This termination competes with the radical branching reaction



in which one reactive H atom initially forms two reactive radicals. Competition between H.9.M and H.1 is, in part, responsible for a wide range of combustion phenomena in systems involving H_2 as well as more complex fuels. Nevertheless, relatively large uncertainty remains in the determination of the rate coefficient for the H.9.M reaction system despite its centrality in combustion chemistry. Reduction of uncertainty in $k_{\text{H.9.M}}$ is complicated by the dependence of this reaction on pressure as well as the identity of bath gas M. The relative rates of H.9.M associated with different bath gases M may vary nearly thirty fold (Michael *et al.*, 2002), which highlights the importance M as a parameter in controlling competition between H.1 and H.9.M.

A relatively large body of experiment- and theory-based pressure-dependent $k_{\text{H.9.M}}$ determinations exist for $\text{M} = \text{Ar}$ and N_2 . Consequently, rate coefficients for H.9.Ar and H.9.N2 determined from HPLFR experiments can be compared to these literature $k_{\text{H.9.M}}$ values to validate the ability of the new HPLFR facility to measure $k_{\text{H.9.M}}$. This chapter provides discussion of this validation process. Section 3.1 discusses the quasi-steady state plateau (QSSP) condition under which the HPLFR measurements were taken, while Section 3.2 establishes the ability of the HPLFR and the QSSP technique to measure $k_{\text{H.9.M}}$ through validation against the existing rate coefficients for $\text{M} = \text{Ar}$ and N_2 , which are better known than many other species such as CO_2 . Because the QSSP technique measures the relative rates of H.9.M and



the same experimental HPLFR-QSSP measurements may be used to establish $k_{\text{N.1}}(\text{T})$ given a known value of $k_{\text{H.9.M}}(\text{T,P})$. Section 3.3 provides alternative validation of the HPLFR-QSSP technique by comparing experimentally-derived $k_{\text{N.1}}$ values against existing, well-established $k_{\text{N.1}}$ determinations from the literature. Additional demonstration of the HPLFR facility appears in the propene oxidation study of Burke *et al.* (2014), but this will not be further discussed here.

3.1 Description of the Quasi-Steady State Plateau (QSSP) Condition

Ashmore & Tyler (1962) studied the reaction of H_2 and O_2 in the presence of small, sensitizing concentrations of NO_2 at 633 K and relatively low pressures. They diluted reactants into each of several bath gases and introduced individual mixtures into an aged static reactor, where both the evolution of total pressure and partial pressure of NO_2 were monitored during the reaction induction period. Under certain conditions, they noted that a stationary (quasi-steady) partial pressure P_s of NO_2 manifested during the induction period, even as the overall reaction progressed as indicated by a reduction in the total pressure in the reactor (Figure 3.1). This quasi-steady P_s was found to be generally insensitive to the initial NO_2 partial pressure, P_0 , added to the reacting mixture (Figure 3.2); moreover, P_s was found to be linearly proportional to both the partial pressure of oxygen P_{O_2} as well as the total pressure P_M (Figure 3.3). Based on additional details, these authors go on to rationalize that, at QSSP conditions, the reaction system obeys the relationship

$$[\text{NO}_2]_s = [\text{NO}_2]_{\text{QSSP}} = (k_{\text{H.9.M}}/k_{\text{N.1}})[\text{M}][\text{O}_2]_{\text{QSSP}}. \quad (3.1)$$

In Equation 3.1, the partial pressure relationships originally discussed by Ashmore & Tyler have been transformed to molar concentration basis for further generality. The kinetic system described by the algebraic relationship in this equation is a tremendous simplification of the dozens of coupled ordinary differential equations among scores of free parameters that would otherwise be used to model the ideal static reactor oxidation of $\text{H}_2/\text{O}_2/\text{NO}_2/\text{M}$ mixtures. Under QSSP conditions, one of $k_{\text{H.9.M}}$ or $k_{\text{N.1}}$ may be determined from the value of the other rate coefficient and experimentally measured concentrations of NO_2 , O_2 , and total gas concentration M . This forms the basis for experimental HPLFR measurements of

kH.9.M discussed later in this chapter, which are determined relative to the well-known rate coefficient for N.1.

3.1.1 The Simplified QSSP Reaction System

Additional insight into QSSP conditions can be obtained from considering the specific subset of elementary reactions active at these conditions. In accordance with experimental observations by Ashmore & Tyler, conversion of H₂ to H₂O under QSSP conditions is a relatively slow process, which indicates that a subset of non-explosive H₂/O₂ chemistry dominates the QSSP system. The NO₂ present must react with species in the H₂/O₂ chemical system to establish a quasi-steady concentration even as slow oxidation of H₂ occurs. Assuming a relatively slow initiation reaction such as



has occurred (proceeding from right to left) to produce an initial radical pool, the reactions immediately below represent a minimal closed elementary reaction set to describe the QSSP system:

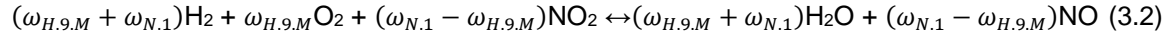


In this system the total NO_x is conserved in a catalytic cycle as NO₂ consumes H atoms to form NO in N.1 and NO consumes HO₂ to form NO₂ in N.2. Both of these reactions produce OH, which quickly reacts with H₂ in H.3 to form H₂O and H atom. The H atoms produced from H.3 associate with O₂ through termolecular reaction H.9.M to form HO₂ or re-enter the reaction cycle in N.1. Any HO₂ produced by H.9.M re-enters the reaction cycle in N.2.

A consequence of the catalytic NO_x cycle is that after an initiation reaction such as H.10, reaction may begin with trace NO₂ dopant (as investigated in the experiments of Ashmore & Tyler), trace NO dopant, or a mixture of NO and NO₂. In any case, the system relaxes to the same quasi-steady NO₂ plateau concentration through a transient response, as illustrated in Figure 3.4. This observation suggests that the NO₂ plateau concentration is also insensitive to the initial concentration of NO+NO₂ as

long as QSSP conditions prevail. The HPLFR experiments described later take advantage of this result and use NO as the sensitizing NO_x species.

The preceding description of the minimal reaction set suggests that the relative rate ratio of the H-consuming reactions H.9.M and N.1 may be important in the QSSP system dynamics. Assuming that under conditions favoring establishment of the QSSP, H.9.M and N.1 are rate-limiting reactions compared to N.2 and H.3, then the net reaction over one cycle of this system can be expressed as



where inclusion of reaction rates ω_k for H.9.M and N.1 explicitly consider competition of these two reactions for H atoms. The relationship in Equation 3.2 reveals system behavior during both the transient leading up to the QSSP as well as the plateau period itself. In the latter case, the concentration of NO₂ (and, hence NO) is quasi-steady, so Equation 3.2 reduces to

$$\omega_{H.9.M} = \omega_{N.1} = \omega \quad (3.3)$$

and the net reaction is



Equation 3.4 is consistent with the experimental observations of Ashmore & Tyler, which indicate that the QSSP condition permits the slow reaction of H₂ and O₂ to form H₂O despite little change in the concentration of NO₂ from P_s. Also, because no radical or NO_x species appears in this QSSP net reaction (Equation 3.4), all of these reactive species must be present in quasi-steady state. As discussed in the following subsection, this observation is additionally supported by more formal solution of the coupled ordinary differential equations for the minimal reaction set under quasi-steady state assumptions.

Equation 3.2 also describes the transient behavior of the minimal reaction system as it seeks the QSSP condition. In the extreme limiting case of initial system sensitization with NO₂ only, NO is initially not present and the system begins to react by N.1, leading to an overall reaction transient for which H.9.M is the rate-limiting reaction step. As this overall reaction proceeds, NO₂ is initially depleted at a rate of $\omega_{H.9.M}$ to form NO, but, after some time, the rates of H.9.M and N.1 approach each other to find the QSSP condition described by Equations 3.3 and 3.4. Similarly, the extreme limiting case of initial sensitization

with only NO begins with N.1 acting as the rate-limiting reaction step. Then NO is initially depleted at a rate of $\omega_{N,1}$ to form NO₂, and after some time, the rates of H.9.M and N.1 approach each other to find the QSSP condition. Initial sensitizer mixtures of NO+NO₂ follow similar, superposed phenomenology in the transition from transient to QSSP (Figure 3.4).

Two additional limiting cases should be considered for this illustrative analysis. Assuming the QSSP condition has been established, slow oxidation of H₂ and O₂ will form H₂O according to Equation 3.4, and after some time, either H₂ or O₂ will become depleted depending on the overall stoichiometry. In both cases, depletion of one of these reactants effectively stops the overall reaction. In the case of complete H₂ depletion, the algebraic QSSP condition given by Equation 3.1 continues to hold since the oxidation of remaining NO to NO₂ by the remaining O₂ is a relatively slow process. In other words, the reactant concentrations are essentially frozen after H₂ depletion. This case is illustrated in Figure 3.5 and is relevant to some of the flow tube measurements of Ashman (1999)/Ashman & Haynes (1998) at QSSP conditions. However, in the case that O₂ is completely depleted and some H₂ remains, the frozen reactant condition is not achieved. Owing to O₂ (and subsequent HO₂) depletion, only reactions H.3 and N.1 are left to participate in the QSSP reaction cycle. Any H atoms formed by H.3 react by N.1 to convert remaining NO₂ to NO and OH; this OH reacts with remaining H₂ to form H₂O and H. The reduced reaction cycle repeats until NO₂ is depleted. This analysis suggests that results of QSSP-like experiments with H₂ in stoichiometric excess may require additional scrutiny to ensure that measurements were taken at conditions pertinent to the QSSP condition.

The mathematical manipulations of Equations 3.2-3.4 reveal additional information regarding features of the QSSP system. Coupled with the stoichiometry of the minimal reaction set, the result of Equation 3.3 implies that the rates of N.2 and H.3 at the QSSP condition are ω and 2ω , respectively – that is, they are set by the (equal) rates of H.9.M and N.1, which is *the* characteristic reaction rate for this system. Importantly, this rate ω determines a single relevant chemical reaction timescale necessary for consideration in the laminar reactor analysis presented in Section 2.5. Importantly, at QSSP conditions there is no spectrum of chemical timescales to be accounted for in interpretation of flow reactor measurements (*e.g.*, Dryer *et al.*, 2014).

The preceding analysis is self-consistent in the prescription of H.9.M and N.1 as rate limiting steps. To further support these assumptions and the analysis developed in this section, normalized sensitivity coefficients have been computed from complex kinetic modeling of the QSSP condition at conditions representative of the experiments of both Ashmore & Tyler and the present HPLFR studies. These modeling results appear in Figures 3.6 and 3.7, respectively, and show that H.9.M and N.1 are by far the most sensitive reactions in determining the NO₂ concentration profiles at QSSP conditions. The QSSP concentration of NO₂ is, in turn, generally the most sensitive experimental measurement for determining H.9.M by Equation 3.1.

3.1.2 Departures from the QSSP Condition (Extended QSSP Conditions)

Using the same assumed minimal four reaction set discussed above but applying together the experimental observation of quasi-steady NO₂ concentration with the *a priori* assumption of quasi-steady HO₂ concentration, straightforward solution of the homogeneous gas phase chemistry differential rate laws reveals the results of Equations 3.1 and 3.3:

$$d[\text{HO}_2]/dt \approx 0|_{QSSP} = k_{H.9.M}[\text{M}][\text{H}][\text{O}_2] - k_{N.2}[\text{HO}_2][\text{NO}] \quad (3.5)$$

$$d[\text{NO}_2]/dt \approx 0|_{QSSP} = k_{N.2}[\text{HO}_2][\text{NO}] - k_{N.1}[\text{H}][\text{NO}_2] \quad (3.6)$$

and by simple substitution

$$k_{N.1}[\text{H}][\text{NO}_2]_{QSSP} = k_{H.9.M}[\text{M}][\text{H}][\text{O}_2]_{QSSP} \quad (3.7)$$

yielding the algebraic QSSP relationship

$$[\text{NO}_2]_{QSSP} = (k_{H.9.M}/k_{N.1})[\text{M}][\text{O}_2]_{QSSP}, \quad (3.1)$$

as well as implying

$$\omega_{H.9.M} = \omega_{N.1} = \omega \quad (3.3)$$

during quasi-steady reaction. Other consequences of the QSSP condition highlighted phenomenologically in the preceding subsection also hold under this alternative steady-state analysis. However, this derivation of the general features of the QSSP condition also lends itself, upon some modification, to analyzing the behavior of the kinetic system when side reactions or other departures from

steady-state may be important. Such departures can be considered as an overall deviation σ_k in either kH.9.M or kN.1 found from the governing QSSP relationship given by Equation 3.1:

$$k_{H.9.M} = k_{N.1} [\text{NO}_2]/[\text{M}][\text{O}_2] + \sigma_{H.9.M}, \quad (3.8a)$$

$$k_{N.1} = k_{H.9.M} [\text{M}][\text{O}_2]/[\text{NO}_2] + \sigma_{N.1}. \quad (3.8b)$$

These deviation terms arise from relaxing the basic QSSP assumptions to allow for side reactions in addition to the minimal reaction set as well as deviations from truly steady-state HO₂ and NO₂ concentrations. Equations 3.5 and 3.6 generalize to

$$d[\text{HO}_2]/dt = \sum_{k=1}^N \omega_k \delta_{k,\text{HO}_2} = \omega_{H.9.M} - \omega_{N.2} + \sum_{k \neq H.9.M, N.2}^N \omega_k \delta_{k,\text{HO}_2} \quad (3.9)$$

and

$$d[\text{NO}_2]/dt = \sum_{k=1}^N \omega_k \delta_{k,\text{NO}_2} = \omega_{N.2} - \omega_{N.1} + \sum_{k \neq N.1, N.2}^N \omega_k \delta_{k,\text{NO}_2}. \quad (3.10)$$

For notational convenience in later discussion, the rightmost summations in Equations 3.9 and 3.10 are defined as $\sum \omega_{\text{HO}_2}$ and $\sum \omega_{\text{NO}_2}$, respectively. These summations indicate contributions to changes in respective HO₂ and NO₂ concentrations due to side reactions outside of the minimal QSSP reaction set. The $\delta_{k,i}$ in these equations is the net stoichiometric coefficient of species i in reaction k of the N equation kinetic source term model. For example, $\delta_{k,i} = 1$ if one i molecule is produced in reaction k and $\delta_{k,i} = -2$ if two i molecules are consumed by reaction k . Note also that this formulation requires an estimate of the k_k rate coefficient of interest to evaluate terms in Equations 3.9 and 3.10.

A form similar to Equation 3.8a appears after summing together Equations 3.9 and 3.10 and solving for $k_{H.9.M}$:

$$k_{H.9.M} = k_{N.1} [\text{NO}_2]/[\text{M}][\text{O}_2] + \{d([\text{HO}_2] + [\text{NO}_2])/dt - \sum \omega_{\text{HO}_2} - \sum \omega_{\text{NO}_2}\}/[\text{M}][\text{H}][\text{O}_2]. \quad (3.11)$$

Then the $\sigma_{H.9.M}$ deviation from ideal QSSP behavior is defined as

$$\sigma_{H.9.M} = \{d([\text{HO}_2] + [\text{NO}_2])/dt - \sum \omega_{\text{HO}_2} - \sum \omega_{\text{NO}_2}\}/[\text{M}][\text{H}][\text{O}_2], \quad (3.12)$$

where individual contributing deviation terms due to both non-steady HO₂ and NO₂ concentrations as well as those due to side reactions affecting HO₂ and NO₂ pools become apparent. Similar mathematical

manipulation beginning with Equation 3.8b yields $\sigma_{N,1}$. Though the following discussion focuses on kH.9.M, similar consequences hold for kN.1.

For a perfectly certain chemical source term model, including a pre-supposed value for kH.9.M, Equation 3.12 gives the departure from the QSSP-derived value of kH.9.M exactly for the case of isothermal, isobaric reaction conditions with no net change in mole number or third body efficiency for all N reactions in the kinetic model. These idealizations give rise to uncertainties in $\sigma_{H,9,M}$ stemming from both the uncertainties inherent in real chemical source term models as well as any departures from the additional restrictions assumed when using Equation 3.12. Accordingly, a more refined notional definition of $\sigma_{H,9,M}$ is that it represents a model-informed (and therefore, model-dependent) estimator for the extent of departure of kH.9.M from the idealized QSSP condition.

Model-computed values of $\sigma_{H,9,M}$ come from the time-dependent reaction rate and species concentration information generated from integrating the homogeneous chemical source term model. Importantly, this parameter can be used both to check that kH.9.M values have been obtained under QSSP conditions ($\sigma_{H,9,M}/k_{H,9,M} \ll 1$) as well as to correct kH.9.M values that have been obtained under nearly QSSP conditions ($\sigma_{H,9,M}/k_{H,9,M} < 1$; termed here “extended” QSSP conditions). In both of these cases, $\sigma_{H,9,M}$ can be considered one uncertainty in the determination of kH.9.M. Model- and condition-dependent uncertainties in $\sigma_{H,9,M}$ are essentially the *uncertainty of an uncertainty* for kH.9.M values determined by Equation 3.1 and should be relatively negligible for QSSP and near-QSSP conditions. Figures 3.8 and 3.9 demonstrate application of the presently developed $\sigma_{H,9,M}$ analytical tool in the evaluation of QSSP experiments.

3.2 Validation of HPLFR for QSSP Measurements of kH.9.M

The preceding section establishes the QSSP technique as a relatively robust method for measuring kH.9.M by the simple algebraic relationship

$$[\text{NO}_2]_{QSSP} = (k_{H,9,M}/k_{N,1})[\text{M}][\text{O}_2], \quad (3.1)$$

under the assumption of an isolated, temporally-evolving chemical source term described by the ideal flow reactor initial value problem (IVP)

$$dY/dt = \hat{\omega}(Y). \quad (2.8)$$

The term $\sigma_{H.9.M}$ developed above serves to check for and/or correct small departures from the QSSP condition. Departures from the idealized IVP depend on experimental conditions accessed in the HPLFR, as initially discussed in Section 2.5 and elaborated on below. Only under certain conditions will HPLFR experiments well approximate the zero-dimensional idealization underlying the preceding zero-dimensional interpretation of the QSSP condition. At these conditions, HPLFR measurements of $[\text{NO}_2]$, $[\text{O}_2]$, P, and T can determine the ratio of $k_{H.9.M}$ to $k_{N.1}$. Either rate coefficient can then be determined *relative* to the other given T, P, and the local gas composition.

This section establishes the ability of the HPLFR facility to measure values of $k_{H.9.M}$ by the QSSP method outlined in the preceding paragraph. For this purpose, use of the HPLFR facility combined with the QSSP technique is considered validated if measured $k_{H.9.M}$ or $k_{N.1}$ values are consistent with existing, independently established $k_{H.9.M}$ or $k_{N.1}$ determinations from the literature. Two series of HPLFR QSSP experiments, one in Ar and the other in N_2 bath gas, serve as these validation measurements since $k_{H.9.M}$ is reasonably well-known for these two bath gases. The rate coefficient for N.1 is also considered well-known (Su *et al.*, 2002) and provides an additional validation comparison (Section 3.3).

3.2.1 Plug Flow Assumption Consideration for QSSP Experiments

The QSSP validation experiments subsequently described are characterized by a long induction distance of transient NO/NO₂ conversion with negligible overall reaction $2\text{H}_2 + \text{O}_2 \rightarrow 2\text{H}_2\text{O}$. As indicated by HPLFR experimental data provided in Figures 3.10-3.12, this induction distance is followed by a region in which QSSP conditions apparently prevail. However, the induction length typically exceeds the hydrodynamic entry length as measured from the end of the reactor duct taper, so velocity profiles in the QSSP test section can be expected to approach the fully-developed paraboloid characteristic of laminar pipe flow. This challenges the plug flow IVP assumption underlying the QSSP analysis developed above, for diffusion and residence time distributions may participate non-negligibly in determining both axial and radial species profiles.

The four M = Ar validation experiments listed in Table 3.1 were simulated using the CHEMKIN-PRO (Reaction Design, 2011) cylindrical reacting shear layer flow (CRESLAF) reactor model in order to resolve the differences between two-dimensional developed laminar flow and one-dimensional plug flow interpretations of QSSP experiments. Simulations indicate that, despite a non-plug *velocity* field, the profiles for QSSP species satisfy plug flow (radially uniform) assumptions to a very high degree after the induction length has been passed. Accordingly, the plug flow interpretation of the QSSP condition discussed above remains valid, with flow field effects adding relatively minimal 2-4% uncertainty to the determination of the $k_{H.9.M}/k_{N.1}$ ratio at any axial location in the post-induction test section.

Figure 3.13 plots species profiles predicted by the CRESLAF simulations for an exemplar condition. The similarity in two-dimensional and plug flow results occurs because the QSSP reactions proceed at rates permitting radial diffusion to homogenize species profiles at each axial reactor location beyond the induction length. Because diffusion coefficients for the QSSP species do not change appreciably among the Ar and N₂ bath gases and pressure ranges considered in this chapter, the present effective plug flow result also holds for the N₂ results discussed later. In all of these cases, the quasi-steadiness in radical and NO_x QSSP species leads to negligible axial and radial gradients for these molecules. Further, the relatively modest axial changes in H₂, O₂, and H₂O driven by the slow overall reaction $2H_2 + O_2 \rightarrow 2H_2O$ likewise permits radial homogenization of these species by diffusion, and consequently, effectively plug flow for all species participating in the QSSP reaction.

3.2.2 Validation Experiments Using M = Ar

A series of four experiments using Ar bath gas was conducted as part of the HPLFR validation for measurement of $k_{H.9.M}$ by the QSSP method. The nominal temperature for these experiments was held nearly constant (752 ± 5 K), and axially-resolved measurements indicate each experiment proceeded under effectively isothermal conditions. Pressure was essentially constant during each experiment, but varied from 12.0-18.0 atm among the experiments.

To establish both the low axial gradient criterion discussed above as well as determine the ratio $k_{N.1}/k_{H.9.Ar}$ by Equation 3.1, axially-resolved profiles of [H₂], [O₂], [NO₂], and T were measured for each experiment. For ease of kinetic model comparison, the axial coordinates for these profiles were transformed into temporal coordinates using the total volumetric reactant flow rate corrected to reaction

temperature and pressure, with the additional assumption of plug flow velocity in the 10 mm ID quartz duct employed for these experiments. This plug flow treatment is consistent with the preceding analysis of the laminar reacting flow under the presently studied QSSP conditions.

Results for Experiment 3/I and 3/II are given in Figures 3.10 and 3.11, respectively. Experiments 3/IIIa and 3/IIIb were run immediately in sequence at the same pressure and reactant feed rates, so results of both experiments are presented in Figure 3.12. The nominal initial reaction conditions for each experiment are listed in Table 3.1. However, neither $k_{N.1}$ (Figure 3.14) nor $k_{H.9.M}$ is particularly sensitive to temperature, so QSSP results from this series of experiments can be fairly compared using 752 K as the single characteristic temperature.

Comparison of these QSSP results to existing literature values is somewhat complicated by the relatively high pressures of the experiments, which puts $k_{H.9.M}$ in falloff. Moreover, multiple parameterizations for $k_{H.9.M}$ and $k_{N.1}$ exist in the literature. Because the QSSP result given by Equation 3.1 is *relative* in nature, one of $k_{H.9.M}$ or $k_{N.1}$ must be assumed in the measurement of the other rate coefficient. Comparisons of the present data to literature $k_{H.9.Ar}$ rate coefficient values (assuming $k_{N.1}$) are detailed below.

3.2.2.1 Nominal $k_{N.1}$ Expression for $k_{H.9.M}^{QSSP}$ Interpretation

Aside from the study of Haas & Dryer (2015) that is derivative from the present work, the most recent comprehensive study of reaction N.1 appears to be that of Su *et al.* (2002), which measures $k_{N.1}$ between 1100 and 2000 K using two different shock tube techniques. Based on their experimental data, the authors recommend a value of $k_{N.1HT}$ of 9.88×10^{13} cm³/mol/s ($\Delta k_{N.1}/k_{N.1} = \pm 37\%$ at 2σ uncertainty) for this temperature range. This study also compiles experimental rate coefficient measurements from several other studies measuring $k_{N.1}$ by a variety of techniques. Based on combining their own measurements with this additional literature experimental data, Su *et al.* alternatively recommend a temperature-independent value of $k_{N.1EXP} = 8.85 \times 10^{13}$ cm³/mol/s ($\pm 35\%$ at 2σ uncertainty) for temperatures between 195 and 2000 K.

Moreover, Su *et al.* compute $k_{N.1}$ using variable reaction coordinate flexible transition state theory (VRC-FTST) applied to an *ab initio* potential energy surface for the N.1 reaction system. Their calculation supports a mild increase in $k_{N.1}$ with increasing temperature, as qualitatively consistent with

elementary kinetic theory. This VRC-FTST theoretical rate coefficient is also consistent with the literature experimental data, and a present fit to the computed expression gives $k_{N.1\text{VRC-FTST}} = 2.5 \times 10^{13} \times T^{0.218}$ cm³/mol/s from 195-2000 K, with fitting errors not exceeding ~10% over this entire temperature range. At temperatures above ~500 K, this expression is in good agreement with both the Su *et al.* $k_{N.1\text{HT}}$ expression and an extrapolation of the temperature-dependent, experiment-based recommendation of Ko & Fontijn (1991) for $296 \leq T \text{ (K)} \leq 760$. This latter recommendation is among the selected reaction rate parameterizations in the recent NO_x chemistry compilation of Klippenstein *et al.* (2011) and the NO_x kinetic model of Mueller *et al.* (1999b).

Figure 3.14 compares these four $k_{N.1}$ rate coefficient expression alternatives for temperatures between 200 and 2000 K. Considering uncertainties implicit in the extrapolated rate coefficient of Ko & Fontijn (1991) ($k_{N.1\text{KF}}$) and the theoretical rate coefficient computation $k_{N.1\text{VRC-FTST}}$, all four expressions are in remarkably good agreement. Though the scatter and uncertainties in the experimental $k_{N.1}$ data admit multiple interpretations regarding the temperature (in)dependence of $k_{N.1}$, the weight of both the Su *et al.* high temperature data and theoretical computations suggests a mild increase in rate coefficient with temperature. For the present purposes of $k_{H.9.M}$ determination by the QSSP technique, the temperature-dependent fit to the Su *et al.* $k_{N.1\text{VRC-FTST}}$, with 2σ uncertainty $\Delta k_{N.1}/k_{N.1} = \pm 35\%$ taken from $k_{N.1\text{EXP}}$, is used as the *nominal* $k_{N.1}$ basis. This expression is consistent with both experiment and theory, and the estimated uncertainty bands overlap the alternative $k_{N.1}$ expressions over the entire 200-2000 K temperature range.

It is important to again stress that experimental QSSP measurements of [NO₂], [O₂], T, and P return the *relative ratio* between $k_{N.1}$ and $k_{H.9.M}$ by Equation 3.1. *The ratio between [NO₂] and [O₂] is the fundamental experimental measurement* and remains invariant under alternative choices of nominal $k_{H.9.M}$ or $k_{N.1}$ reference rate coefficient expressions. Accordingly, Table 3.2 reports the rate coefficient-independent value of [O₂]/[NO₂] determined from each HPLFR-QSSP validation experiment. Specific evaluation of either $k_{N.1}$ or $k_{H.9.M}$ using the other rate coefficient as reference assumes the additional uncertainty of the reference rate coefficient and may permit alternative interpretations of the experimental data. As discussed below, this added uncertainty does not appear to affect the present validation of the HPLFR for QSSP measurements using either M = Ar or N₂. However, the present QSSP experimental

data remains subject to future reinterpretation using either alternative assumptions or presumably lower-uncertainty reference rate coefficient expressions.

3.2.2.1 Determination of $k_{H.9.Ar}^{QSSP}$

Having now established a nominal $k_{N.1}$ value for use with Equation 3.1, the experimental HPLFR-QSSP data indicated with Figures 3.10-3.12 can be used to determine $k_{H.9.Ar}(T,P)^{QSSP}$. Experimental measurements of nominal temperature and pressure, NO_2 mole fraction, and O_2 mole fraction from each axial (temporal) station in the plateau region of the $M = Ar$ experiments are used to solve Equation 3.1 for $k_{H.9.M}^{QSSP}$ subject to the reference value of $k_{N.1}$ at the nominal reaction temperature. Assuming linear bath gas effects apply for the H.9 system (which is reasonable, though see e.g., Burke *et al.*, 2012), this $k_{H.9.M}^{QSSP}$ value represents the mole fraction-weighted average of $k_{H.9.M}$ for all M in the reacting flow. Because the flow is almost entirely composed of H_2 , O_2 , Ar , and H_2O , the value of $k_{H.9.Ar}^{QSSP}$ measured at a given sampling station can be determined from $k_{H.9.M}^{QSSP}$ through the simple linear bath gas correction

$$k_{H.9.Ar}^{QSSP} = k_{H.9.M}^{QSSP} / ([1 - X_{O_2} - X_{H_2} - X_{H_2O}] + \epsilon_{O_2/Ar} X_{O_2} + \epsilon_{H_2/Ar} X_{H_2} + \epsilon_{H_2O/Ar} X_{H_2O}) \quad (3.16)$$

where $\epsilon_{i/Ar}$ is the assumed collisional efficiency of species i relative to Ar for reaction H.9.M. For Ar , $\epsilon_{i/Ar}$ is unity by definition. This equation can be similarly applied to bath gases M other than Ar .

Some representative values of $\epsilon_{i/Ar}$ for $i = H_2$, O_2 , and H_2O used in kinetic models are respectively 3.0, 1.1, and 21.0 (Burke *et al.*, 2012) or 3.33, 1.33, and 16 (Mueller *et al.*, 1999a). Other sets of collisional efficiency values exist in the literature (e.g., Michael *et al.*, 2002); however, the difference in resulting corrections is typically small for the $M = Ar$ and N_2 HPLFR validation experiments. Among the $M = Ar$ experiments, the *maximum* effect of the Equation 3.16 correction on $k_{H.9.M}^{QSSP}$ using the two sets of collisional efficiencies enumerated above is a reduction by 13.2 and 11.6%, respectively, to yield $k_{H.9.Ar}^{QSSP}$ for Experiment 3/IIIb. Here, the magnitude of the correction is significant relative to overall experimental uncertainties discussed below, but the difference between particular model-advised choices of $\epsilon_{i/Ar}$ values is relatively unimportant to the nominal value and uncertainties determined for $k_{H.9.Ar}^{QSSP}$. The magnitude of the correction from this example case also reveals the value in measuring the H_2 mole fraction (and thereby H_2O by atom balance) in addition to NO_2 , O_2 , T , and P . For the present interpretation of HPLFR QSSP experiments, the Burke *et al.* values are used unless otherwise noted.

Individual $k_{H.9.Ar}^{QSSP}$ results determined by Equation 3.16 for a fixed axial location are averaged for each M = Ar experiment to return a profile-averaged $k_{H.9.Ar}^{QSSP}$ with an associated overall uncertainty due to both uncertainties in the experimental measurements and the $k_{N.1}$ reference rate coefficient. Relative standard error (2σ) of the profile-averaged $k_{H.9.Ar}^{QSSP}$ value does not exceed 5% for any of the M = Ar experiments. Assuming the QSSP condition of Equation 3.1 is satisfied, additional, conservative 2σ experimental measurement uncertainty estimates include (a) up to 10% in NO_2 mole fraction largely based on experimental gas blend accuracy, FTIR calibration uncertainty, FTIR quantification uncertainty for a given calibrated method, and method-to-method variation found from comparing nominal NO_2 values determined by three different FTIR NO_x spectrum interpretation methods applied to each experimentally acquired spectrum; (b) up to 5% in O_2 mole fraction based on micro GC measurement repeatability; (c) up to ± 15 K ($\sim 2\%$) in absolute temperature measurement due to combined systematic thermocouple uncertainty and assumptions of isothermality at the nominal reaction temperature; (d) 8% due to two-dimensional flow field departures from plug flow; (e) and up to 4% in absolute pressure due to both systematic uncertainties and slight fluctuations about the nominal pressure during each experiment.

Unless stated otherwise, linear (additive) uncertainties of the form $\pm \Delta f/f =$ “uncertainty in quantity f ” are assumed herein. This is to be distinguished from logarithmic (multiplicative) “uncertainty factors” also frequently used in the kinetic literature (e.g., Baulch *et al.*, 2005 and Sheen *et al.*, 2009). Present linearized uncertainties used in interpretation of experiments are further considered to be random, normally-distributed, unbiased, and independent, permitting summation in quadrature under the assumption of small relative magnitude.

At M = Ar experiment conditions, overall 2σ uncertainty applicable to the $[O_2]/[NO_2]$ values in Table 3.2 is $\sim 16\%$. Excepting the minimal additional uncertainty due to treatment of ε_i in Equation 3.16, this *experimental* uncertainty also applies to $k_{H.9.Ar}^{QSSP}$. This uncertainty also equivalently applies to the fundamental experimental profile-averaged QSSP rate coefficient ratio measurement since the preceding discussion of uncertainty makes no assumptions about the $k_{N.1}$ reference rate coefficient. In any of these interpretations, the important result of this analysis is that the HPLFR QSSP experimental uncertainty is principally dominated by the uncertainty in the NO_2 measurement.

However, to fully characterize the uncertainty in a profile-averaged HPLFR $k_{H.9.Ar}^{QSSP}$ determination, the $\pm 35\%$ uncertainty of the $k_{N.1}$ reference rate coefficient expression must be combined with the $\pm 16\%$ experimental measurement uncertainty. Such combination in quadrature yields $\pm 38.5\%$ overall uncertainty for present $k_{H.9.Ar}^{QSSP}$ determinations. This may be compared with representative reported literature experimental $k_{H.9.M}$ ($M = Ar, N_2$) uncertainties of $\Delta k_{H.9.M}/k_{H.9.M} = +35/-23\%$ (Mueller *et al.*, 1998) and $+53/-38\%$ (Michael *et al.*, 2002).

Clearly, the uncertainty of the reference rate coefficient substantially dominates any of the experimental uncertainties. Under the present assumption of uncertainty summing in quadrature, this observation holds even for substantially reduced uncertainties in the $k_{N.1}$ reference rate. If uncertainties for the reference $k_{N.1}$ value were only $\pm 20\%$, total linear uncertainty in $k_{H.9.Ar}^{QSSP}$ determinations would be roughly $\pm 25.5\%$ - a result still dominated by the uncertainty in the relative rate coefficient. This observation regarding the importance of the relative rate coefficient uncertainty can be generalized to many other instances of rate coefficient determinations by the relative rate method, for example, in chemical thermometry (*e.g.*, Heyne & Dryer, 2013).

Figure 3.15 reports experimental HPLFR $k_{H.9.Ar}^{QSSP}$ determinations and uncertainties as described above. Lingering systematic uncertainties in the departure from the ideal QSSP chemistry condition determined by $\sigma_{H.9.M}$ in Equation 3.12 have additionally been considered for these measurements and factored into the uncertainties stated above. For all of the $M = Ar$ experiments, results of isothermal, isobaric zero-dimensional kinetic modeling show that the $\sigma_{H.9.M}$ departure from ideal QSSP chemistry does not exceed more than a few percent for all data points considered. A hybrid kinetic model based on the H_2 submodel of Li *et al.* (2004) and the NO_x submodel of Mueller *et al.* (1999a) modified with the present nominal $k_{N.1}$ expression was used to compute $\sigma_{H.9.M}$. Computed values of $\sigma_{H.9.M}$ using the nominal, pressure-dependent $k_{H.9.M}$ expression embedded in the Li *et al.* model gives maximum $\sigma_{H.9.M}$ values of $\sim 2\%$, 5% , and 2% for Experiments 3/I, 3/II, and 3/III (both runs a & b, subject to $T = 754$ K). These maximum values reduce to below 2% for all cases when the default $k_{H.9.Ar}$ expression in the model is replaced with the nominal measured value of $k_{H.9.Ar}^{QSSP}$ determined for each experiment. Under either case of $k_{H.9.M}$ modeling assumption used to determine $\sigma_{H.9.M}$, the simulation

results suggest deviation from QSSP chemical ideality is negligible compared to the overall measurement uncertainty.

The nominal $k_{H.9.Ar}^{QSSP}$ values determined from Experiments 3/I-3/III are shown in Figure 3.15 to be in excellent agreement with the pressure-dependent $k_{H.9.M}$ expressions from the literature, particularly those based on fundamental $k_{H.9.M}$ studies of Bates *et al.* (2001), Fernandes *et al.* (2008), and Sellevåg *et al.* (2008).

3.2.3 Validation Experiments Using $M = N_2$

Much of the discussion in the preceding subsection for $M = Ar$ remains relevant for subsequent discussion of a series of HPLFR-QSSP experiments using N_2 bath gas. Consequently, only important details of these five $M = N_2$ experiments are discussed here. These experiments are divided into two groups according to nominal reaction temperature: either 739 ± 3 K for Group 1 or 825 ± 1 K for Group 2. As with the $M = Ar$ experiments, these $M = N_2$ experiments proceeded under essentially isothermal, isobaric, chemically plug flow conditions. Nominal initial reaction conditions for each experiment are listed in Table 3.1 and profile-averaged $[O_2]/[NO_2]$ values are listed in Table 3.2.

Relative standard error (2σ) of the profile-averaged $k_{H.9.N_2}^{QSSP}$ values does not exceed ~6% and 2% for any of the Group 1 and Group 2 experiments, respectively. Uncertainties in NO_2 quantification, O_2 quantification, absolute temperature, plug flow interpretation, and absolute pressure are estimated to be very similar to the $M = Ar$ experiments, so an experimental 2σ uncertainty in $[O_2]/[NO_2]$ of ~16% applies for the $M = N_2$ experiments unless otherwise indicated.

The Group 1 experiments were conducted at 20.0 and 17.3 atm pressure for Experiments 3/IV and 3/V (a & b), respectively. Measured H_2 , O_2 , and NO_2 mole fraction profiles from these experiments are reported in Figures 3.16 and 3.17. Experiments 3/Va and 3/Vb were run immediately in sequence at the same pressure and reactant feed rates, so results of both experiments are presented together in Figure 3.17. Following the same Equation 3.16 extraction procedure for $k_{H.9.Ar}^{QSSP}$ described in the preceding section, values of $k_{H.9.N_2}^{QSSP}$ for these three Group 1 experiments were determined using ϵ_{i/N_2} values of 2.0, 0.78, and 14.0 for $i = H_2$, O_2 , and H_2O (Burke *et al.*, 2012). Figure 3.18 compares these HPLFR experimental determinations with several pressure-dependent $k_{H.9.M}$ expressions used in the literature. As is the case with $M = Ar$, the present Group 1 determinations of $k_{H.9.N_2}^{QSSP}$ are in very good

agreement with rate coefficient expressions based both on fundamental $k_{H.9.M}$ studies as well as rate coefficient expressions used in many combustion kinetic models. Further, negligibly small computed values of $\sigma_{H.9.M}$ for these conditions indicate that the *a priori* assumption of QSSP chemistry is valid.

Figures 3.19 and 3.20 display measured mole fraction profiles for Group 2 Experiments 3/VI (12.5 atm) and 3/VII (10 atm), respectively. The values of $k_{H.9.N_2}^{QSSP}$ derived from these profiles are compared to literature $k_{H.9.N_2}$ expressions in Figure 3.21. The results of Experiment 3/VII return an experimentally-determined $k_{H.9.N_2}^{QSSP}$ value somewhat less than what is suggested by literature rate coefficient expressions; however, there is significant overlap in 2σ uncertainty bands for both the experimental data point ($\pm 38.5\%$) and uncertainties inherent in the literature $k_{H.9.N_2}$ determinations.

For the case of Experiment 3/VII, $\sigma_{H.9.M}$ is a negligibly small fraction of $k_{H.9.N_2}^{QSSP}$, suggesting that the *a priori* assumption of QSSP chemistry is valid for interpretation of this experiment. However, experimental observations and kinetic modeling reveal that measurements taken in Experiment 3/VI may be confounded by non-QSSP chemistry since the QSSP NO_x cycle appears saturated (exhibiting essentially complete conversion of NO to NO_2) and the quotient $\sigma_{H.9.M}/k_{H.9.N_2}^{QSSP}$ is a significant fraction of unity (see also Section 3.1.2 and the explanation of Figure 3.9). As detailed in the following paragraphs, correction of the *apparent* measured $k_{H.9.N_2}$ value from this experiment with a model-estimated $\sigma_{H.9.M}$ for these conditions significantly improves the Experiment 3/VI $k_{H.9.N_2}$ determination relative to representative literature rate coefficient expressions.

The $\sigma_{H.9.M}$ correction accounting for secondary chemistry is consistent both with prior theoretical description of the “extended” QSSP condition (Section 3.1.2) as well as model-dependent treatment of secondary chemistry evident throughout the rate coefficient determination literature (*e.g.*, Bates *et al.*, 2001; Su *et al.*, 2002; or Vasu *et al.*, 2011). Consequently, there is little basis for objecting to the present modeling of secondary chemistry as an additional tool to aid in HPLFR-QSSP validation. However, the additional uncertainty and information content contributed by the correction must be thoroughly considered.

The model-dependent value of $\sigma_{H.9.M}$ computed for Experiment 3/VI was derived from kinetic modeling using a hybrid H_2/NO_x chemistry model from Li *et al.* (2004)/Mueller *et al.* (1999a) subject to varying assumed values of $k_{H.9.M}$ and $k_{N.1}$. To achieve a large, conservative range in the sensitive ratio

of kH.9.M and kN.1 describing the primary chemistry, the extremal kH.9.N2 rate coefficient values of Li *et al.* (2004) and Ranzi *et al.* (CRECK, 2012) (Figure 3.21) were paired together with the kN.1 VRC-FTST and experimental expressions of Su *et al.* (2002) as well as the extrapolated recommendation of Ko & Fontijn (1991) (Figure 3.14) to generate six variants of the base hybrid kinetic model representing a wide range of kH.9.N2/kN.1 ratios.

Zero-dimensional, isobaric, isothermal simulations at the nominal initial experimental conditions (Table 3.1) were generated from each model variant for use in Equation 3.12. Results of each simulation were time-shifted (Dryer *et al.*, 2014) such that the predicted steep initial NO₂ formation gradient coincided with the NO₂ mole fraction measurements at ~0.55 seconds relative plug flow time (Figure 3.19). Values of $\sigma_{H.9.M}$ specific to each kinetic model variant were then derived from an average value across the simulated apparent quasi-steady NO₂ plateau corresponding to 0.94 to 2.08 seconds relative plug flow time. Aside from the reference of the time-shift to the experimental data, the computed values of $\sigma_{H.9.M}$ result purely from model simulations and have magnitudes that are essentially independent of experimental measurements.

Modeling results are summarized together with apparent experimental kH.9.N2 values in Table 3.3 and plotted in Figure 3.21. These results reveal remarkable features of extended QSSP chemistry and the $\sigma_{H.9.M}$ term developed in Section 3.1. For a given assumed value of kH.9.N2, $\sigma_{H.9.M}$ may vary by up to nearly a factor of 2 depending on kN.1 expression assumed by the kinetic model. Moreover, $\sigma_{H.9.M}$ varies by nearly a factor of 3.5 among all six model variants considered. However, for a given assumed value of kH.9.N2, the model-corrected kH.9.N2 values based on the summation of *essentially independent* experimental and modeling results yield highly consistent values – within 1.2% – among all kN.1 model variants and the assumed kH.9.N2.

This behavior may appear tautological in the sense that each model variant presupposes a value of kH.9.N2 and then estimates very nearly the same value of kH.9.N2. However, it is important to emphasize that $\sigma_{H.9.M}$ determined from each model variant, including the assumed value of kN.1, only contributes between 19 and 46% of the final corrected kH.9.N2 value. The balance of the corrected kH.9.N2 value comes from the *independent* Experiment 3/VI measurements. This strongly suggests that the experimental data upon which the corrected value of kH.9.N2 is based are both accurate as well as

free from fortuitous cancellation of errors. For example, if the experimentally-determined ratio of NO₂ and O₂ were too high or too low by 10%, the essentially independent modeling corrections would fail to converge the corrected kH.9.N2 values to the presupposed model value by non-negligible deviations of ~5-8%, depending on specific model variant. Further, the extremely good agreement in corrected kH.9.N2 values among model variants would also be reduced.

The present analysis also illustrates the model-dependencies of $\sigma_{H.9.M}$ in correcting apparent kH.9.M values derived from such conditions. Because the present model-advised interpretations nearly span the literature kH.9.N2 range (Figure 3.21), no distinct corrected kH.9.N2 value is presently offered for Experiment 3/VI. The implicit model-dependent uncertainties relative to the apparent uncertainty of kH.9.N2 described in the curves of Figure 3.21 render moot any such quantitative recommendation. In the context of this thesis, the more important result of these interpretations of Experiment 3/VI is the additional demonstration of the experimental fidelity of the HPLFR facility in making measurements at (extended) QSSP conditions.

3.3 Alternative Validation of HPLFR with QSSP Measurements of kN.1

As demonstrated in the preceding section, determinations of kH.9.Ar^{QSSP} and kH.9.N2^{QSSP} premised on the literature kN.1_{VRC-FTST} expression compare favorably to independent kH.9.M expressions based on both fundamental studies of the H.9.M system as well as kinetic model Consensus. Due to the relative rate nature of the QSSP technique (Equation 3.1), HPLFR QSSP measurements may also be used to determine kN.1. A comparison of HPLFR-measured and literature kN.1 values provides an independent check of the HPLFR QSSP technique presently employed. This comparison is made in a recent publication (Haas & Dryer, 2015) and will not be repeated here in full. However, Figure 3.22 provides a graphical comparison of HPLFR kN.1 determinations, several literature experimental kN.1 determinations, and several literature kN.1 expressions. The present kN.1^{QSSP} determinations are based on the “Consensus” kH.9.M values discussed in the explanation of Figures 3.15 and 3.18. These HPLFR measurements are in very good agreement with the nominal experimentally-determined kN.1 values of Ko & Fontijn (1991) near 750 K as well as the three previously presented temperature-dependent kN.1 rate coefficient expressions (Figure 3.14) covering the temperature range below 1000 K.

Notably, the HPLFR QSSP values extend the pressure range of reported experimental $k_{N.1}$ values by up to 2 orders of magnitude. Further interpretation of QSSP flow reactor data from Ashman (1999) and Mueller *et al.* (1998) can also add additional $k_{N.1}$ data at relatively higher pressures than presently represented in the literature. Moreover, these studies can provide data in the $760 \leq T \leq 1100$ K range where no experimental data appears. Reinterpretation of these studies is, however, beyond the scope of this thesis.

Table 3.1 – Nominal initial conditions for HPLFR kH.9.M validation experiments in Ar, N₂ bath gases

Experiment Reference	Bath Gas	Pressure (atm)	Temperature (K)	H₂ (ppm)	O₂ (ppm)	NO (ppm)
3/I	Ar	18.0	747	12622	13100	97
3/II	Ar	15.0	752	19223	16851	96
3/IIIa	Ar	12.0	755	19215	18847	96
3/IIIb	Ar	12.0	751	19215	18847	96
3/IV	N ₂	20.0	737	23961	11677	184
3/Va	N ₂	17.3	738	21374	13957	185
3/Vb	N ₂	17.3	742	21374	13957	185
3/VI	N ₂	12.5	824	11017	19625	94
3/VII	N ₂	10.0	825	10717	19920	94

Table 3.2 – Measured profile-averaged ratio of O₂ and NO₂ mole fractions from HPLFR-QSSP validation experiments

Experiment Reference	Bath Gas	Nominal Pressure (atm)	Nominal Temperature (K)	[O ₂]/[NO ₂] ^a	kN.1/kH.9.M ^a	Estimated 2σ Uncertainty in [O ₂]/[NO ₂] ^b
3/I	Ar	18.0	747	150.0	159.9	16%
3/II	Ar	15.0	752	167.0	185.5	16%
3/IIIa	Ar	12.0	755	194.5	219.1	16%
3/IIIb	Ar	12.0	751	194.6	220.2	16%
3/IV	N ₂	20.0	737	75.1	79.2	16%
3/Va	N ₂	17.3	738	87.9	92.8	16%
3/Vb	N ₂	17.3	742	91.3	95.3	16%
3/VI	N ₂	12.5	824	208.1 ^c	213.2 ^c	12.5% ^c
3/VII	N ₂	10.0	825	219.5	225.2	16%

^a Profile-averaged values of [O₂]/[NO₂] give kN.1/kH.9.M (for M = Bath Gas) under Equation 3.1 QSSP assumptions, with correction by Equation 3.16 and assumed collisional efficiencies for M = H₂O, H₂, and O₂ relative to Ar and N₂ (see Sections 3.2.2 and 3.2.3). ^b Uncertainty estimated from contributions due to profile averaging, NO₂ and O₂ quantification, variations in absolute pressure and temperature, and plug-flow and QSSP idealizations. ^c This condition deviates significantly from QSSP assumptions. The QSSP NO_x cycle appears saturated and most of the NO_x exists as NO₂. Consequently, the ~10% propagated uncertainty due to NO₂ quantification applicable to other experiments has been omitted in this case.

Table 3.3 – Model-derived estimates of $\sigma_{H,9,M}$ for Experiment 3/VI

kH.9.N2 expression reference/value (cm³/mol.s)	kN.1 expression reference (see Figure 3.14)	A $\sigma_{H,9,M}$ (cm³/mol.s)	B Uncorrected kH.9.N2 (cm³/mol.s)^a	A+B Corrected kH.9.N2 (cm³/mol.s)
Li <i>et al.</i> (2004) 7.82×10¹¹	Su <i>et al.</i> (2002) VRC-FTST	2.65×10 ¹¹	5.07×10 ¹¹	7.72×10¹¹
	Ko & Fontijn (1991)	2.76×10 ¹¹	4.96×10 ¹¹	7.72×10¹¹
	Su <i>et al.</i> (2002) EXP	3.59×10 ¹¹	4.15×10 ¹¹	7.74×10¹¹
Ranzi <i>et al.</i> (2012) 6.05×10¹¹	Su <i>et al.</i> (2002) VRC-FTST	1.02×10 ¹¹	5.07×10 ¹¹	6.09×10¹¹
	Ko & Fontijn (1991)	1.13×10 ¹¹	4.96×10 ¹¹	6.09×10¹¹
	Su <i>et al.</i> (2002) EXP	1.95×10 ¹¹	4.15×10 ¹¹	6.10×10¹¹

^a Based on bath gas-corrected kN.1/kH.9.N2 values of Table 3.2 and particular kN.1 expression listed in 2nd column, preserving self-consistency in kN.1 values used. "(Un)Corrected" refers here to the consideration of the $\sigma_{H,9,M}$ correction for departure from QSSP conditions.

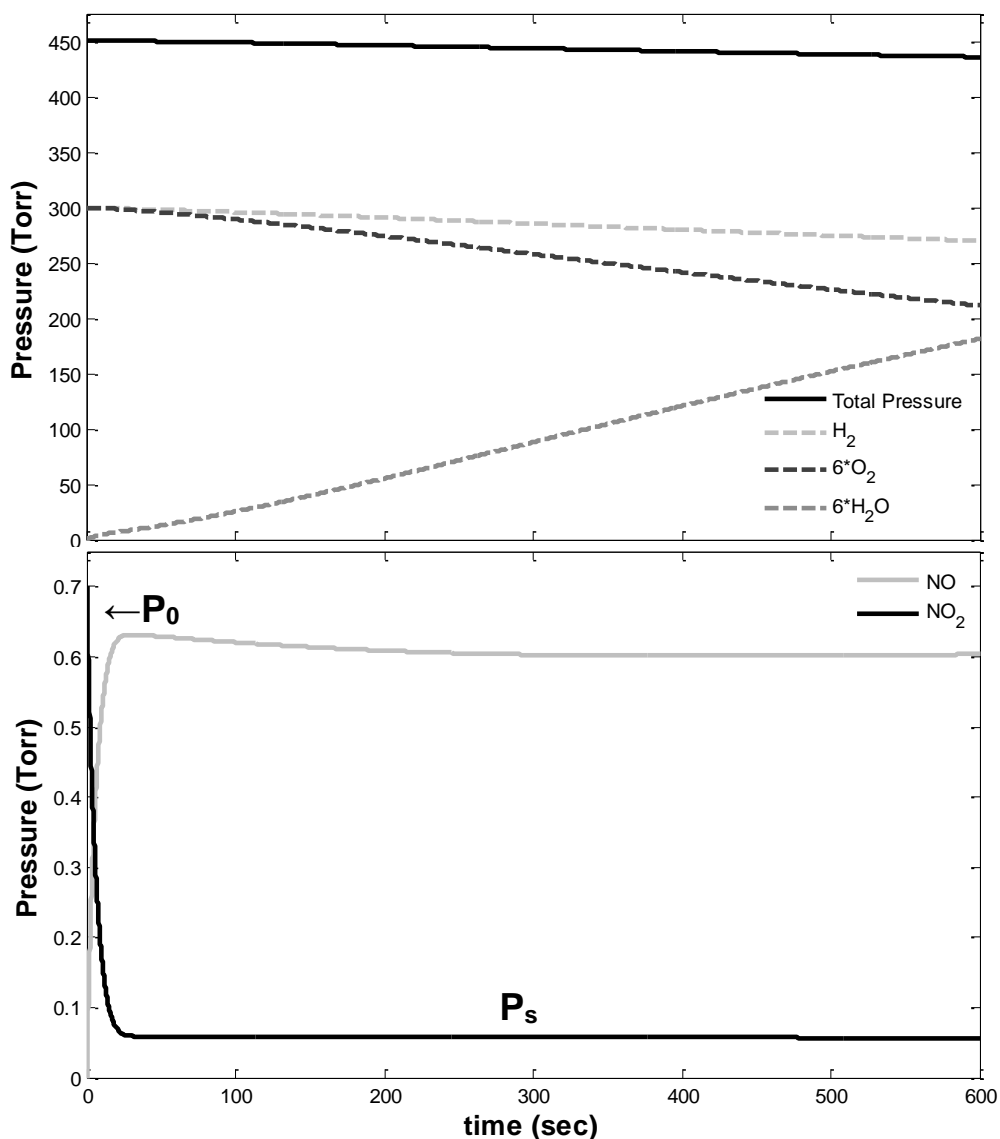


Figure 3.1 – Illustration of quasi-steady state plateau (QSSP) features: Base Case conditions.

Ashmore & Tyler (1962) do not report temporally-resolved data, so Figures 3.1-3.4 have been generated from a kinetic model to illustrate some features of the QSSP condition relevant to the present discourse. At this stage of discussion, particular details of the kinetic model employed are not important relative to the QSSP phenomenology addressed by the figures.

Present figure conditions are representative for the Ashmore & Tyler experiments: isothermal, constant volume with 300/100/50/0.7 Torr $H_2/N_2/O_2/NO_2$ initial reactant composition at 633K. The initial and plateau pressures for NO_2 are indicated by P_0 and P_s , respectively. Slow oxidation of H_2 into H_2O , even during the plateau period, is apparent both from the simulated species profiles as well as the Total Pressure profile.

The particular conditions of this figure serve as a basis for comparison for additional figures describing the QSSP condition. Note that the $H_2/N_2/O_2$ system without added NO/NO_2 is essentially unreactive at these conditions for the timescales shown.

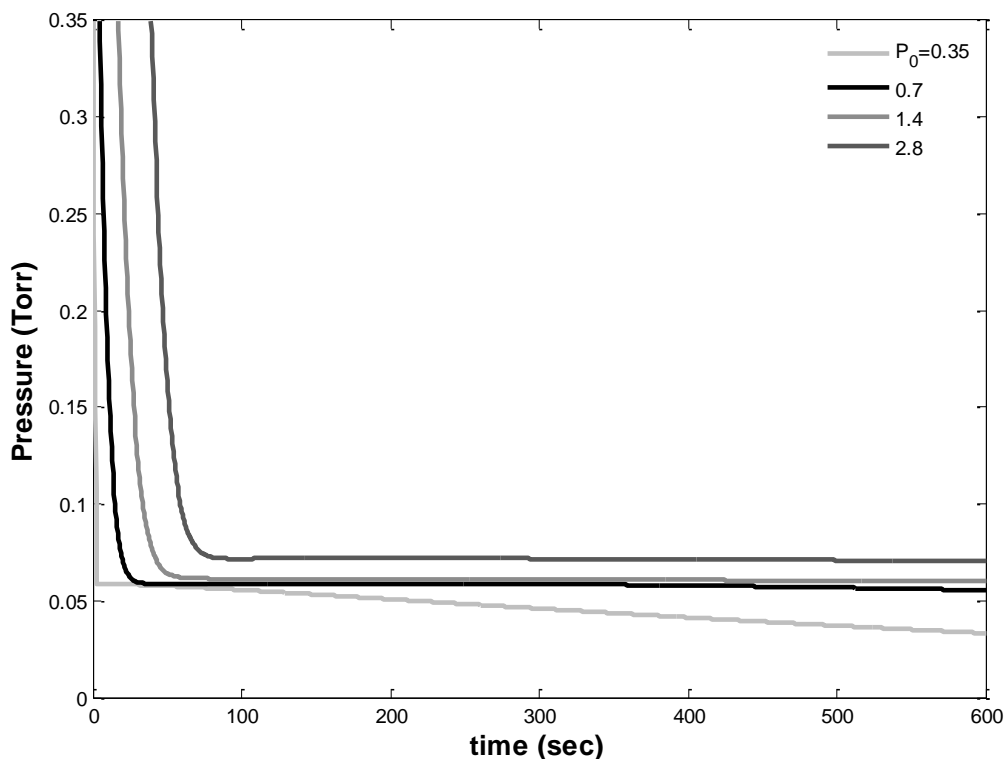


Figure 3.2 – Response of P_s to initial NO_2 level.

The Base Case simulation of $P_0 = 0.7$ Torr from Figure 3.1 is indicated by the bold black line. For the fixed reactant composition 300/100/50 Torr $\text{H}_2/\text{N}_2/\text{O}_2$ and $T = 633$ K, these simulations illustrate convergent QSSP P_s behavior for an 8-fold variation in P_0 . The three cases of $P_0 = 0.35, 0.7,$ and 1.4 Torr approach an initial $P_s \approx 0.06$ Torr. The falling P_s in the case of $P_0 = 0.35$ Torr is due to the relatively faster overall reaction rate, which more quickly depletes O_2 and reduces vessel pressure. Both of these effects reduce P_s , in accordance with Equation 3.1. The higher P_s in the $P_0 = 2.8$ Torr case may be due to increased side reactions of species formed from NO_x conversion. Such reactions are not accounted for in the simplified reaction scheme discussed in Section 3.1.1. These side reactions may include



and



QSSP NO_2 profiles may exhibit small sensitivities to these reactions at longer times (see Figures 3.6 and 3.7).

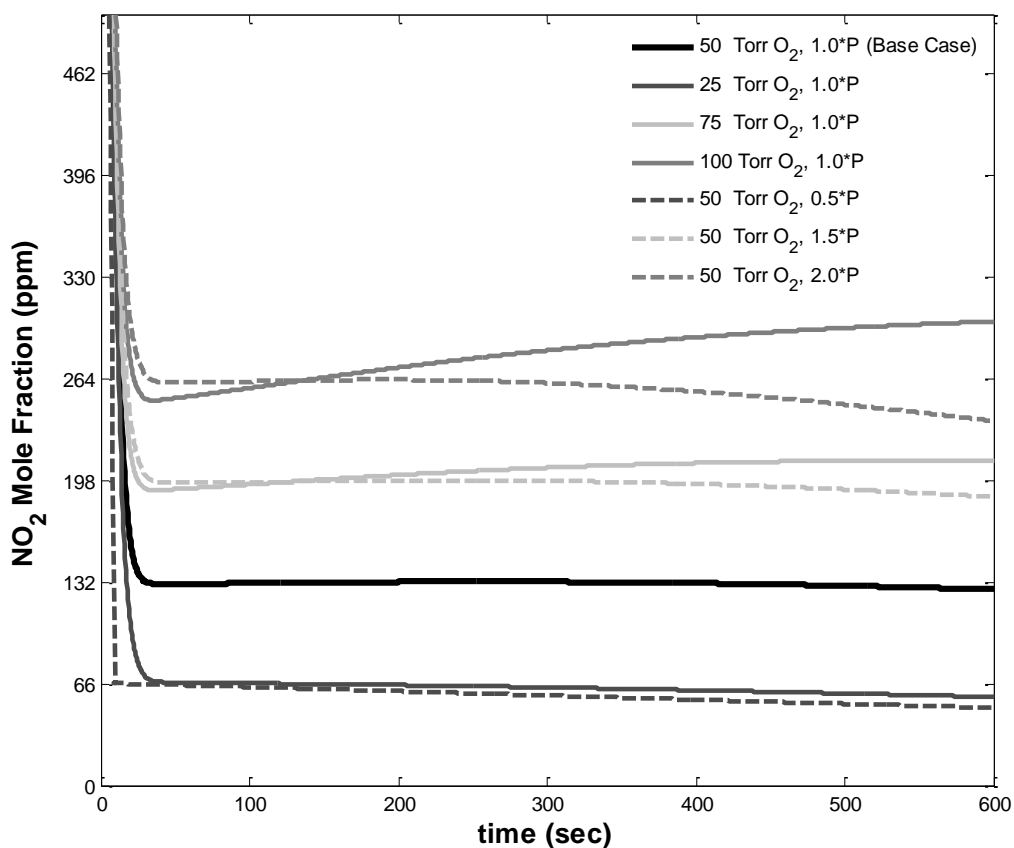


Figure 3.3 – Scaling of P_s with both initial O_2 pressure and initial total reactor pressure.

The Base Case simulation from Figure 3.1 is indicated by the bold black line and is compared to simulations in which either the base O_2 pressure (50 Torr) or base total reactor pressure (450.7 Torr) is multiplied by a factor of 0.5, 1.5, or 2.0. The interval on the y-axis has been selected to highlight the essentially linear scaling of the NO_2 plateau with both O_2 concentration and pressure, as expressed by Equation 3.1. Second-order effects explain the specific departures of P_s from completely linear behavior. Such effects include O_2 depletion, reduction of total reactor pressure as reaction progresses, side reactions, and H_2O formation.

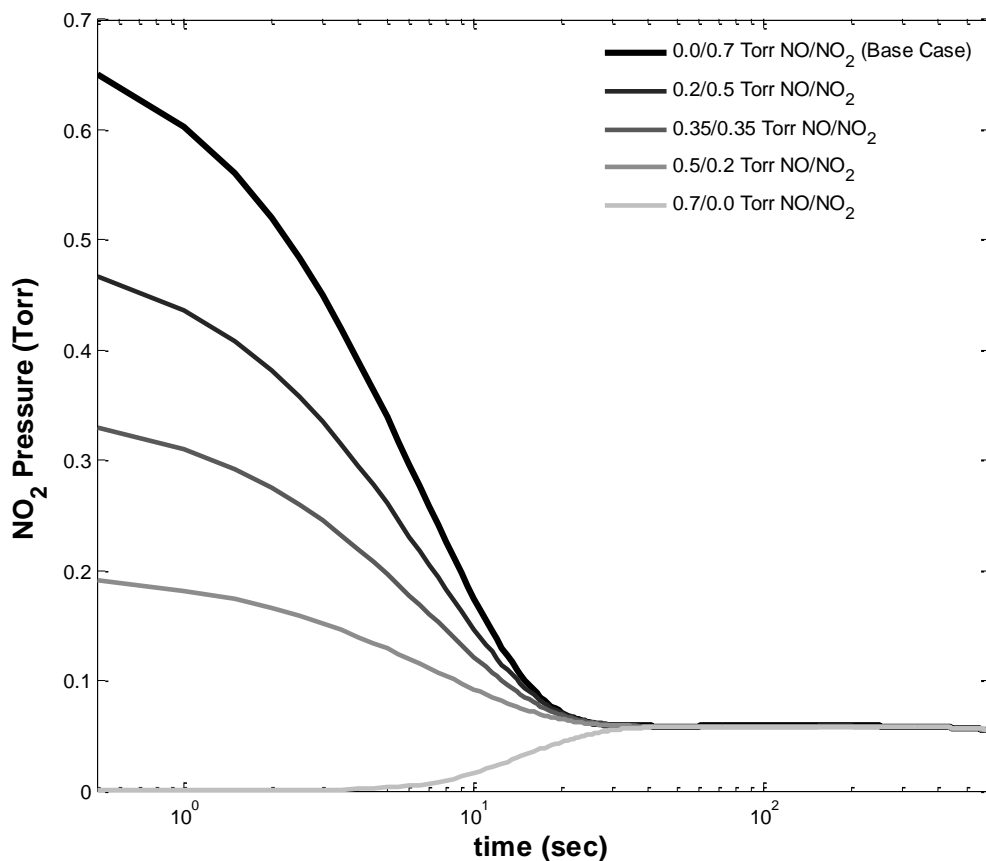


Figure 3.4 – Response of P_s to NO+NO₂ sensitizer composition.

The Base Case simulation of $P_0 = 0.7$ Torr from Figure 3.1 is indicated by the bold black line. The additional simulations shown here have fixed initial total NO+NO₂ levels of 0.7 Torr and demonstrate the insensitivity of the QSSP condition to the (NO+NO₂) sensitizer composition. The logarithmic axis for time clearly distinguishes the transient conversion of NO₂↔NO, after which the P_s trajectories essentially converge. Transients converge at ~30 seconds, which accounts for only a small fraction of the QSSP timescale, shown here to extend to at least 600 seconds.

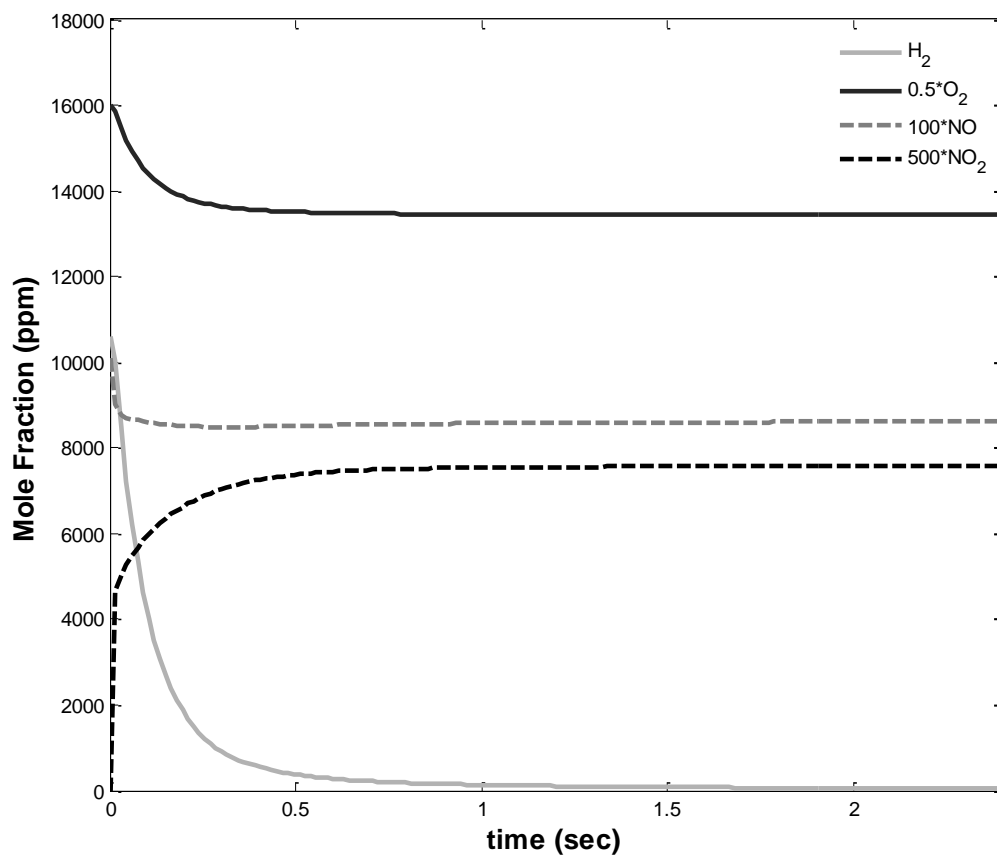


Figure 3.5 – Response of QSSP condition to complete H₂ consumption.

Conditions are representative for experiments of Ashman (1999): isothermal and isobaric with 1.06%/3.20%/101ppm H₂/O₂/NO in N₂ initial reactant composition at 850K and 1 atm. Effective depletion of H₂ does not change the QSSP NO₂ and O₂ profiles on the timescale of the modeled experiment. Additional simulations show essentially invariant O₂, NO, and NO₂ mole fraction profiles extending for hundreds of seconds.

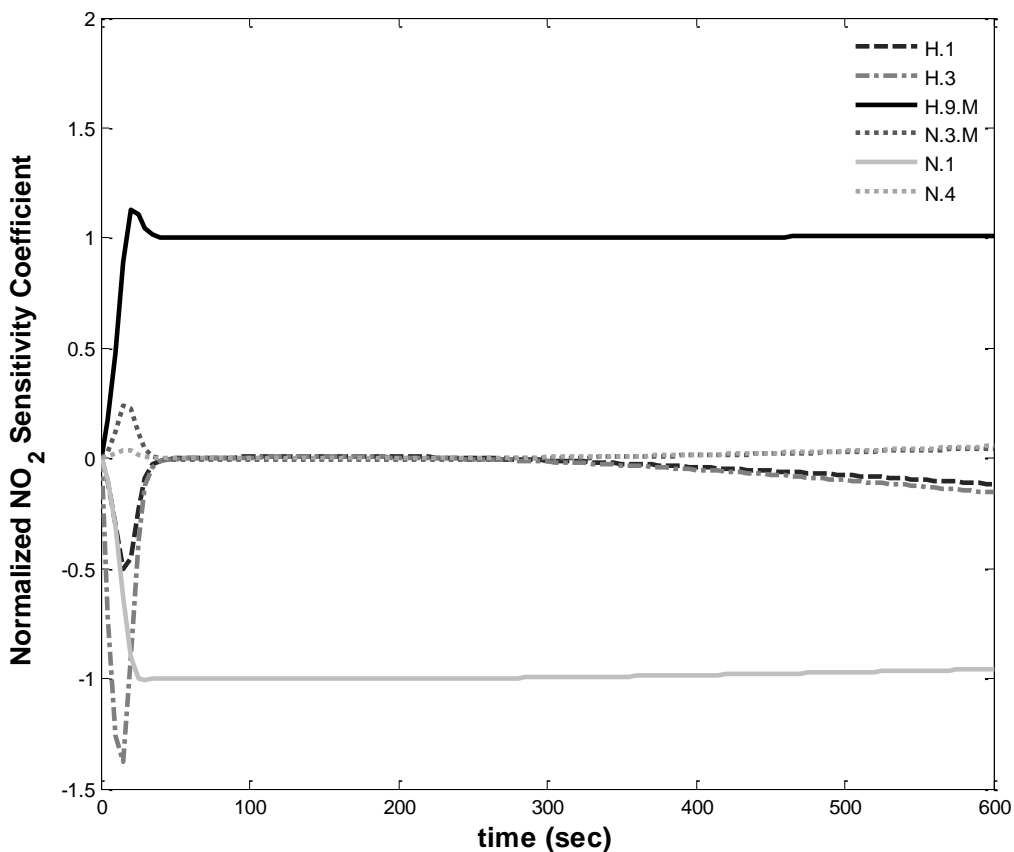


Figure 3.6 – Sensitivity of P_s to rates of key reactions, Base Case conditions.

The normalized sensitivity coefficient $S_{I,k}$ for an observable I to the rate of reaction k is given by

$$S_{I,k} = \frac{\partial \ln I}{\partial \ln \omega_k}, \quad (3.17)$$

which can be rearranged to give

$$S_{I,k} \frac{\partial \omega_k}{\omega_k} = \frac{\partial I}{I}. \quad (3.18)$$

This interpretation reveals that $S_{I,k}$ represents a gain reflecting the expected fractional change in observable I due to a fractional change in ω_k under small, linear perturbation of the assumed chemical source term model. In the present illustration, I indicates the mole fraction of NO_2 .

These sensitivity results indicate that under Base Case QSSP conditions, the mole fraction of NO_2 essentially scales as indicated by Equation 3.1: on a fractional basis, an increase/decrease of $\omega_{H.9.M}$ will lead to the same fractional increase/decrease for $[\text{NO}_2]_{\text{QSSP}}$, while an increase/decrease of $\omega_{N.1}$ leads to the same fractional decrease/increase. Variation of the rates assigned to other reactions adopted in the chemistry model, including N.1 and H.3, are not expected to significantly affect $[\text{NO}_2]_{\text{QSSP}}$ over the time interval indicated.

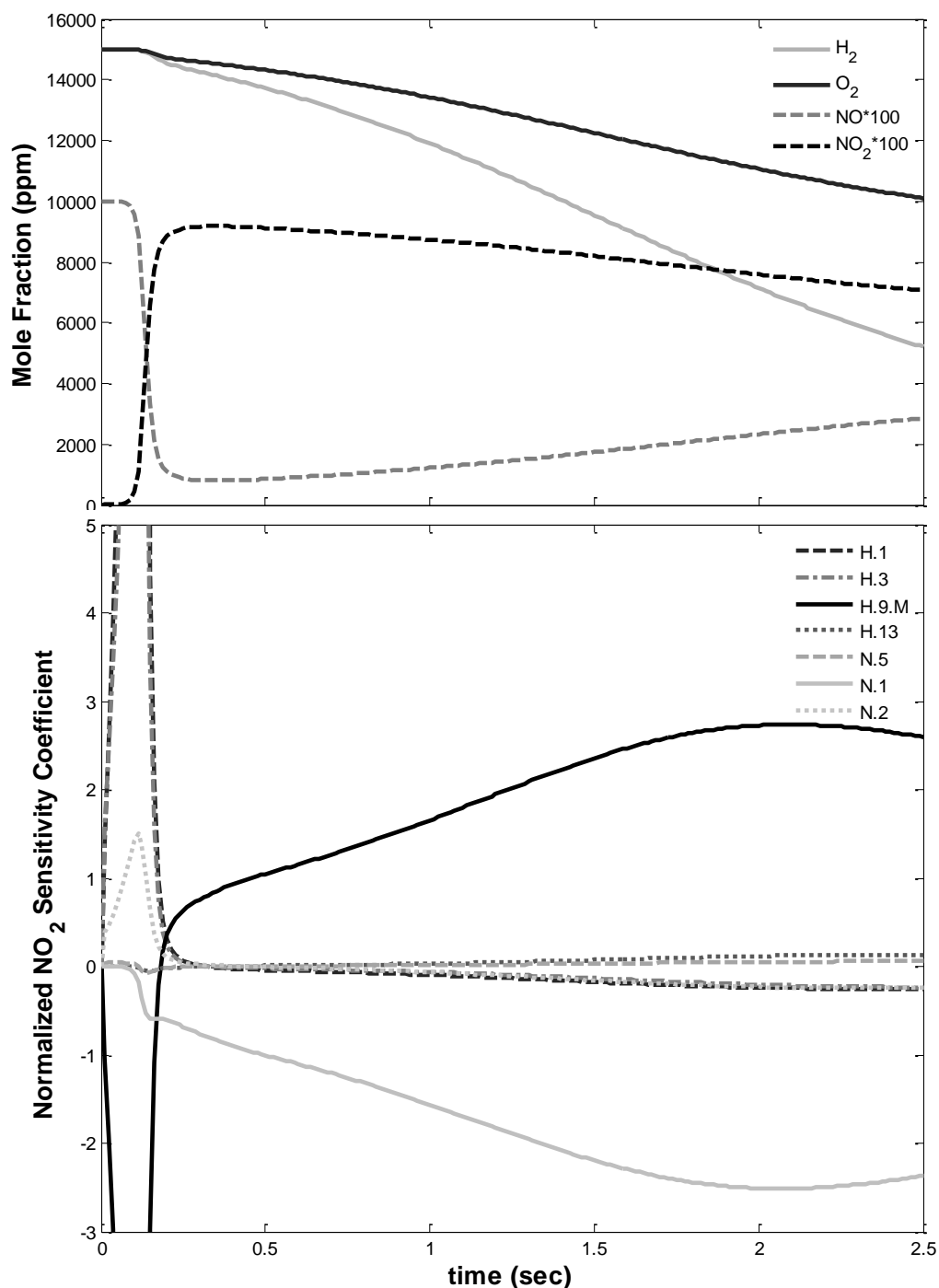


Figure 3.7 – QSSP features and P_s sensitivity to rates of key reactions at conditions representative of HPLFR experiments.

Conditions represent those of HPLFR experiments: isothermal and isobaric with 1.5%/1.5%/100ppm $H_2/O_2/NO$ in N_2 initial reactant composition at 800K and 10 atm. Reactions H.9.M and N.1 remain the most sensitive at these conditions. Unlike the base case, normalized NO_2 profile sensitivities exceed unity in magnitude since at these timescales the overall reaction rate governed by H.9.M/N.1 couples strongly with the O_2 , NO_2 , and H_2O concentration profiles.

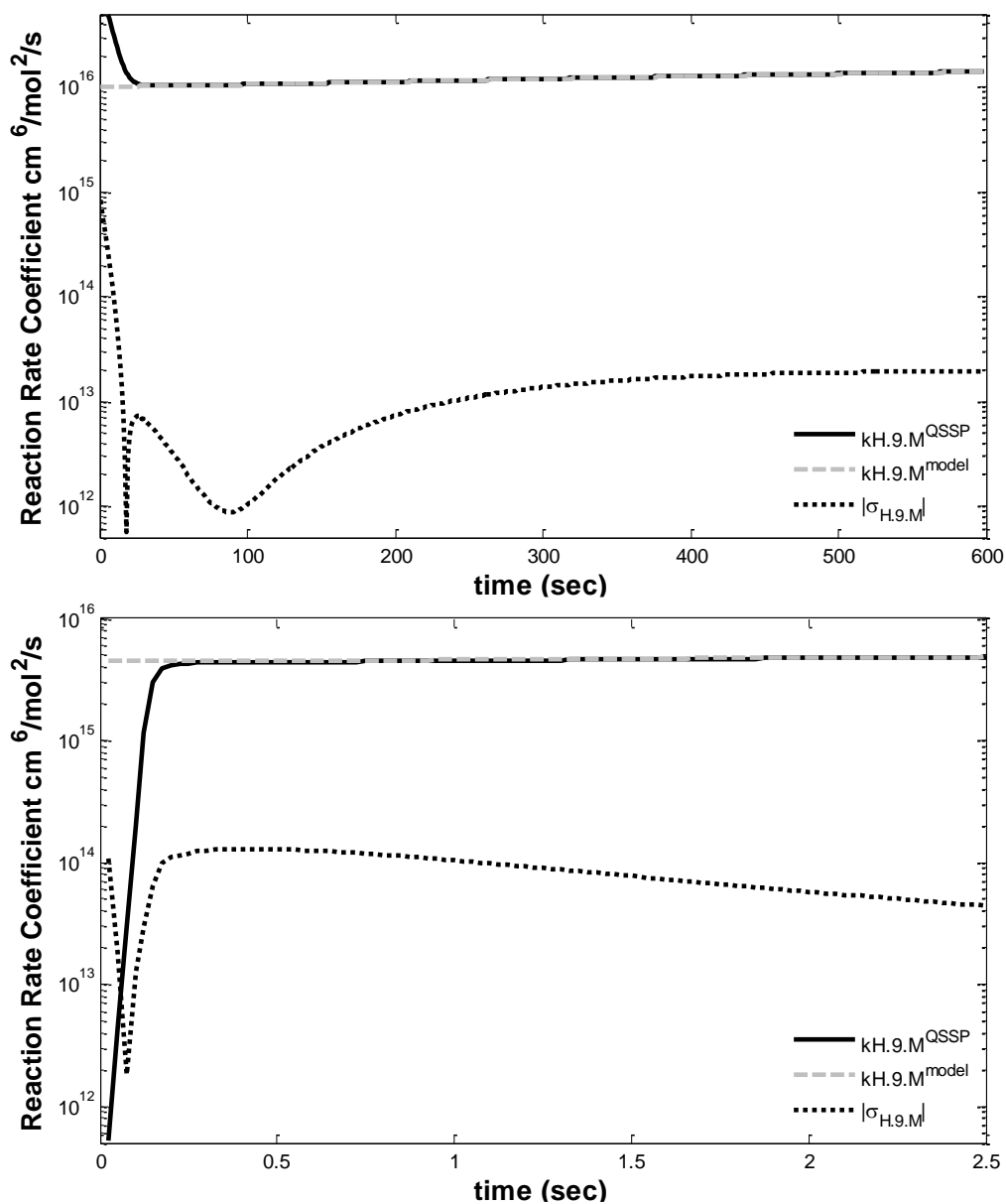


Figure 3.8 – Illustration of departures from QSSP condition estimated by $\sigma_{H,9,M}$.

The top panel has been computed for the Ashmore & Tyler Base Case conditions of Figure 3.1. Between the initial transient and $t = 600$ sec, $\sigma_{H,9,M}$ remains less than 0.15% of $k_{H,9,M}^{model}$ and $k_{H,9,M}^{QSSP}$, indicating that at these conditions, effectively ideal QSSP conditions are satisfied for measurement of $k_{H,9,M}$. The values of $k_{H,9,M}^{QSSP}$ and $k_{H,9,M}^{model}$ are within $\sim 1\%$ of each other over this time span. The bottom panel corresponds to the nominal HPLFR conditions of Figure 3.7, where maximum QSSP deviations after the transient do not exceed 3% from ideality.

The distinction between $k_{H,9,M}^{QSSP}$ and $k_{H,9,M}^{model}$ is that the former is computed by Equation 3.1 and model values for $k_{N,1}$, $[NO_2]$, $[O_2]$, P , and T , according to the treatment of experimental QSSP $k_{H,9,M}$ determinations, while the latter is derived from model values for $\omega_{H,9,M}$, $[H]$, $[O_2]$, P , and T using the direct definition of $k_{H,9,M} \equiv \omega_{H,9,M}/[H][O_2][M]$.

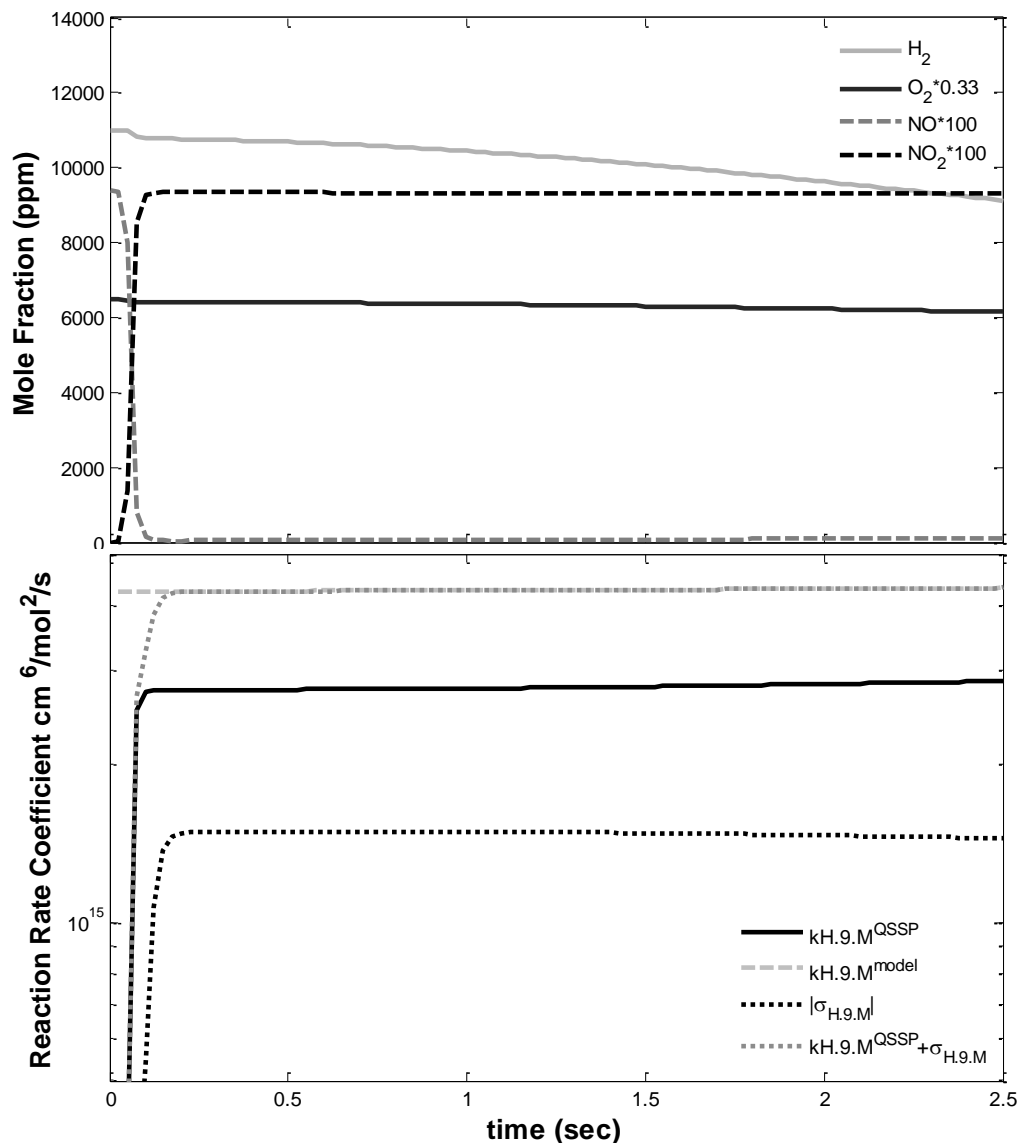


Figure 3.9 – Correction of simulated $k_{H.9.M}^{QSSP}$ measurement using $\sigma_{H.9.M}$.

Conditions are the same as for HPLFR Experiment 3/VI discussed in Section 3.2.3: isothermal and isobaric plug flow with 1.10%/1.96%/94ppm H₂/O₂/NO in balance N₂ initial reactant composition at 824 K and 12.5 atm. At these conditions, the QSSP NO_x cycle is saturated, and there is insufficient NO/NO₂ to react with HO₂/H by reactions N.2/N.1. Like ideal QSSP conditions, both slow H₂ oxidation and steady NO₂ plateau are achieved (top); however, side reactions and slow radical pool growth cause this system to depart significantly from ideal QSSP behavior. The $k_{H.9.M}^{QSSP}$ that would be apparent from experimental measurements is significantly lower than the true value embodied by $k_{H.9.M}^{model}$. However, as the figure indicates, the sum of $k_{H.9.M}^{QSSP}$ and $\sigma_{H.9.M}$ yields $k_{H.9.M}^{model}$ to within 1% (excluding the initial transient). Hence, $\sigma_{H.9.M}$ may be used to approximately correct $k_{H.9.M}^{QSSP}$ at conditions that do not depart too severely from ideal QSSP behavior.

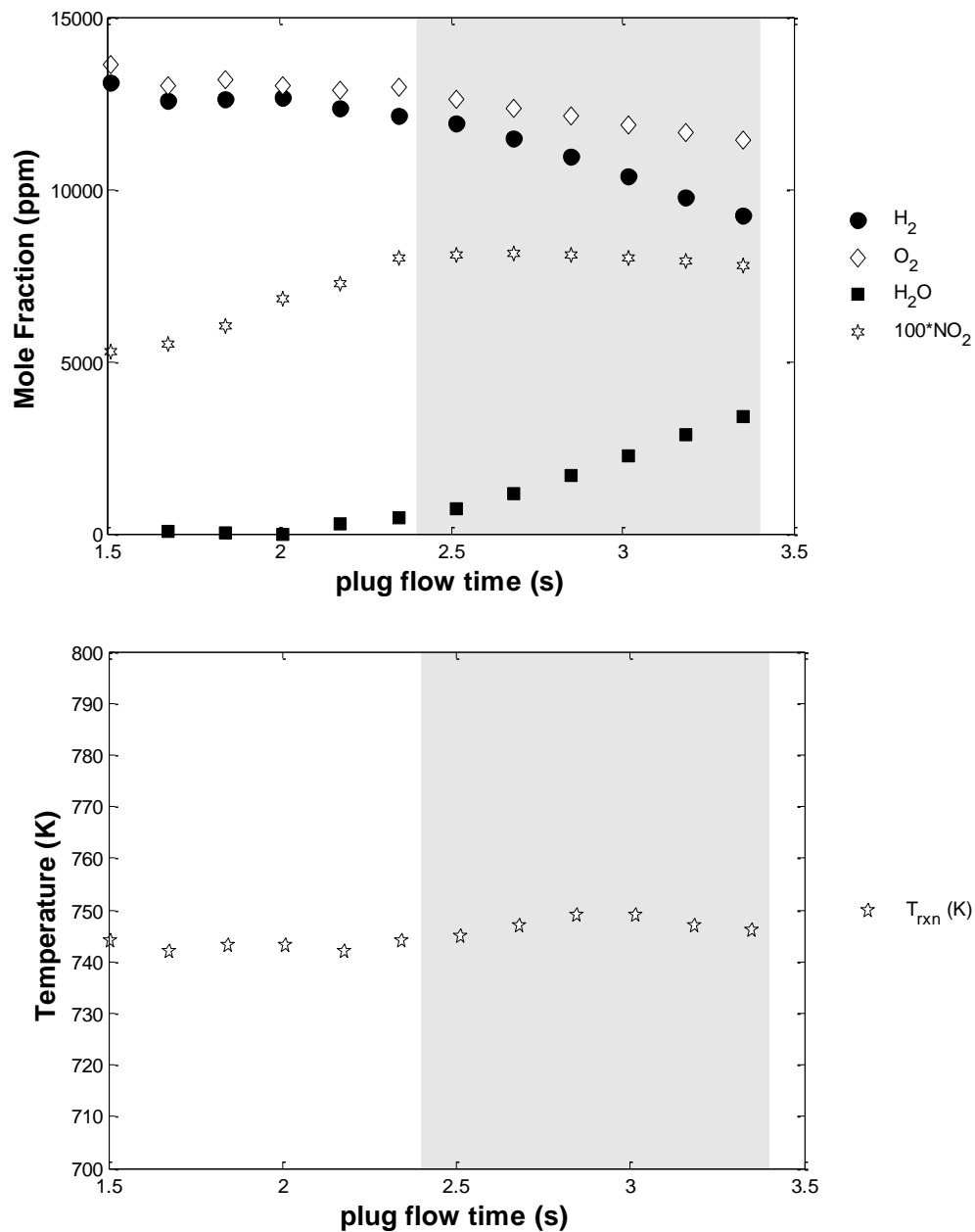


Figure 3.10 – Measured species and temperature profiles for HPLFR QSSP Experiment 3/l.

Nominal initial reaction conditions are 12622/13100/97 ppm $H_2/O_2/NO$ in balance Ar bath gas at 18 atm. The water profile is computed based on H atom balance. Temperature is nominally 747 K over the quasi-steady plateau indicated by shading, and the reaction proceeds essentially isothermally.

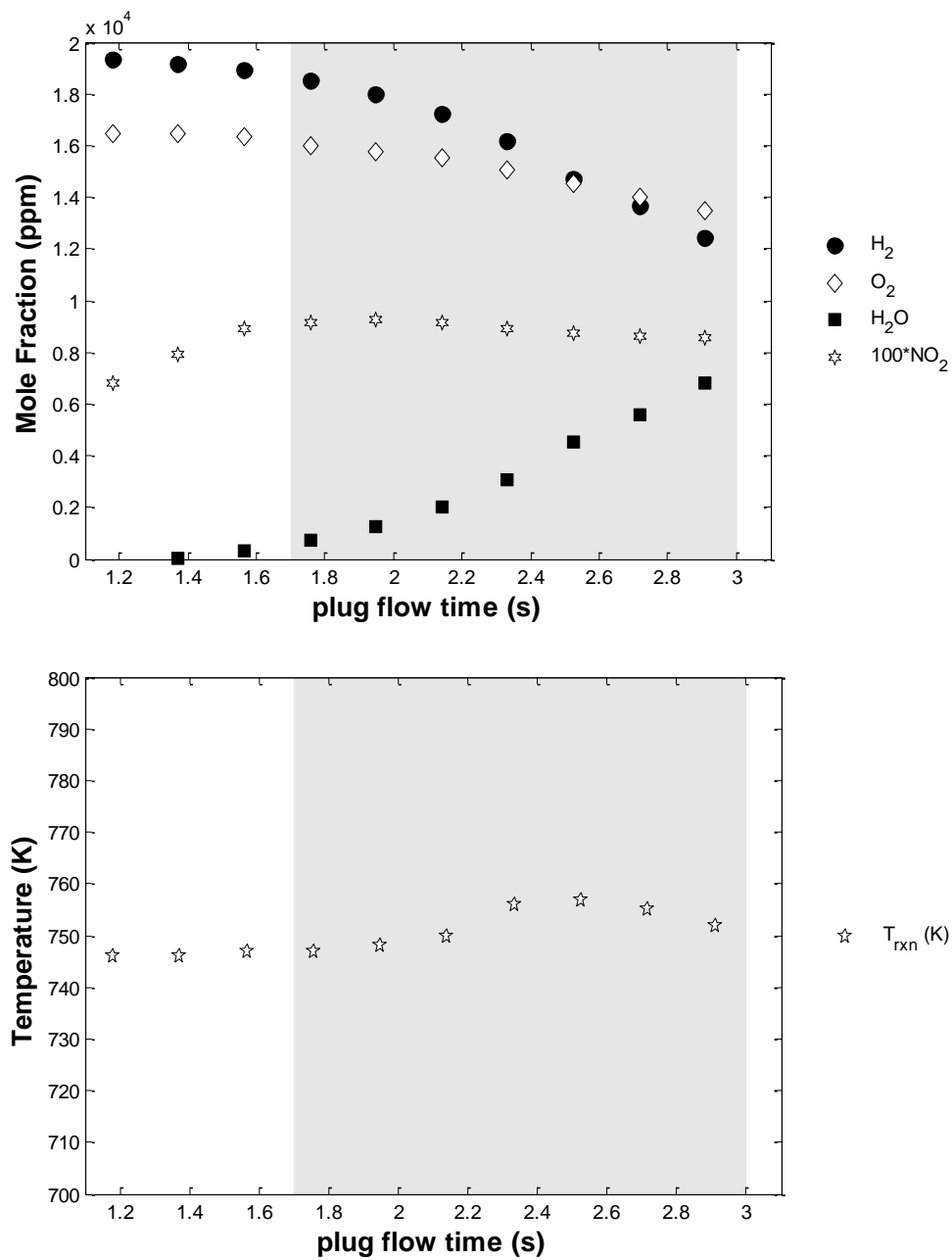


Figure 3.11 – Measured species and temperature profiles for HPLFR QSSP Experiment 3/II.

Nominal initial reaction conditions are 19223/16851/96 ppm $H_2/O_2/NO$ in balance Ar bath gas at 15.0 atm. The water profile is computed based on the H atom balance. Temperature is nominally 752 K over the quasi-steady plateau indicated by shading, and the reaction proceeds essentially isothermally.

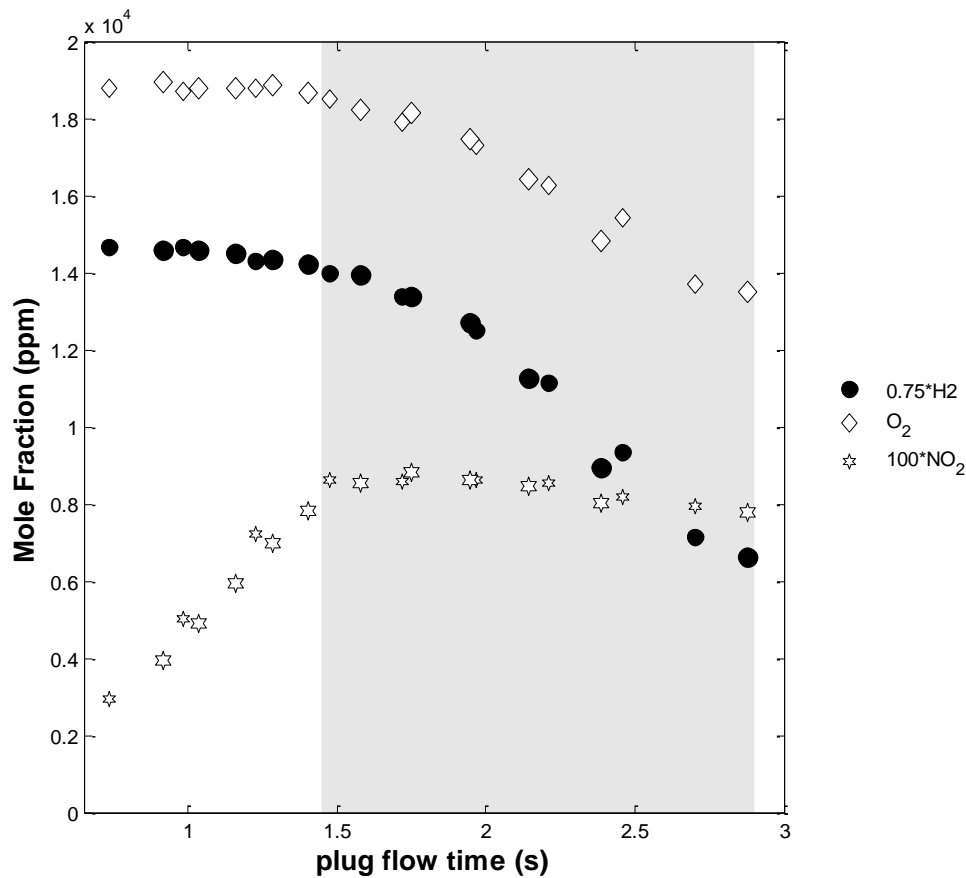


Figure 3.12 – Measured species profiles for HPLFR QSSP Experiments 3/IIIa and 3/IIIb.

Nominal initial reaction conditions are 19215/18847/96 ppm H₂/O₂/NO in balance Ar bath gas at 12.0 atm. Small markers correspond to Experiment 3/IIIa, and large markers correspond to Experiment 3/IIIb. Due to the similarity of reaction conditions for these two experiments, conducted back-to-back, the results have been superimposed by shifting the relative plug flow time of Experiment 3/IIIb by 0.3 seconds to achieve the present overlap in species profiles. Despite this ambiguity in interpretation of the initial conditions for the QSSP-IVP idealization, the species *gradients* in the shaded plateau region provide extremely consistent profile-averaged NO₂/O₂ ratios (Table 3.2) for experiments 3/IIIa and 3/IIIb, respectively. These ratios are the important experimental species observables for kH.9.Ar or kN.1 determination by Equation 3.1. The present observation regarding initialization and gradient measurements is consistent with both prior discussion of the robustness of the QSSP condition to variations in initial conditions as well as other discussions on flow reactor measurements (e.g., Dryer *et al.*, 2014 and in the supplementary material to Zhao *et al.*, 2008).

Temperature profiles (not shown) are essentially isothermal as in the cases of Experiments 3/I and 3/II. Based on measured temperatures in the quasi-steady reaction plateau indicated by shading, nominal temperatures are 755 and 751 K for Experiments 3/IIIa and 3/IIIb, respectively.

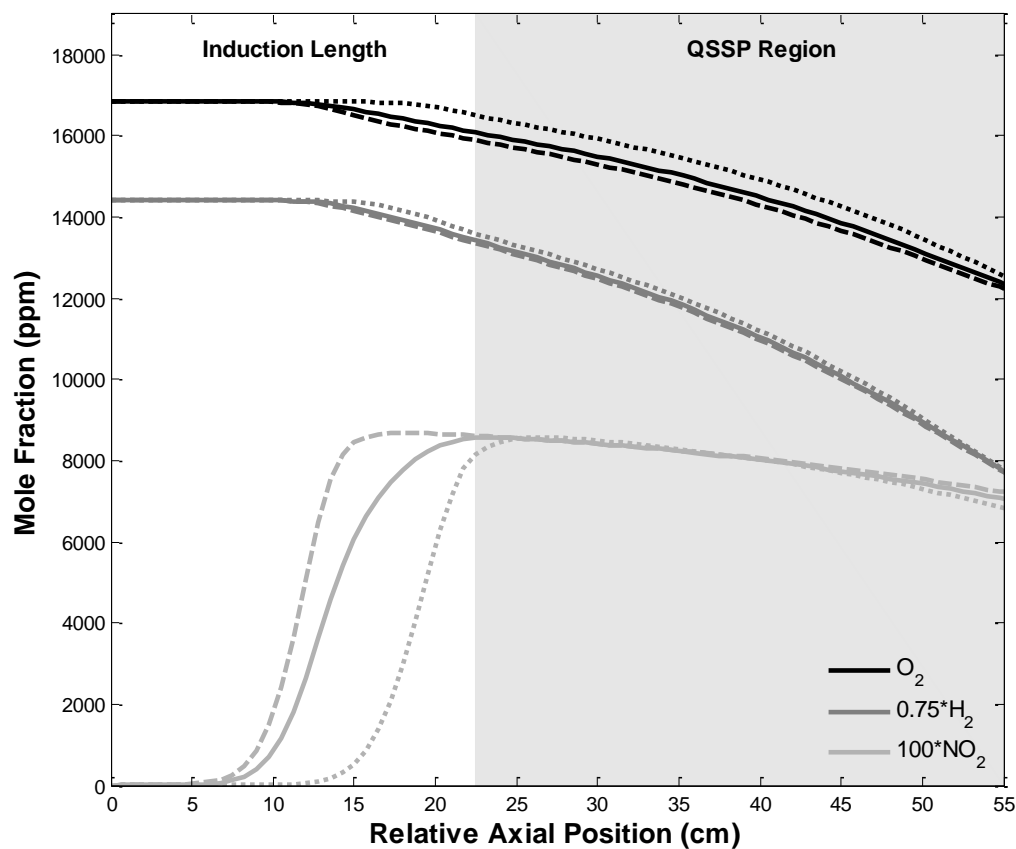


Figure 3.13 – Area-averaged, wall, and centerline axial species profile results from two-dimensional simulation of M = Ar experiment 3/II.

The shaded region corresponds to the quasi-steady reaction plateau following the induction-affected length. Two-dimensional isobaric (15 atm) simulations assume fully-developed laminar flow satisfying no-slip conditions at the reactor wall; non-reactive, isothermal (752 K) reactor walls; and solution of the coupled, steady energy and species equations for the reactor interior.

The simulations indicate that species important for H.9.M^{QSSP} interpretation are well-represented by plug-flow interpretation. Predicted species mole fractions based on cross sectional area-averaged results (solid lines) agree to within a few percent of both the wall (dashed lines) and centerline (dotted lines) profiles. Results presented for this condition are representative of other QSSP experiments.

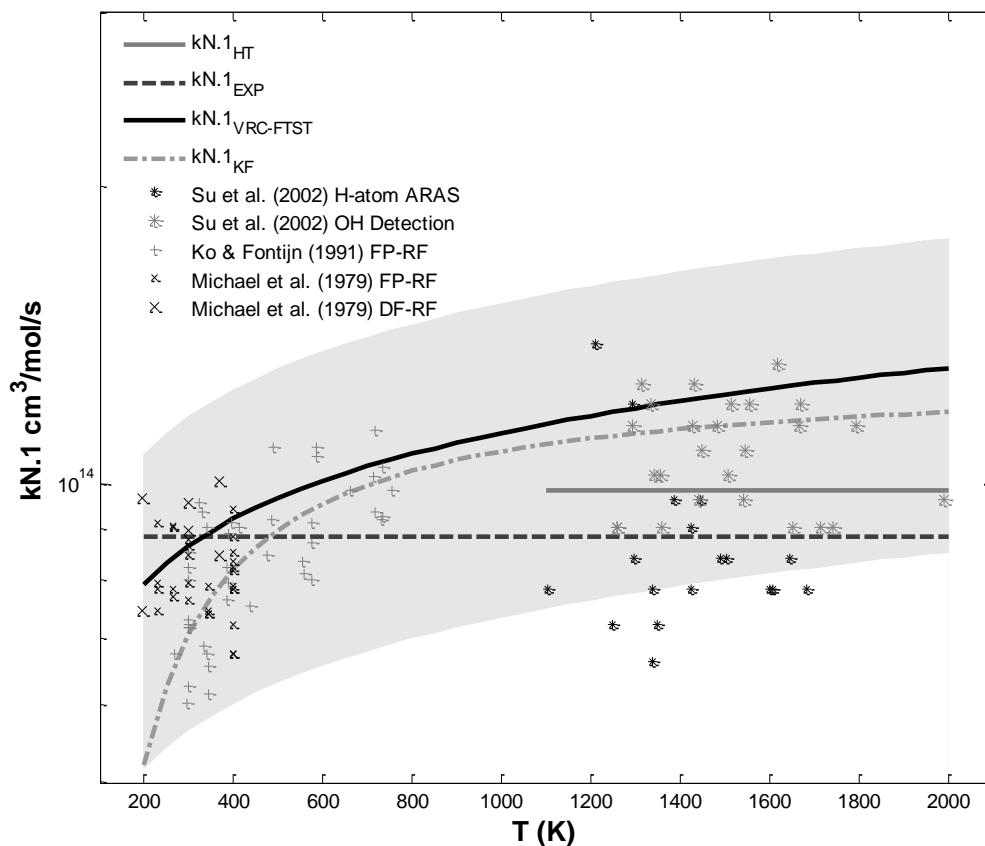


Figure 3.14 – Comparison of literature experimental determinations and several expressions for $k_{N.1}$ ($H + NO_2 \rightarrow OH + NO$) for $200 \leq T \leq 2000$ K.

The shaded region corresponds to the $\pm 35\%$ linear uncertainty band presently adopted for $k_{N.1_{VRC-FTST}}$ based on the linear uncertainty band given by Su *et al.* (2002) for $k_{N.1_{EXP}}$. Note that symmetric linear (additive) uncertainties about the nominal rate coefficient expression translate into asymmetric uncertainties in the logarithmic (multiplicative) sense.

The expression for $k_{N.1_{KF}}$ extrapolates the original Ko & Fontijn (1991) experiment-based temperature limits of 296-760 K to the full 200-2000 K range considered by the figure.

Nominal experimental rate coefficient values from the studies of Michael *et al.* (1979), Ko & Fontijn, and Su *et al.* demonstrate both the potential for ambiguity in reasonable rate coefficient assignment as well as the relatively good agreement among various experimental techniques: H-atom atomic resonance absorbance spectroscopy (ARAS), OH detection, flash photolysis-resonance fluorescence of H-atom (FP-RF), and discharge flow-resonance fluorescence of H-atom (DF-RF). Note that the DF-RF data points represent averages of many individual experiments, whereas all other points represent a single experimental determination.

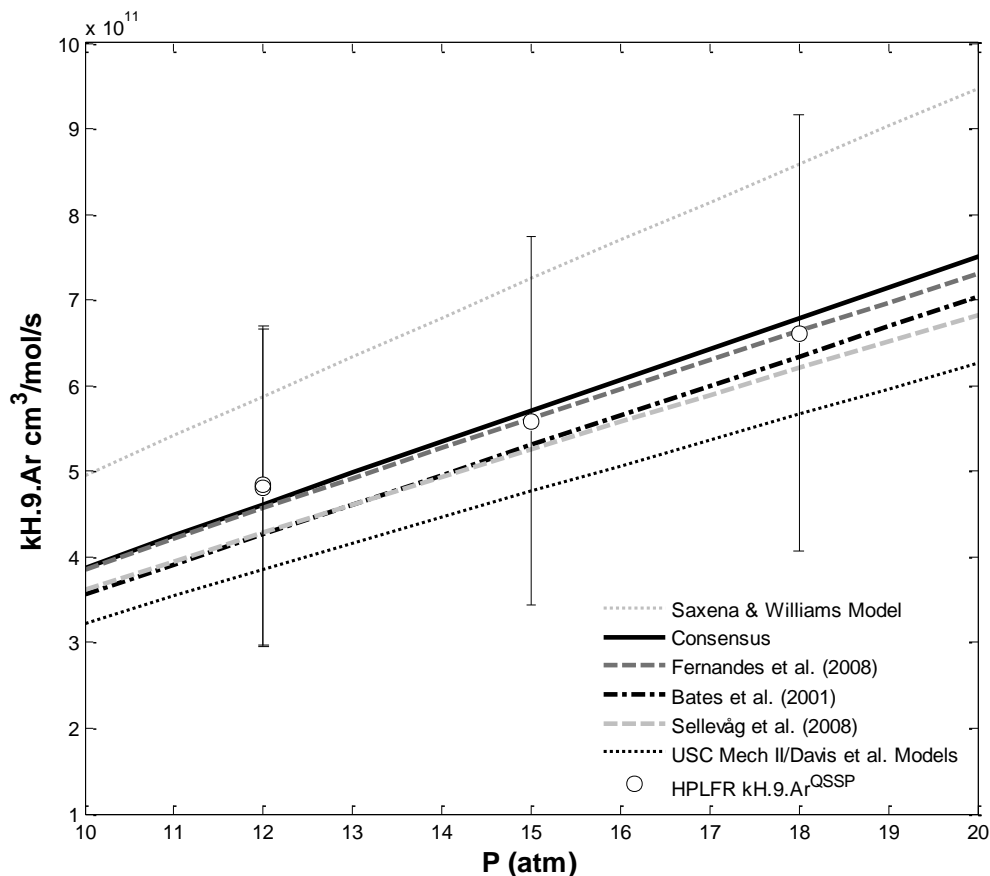


Figure 3.15 – Comparison of presently determined $k_{H.9.Ar}^{QSSP}$ rate coefficients to several literature-based pressure-dependent rate coefficients for $M = Ar$ at 752 K.

The “Consensus” curve indicates a $k_{H.9.Ar}$ expression developed by taking the arithmetic mean of the unique $k_{H.9.Ar}$ expressions used by the twelve best performing H_2 combustion models in the literature as recently determined by Zsély *et al.* (2013). Only ten *unique* expressions were used to develop this mean rate coefficient expression as the “NUIG NGM c5_49” model of Curran *et al.* (2010) shares a common $k_{H.9.Ar}$ expression with the one used by Ó Conaire *et al.* (2004) and USC Mech II (Wang *et al.*, 2007) shares a common expression with the model of Davis *et al.* (2005).

The highest and lowest $k_{H.9.Ar}$ expressions from these twelve models correspond to expressions of Saxena & Williams (2006) and USC Mech II/Davis *et al.*, respectively. To varying degrees, all kinetic model-based rate coefficient expressions considered here are premised on fundamental experimental rate coefficient measurements and theory, with possible additional fitting/optimization intended to better predict systems-type experimental targets. Consequently, the range in $k_{H.9.M}$ shown here is indicative of the present Consensus uncertainty for this reaction rate coefficient at these conditions.

Experimental uncertainties presented here are based on the $\pm 38.5\%$ 2σ uncertainty band for the $M = Ar$ experiments discussed in Section 3.2.2.

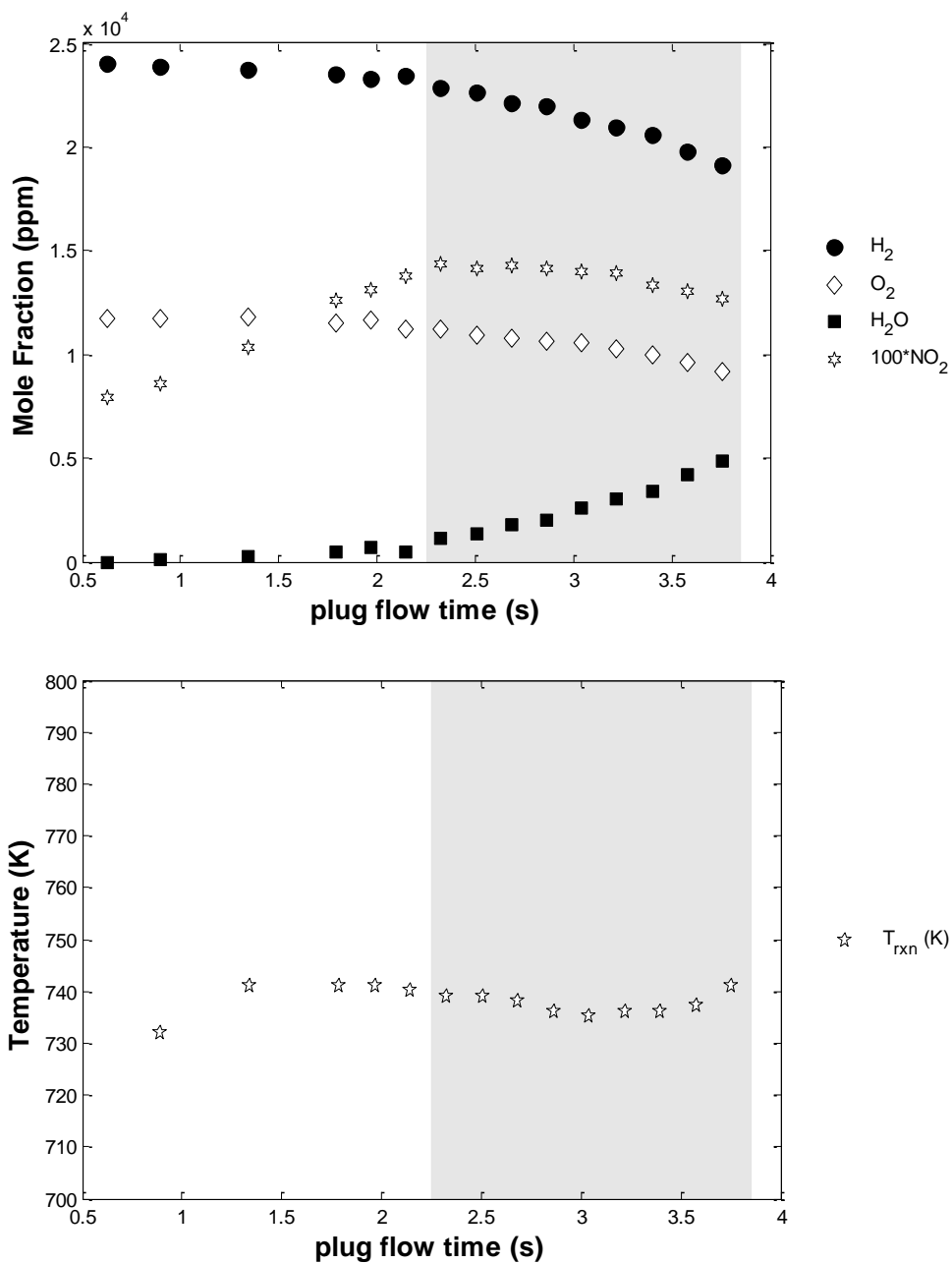


Figure 3.16 – Measured species and temperature profiles for HPLFR QSSP Experiment 3/IV.

Nominal initial reaction conditions are 23961/11677/184 ppm $H_2/O_2/NO$ in balance N_2 bath gas at 20.0 atm. The water profile is computed based on the H atom balance. Temperature is nominally 737 K over the quasi-steady plateau indicated by shading, and the reaction proceeds essentially isothermally.

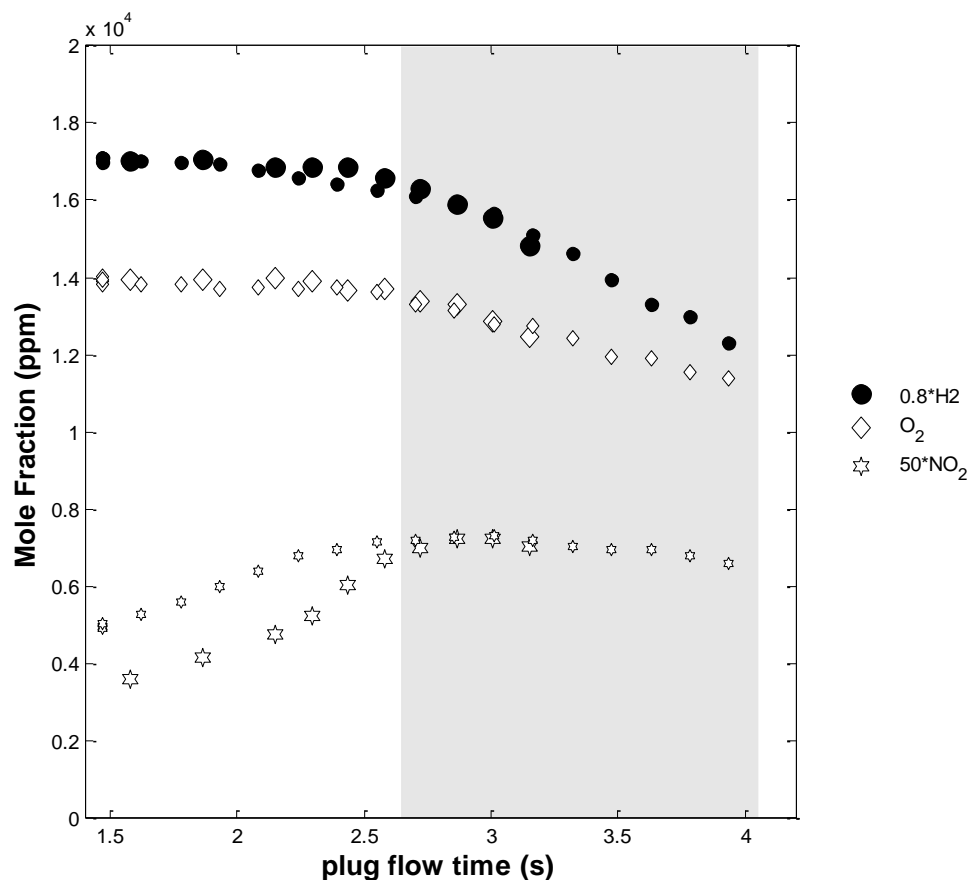


Figure 3.17 – Measured species profiles for HPLFR QSSP Experiments 3/Va and 3/Vb.

Nominal initial reaction conditions are 21374/13957/185 ppm H₂/O₂/NO in balance N₂ bath gas at 17.3 atm. Small markers correspond to Experiment 3/Va, and large markers correspond to Experiment 3/Vb. Due to the similarity of reaction conditions for these two experiments, conducted back-to-back, the results have been superimposed by shifting the relative plug flow time of Experiment 3/Vb by 0.075 seconds to achieve the present overlap in species profiles. Though the dataset is limited, measurements indicate the robustness of the QSSP condition to perturbations in the induction chemistry (see also Figure 3.12 for M = Ar). Temperature profiles (not shown) are essentially isothermal and do not deviate in the shaded QSSP region by more than ± 4 K from nominal values of 738 K (Experiment 3V/a) and 742 K (Experiment 3V/b).

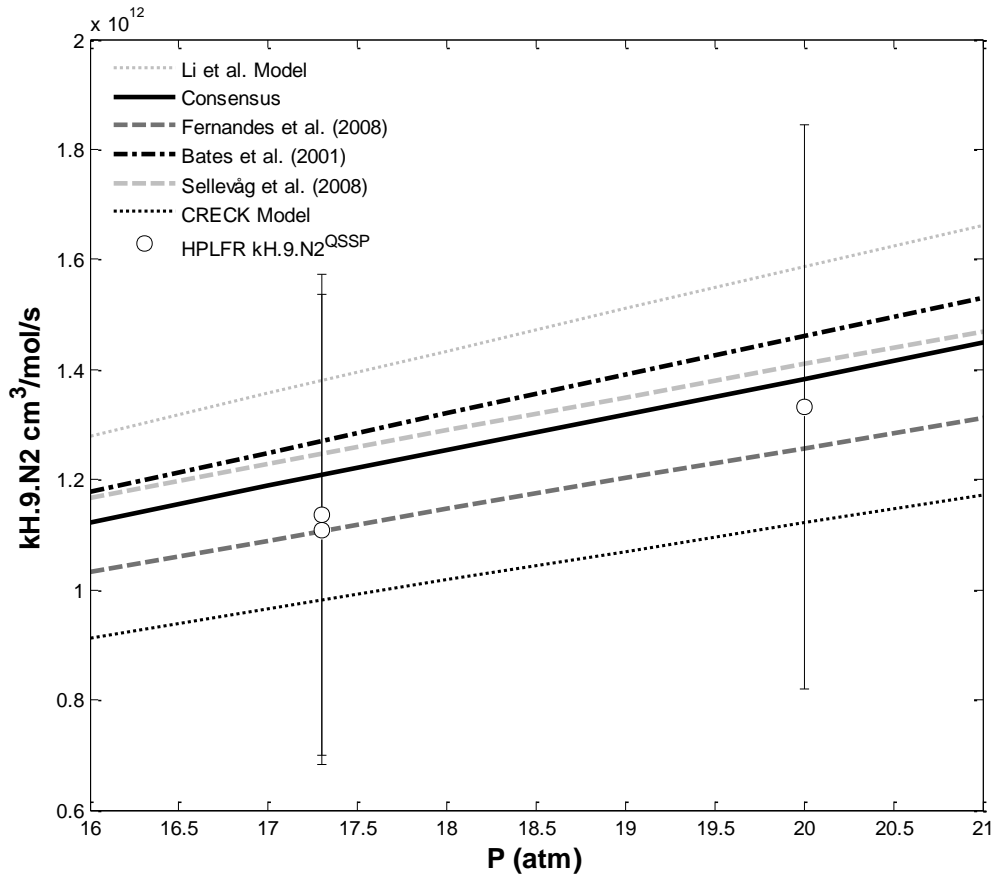


Figure 3.18 – Comparison of presently determined $k_{H.9.N_2}^{QSSP}$ rate coefficients to several literature-based pressure-dependent rate coefficients for $M = N_2$ at 739 K.

The “Consensus” curve indicates a $k_{H.9.N_2}$ expression developed by taking the arithmetic mean of $k_{H.9.N_2}$ expressions used by the twelve best performing H_2 combustion models in the literature as recently determined by Zsély *et al.* (2013). As for $M = Ar$, only ten unique expressions from among these models were used to develop this mean rate coefficient expression (see further details in explanation of Figure 3.15).

The highest and lowest $k_{H.9.N_2}$ expressions from these twelve models correspond to expressions of Li *et al.* (2007) and Ranzi *et al.* (CRECK, 2012), respectively.

Experimental uncertainties presented here are based on the $\pm 38.5\%$ uncertainty band for the $M = N_2$ experiments discussed in Section 3.2.3.

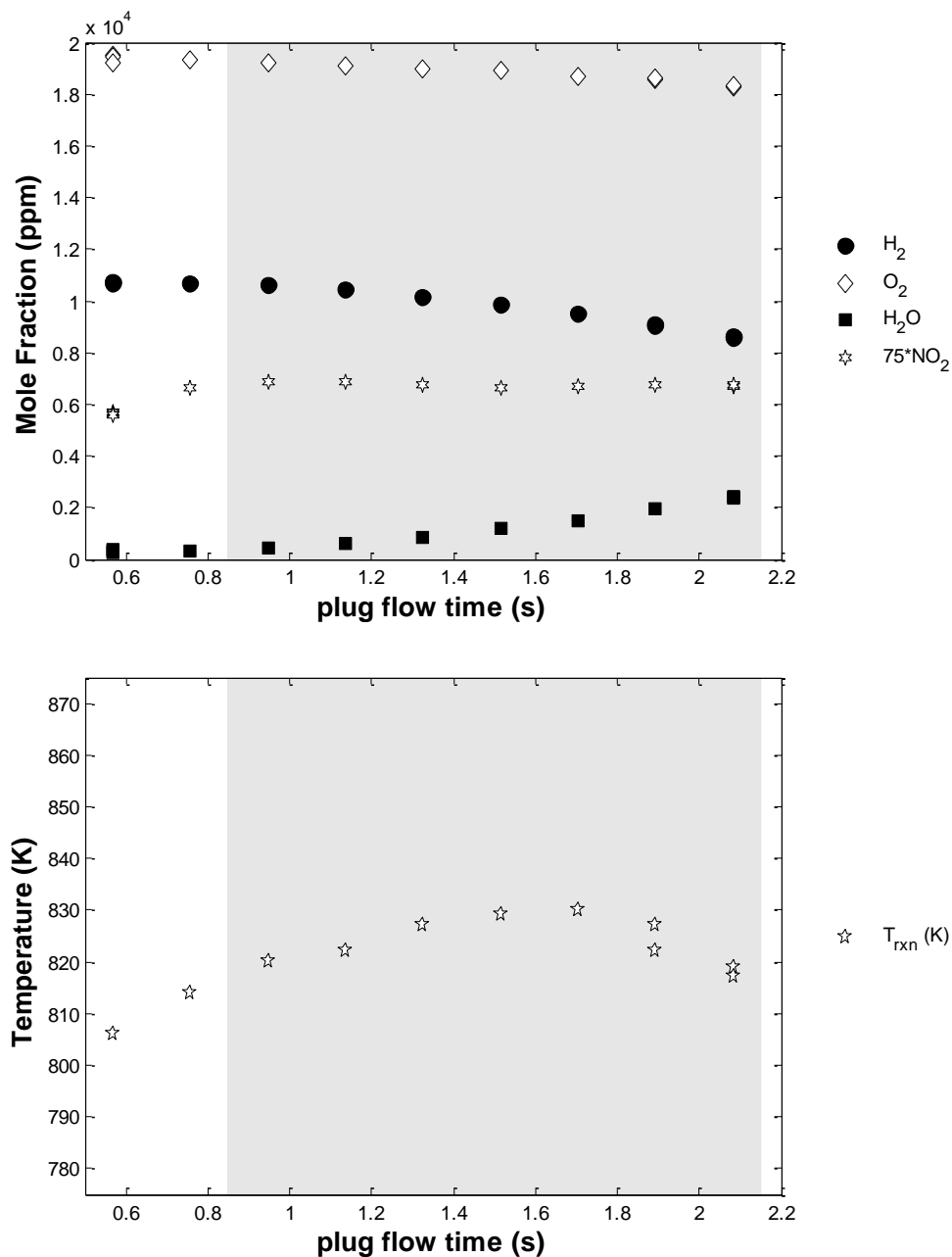


Figure 3.19 – Measured species and temperature profiles for HPLFR QSSP Experiment 3/VI.

Nominal initial reaction conditions are 11017/19625/94 ppm $\text{H}_2/\text{O}_2/\text{NO}$ in balance N_2 bath gas at 12.5 atm. The water profile is computed based on the H atom balance. Temperature is nominally 824 K over the time range indicated by shading, and the reaction proceeds essentially isothermally. For these conditions, kinetic modeling suggests that the QSSP NO_x cycle is saturated, so kinetic modeling of secondary reactions may be necessary for determination of kH.9.N2 from these measurements; see further discussion in Section 3.2.3 and explanation of Figure 3.21.

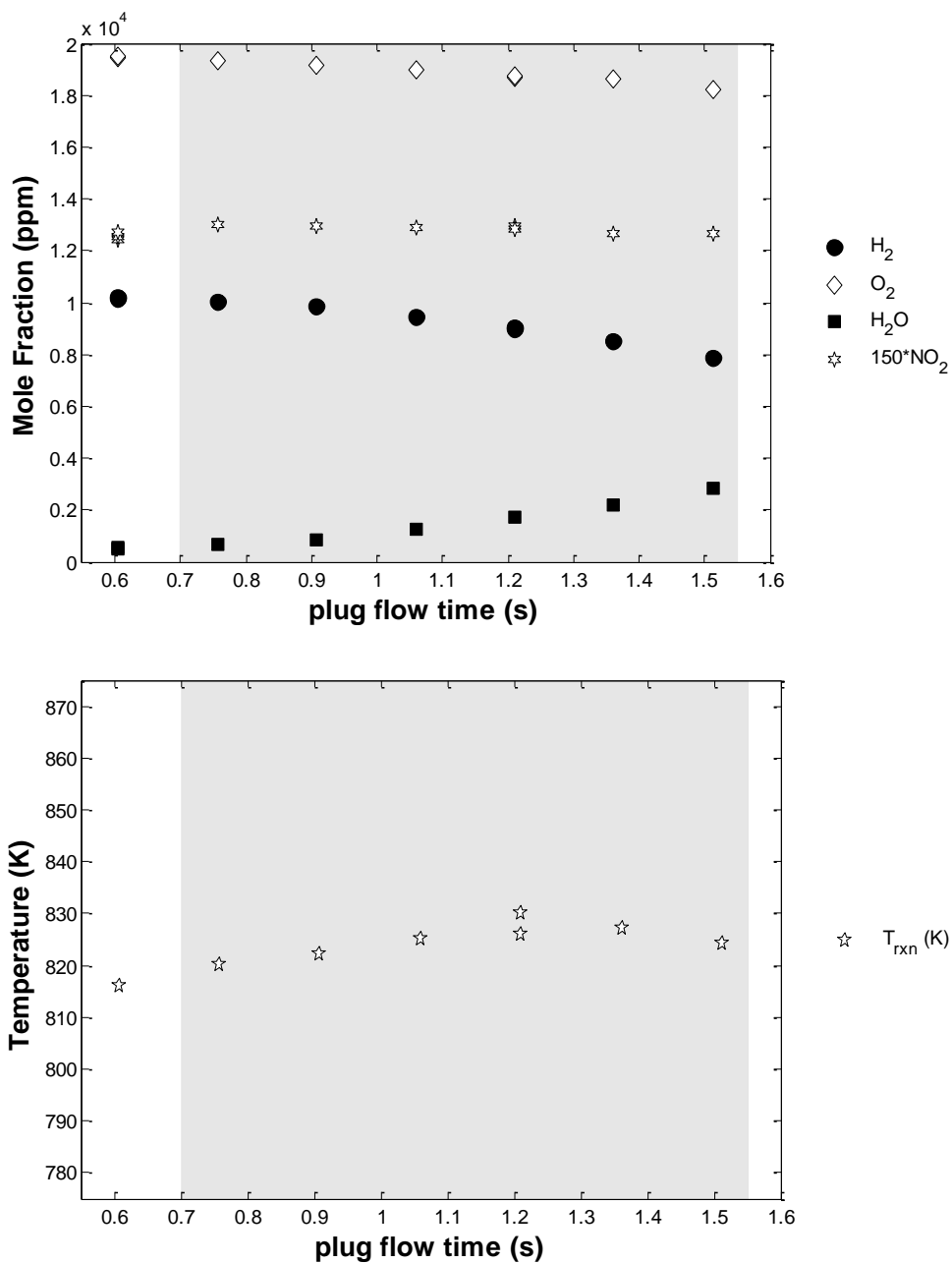


Figure 3.20 – Measured species and temperature profiles for HPLFR QSSP Experiment 3/VII.

Nominal initial reaction conditions are 10717/19920/94 ppm H₂/O₂/NO in balance N₂ bath gas at 10.0 atm. The water profile is computed based on the H atom balance. Temperature is nominally 825 K over the quasi-steady plateau indicated by shading, and the reaction proceeds essentially isothermally.

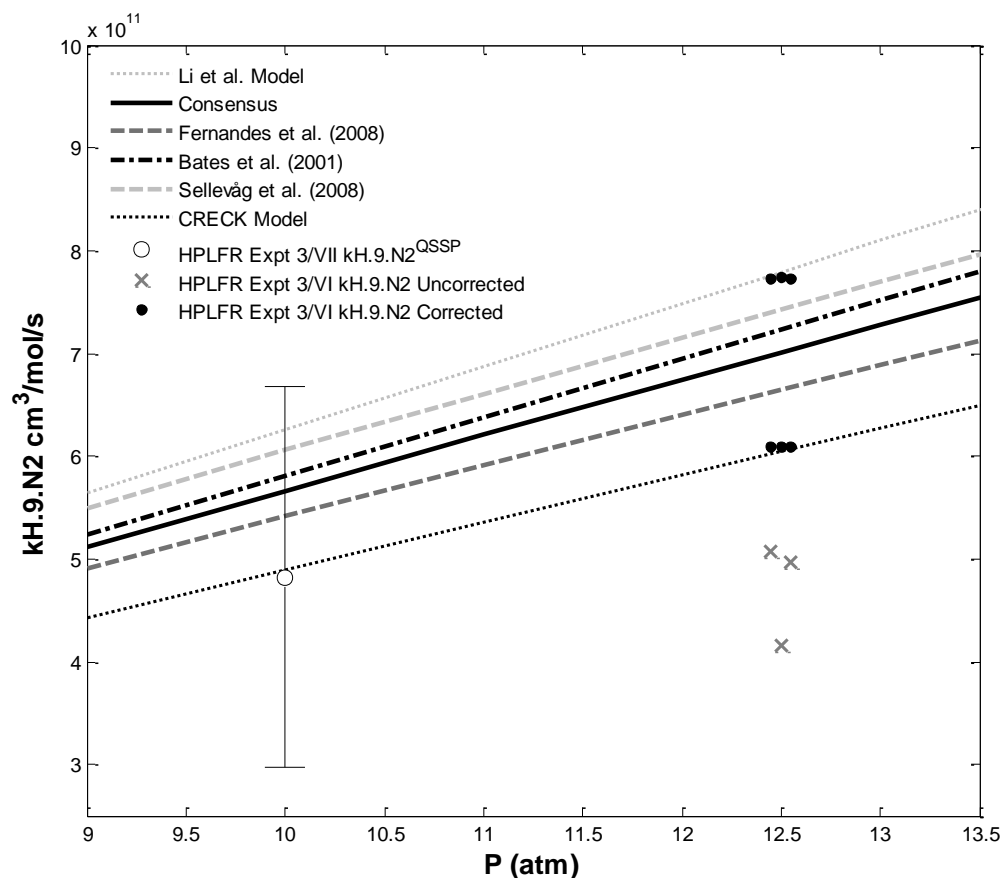


Figure 3.21 – Comparison of presently determined $k_{H.9.N_2}^{QSSP}$ rate coefficients to several literature-based pressure-dependent rate coefficients for $M = N_2$ at 825 K.

The “Consensus” and highest and lowest $k_{H.9.N_2}$ curves are as discussed in Figure 3.18. The experimental uncertainties ascribed to the Experiment 3/VII point (10 atm) are based on the $\pm 38.5\%$ uncertainty band for the $M = N_2$ experiments discussed in Section 3.2.3.

Because Experiment 3/VI deviated significantly from the QSSP condition, interpretation of the data requires kinetic modeling to account for secondary chemistry embodied in $\sigma_{H.9.M}$. Shown here are both the uncorrected (x) and model-corrected (●) $k_{H.9.N_2}$ results discussed in Section 3.2.3 and presented in Table 3.3. Results using different assumed $k_{N.1}$ expressions (Figure 3.14) have been offset from the nominal 12.50 atm abscissa by 0.05 atm for clarity: 12.45 atm corresponds to $k_{N.1}^{VRC-FTST}$, 12.50 atm corresponds to $k_{N.1}^{EXP}$, and 12.55 atm corresponds to $k_{N.1}^{KF}$. Error bars for these points have also been suppressed for clarity. Despite the scatter in uncorrected $k_{H.9.N_2}$ values, model-corrected values are in extremely good agreement with each other as well as the base $k_{H.9.N_2}$ expression assumed in kinetic modeling (demonstrated here for both the Li *et al.* (2007) and Ranzi *et al.* (CRECK, 2012) expressions). As discussed in the body text, the consistency among corrected $k_{H.9.N_2}$ values further serves as validation of the HPLFR facility for $k_{H.9.M}$ determination by QSSP measurements. However, the present interpretation suggests that prescribing a single nominal corrected $k_{H.9.M}$ value for Experiment 3/VI is inadvisable due to the strong model-dependence of corrected $k_{H.9.M}$ determinations.

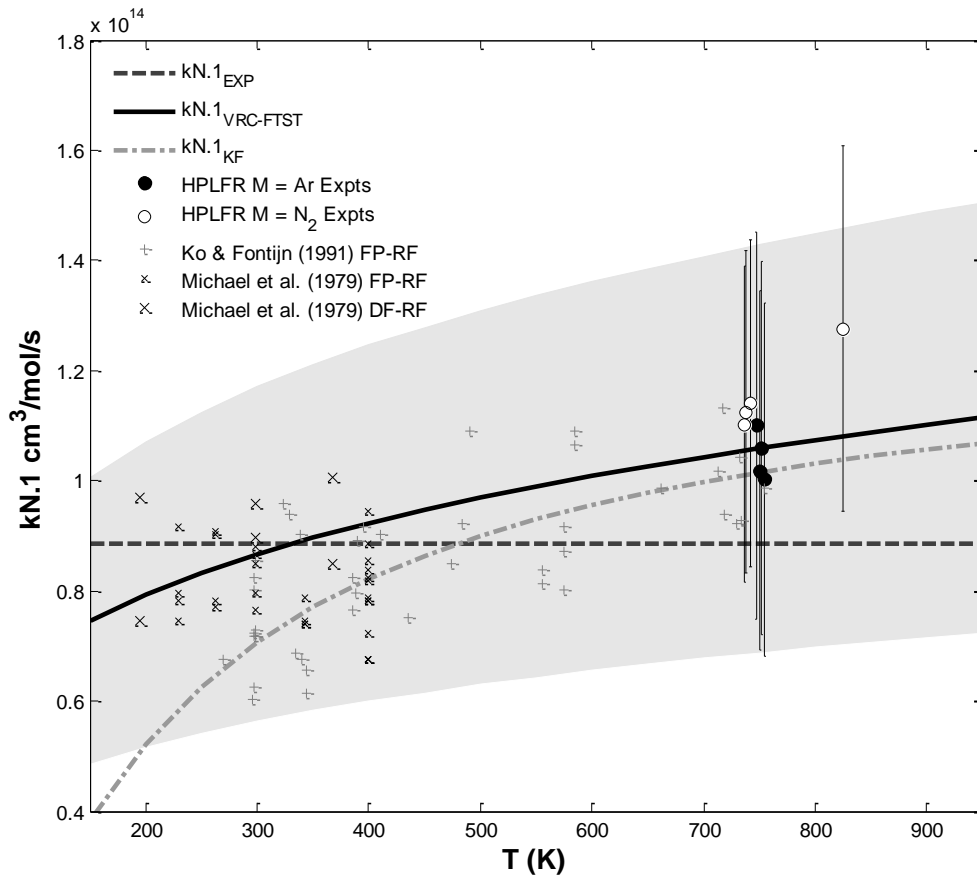


Figure 3.22 – Comparison of presently determined $k_{N.1}^{QSSP}$ rate coefficients to literature $k_{N.1}$ expressions and experimental determinations.

Experimental HPLFR $k_{N.1}^{QSSP}$ determinations are derived from the experimental temperatures, pressures, and $k_{N.1}/k_{H.9.M}$ ratios presented in Table 3.2 with further interpretation using the “Consensus” $k_{H.9.M}(T,P,M)$ values discussed in detail in the explanation to Figures 3.15 and 3.18. At HPLFR experiment conditions, the “Consensus” $k_{H.9.M}$ yields excellent agreement with recent pressure-dependent $k_{H.9.M}$ expressions based on experimental and theoretical rate coefficient studies for the H.9.M system (Figures 3.15, 3.18, and 3.21). Note that the point corresponding to Experiment 3/VI, which deviates significantly from the QSSP condition, has been omitted here. Present $k_{N.1}^{QSSP}$ 2σ uncertainties of ~32/26% for $M = \text{Ar}/\text{N}_2$ are assigned based on the ~16% experimental uncertainty in $k_{N.1}/k_{H.9.M}$ summed in quadrature with twice the relative standard error of the ten unique $k_{H.9.M}$ expressions used to derive the “Consensus” values for $M = \text{Ar}$ and N_2 .

Chapter 4: Rate Coefficient Determination for $\text{H} + \text{O}_2(+\text{CO}_2) \rightarrow \text{HO}_2(+\text{CO}_2)$

The present chapter focuses on determination of $k_{\text{H.9.M}}$ for $M = \text{CO}_2$. In combustion applications, CO_2 appears in relatively high concentrations as either a diluent in the unburned gas (e.g., in exhaust gas recirculation) or as a product formed during carbonaceous fuel oxidation. Carbon dioxide is ubiquitous in virtually all practical combustion systems; however, there are comparatively fewer measurements for $k_{\text{H.9.M}}$ in CO_2 bath gas relative to measurements in bath gases such as N_2 , Ar, or H_2O , for example.

Determination of this rate coefficient presently involves combining new experimental measurements from the HPLFR facility described in Chapter 2 with critically reviewed and reevaluated measurements taken from the literature. These literature measurements, derived from a variety of techniques and acquired over the span of five decades, often depend on determination by relative rate or complex kinetic modeling analyses. The present reevaluation serves to align each of these measurements along a common, modern combustion chemistry basis.

Section 4.1 of this chapter discusses HPLFR QSSP measurements for $M = \text{CO}_2$ generated as part of this thesis work. Section 4.2 then describes the reevaluation of additional literature measurements for $k_{\text{H.9.CO}_2}$. Literature and HPLFR $k_{\text{H.9.CO}_2}$ determinations are combined in Section 4.3 to provide a final recommendation for the absolute low pressure limit (LPL) rate coefficient for H.9.CO_2 .

4.1 HPLFR Measurement of $k_{\text{H.9.CO}_2}$ Using QSSP Conditions

Seven HPLFR QSSP experiments were conducted using CO_2 bath gas in order to determine low pressure limit values of $k_{\text{H.9.CO}_2}$. Reaction conditions for these experiments ranged between ~2.1 and 8.0 atm at temperatures around 800 K. Nominal initial conditions for these experiments are reported in Table 4.1.

Specific details of the essentially isothermal, isobaric, spatially-resolved CO_2 experiments (labeled 4/I, 4/II, 4/IVa, 4/Va, and 4/Vb) are extremely similar to the $M = \text{Ar}$ and N_2 QSSP experiments discussed in Chapter 3 and will not be discussed further. Results for these experiments are presented in Table 4.2 and Figures 4.1-4.4. Relative standard error (2σ) of the profile-averaged $k_{\text{N.1}/k_{\text{H.9.CO}_2}$ values

does not exceed ~7% for any of these experiments. Uncertainties in NO₂ and O₂ quantification, absolute temperature, chemical plug flow interpretation, and absolute pressure are estimated to be similar to the M = Ar and N₂ experiments, so a 2σ overall experimental uncertainty in k_{N.1/kH.9.CO2} of ~16% applies for this subset of the M = CO₂ experiments.

In experiments 4/III and 4/IVb, the HPLFR sample probe position was maintained at a constant axial location while the reactor pressure was varied. In addition to providing values of k_{H.9.CO2}, these varying pressure experiments serve to demonstrate the additional ability of the HPLFR to operate as a fixed sampling location facility, similar to many other flow reactors described in the literature (*e.g.*, Ashman, 1999; Rasmussen *et al.*, 2008; Guo *et al.*, 2013). Provided the QSSP condition prevails, measurement of [NO₂], [O₂], P, and T at a fixed sampling point permits solution of Equation 3.1 for k_{N.1/kH.9.M}. The lack of spatial resolution in these experiments complicates explicit experimental observation of the spatial/temporal QSSP NO₂ plateau evident in many of the experimental and model-generated examples provided thus far. However, one consequence of QSSP behavior is essentially linear scaling of quasi-steady NO₂ mole fraction with reaction pressure at fixed [O₂] (*e.g.*, Figure 3.3). This behavior can be used to identify QSSP measurements from those that may deviate from QSSP behavior due to NO_x cycle saturation, for example.

Species and temperature measurements for Experiment 4/III are presented in Figures 4.5 and 4.6. The NO₂ mole fraction versus pressure data indicates that, at the sampling point, QSSP conditions are satisfied for P < 3.0 atm even under very low extent of overall reaction. However, above this pressure threshold, the NO₂ profile appears to approach saturation (~100 ppm). This observation is further supported by the kinetic modeling presented in Figure 4.7. Consequently, measurements at P > 3.0 atm have been excluded from further QSSP analyses. Similar behavior is evident in species profiles for Experiment 4/IVb (Figure 4.8), although at these particular reaction conditions, the QSSP pressure threshold can be extended to at least 3.5 atm.

To determine nominal rate coefficient values from these two varying pressure experiments, measurement of [NO₂], [O₂], P, and T at each sub-threshold pressure was first treated as an individual QSSP observation. Each measured value of [O₂]/[NO₂] was corrected for non-CO₂ third body collider effects to give k_{N.1/kH.9.CO2} at the nominal reaction temperature, pressure, and overall concentration

[M]. To remove first-order linear dependencies in $k_{N.1}/k_{H.9.CO_2}$ due to pressure variation, this rate coefficient ratio was normalized by $1/[M]$, thereby transforming the effective treatment of $k_{H.9.CO_2}$ from bimolecular to termolecular. The resulting values of $k_{N.1}/k_{H.9.CO_2_{TER}}$ show a slightly increasing trend with increasing pressure, which may suggest falloff in the $H.9.CO_2$ reaction (*i.e.*, $k_{H.9.CO_2_{TER}}$ reduces with increasing pressure) or other second-order effects. However, these effects are fairly small – about 6.5% standard error (2σ) for Experiment 4/IVb – so the profile-averaged $k_{N.1}/k_{H.9.CO_2_{TER}}$ is used to reasonably represent each entire experiment. The standard error of this rate coefficient ratio contributes to measurement uncertainty in the same way and magnitude that profile averaging does for spatially-resolved experiments discussed above for Ar, N_2 , and CO_2 .

Results of these pressure-dependent rate ratio calculations are presented in Table 4.3. Effective experimental uncertainties for Experiments 4/III and 4/IVb are ~18.5% and 16%, respectively, based on ~11.5% and 6.5% standard errors (2σ) in $k_{N.1}/k_{H.9.CO_2_{TER}}$ and the prevailing experimental uncertainties for NO_2 and O_2 quantification, absolute temperature and pressure, and chemical plug flow interpretation.

4.1.1 Low Pressure Limit Determinations of $k_{H.9.CO_2}$ from HPLFR Data

With reference to a specific $k_{N.1}$ expression and overall concentration $[M]$, $k_{N.1}/k_{H.9.CO_2}$ values from spatially-resolved experiments (Table 4.2) and experiment-averaged $k_{N.1}/k_{H.9.CO_2_{TER}}$ values (Table 4.3) are simply transformed into values of $k_{H.9.CO_2(T,P)}$. However, these values pertain to the average experimental pressure, which may exist at conditions in which $k_{H.9.CO_2}$ exhibits falloff. Falloff effects may be significant and should not be ignored for quantitative determination of $k_{H.9.M}$. For example, in the $M = Ar$ experiments described in Chapter 3, falloff contributes an estimated ~17% depression in $k_{H.9.Ar}$ relative to extrapolated low pressure limit values.

Owing to the scarce database for experimental and theoretical $k_{H.9.CO_2}$ values, the falloff behavior for this rate coefficient is highly uncertain. It is therefore not advisable to make direct comparisons of experimental $k_{H.9.CO_2(T,P)}$ determinations with literature and Consensus expressions as was done with $k_{H.9.Ar}$ and $k_{H.9.N_2}$ in Chapter 3 (Figures 3.15, 3.18, and 3.21). Instead, present $k_{H.9.CO_2(T,P)}$ values have been falloff-corrected to the low pressure limit. Consequently, resulting values of $k_{H.9.CO_2_{LPL}(T)}$ have uncertainty due to falloff correction in addition to contributions from experimental and relative rate uncertainty.

For a particular temperature and pressure, the falloff correction procedure involves determining Consensus $k_{H.9.M}$ (Chapter 3) falloff depressions for the better-known bath gases $M = \text{Ar}$ and N_2 . The average of these depressions is used to transform $k_{H.9.CO_2}(T,P)$ into $k_{H.9.CO_2_{LPL}}(T)$. Given the uncertainty level of the present experimental rate coefficient determinations as well as the poorly established falloff behavior for $k_{H.9.CO_2}$, a small secondary correction ($< \sim 5\%$) accounting for the higher falloff depression expected from the more collisionally efficient CO_2 (relative to Ar and N_2) has been incorporated into the uncertainty of the nominal $k_{H.9.CO_2_{LPL}}$ determinations. This enhanced falloff depression uncertainty estimate is advised by representative values from Consensus models containing rate coefficient expressions or collisional efficiencies for $M = \text{CO}_2$ in addition Ar and/or N_2 . Results of the overall falloff correction procedure are presented in Table 4.4. Given the range of pressures and reactant mole fractions considered, the $k_{H.9.CO_2_{LPL}}$ determinations are remarkably consistent, exhibiting low scatter about a representative value of $1.25 \times 10^{16} \text{ cm}^6/\text{mol}^2/\text{s}$ near 800 K.

4.2 Reassessment of $k_{H.9.CO_2}$ from Literature Sources

The HPLFR measurements discussed above were acquired over the relatively narrow temperature window of $\sim 800 \pm 25 \text{ K}$, so additional measurements of $k_{H.9.CO_2}$ are desirable both to better establish the temperature dependence of this reaction rate coefficient and to corroborate present HPLFR measurements. Additional studies considered here extend the nominal $k_{H.9.CO_2}$ temperature range examined from 633 to 1305 K.

Literature review of studies targeting $k_{H.9.CO_2}$ reveals only a handful of experiments attempting to determine this rate coefficient using relatively well-defined, isolating experimental conditions. However, like the HPLFR measurements, none of these studies involves “direct” measurement of the rate coefficient. Instead, each relies on relative rate or complex model fitting techniques. From the discussions in Chapter 3 regarding HPLFR $k_{H.9.M}$ ($M = \text{Ar}, \text{N}_2$) uncertainties attributable to choice of $k_{N.1}$ interpretive basis, it should be evident that these indirect rate coefficient measurement techniques may be subject to significant interpretive uncertainty in addition to uncertainty of the underlying experimental measurements. For this reason, these literature rate coefficient determinations are

presently reinterpreted as described in the following subsections, which are generally organized in terms of increasing experimental temperature.

4.2.1 Static Reactor Experiments of Ashmore & Tyler

Ashmore & Tyler (1962, also referred to here as AT62) used an aged static reactor to measure bath gas effects on the QSSP condition at 633 K and sub-atmospheric pressures. First, these authors established the existence of the QSSP condition, and then they verified that the static reactor surface to volume ratio did not impact their measurements of P_s , the QSSP partial pressure of NO_2 . This latter result is an important indication that the AT62 measurements are not significantly affected by wall reactions, which had been extensively implicated in earlier, higher temperature static reactor studies discussed later in this chapter (e.g., von Elbe & Lewis, 1942) as having a large potential for confounding experimental interpretations of homogeneous gas phase kinetics. Cross-comparison of AT62 relative reaction rates for $M = \text{O}_2, \text{N}_2, \text{CO}_2,$ and He to those found by von Elbe & Lewis (at 803 K) further supports the reliability of the Ashmore & Tyler measurements, although, as discussed later, the von Elbe & Lewis measurements are probably best regarded as highly uncertain.

The general AT62 experimental approach for studying effects of test gases M involved optically measuring the quasi-steady value of P_s established after premixing reactants R ($2\text{H}_2+\text{O}_2$), NO_2 (P_0), and M by the partial pressure method and introducing the mixture to reaction conditions. Based on the slopes of best fit lines through $P_{\text{NO}_2}/P_{\text{O}_2}$ versus P_M measurements, they tabulated values of k_M for various M , including $k_{\text{CO}_2} = 3.68 \times 10^{-6} \text{ mmHg}^{-1}$. They state that tabulated k_M values include self-consistent (to their study) correction for the effects of collision partners other than the designated bath gas M (ostensibly similar to Equation 3.16 used here). Using present terminology and converting the originally reported partial pressure-based units (at constant $T = 633 \text{ K}$) to absolute concentrations, the AT62 k_{CO_2} determination becomes $k_{\text{H.9.CO}_2\text{TER}}/k_{\text{N.1}} = 145.3 \text{ cm}^3/\text{mol}$. The reciprocal quantity is $k_{\text{N.1}}/k_{\text{H.9.CO}_2\text{TER}} = 6.884 \times 10^{-3} \text{ mol/cm}^3$, which may be more easily compared to values in Table 4.3.

Falloff correction for the Ashmore & Tyler measurement is complicated by the fact that details of the experimental measurements for $M = \text{CO}_2$ are not disclosed in their paper. The highest nominal pressure apparently considered in their study is 600 mmHg, so this value is used to estimate a maximum falloff depression of 10.5% based on literature Consensus (Figure 3.18) for $k_{\text{H.9.N}_2}$ by using the

approach discussed in Section 4.1.1 and Table 4.4. Assuming instead a value of 150 mmHg total experimental pressure yields a falloff depression of 8.6%, suggesting the magnitude of the falloff depression is not particularly sensitive to pressure over the experimental range considered in AT62.

After applying the falloff correction, present QSSP reinterpretation of the original AT62 k_{CO_2} value via $k_{\text{N.1.VRC-FTST}}$ gives $k_{\text{H.9.CO}_2\text{LPL}} = 1.64 \times 10^{16} \text{ cm}^6/\text{mol}^2/\text{s}$. This value of $k_{\text{H.9.CO}_2\text{LPL}}$ is to be compared with estimates of $k_{\text{H.9.CO}_2}$ implied by AT62 based on their experimentally observed reaction rate for CO_2 relative to H_2 ($\epsilon_{\text{CO}_2/\text{H}_2} = 1.39$) and contemporary $k_{\text{H.9.H}_2}$ values attributed to both Hoare & Walsh (1957) and Voevodsky & Kondratiev (1961), which differ by a factor of four. The inferred, circa 1962 values of $k_{\text{H.9.CO}_2}$ are 3.1×10^{16} and $7.6 \times 10^{15} \text{ cm}^6/\text{mol}^2/\text{s}$, respectively.

Excepting the ~10% falloff correction, the present $k_{\text{H.9.CO}_2\text{LPL}}$ reinterpretation based on the k_{CO_2} value of AT62 and $k_{\text{N.1.VRC-FTST}}$ (henceforth interpretive Method 1) is independent of reference to historical or present day $k_{\text{H.9.M}}$ values. Alternatively, the AT62 study could be reinterpreted independently of $k_{\text{N.1}}$ using the tabulated AT62 relative rate coefficient ratios and modern reference $k_{\text{H.9.M}}$ values in a similar manner as the Hoare & Walsh and Voevodsky & Kondratiev rate coefficient determinations discussed above (henceforth interpretive Method 2). At 633 K and 600 mmHg, the literature Consensus $k_{\text{H.9.N}_2\text{LPL}}$ rate coefficient is computed to be $6.34 \times 10^{15} \text{ cm}^6/\text{mol}^2/\text{s}$, while the AT62 value for relative reaction rates between CO_2 and N_2 ($\epsilon_{\text{CO}_2/\text{N}_2}$) is 2.53. In absolute terms, $k_{\text{H.9.CO}_2\text{LPL}}$ by Method 2 is $1.61 \times 10^{16} \text{ cm}^6/\text{mol}^2/\text{s}$, which compares very favorably (within 3%) to the value determined by Method 1. The agreement between the two reinterpretation approaches is remarkable considering the different relative rate coefficient basis underpinning the analyses ($k_{\text{N.1.VRC-FTST}}$ versus Consensus $k_{\text{H.9.N}_2}$). Table 4.5 summarizes the results of both reinterpretations of the AT62 experiments.

4.2.1.1 Uncertainty Estimation for Ashmore & Tyler Measurements

Ashmore & Tyler do not provide estimated experimental uncertainties for their k_{CO_2} determination, although uncertainties are provided for the other k_{M} considered in their study. The average k_{M} reported uncertainty is $\pm 16\%$ (presumably at 1σ), so the present study assigns an experimental 2σ uncertainty of $\pm 32\%$ to k_{CO_2} . Considering uncertainties of 35% due to $k_{\text{N.1}}$ and ~5% due to falloff correction, an overall estimate for the quadrature-based uncertainty of $k_{\text{H.9.CO}_2\text{LPL}}$ by Method 1 is ~48% (2σ).

The estimated uncertainty is approximately the same when considering Method 2. In this case, the 2σ standard error of modern reference $k_{H.9.N_2}$ rate coefficients is 21% at 633 K and 600 mmHg, which is significantly lower than the ~200% range in $k_{H.9.H_2}$ considered by AT62 in 1962. Additional uncertainties of $\pm 32\%$ are attributable (as above) to each of the k_{CO_2} and k_{N_2} measurements. The overall estimated 2σ uncertainty of Method 2 is therefore ~50% under present assumptions.

4.2.1.2 $k_{H.9.H_2O}$ Determinations from Ashmore & Tyler Measurements

Although this chapter focuses on determination of $k_{H.9.CO_2}$, the AT62 measurements and recently discussed reinterpretation methods can easily be applied to determine nominal $k_{H.9.H_2O_{LPL}}$ values. The present digression serves to inform discussion of $k_{H.9.H_2O}$ to appear in Chapter 5. For H_2O , the effects of falloff might be more significantly underestimated than for $M = CO_2$. This is not specifically addressed here, so nominal $k_{H.9.H_2O_{LPL}}$ values suggested here may be slightly higher than found by more rigorous application of Method 1 and Method 2 variants.

Ashmore & Tyler measured $k_{H_2O} = 17.6 \times 10^{-6} \text{ mm}^{-1}$ and $\epsilon_{H_2O/N_2} = 12.1$. At 633 K, these measurements return the highly consistent values (within ~2%) of $k_{H.9.H_2O_{LPL}} = 7.83 \times 10^{16} \text{ cm}^6/\text{mol}^2/\text{s}$ and $7.67 \times 10^{16} \text{ cm}^6/\text{mol}^2/\text{s}$ by Method 1 and Method 2, respectively. These values compare favorably to values of $k_{H.9.H_2O_{LPL}}$ computed from a sampling of kinetic models considered for $k_{H.9.M}$ Consensus: $7.04 \times 10^{16} \text{ cm}^6/\text{mol}^2/\text{s}$ (Li *et al.*, 2004), $5.84 \times 10^{16} \text{ cm}^6/\text{mol}^2/\text{s}$ (Hong *et al.*, 2011), $8.93 \times 10^{16} \text{ cm}^6/\text{mol}^2/\text{s}$ (Burke *et al.*, 2012), and $6.22 \times 10^{16} \text{ cm}^6/\text{mol}^2/\text{s}$ (Kéromnès *et al.*, 2013).

Notably, the $k_{H.9.H_2O_{LPL}}$ values determined from these kinetic model exemplars are substantially supported by existing, fundamental studies of $k_{H.9.M}$: the Li *et al.* and Burke *et al.* values are based on collisional efficiency ratios relative to the same $M = N_2$ LPL rate coefficient determination from the fundamental $k_{H.9.M}$ study of Michael *et al.* (2002), the value of Hong *et al.* is taken directly from the $k_{H.9.M}$ study of Bates *et al.* (2001) for $M = H_2O$, and the Kéromnès *et al.* value comes from the $M = N_2$ LPL and $\epsilon_{H_2O/N_2} = 10$ recommendations from the $k_{H.9.M}$ study of Fernandes *et al.* (2008). Such favorable comparison offers an additional measure of confidence in the reliability of the AT62 experiments.

4.2.2 Atmospheric Pressure Flow Reactor Experiments of Ashman & Haynes

Ashman & Haynes (1998, also referred to here as AH98) used an atmospheric pressure laminar flow reactor to measure bath gas effects on the reaction of H_2 and O_2 in the presence of trace NO . The

original $k_{H.9.M}$ interpretations derived from these experiments reference plug flow assumptions and the complex kinetic model of Bromly *et al.* (1995), which adjusted $k_{H.9.N_2}$ to fit experimental measurements of NO-perturbed H_2 oxidation at atmospheric pressure. While the plug flow interpretation is justifiable for reasons similar to those given for the HPLFR experiments described earlier, some consideration of the kinetic modeling used for interpretation is warranted.

Validation of the Bromly *et al.* interpretive kinetic model used in AH98 appears limited to the relatively narrow parameter space considered by the NO_x -perturbed experiments discussed in the Bromly *et al.* study. At a representative temperature of 800 K and fixed pressure of 1.0 atm, the pressure-independent termolecular $k_{H.9.N_2}$ expression recommended by Bromly *et al.* returns a value ~44% above the Consensus value (itself with 2σ standard error of only $\pm 15\%$). Moreover, the Bromly *et al.* value is above the result of every pressure-dependent $k_{H.9.N_2}$ expression used to form the Consensus. Additional consideration across a broader temperature range suggests that the Bromly *et al.* expression is an outlier that may also significantly influence the referencing AH98 $k_{H.9.M}$ interpretations, particularly when considering values of $k_{H.9.M}$ described in terms of absolute rate coefficients.

Expanded discussion of these same Bromly *et al.* experiments and their interpretation appears in the thesis of Ashman (1999). This thesis offers a revision to the Bromly *et al.* $k_{H.9.N_2}$ expression that at 1 atm and 800 K, lies ~25% higher than Consensus. However, this slightly updated pressure-independent expression also appears to be an outlier relative to the ensemble of more recent, pressure-dependent rate coefficient expressions used to form the present Consensus.

Rate coefficient interpretations in the Ashman thesis could be considered to supersede those from the earlier AH98 study; however, the N_2 -referenced values of $k_{H.9.M}$ ($M \neq N_2$) appearing in the thesis do not appear to reflect the revised $k_{H.9.N_2}$ recommendation in Ashman's thesis. In other words, absolute rate coefficients for $k_{H.9.M}$ ($M \neq N_2$) are inconsistent between AH98 and Ashman (1999), despite being supported by the exact same experiments. This follows as a direct consequence of both studies recommending the exact same relative (to N_2) collisional efficiencies. In terms of absolute rate coefficient values for $k_{H.9.M}$, the two studies disagree by the propagated, constant ~14% difference from the base $k_{H.9.N_2}$ expressions. Since the model-based $k_{H.9.M}$ determination approach employed by AH98/Ashman ultimately requires absolute rate coefficient values as inputs for the kinetic model, this

disagreement presents a quantitatively significant inconsistency or ambiguity in interpretation of the same AH98/Ashman experiments interpreted by the same basis Bromly *et al.* kinetic model. For this reason, the AH98/Ashman experiments have been reinterpreted here.

4.2.2.1 Reevaluation of Ashman & Haynes Recommendations by Collisional Efficiency Approach

The differing, pressure-independent $k_{H.9.N_2}$ expressions and ambiguous interpretations of AH98/Ashman suggest that their recommended values of $k_{H.9.CO_2}$ require reassessment prior to inclusion as part of the basis for the present rate coefficient recommendation. Following elements of Method 2 described for reinterpretation of the Ashmore & Tyler (1962) experiments, one simple way to reinterpret the reported AH98/Ashman $k_{H.9.CO_2}$ values is to rescale the absolute rate coefficient recommendations by the ratio of $k_{H.9.N_2}(T, 1 \text{ atm})$ values from the Consensus and the original AH98 studies. This relative collisional efficiency scaling propagates the AH98 model-derived $k_{H.9.M}$ results and assumes essentially linear behavior for the model-based $k_{H.9.M}$ determination approach. Although the latter assumption is not unreasonable for the near-QSSP conditions of the AH98/Ashman experiments, the former assumption of simple propagation of model-determined results is subject to further scrutiny in the following subsections.

To be consistent with $k_{H.9.CO_2LPL}$ values discussed throughout this chapter, the Consensus-rescaled AH98/Ashman $k_{H.9.CO_2}(T, 1 \text{ atm})$ presented in Table 4.6 must be corrected for falloff depression, which is roughly 10% for $M = N_2$ from 800-900 K. The $k_{H.9.CO_2LPL}$ result at 800 K is somewhat lower than, but in reasonable agreement with, values derived from HPLFR QSSP techniques at similar temperatures (Table 4.4).

4.2.2.2 Reevaluation of Ashman & Haynes Recommendations Using QSSP Analysis

Several of the AH98/Ashman $M = CO_2$ experiments can also be interpreted using the same QSSP approach as employed for HPLFR experiments, which avoids the need to reference complex kinetic models or $k_{H.9.M}$ expressions (excepting falloff correction). Experiment-informed determinations of $[NO_2]$, $[O_2]$, and T necessary for QSSP analysis have been obtained from the Ashman thesis since such data do not appear in AH98 for $M = CO_2$. The reported *apparent* NO_2 mole fraction (henceforth NO_2^{**}) may also include undifferentiated contributions from HONO, HNO_3 , and sample probe quenching. The O_2 mole fraction is computed by atom balance from among the nominal initial O_2 reactant feed level,

O atoms presumed to be consumed in $\text{NO} \rightarrow \text{NO}_2$ formation, and the extent of reaction based on the nominal initial H_2 reactant feed level and the average of measured H_2 and H_2O mole fractions. Such averaging is employed for extent of reaction to balance uncertainties due to the ~5% stated experimental uncertainty in H_2O measurement and the uncertainty of more precise H_2 measurements that may be sensitive to systematic influences of wall reactions and diffusion or fluid mechanical dispersion. Measurement and interpretive uncertainties will be further discussed in the following subsection. However, it is worth noting now that Ashman provides sufficiently convincing characterization of these experiments – including H_2 , H_2O , and NO_2^{**} mole fraction measurements; discussion of factors impacting NO_2^{**} measurement, sample quenching, wall reactions, fluid mechanical dispersion, and inlet NO_x conversion; supporting kinetic modeling; and QSSP-plateau achievement results – such that the present QSSP reevaluation is possible.

Reanalysis of the Ashman data follows the approach described earlier for HPLFR experiments except that each measurement at fixed (T , $P = 1 \text{ atm}$) is considered to be an individual, independent experiment conducted under isothermal, isobaric conditions. The QSSP analysis results presented in Table 4.7 consider $M = \text{CO}_2$ experiments at all reported temperatures from 760-1000 K. Notably, the QSSP-reinterpreted Ashman $\text{kH.9.CO2}_{\text{LPL}}$ result at 800 K is in excellent agreement with the higher pressure QSSP results from HPLFR experiments near 800 K (Table 4.4). This 800 K experiment therefore serves as an independent corroboration of the HPLFR experiments.

However, some of the experiments described by Table 4.7 likely violate QSSP assumptions. These have been identified in the table to be excluded as basis points for the present kH.9.CO2 recommendation and from any subsequent comparisons of kH.9.CO2 values. Additionally, analysis of the 760 K case (below) suggests that, more generally, non-unique solutions may be found by the complex kinetic model kH.9.M determination approach used by AH98/Ashman. This suggests an unquantified, model-dependent uncertainty for the propagated model-determined AH98 absolute rate coefficient results used in the Method 2 collisional efficiency rescaling discussed above. For this reason, the QSSP interpretation (Method 1) discussed in this subsection is to be preferred for kH.9.CO2 values determined from Ashman's work.

Exclusion of the 760 K Experiment and Inadequacies of Model-Based $k_{H.9.M}$ Determination

The measured extent of reaction for the experiment at 760 K is essentially zero (Figure 4.9), and the NO_2^{**} concentration may still be reaching the quasi-steady plateau condition as demonstrated for HPLFR simulations and experiments (e.g., Figures 3.12, 3.13, 4.1, and 4.3). The lack of spatial (temporal) resolution in the Ashman experiments frustrates conclusive diagnosis based on experimental data, but kinetic modeling offers some insight on the ambiguity associated with the 760 K result. Present modeling predictions from variants of the hybrid model described with text accompanying Figure 4.7 suggest that, within reasonable experimental uncertainty, achievement of the nominally measured 48.7 ppm NO_2^{**} depends strongly on the to-be-determined assumed value of $k_{H.9.CO2}$ (provided spatial/temporal coordinate shifting as an interpretive tool (*i.e.*, effective residence time is not the nominal experimental residence time)).

For a relative collisional efficiency $\epsilon_{CO2/Ar} = 5.4$ serving as a proxy handle to change the value of $k_{H.9.CO2}$, only one reasonable model matching point exists for NO_2^{**} mole fraction, and this point is in the pre-QSSP induction transient. For $\epsilon_{CO2/Ar} = 3.45$, there are no reasonable matching points between model and experiment. Finally, for $\epsilon_{CO2/Ar} = 4.5$, which is the value used in the model described with Figure 4.7, a range of points in the late induction transient as well as essentially *all* times in the quasi-steady plateau will satisfy NO_2^{**} matching. Although the $\epsilon_{CO2/Ar} = 3.45$ result appears to set a bound on acceptable relative rates between H.9.CO2 and N.1, the potential for multiple interpretations outside of QSSP conditions is clear cause to exclude the 760 K measurement from the QSSP re-analyzed data set.

It is worth noting that Ashman's own kinetic modeling did not find *any* point of NO_2^{**} matching for the 760 K experiment. Instead, these predictions suggest a clearly measurable extent of reaction (~20%, based on H_2 consumed) should occur for the nominal 760 K experimental conditions, for which the predicted NO_2^{**} mole fraction would be ~20% higher than measured. Assuming Ashman's model is sufficiently predictive, such results suggest a lag between the nominal experimental and model times, which can be accommodated by the coordinate shifting employed by the present modeling approach described above. Such a lag is indicative of uncharacterized induction processes that can often be lumped into a relative spatial/temporal coordinate shift for the purposes of flow reactor interpretation.

This has been explored extensively in the recent review of Dryer *et al.* (2014) and is also evident in shock tubes (e.g., Urzay *et al.*, 2014).

However, Ashman specifically discounts coordinate shifting in a criticism of kH.9.M determinations by Mueller *et al.* (1998). Ashman's reluctance to coordinate shift may be a reason to more generally (than for $M = \text{CO}_2$) discount the quantitative results of AH98/Ashman premised on kinetic modeling, including the Method 2 reinterpretation of propagated modeling results using relative collisional efficiencies presented earlier. Further reasons to disregard the model-based results of AH98/Ashman are not addressed in depth here; however, it should be apparent from the $\epsilon_{\text{CO}_2/\text{Ar}} = 4.5$ modeling results described here that model-based apparent NO_2 matching interpretations of the Ashman experiments at QSSP conditions may be satisfied by a range of reaction extents. Without additional constraint imposed by a coordinate shift to match the extent of reaction, Ashman's use of apparent NO_2 as a target for kH.9.M optimization is alone insufficient to deliver unambiguous results. Moreover, model-experiment matching interpretations may be single-valued ($\epsilon_{\text{CO}_2/\text{Ar}} = 5.4$), multi-valued ($\epsilon_{\text{CO}_2/\text{Ar}} = 4.5$), or even without solution ($\epsilon_{\text{CO}_2/\text{Ar}} = 3.45$ and Ashman's own predictions) with respect to reaction extent depending on the assumed kinetic model, coordinate shifting interpretation, and even flow field model (Figure 3.13).

Exclusion of 950 and 1000 K Experiments, Consideration of Extended QSSP Conditions at 900 K

At 950 and 1000 K, predictions of the present interpretive kinetic model ($\epsilon_{\text{CO}_2/\text{Ar}} = 4.5$) show that NO_2 and O_2 attain quasi-steady plateaus even with complete conversion of H_2 to H_2O . Despite the apparent quasi-steady plateau behavior at these conditions, NO_2 is depleted back to NO by O (N.5) in addition to HO_2 (N.1). The source of O for N.1 is the $\text{H}+\text{O}_2$ branching reaction H.1, which is competitive with H.9.M at these conditions. Reaction H.1 also generates OH radicals that react with HO_2 via H.13. This reaction tends to deplete HO_2 before it can react with NO by N.2 to form NO_2 . The significant participation of H.1, N.5, and H.13 in the overall reaction scheme violates QSSP assumptions. Similar phenomenology holds even if kH.9.CO2 is increased by ~20% by using $\epsilon_{\text{CO}_2/\text{Ar}} = 5.4$. The present conclusion is that experiments at 950 and 1000 K deviate from QSSP conditions, and this appears to depend little on the assumed value of kH.9.M. Consequently, these experiments have also been excluded from the QSSP re-analyzed data set of Table 4.7. It is also worth noting that Ashman excludes

these two data points from determination of $k_{H.9.M}$ due to potential for wall reactions, which his modeling indicates may become non-negligible above 900 K.

Present interpretive model predictions ($\epsilon_{CO_2/Ar} = 4.5$) of the 900 K experiment suggest that even though nearly full H_2 conversion occurs during the effective experimental residence time (Figure 4.9), deviation from QSSP is not too severe at these conditions. Sensitivity coefficient magnitudes for the NO_2 profile are near unity for H.9.M and N.1, which is indicative of near-QSSP behavior, as also indicated in Figure 3.6. Some influence on NO_2 due to H.1 and subsequent reactions is predicted; however, the effect on NO_2 mole fraction is near the expected NO_2^{**} measurement uncertainty discussed in the following section. Present model predictions at 517 ppm H_2 remaining (equivalent to the experimental extent of reaction, Figure 4.9) return a value of $\sigma_{H.9.M}$ that is 14% of the effective $k_{H.9.M}$ value used by the model (including effects of $M \neq CO_2$). Predicted NO_2^{**} is 27.1 ppm for $\epsilon_{CO_2/Ar} = 4.5$, compared to 32.8 ppm found in experiment. This suggests that better agreement with the model occurs for $\epsilon_{CO_2/Ar} \sim 5.4$, which would also result in smaller values of $\sigma_{H.9.M}$. Manipulations of $\epsilon_{CO_2/Ar}$ and corresponding values of $\sigma_{H.9.M}$ are expected to yield similar model-corrected values for $k_{H.9.CO_2}$ (*cf.* Figure 3.21), so additional modeling is not pursued here. Present treatment of the 900 K Ashman experiment maintains the nominal QSSP-derived $k_{H.9.CO_2LPL}$ value found in Table 4.7 but adds an additional +14% one-sided uncertainty to account for bias resulting from extended QSSP behavior.

4.2.2.3 Uncertainty Estimation for Ashman & Haynes Measurements

Several uncertainties affecting the AH98/Ashman experiments are discussed in the Ashman thesis. Of relevance to QSSP values presented in Table 4.7 are estimated 2σ uncertainties of (a) up to 20% in NO_2^{**} measurement, particularly including potential probe quenching effects; (b) up to 5% in O_2 mole fraction based on atom balance, reactant flow rates, and measured mole fractions of H_2 , H_2O , and NO_2^{**} ; and (c) up to 6% due to two-dimensional flow field departures from plug flow. The 2σ experimental uncertainty applicable to values in Table 4.7 is $\sim 21.5\%$, and including the $\pm 35\%$ uncertainty of the $k_{N.1VRC-FTST}$ reference rate coefficient expression yields a quadrature-propagated overall uncertainty of $\sim 41\%$ for these measurements. As discussed above, the point at 900 K is subject to an additional uncertainty of +14% to correct for extended QSSP bias. Since accounting for a bias, this uncertainty adds linearly to the quadrature-propagated uncertainty derived for QSSP conditions.

4.2.3 Static Reactor Experiments of von Elbe & Lewis, Willbourn & Hinshelwood, and Linnett & Selley

Relative collisional efficiencies of several bath gases M, including CO₂, were determined by von Elbe & Lewis (1942, also referred to here as vEL42), Willbourn & Hinshelwood (1946, WH46), and Linnett & Selley (1963, LS63) by measuring explosion limit threshold behavior in static reactors at fixed temperatures ranging from ~753-853 K, relatively low pressures, and non-dilute reactant conditions. The vEL42 study carefully investigates factors such as vessel surface-to-volume ratio, reactor surface chemistry (de)activation with coatings, reactor non-isothermality, and H₂O formation during mixture preparation (from pre-reaction), all of which may contribute to unreliable static reactor H₂-O₂ explosion limit observations.

Despite this careful investigation of non-ideal experimental artifacts, as well as the good consistency of the isothermal H₂-O₂ second explosion limit data, the results presented in Table III of vEL42 may be only semi-quantitatively accurate. The tabulated results hold only within the interpretive context of the simplified gas phase reaction scheme used by vEL42 to describe explosion pressure (P_{expl}) scaling at the second limit. While this scheme includes only the reactions H.1-H.3 and H.9.M, the bulk of the vEL42 study further presents detailed analyses suggesting that secondary chemistry – including reactions of H₂O₂, potential wall reactions, and induced spatial inhomogeneity – significantly perturbs the classical H₂-O₂ second explosion limit criterion of $P_{\text{expl}} \sim [M] = 2 \times k_{\text{H.1}}/k_{\text{H.9.M}}$ at the static reactor conditions considered.

The WH46 and LS63 studies cite vEL42 and are presumably aware of the difficulties that may be encountered in interpreting experimental static reactor explosion limit data. Second limit collisional efficiencies reported by WH46 for uncoated and KCl-coated silica reactors suggest a non-negligible depression in collisional efficiency (relative to H₂) due to the presence of the wall coating, which is thought to more effectively break radical chains and therefore suppress overall system reactivity. Linnett & Selley notably use KCl coating as well, though they do not explore the effect of coating on apparent explosion limit behavior.

The weight of the evidence in these studies suggests that quantitative collisional efficiency determinations from static reactor explosion limit experiments must be regarded with some reservation since secondary chemistry and wall effects non-negligibly participate in the overall reaction. Although the

vEL42 study does provide empirical measurements and a kinetic model with which it may be possible to reinterpret the collisional efficiency results in light of secondary chemistry and wall effects, the model is premised on a reaction scheme that is at odds with the present consensus mechanistic understanding of H₂-O₂ oxidation. Accordingly, reinterpretation of the von Elbe & Lewis results (or those of Willbourn & Hinshelwood and Linnett & Selley) is a significant task well beyond the scope of this thesis.

The present treatment of these studies is to exclude M = CO₂ static reactor k_{H.9.M} determinations from influence on the present k_{H.9.CO₂LPL} recommendation. However, for completeness, Table 4.8 shows present Method 2 (apparent collisional efficiency) reinterpretations of the *nominal* static reactor measurements. No attempts have been made to estimate uncertainties for these k_{H.9.CO₂LPL} reinterpretations. Despite the probable, unaccounted influence of secondary chemistry and excepting the Ar-referenced interpretation from LS63, these nominal values for k_{H.9.CO₂LPL} from static reactor experiments are in reasonably good agreement with the 1 atm Ashman & Haynes/Ashman and higher pressure HPLFR measurements between ~800 and 850 K (*cf.* Table 4.7 and Table 4.4).

4.2.4 Atmospheric Pressure Flow Reactor Experiments of Dryer

A summary report of Dryer (1987) gives relative collisional efficiencies for M = CO₂ and H₂O relative to N₂, determined from atmospheric pressure turbulent flow reactor experiments in CO₂/H₂O sensitized mixtures of H₂/O₂ and CO/H₂O/O₂ for temperatures ranging from ~980-1180 K. A recommended value of $\epsilon_{\text{CO}_2/\text{N}_2} = 2.7$ was determined by least-squares kinetic model fitting to experimentally measured stable species and temperature profiles. However, few details of the experiments or determination methodology are disclosed either by Dryer or the preliminary, associated paper of Stein *et al.* (1986).

Because this work cannot be subjected to careful reinterpretation, the present work excludes the Dryer/Stein *et al.* $\epsilon_{\text{CO}_2/\text{N}_2}$ determination from influence on the present k_{H.9.CO₂LPL} recommendation, which is similar to the treatment of static reactor experiments discussed above. However, for completeness, the *nominal* rate coefficient data presented in Table I of the Dryer report is reinterpreted by Method 2 (apparent collisional efficiency), and present results appear in Table 4.9. As will be shown, these uncertainty-unquantified reinterpretations are in reasonably good – though possibly fortuitous –

agreement with the final $\text{kH.9.CO2}_{\text{LPL}}$ recommendation developed from other experiments discussed in this chapter.

Finally, it should be noted that the Dryer (1987) value of $\epsilon_{\text{CO2/N2}} = 2.7$ supersedes the $\epsilon_{\text{CO2/N2}} \sim 14$ value initially reported by Dryer's group as a preliminary measurement (Stein *et al.*, 1986). Although details are lacking, it appears that Stein *et al.* attempted to model ratios of ignition delay times to arrive at their result. Even small perturbations to reaction initialization may significantly impact ignition timescales (e.g., Dryer *et al.*, 2014; Urzay *et al.*, 2014; and many of the references therein), thereby leading to outlying results skewed by undetermined coordinate (time) shifts. Relative to the initial ignition delay analysis, the subsequent interpretation of the same/similar turbulent flow reactor data broadly discussed by Dryer (1987) is significantly more constrained by multi-species and temperature profiles that define the principal reaction gradient (Dryer *et al.*, 2014).

4.2.5 Shock Tube OH Time Histories of Vasu *et al.*

Vasu *et al.* (2011, also referred to here as VDH11) provide the final set of $M = \text{CO}_2$ data to inform the present $\text{kH.9.CO2}_{\text{LPL}}$ recommendation. The VDH11 study measures both ignition delay time and time-resolved OH profiles for mixtures of relatively high CO_2 content. However, no ignition delay measurements from this study are considered for explicit constraint of kH.9.CO2 . This is justifiable both for the initialization reasons discussed immediately above and because predictions of several kinetic models suggest that ignition delay time is significantly more sensitive to kH.1 than kH.9.M (for $M = \text{CO}_2$, N_2 , or CO_2 and N_2) for virtually all of the ignition delay conditions measured by VDH11. The CO_2 -perturbed, relative ignition delay times of Brabbs & Robertson (1987) have similarly been excluded from consideration as constraints for kH.9.CO2 .

The rate coefficient determination approach of VDH11 is based on three temporally-resolved OH mole fraction profiles measured by laser absorption in the reaction of a shock-heated 0.5/0.25/30/69.25 blend of $\text{H}_2/\text{O}_2/\text{CO}_2/\text{Ar}$. Nominal initial experimental conditions are at relatively higher reflected shock pressures (~ 8 atm) and temperatures (~ 1290 K). This thesis regards these experimental OH profile measurements to be of high quality in terms of initial reaction conditions and their ability to be well-approximated by idealized zero-dimensional shock tube assumptions subject to perturbed initialization.

Vasu *et al.* determine rate coefficients by matching experimentally measured and model-predicted OH profiles, subject to physical model assumptions of a zero-dimensional chemical-dynamical system reacting at fixed internal energy and volume (*i.e.*, the constant U,V assumption). Nominal values for kH.9.CO2 are determined from the OH profiles by adjusting *only* the value of kH.9.CO2 assumed by a *single* and *unvalidated* complex kinetic model – namely *a modified version of GRI-Mech 3.0* (Smith *et al.*, 1999) – such that model predictions of OH “*best*” match the experimental OH rise and peak. Each italicized term in the preceding sentence is a source of interpretive uncertainty in kH.9.CO2 determinations. Many of these terms were not thoroughly considered in the original VDH11 study but are considered below in detail.

Coordinate shifting, a subject discussed extensively by Dryer *et al.* (2014), is yet another potential source of interpretive uncertainty in these experiments. However, this technique was employed by VDH11 to facilitate alignment of the experimental and predicted OH evolution profiles, so the following discussions will not emphasize the importance of coordinate shifting in interpretation of the VDH11 experiments. Vasu *et al.* themselves demonstrate equivalent OH profile shifts by both H-atom doping and time shifting, so no distinction between these shifting methods is made in the following discussions.

4.2.5.1 Reconstruction of GRI-VDH - The VDH11 Modified GRI 3.0 Interpretive Model

To inform later discussion, some description of the modified version of GRI-Mech 3.0 (henceforth, GRI-VDH) assembled and used by VDH11 for kH.9.CO2 determinations is necessary. The transformation of GRI-Mech 3.0 into GRI-VDH includes an update to thermochemistry (for OH and HO₂ especially) and replacement of several kH.9.M expressions from GRI-Mech 3.0 with the pressure-dependent expressions referenced to Bates *et al.* (2001), as compiled by Hong *et al.* (2011). The VDH11 treatment of the kH.9.M expressions for M = O₂ and M = Other (including CO₂, CO, and C₂H₆) is unclear. For the present experimental interpretations, M = CO and C₂H₆ may be reasonably ignored. For M = O₂, the present re-construction of the GRI-VDH model takes the unmodified, pressure-independent kH.9.O2 expression directly from GRI-Mech 3.0, while kH.9.CO2 is treated as a free, constant-valued parameter following the treatment of VDH11.

Direct comparison between the 1277 and 1291 K GRI-VDH modeling results of VDH11 (S.S. Vasu, personal communication 2011) and the present reconstruction of GRI-VDH differ negligibly (*e.g.*,

Figure 4.10), with the most likely sources of any discrepancy arising from input parameter round-off error, numerical integration parameters, or present treatment of kH.9.O_2 . All reinterpretations of the VDH11 results presented here are premised on the reconstructed GRI-VDH model as described above.

Despite the significant difference in the performance of GRI-Mech 3.0 and GRI-VDH at VDH11 experimental conditions (e.g., Figure 4.10), no broad validation of the GRI-VDH model is evident in the literature. This thesis views chemical kinetic models primarily as interpretive tools with varying degrees of predictive capacity, so the lack of validation provenance for GRI-VDH suggests that this model variant should be viewed as no more than a weakly constraining framework, at least until a broader validation envelope is established. Indeed, later results will show that the original GRI 3.0 model, used in place of GRI-VDH for kH.9.CO_2 determination, can generate substantially similar OH profile predictions (hence interpretations) as GRI-VDH. For otherwise identical treatment, the difference in kH.9.CO_2 determinations among interpretive models presents an ambiguity and quantifiable interpretive uncertainty associated with the nominal kH.9.CO_2 values. It may be argued that the present quality of GRI-VDH model prediction of VDH11 experiments local to (~ 1290 K, ~ 8 atm) justifies its use; however, this may be only a consequence of fortuitous interplay of “secondary chemistry,” as further addressed below.

4.2.5.2 GRI-VDH Model-Consistent Reinterpretation of VDH11 kH.9.CO_2 Determinations to the LPL

While Vasu *et al.* report a “low-pressure limiting” rate coefficient expression supported by their kH.9.CO_2 determinations, the nominal values for their kH.9.CO_2 determinations do not appear to have been corrected to the low pressure limit (LPL). Instead, these determinations are termolecular values of $\text{kH.9.CO}_2(T,P)$ associated with falloff conditions in the H.9.M reaction system. Table 4.10 presents a GRI-VDH model-consistent reinterpretation of the nominal VDH11 values using the high pressure limit (HPL) and $M = \text{Ar}$ (and N_2) falloff parameters of Hong *et al.* (2011), which are attributed to Bates *et al.* (2001). Note also that there is an inconsistency between the HPL expressions given in these two studies, but the HPL expression of the former has been used in the present reconstruction of GRI-VDH. For this reason, the Hong *et al.*-based LPL correction is to be preferred.

This LPL correction effectively shifts the nominal values of the VDH11 rate coefficient determinations higher by about 7%, while the Bates *et al.*-based correction increases kH.9.CO_2 values by 12-13% compared to nominal. Considering the *less than* $\pm 25\%$ overall uncertainty in kH.9.CO_2 explicitly

assumed by Vasu *et al.* (based on an earlier uncertainty analysis of Davidson *et al.* (1996)), the presently determined magnitudes of one-sided bias due to falloff are significant.

The Hong *et al.*-basis LPL-corrected kH.9.CO₂ values address the falloff/LPL inconsistency identified in the VDH11 reported rate coefficients. Henceforth, reference to the VDH11 rate coefficient “determinations” will indicate these Hong *et al.*-basis LPL-corrected values unless noted otherwise.

4.2.5.3 Secondary Chemistry Effects

The preceding reinterpretation of kH.9.CO₂ determinations serves as only a simple continuation of the original Vasu *et al.* model-based determinations for kH.9.CO₂(T,P) to the low pressure limit kH.9.CO₂(T)_{LPL}. An extension to reinterpretation of these experiments follows the approach of VDH11 but expands the interpretive framework to better account for “secondary chemistry” effects. Of course, the term “secondary” may be purely semantic in this case: similar to the previously excluded VDH11 and Brabbs & Robertson ignition delay time measurements, the highly-resolved OH histories presently considered are significantly more sensitive to kH.1 than kH.9.M, as demonstrated both in Figure 5 of VDH11 by GRI-VDH model simulations and here in Figures 4.11 and 4.12 for the Li *et al.* (2007) C₁ model (henceforth Li-C₁) and the Kéromnès *et al.* (2013) syngas model, respectively. The simulations suggest that while reaction H.9.CO₂ is the “primary” reaction of interest, it is clearly a “secondary” reaction relative to H.1 since it is uniformly and significantly less influential in determining OH evolution. In fact, reaction H.9.M neither produces nor consumes OH directly. Instead, reaction H.1 directly forms OH as a product, while reaction H.9.M competes with H.1 for reactants and influences OH evolution only as a reactant sink.

For sake of clear discourse, H.9.CO₂ will be considered in the present context as the “primary” reaction, while H.1 participates in “secondary” chemistry. According to simulations of the GRI-VDH, Li-C₁, and Kéromnès *et al.* models, additional secondary reactions of non-negligible sensitivity relative to H.9.CO₂ include H.2, H.3, H.9.Ar, H.10, H.11, and C.1. Imperfect model assumptions regarding any of these reactions – proceeding in either forward or reverse direction – may influence quantitative kinetic model determinations of kH.9.CO₂ based on simulated OH profiles and matching to experiment.

In GRI-Mech 3.0, rate coefficients for H.10 and H.11 were optimized relative to the fixed parameters for kH.9.M, as well as OH and HO₂ thermochemistry. Since GRI-VDH uses other expressions for kH.9.M and for thermochemistry of OH and HO₂, the VDH11 “updated” model is at least

inconsistent, if not inaccurate, in its adoption of the forward expressions for kH.10 and kH.11 from GRI-Mech 3.0 as well as *all* reverse reactions that depend on OH- and HO₂-thermochemistry expressions (*cf.* Table 1.1). A complete quantitative determination of how these and other *ad hoc* GRI-VDH adjustments to GRI-Mech 3.0 influence model predictions is beyond the scope of the present work; however, the impact of these adjustments may be inferred from some of the results presented here. For example, Figure 4.13 (further explained below) shows that the difference in non-H.9.M secondary chemistry between GRI-Mech 3.0 and GRI-VDH accounts for ~50% difference in determined values for kH.9.CO2.

Phenomenological Dependence of kH.9.M on Secondary Chemistry – A Generalized Model

The role of H.9.M among the important secondary chemistry reactions becomes clear when considering simplified chain-branched explosion chemistry involving reactions H.1-H.3 and H.9.M and treating OH mole fraction as a quantitative indicator of the H atom pool size. For homogeneous conditions such described for idealized constant U,V shock tube experiments, growth of the OH pool is given by

$$d[\text{OH}]/dt = kH.1[\text{H}][\text{O}_2] + kH.2[\text{O}][\text{H}_2] - kH.3[\text{OH}][\text{H}_2], \quad (4.1)$$

which appears to be entirely independent of kH.9.M. However, kH.9.M controls growth of the H pool, which can be linked to growth of the OH pool by

$$d[\text{OH}]/dt = d[\text{H}]/dt + kH.9.M[\text{H}][\text{O}_2][\text{M}] + 2(kH.1[\text{H}][\text{O}_2] - kH.3[\text{OH}][\text{H}_2]), \quad (4.2a)$$

or equivalently,

$$d[\text{OH}]/dt = 2kH.2[\text{O}][\text{H}_2] - kH.9.M[\text{H}][\text{O}_2][\text{M}] - d[\text{H}]/dt \quad (4.2b)$$

where units of concentration are indicated here as reasonable substitutes for mole fractions due to the small temperature and pressure changes associated with the VDH11 experiments. Equations 4.2 mathematically couple the OH profile to the pool of chain carrying H atoms.

On a small time interval [A,B], the H atom pool is governed by local exponential growth/decay characterized by an overall growth rate constant ω , which can be decomposed into an explosive, strictly positive term ω^+ and a terminating, strictly negative term ω^- . These terms correspond to the net quasi-steady state (in O and OH) chain branching reaction $\text{H} + 3\text{H}_2 + \text{O}_2 \leftrightarrow 3\text{H} + 2\text{H}_2\text{O}$ (H.1 + H.2 + 2xH.3) and the effective termination reaction H.9.M, respectively. If, as in the analysis of VDH11, H.9.Ar and

H.9.CO2 are treated as completely separate reactions proceeding at rates that, together, sum to $\omega^- = \omega_{H.9.M}$, then ω^- may be decomposed into ω^{Ar^-} and ω^{CO2^-} . These effective reaction rates correspond to (strictly positive) reaction rate coefficients such that

$$d[H]/dt = \omega = \omega^+ + \omega^{Ar^-} + \omega^{CO2^-} = \omega^+ - X_{Ar}k_{H.9.Ar}[H][O_2][M] - X_{CO2}k_{H.9.CO2}[H][O_2][M]. \quad (4.3)$$

Assuming that the net rate of chain branching is first order in both [H] and the essentially constant [O₂], the H atom pool grows exponentially over the short interval between times A and B according to

$$[H](t) = [H]_A \exp((k^+ - X_{Ar}k_{H.9.Ar}[M] - X_{CO2}k_{H.9.CO2}[M])[O_2]t). \quad (4.4)$$

In response to [H](t), the OH pool also grows in the interval [A,B], but with a modified growth rate indicated by either form of Equation 4.2. As reaction conditions change outside of the short temporal interval [A,B] (by, e.g., reactant depletion, product formation, or temperature change), so too may the effective rates of chain branching and termination. Because of this, the overall course of the reaction is not bound to a constant growth/decay rate, so even the present simplified branched chain system model of Equations 4.1 through 4.4 can emulate the complex growth and decay inherent in the OH profiles measured by experiment and predicted by more complex kinetic models.

Equations 4.2 and 4.3 may be trivially extended to consider lumped contributions to secondary chemistry not already represented in the four reaction system treated above. Using the base terms ϵ and δ to indicate such contributions to the H and OH pools, respectively,

$$d[H]/dt = \omega^+ + \epsilon^+ - X_{Ar}k_{H.9.Ar}[H][M][O_2] - X_{CO2}k_{H.9.CO2}[H][M][O_2] - \epsilon^-, \quad (4.5)$$

so based on Equation 4.2b,

$$d[OH]/dt = 2k_{H.2}[O][H_2] - (X_{Ar}k_{H.9.Ar} + X_{CO2}k_{H.9.CO2})[H][O_2][M] - (d[H]/dt + \epsilon) + \delta. \quad (4.6)$$

Although the present application of theory is not rigorous, it serves to illustrate some features of secondary chemistry effects on OH evolution. From the perspective that the chain-branched explosion of H atoms drives overall reaction, it is clear that the OH profile

- (1) is directly influenced by H.9.M in the context of branched chain reaction dynamics of the H-atom pool (Equations 4.2 and 4.6), despite no direct consumption or production of OH by this reaction (Equation 4.1);
- (2) is also directly influenced by the “secondary” H₂-O₂ chain branching sequence H.1-H.3, whether in terms of absolute species balance (Equation 4.1) or referenced to the growth of the H atom pool (Equations 4.2), and even if other secondary chemistry effects due to ϵ and δ are negligible (Equation 4.6);
- (3) may be significantly sensitive to other reactions acting on either or both of the H or OH pools if secondary reaction contributions to ϵ or δ are non-negligible (Equation 4.6); and
- (4) depends (via the H atom pool) only on the mole fraction weighted *sum* of kH.9.Ar and kH.9.CO₂ – or more generally, the mole fraction weighted sum over all M contributing to kH.9.M – provided rates of secondary chemistry for H.1-H.3, ϵ , and δ are fixed.

Influence of assumed kH.9.M (M ≠ CO₂) on kH.9.CO₂ Determinations

The first of two interpretive approaches presently considered addresses point (4) above by replacing only the kH.9.M (M ≠ CO₂) expressions from GRI-VDH with fixed kH.9.M expressions from other kinetic models, including several “high performing” models described by Zsély *et al.* (2013) and used earlier to form a kH.9.M “Consensus” for M = Ar and N₂. Although swapping of kH.9.M expressions into the GRI-VDH framework may appear *ad hoc*, this procedure is no different than the tentative VDH11 transformation of GRI-Mech 3.0 into GRI-VDH discussed previously, including the inconsistent treatment of kH.10 and kH.11 therein. Moreover, swapping of uncertain kH.9.M expressions to study secondary model-dependencies on kH.9.CO₂ determination is supported by the results of the elementary branched-chain explosion theory discussed immediately above as a means of determining the sensitivity of kH.9.CO₂ determinations to assumed values of kH.9.M (M ≠ CO₂).

Initial value problem (IVP) simulations with GRI-VDH and “swap” model variants have been pursued for the constant nominal initial conditions of the VDH11 experiments. All secondary reactions embodied by H.1-H.3, ϵ , and δ were held fixed by maintaining all reactions other than kH.9.M to be the same as in GRI-VDH (*i.e.*, all other secondary chemistry is fixed). Other secondary effects due to thermochemistry were held constant by maintaining the same GRI-VDH thermochemistry across all

simulations. Then, provided that the swap model value of $k_{H.9.M}$ (in the net) is equal to the net value used in GRI-VDH at all reaction times to-be-simulated, the H profile computed by the $k_{H.9.M}$ swapped model is expected to nearly exactly match the profile computed by GRI-VDH (Equation 4.5). For fixed secondary chemistry, the swapped model OH profile must also nearly exactly match the OH profile computed by GRI-VDH (Equation 4.6). In practice, “equal” and “exact” matching permits reasonable tolerances both in assumed $k_{H.9.M}$ expressions and quality of OH profile overlap, as will be demonstrated shortly. Note also that the objective is to match the simulated GRI-VDH OH profile to demonstrate alternative secondary chemistry interpretations to the original VDH11 interpretation and *not* to improve agreement of the swap models with the experimental OH profiles. Such “exact” matching between model simulations does not require subjective judgments of “best” fit to achieve this objective; rather, this matching directly adopts the judgments inherent in Vasu *et al.*

Since only the lumped value of the swap model $k_{H.9.M}$ must match the value used by GRI-VDH, any $k_{H.9.M}$ summations satisfying the equality

$$\sum_M X_M k_{H.9.M}|_{**GRI**} = k_{H.9.M} = (X_{Ar} k_{H.9.Ar} + X_{CO_2} k_{H.9.CO_2} + \sum_m X_m k_{H.9.m}) \quad (4.7)$$

should yield swapped models that match the GRI-VDH OH profiles. In Equation 4.7, lowercase m indicates species other than $M = Ar$ and CO_2 . Alternatively, Equation 4.7 can be recast as

$$X_{CO_2} k_{H.9.CO_2}|_{swap} = (X_{Ar} k_{H.9.Ar} + \sum_m X_m k_{H.9.m})|_{swap} - \sum_M X_M k_{H.9.M}|_{**GRI**} \quad (4.8)$$

Equation 4.8 provides a good first-order estimate of $k_{H.9.CO_2,swap}$ since $[Ar]$ and $[CO_2]$ are each nearly constant in the VDH11 experiments and, together, account for ~99% of the overall gas concentration $[M]$. Quantitative determination of $k_{H.9.CO_2,swap}$, including second order effects, may be determined by full IVP simulation of each swap model.

In the context of Equation 4.8, the swap models considered specify $k_{H.9.Ar}$ and $k_{H.9.M}$, including pressure- and temperature-dependence; GRI-VDH specifies $k_{H.9.M}(T,P)_{GRI-VDH}$; and the time-dependent simulations using both models determine respective mole fraction histories for all species M . As with the original VDH11 rate coefficient determination, $k_{H.9.CO_2,swap}$ is a free parameter to be adjusted until the swap model and GRI-VDH OH profiles exactly match. Figure 4.13 demonstrates iteration of $k_{H.9.CO_2,swap}$ to an exact match for the GRI-VDH OH profile at 1277 K. In this case, the original GRI-

Mech 3.0 kinetic model has been used as the swap model since it serves as the initial basis for GRI-VDH by providing *all* of the forward reaction rate coefficients for sensitive secondary chemistry aside from kH.9.M. In light of the foundational representation of GRI-Mech 3.0 in GRI-VDH, consideration of kH.9.M expressions from GRI-Mech 3.0 is therefore as *indisputably consistent* as consideration of the kH.9.M expressions used in GRI-VDH.

The kH.9.CO₂_{swap} result is derived by varying the relative collisional efficiency constant $\epsilon_{\text{CO}_2/M}$ for the (pressure-independent) temperature-dependent kH.9.M expression in GRI-Mech 3.0 since this constant pre-multiplies the reference kH.9.M expression and directly indicates kH.9.CO₂ ($= \epsilon_{\text{CO}_2/M}|_{\text{swap}} \times \text{kH.9.M}|_{\text{swap}}$). At the nominal experimental conditions, values of kH.9.M are generally insensitive to the small changes in both T and P that are expected during reaction, so in practice, this relative collisional efficiency result is equivalent to direct variation of a constant-valued kH.9.CO₂_{swap} following the procedure of VDH11.

Notably, swapping the kH.9.M ($M \neq \text{CO}_2$) expressions from GRI-Mech 3.0 into GRI-VDH returns a value of kH.9.CO₂(1277 K) of $5.85 \times 10^{15} \text{ cm}^6/\text{mol}^2/\text{s}$ (*i.e.*, $\epsilon_{\text{CO}_2/M}|_{\text{swap}} = 0.98$), which is only ~69% of kH.9.CO₂(1277 K) determined by Vasu *et al.* (Table 4.10, pre-LPL correction). Alternatively, the Vasu *et al.* interpretation is 44% higher than the *equally valid* interpretation based on the GRI-Mech 3.0 kH.9.M swap. This re-interpreted value of kH.9.CO₂ further suggests that the less than $\pm 25\%$ (2σ) uncertainty in kH.9.CO₂ assumed by Vasu *et al.* is a *significant understatement* of rate coefficient uncertainty.

It is to be further emphasized that this previously unquantified kH.9.CO₂ uncertainty is due to only a limited chemical modeling re-interpretation. This considers that (a) the present difference is attributable *only* to secondary chemistry embodied in kH.9.M; (b) *no* other secondary chemistry effects have been accounted for; and (c) *no* other experimental, modeling, or fitting uncertainties have been included in present analysis. In other words, yet greater uncertainties due to *experimental interpretation* should be expected.

Table 4.11 summarizes values of kH.9.CO₂_{LPL} determined for several swap models from among the among the Zsély *et al.* (2013) Consensus compilation as well as apparent kH.9.CO₂(P) values determined with GRI-Mech 3.0 at the experimental pressure. These swap model results are primarily illustrative and do not comprehensively explore combinations of kH.9.M expressions extant in the

literature. As such, the full range of “valid” (by present extension of VDH11 methods) $kH.9.CO2_{LPL}$ determinations has not been explored; however, a “best” estimate for $kH.9.CO2_{LPL}$ under the present $kH.9.M$ -limited secondary chemistry framework can be made using nominal, maximal, and minimal Consensus expressions for $kH.9.Ar$. The maximal and minimal expressions represent reasonable – though not exhaustively derived – uncertainties in Consensus $kH.9.Ar$.

Consensus $kH.9.M$ Treatment of $kH.9.CO2$ Determinations

For the sake of consistency with the original VDH11 study and methodological clarity in the present reassessment, this Consensus reinterpretation uses expressions for $kH.9.M(T,P)$ for all other $M \neq (Ar \text{ or } CO_2)$ (primarily H_2 , O_2 , and H_2O) from the present reconstruction of the GRI-VDH model. Over the narrow region of (T,P) space relevant to interpreting the VDH11 experiments, all ten unique termolecular $kH.9.Ar$ expressions used to form the $kH.9.Ar$ Consensus are nearly pressure independent; at any fixed temperature $1277 \leq T \text{ (K)} \leq 1350$, the Consensus value deviates less than 1% over $7.59 \leq P \text{ (atm)} \leq 9.00$. Further, the nominal Consensus expression is very reasonably characterized by a $\pm 25\%$ range describing the maximal and minimal $kH.9.Ar$ expressions in this region of (T,P) space. Based on the local temperature dependence for $kH.9.Ar$, the Consensus $kH.9.Ar$ expression may be accurately described as

$$kH.9.Ar(T,P)|_{Consensus} = 3.8466T^{-1.113} \times 10^{18} \text{ cm}^6/\text{mol}^2/\text{s} \pm 25\% \quad (4.9)$$

for T measured in K. This fit is applicable over pressures of 8.30 ± 0.75 atm and temperatures between 1275 K and 1350 K, with fitting errors $< 1\%$ for this whole (T,P) range. An effectively constant Consensus falloff correction of 11.5% also applies across this (T,P) range. The rate coefficient parameterization evident in Equation 4.9 is used for present Consensus determination of $kH.9.CO2$ values. An alternative, more conservative interpretation of the uncertainty in the $kH.9.Ar$ expression of Equation 4.9 is $\pm 33\%$ standard error (2σ); however, this is not used here.

Table 4.12 summarizes values of $kH.9.CO2_{LPL}$ determined by use of the Consensus $kH.9.Ar$ expression. The $\pm 25\%$ uncertainty bands characterizing the range among the $kH.9.Ar$ expressions that form the Consensus translate into roughly $\pm 10\%$ uncertainty in $kH.9.CO2$. This uncertainty is strictly due to the assumed expression for $kH.9.Ar$ and does not consider any other propagated uncertainties due to other secondary chemistry, fitting of simulations to experimental data, etc. The nominal Consensus-based values of $kH.9.CO2_{LPL}$ are within a few percent of those of Vasu *et al.*, which is unsurprising since

the Hong *et al.*/Bates *et al.* expression for $k_{H.9.Ar}(T,P)$ used in GRI-VDH lies only ~10% below Consensus. It should be emphasized that the present good agreement of Consensus determinations with those of VDH11 is a fortuitous consequence of the expressions for $k_{H.9.Ar}(T,P)$ used by VDH11 and the exact duplication of the VDH11 interpretive technique used here.

Application of the VDH11 interpretation framework has herein demonstrated *substantial, heretofore unquantified interpretive uncertainty* in determined values of $k_{H.9.CO2}$ depending on assumed $k_{H.9.Ar}(T,P)$ expression. The previously justified ensemble of $k_{H.9.Ar}$ expressions presently used achieves the same model predictions as GRI-VDH but returns nominal values of $k_{H.9.CO2}$ which may differ by nearly a factor of 2 – for example, 5.85×10^{15} (Table 4.11) versus 1.01×10^{16} (Table 4.12) $\text{cm}^6/\text{mol}^2/\text{s}$ for the 1277 K case, also depending on LPL treatment. The argument can be made that exclusion of the GRI-Mech 3.0 reinterpretations in Table 4.11 would reduce interpretive uncertainties due to the VDH11 technique; however, such an argument is completely inconsistent with the VDH11 use of GRI-Mech 3.0 as the foundation for all non-H.9.M secondary chemistry in GRI-VDH.

Additional Influence of More General Secondary Chemistry on $k_{H.9.CO2}$ Determinations

A more complete consideration of secondary chemistry is addressed by considering kinetic models other than GRI-VDH for determination of $k_{H.9.CO2}$, which poses an extension of the interpretive approach applied above to investigate the conclusions developed from earlier branched chain explosion analysis. The diversity of secondary chemistry reactions, reaction rate coefficients, and thermochemistry adopted by other models broadens consideration of secondary chemistry effects to include all conclusions (1)-(4) resulting from that analysis. The present interpretation seeks to avoid prescribing which, if any, of GRI-VDH, GRI-Mech 3.0, or the twelve Zsély *et al.* “best performing” H_2 oxidation models may itself be “best” to use for $k_{H.9.CO2}$ determination. Instead, the nominal “best” fits of $k_{H.9.CO2}$ from application of the VDH11 interpretive technique to several of these models is used to represent yet alternative interpretations for $k_{H.9.CO2}$ in addition to those presented in Tables 4.10-4.12. Scatter in these nominal values presents yet another form of kinetic model-based interpretive uncertainty in determinations of $k_{H.9.CO2}$.

It should be acknowledged that, in essence, any of these reasonably predictive kinetic models presents one of many reasonably quantitative frameworks for $k_{H.9.CO2}$ interpretation. Each is based on

(often many of the same) reasonably quantitative fundamental elementary reaction kinetics, thermochemistry, and transport parameters, and each is validated against (often many of the same) fundamental combustion experiments using (often many of the same) physical-chemical model assumptions. In deference to this observation, the adequacy of any one of these models for kH.9.CO2 determination is largely a moot point. Though this conclusion may appear at odds with earlier criticisms regarding use of the *ad hoc* GRI-VDH successor model, it serves to provide an additional, reasonable framework for interpretation of the VDH11 experiments. Certainly much more could be written regarding the histories, discrepancies, (in)consistencies, and respective uncertainties among rate coefficient, thermochemistry, and transport parameters used by these and other kinetic models. However, in the absence of significantly less uncertain predictive models based on significantly less uncertain elementary rate coefficients and experimental interpretations, such discussion would not change the multiplicity of reasonable “best” kH.9.CO2 values determined from this expanded interpretive framework.

Unless otherwise indicated, present discussions are referenced to simulations from either (a) the Kéromnès *et al.* model (Figure 4.12), which gives excellent *a priori* prediction of the VDH11 1277 K experiment *with no adjustments to the kinetic model*, or (b) the Li-C₁ model (Figure 4.11), which may *appear* to be of poorer predictive ability – a point that will be subsequently addressed. Observations based on these models and this experimental condition easily generalize to results from other kinetic models and for the other VDH11 experimental conditions. Complexities of treating non-ideal initialization (time = 0) through time shifting or radical doping (*e.g.*, VDH11 and Dryer *et al.*, 2014) have already been considered, though the following discussion may help inform selection of the “best” matching point to which to shift model predictions.

Along with the sensitivity analyses presented in Figures 4.11 and 4.12 for the 1277 K case, the measured and predicted OH profiles reveal important points to consider when adjusting model values of kH.9.CO2 to “best” fit predictions to experimental measurements. Despite relatively high sensitivity to kH.9.CO2, early reaction times are marked by low OH signal (experimental or predicted) and relatively high experimental noise. Due to the low signal-to-noise ratio (SNR), OH measurements at these times do not provide strong constraint for matching of predicted OH and can be reasonably excluded from further analysis. For the specific conditions of the 1277 K VDH11 experiment, some representative boundaries

for this low SNR region might be $t < 200 \mu\text{s}$ (in “absolute” experimental time) or, similarly, OH mole fractions less than ~10% of the experimentally measured peak OH.

At relatively long reaction times including near-peak OH (~300 μs experimental time) and beyond, the OH profile is uniformly less sensitive to kH.9.CO_2 in absolute terms compared to pre-peak times. The OH profile is also relatively *more sensitive* to the “secondary” reaction H.1 compared to pre-peak times. Because long reaction times both underemphasize sensitivity to H.9.CO_2 and overemphasize the effects of secondary chemistry relative to pre-peak times, OH measurements at long reaction times may also be reasonably excluded from further analysis.

Furthermore, depending on the model chosen for OH profile predictions, both the low absolute sensitivity coefficient magnitude and the sign change in the OH sensitivity profile for H.9.CO_2 also suggest that some kinetic models, such as Li-C₁ (Figure 4.11), will be unable to simultaneously match the OH profiles in the rise and near-peak (roughly $200 \leq t \leq 350 \mu\text{s}$ experimental time) regions if the value kH.9.CO_2 is adjusted according to the approach of VDH11. In such a case, an improvement in near peak/post-peak OH predictions would be attended by deterioration of the OH prediction during the rise time. If such models are indeed predictive, as in the judgment of Zsély *et al.* (2013), then, depending on the (possibly subjective) objective function for “best” fit optimization, attempting to match OH profiles at long residence times may over-constrain or confound model-determined kH.9.CO_2 values, even from models that are “predictive”.

Despite the discussion at the beginning of this subsection that both a) supports broad inclusion of reasonably predictive kinetic models for the present kH.9.CO_2 determinations and b) highlights the futility of quarreling over which of these may be “better” or “the best,” it might still be argued that models such as Li-C₁ are poor choices to use to interpret the Vasu *et al.* experiments. However, this assertion would be at odds with the Zsély *et al.* assessment of “best performing” H_2 oxidation models, in which only the recent Kéromnès *et al.* model exhibits better overall predictive performance than Li-C₁. It would also be at odds with the value of $\text{kH.9.CO}_2^{\text{LPL}}$ whole-model determined using the Li-C₁ model (discussed below). Moreover, in the Li-C₁ model, all of the sensitive elementary reaction rate coefficients (save for kH.9.CO_2) identified in VDH11 and Figures 4.11 and 4.12 are based on rate coefficient and thermochemistry parameterizations from fundamental reaction kinetics literature with several years additional currency

relative to GRI-Mech 3.0 and GRI-VDH (*i.e.*, 2004 for the H₂ submodel contained in Li-C₁ versus 1999 for the GRI variants). The models of Hong *et al.* (Hong-H₂), Burke *et al.* (2012, Burke-H₂), or Kéromnès *et al.*, for example, likewise enjoy more recent currency (2011-2013) than does Li-C₁, yet the former two of these models are of poorer overall predictive power according to Zsély *et al.*

All three of these more recent kinetic models use a kH.1 parameterization due to Hong *et al.* (2011b), which is based on model-determined rate coefficient values from a shock tube laser absorption experiment and determination methodology not dissimilar to that described by Vasu *et al.* Extensive discussion of interpretive uncertainties in the Hong *et al.* kH.1 determinations appears in the recent thesis of Heyne (2014) and will not be further discussed here. Given the more general nature of the present inquiry regarding interpretive uncertainty for shock tube rate coefficient determinations, the circular reasoning implied by preferring any of these models (and the Hong *et al.* kH.1 expression therein) for kH.9.CO₂ determination should be evident. Since consistency does not ensure accuracy and the VDH11 OH profiles are particularly sensitive to kH.1 (Figures 4.11 and 4.12), there is no particular reason to prefer any of the Hong-H₂, Burke-H₂, or Kéromnès *et al.* models for present kH.9.CO₂ determinations. As will be shown for the Burke-H₂ and Kéromnès *et al.* models, there can be significant (nearly factor of 2) differences in kH.9.CO₂ determinations even when using the Hong *et al.* kH.1 expression.

Having now digressed to consider relevant aspects of the kinetic models to be used in quantifying a measure of the influence of secondary chemistry on kH.9.CO₂, this discussion returns to feature analysis of the VDH11 OH profiles. Unlike early and late reaction times, the OH rise region between approximately $200 \leq t \leq 275 \mu\text{s}$ experimental time exhibits relatively high OH signal-to-noise ratio *and* high absolute sensitivity to kH.9.CO₂. This suggests that the OH rise region (excluding near-peak OH) may be most appropriate for kH.9.CO₂ “best” match determination by the VDH11 approach. As with the previously excluded early reaction times and unlike near-peak OH reaction times, the OH rise region is associated with radical chain branching from the H.1-H.3 reaction cycle and effective termination by H.9.M (here, M is primarily CO₂ or Ar). Reactions H.10, H.11, and C.1 parasitically contribute/compete with these four reactions commonly used to describe the second explosion limit for H₂-O₂ mixtures.

Table 4.13 presents several kH.9.CO₂ determinations from the sensitive OH rise portion of the 1277 K OH profile ($200 \mu\text{s} \leq t \leq 275 \mu\text{s}$) previously identified. For sake of consistency in illustrating

interpretive uncertainty due to secondary chemistry, these determinations employ the same models from among GRI-Mech 3.0 and the Zsély *et al.* Consensus models as enumerated in Table 4.11. However, in this case, the entire associated kinetic model and not just $\text{kH.9.M}_{\text{swap}}$ is used for kH.9.CO_2 determination. Additional models not specifically considered serve only to add to – or leave unchanged at best – the scatter in nominal kH.9.CO_2 values included in Table 4.13. Many interpretive parameters relevant to data processing and “best” fit may contribute to uncertainty in the rate coefficient determination (Heyne, 2014), and it is not the intention of the present work to consider these robustly. Results should be expected to change depending on treatment of coordinate shifting, temporal domain used for matching, treatment of signal-to-noise, optimal fitting criteria, *etc.* For present purposes, these tabulated values are considered to satisfy “best” fits to the experimental OH measurements, as presented in Figure 4.14. All model predictions have been coordinate shifted to coincide at the point of 50% of peak experimental OH.

It is interesting to compare the 1277 K results of the kH.9.Ar swapping approach in Table 4.11 to those of the whole-model swapping approach in Table 4.13. The GRI-VDH value serves as a reference and is common between the two tables. The kH.9.CO_2 values associated with GRI-Mech 3.0 are equal, but the models from which these values are derived differ in assumed thermochemistry. From this result, it may be concluded that thermochemistry is not an especially sensitive parameter for kH.9.CO_2 determination, at least depending on the present “best” fit approach.

Like kH.9.CO_2 determinations with GRI-Mech 3.0, both the Li-C₁ and Kéromnès *et al.* models show quantitative similarity between whole model and swap model results. Nominal kH.9.CO_2 values – whether in falloff or at the LPL – differ by less than 9% depending on the determination approach. The reference model with the largest discrepancy (~80%) between the two treatments of secondary chemistry is the Burke-H₂ model. For the Burke-H₂ value of kH.9.CO_2 provided in Table 4.11, the underlying GRI-VDH framework assumed in the swap model approach discussed earlier provides reaction C.1, which at the conditions studied by VDH11, is known to form OH from CO₂ and H. In other words, CO₂ is expected to participate in the overall reaction at these conditions as more than an otherwise inert collision partner in H.9.CO₂. By contrast, the Burke-H₂ model (with reactions and rate parameters taken whole and unmodified from the literature) altogether lacks reaction C.1. The Hong-H₂ model also lacks this reaction, which is one reason that this model was not separately considered in the present analysis.

Absence of the “secondary” C.1 reaction in the Burke-H₂ and Hong-H₂ models suggests that, without modification, neither of these models in their entirety is well-suited for kH.9.CO₂ determination. Nevertheless, it is meaningful to the present consideration of secondary chemistry to compare kH.9.CO₂ determinations from the mechanistically incomplete (for VDH11 conditions) whole Burke-H₂ model and the GRI-Mech 3.0 foundation to GRI-VDH. The differences between nominal kH.9.CO_{2,LPL} determinations (Table 4.13) are only ~20%, despite differing from other kH.9.CO_{2,LPL} determinations by nearly a factor of two. Taken together, these two alternative rate coefficient determinations highlight the very significant influence of secondary chemistry. Imprudent or accidental choice of “poorly performing” secondary chemistry may yield nearly the same value of kH.9.CO₂ as a model that is mechanistically unsuitable for kH.9.CO₂ determination. Likewise, local linearized sensitivity-uncertainty analysis (e.g., Vasu *et al.* based on Davidson *et al.*, 1996) may be insufficient to capture the *interpretive uncertainty* evident in the wide range of kH.9.CO₂ values determined from exactly the same experimental data. Certainly, the local linear sensitivity analysis presented in Figures 4.11 and 4.12 fails to identify the importance of reaction C.1 to making reasonable determinations of kH.9.CO₂ from the experiments of VDH11.

4.2.5.4 Summary of VDH11 Reinterpretations

The reinterpretations of the Vasu *et al.* experiments offered by this thesis clearly suggest that (more generally) the influence of both secondary chemistry and interpretive framework on nominal rate coefficient determinations warrants significant investigation as a means of establishing accurate values of rate coefficients delimited by reasonable uncertainties. Table 4.14 summarizes the ensemble of “valid” kH.9.CO₂(1277 K) interpretations appearing in Tables 4.10-4.13; similar results are expected for the two other cases and have not been pursued here. Aside from the low values attributable to determinations from the C.1-lacking whole Burke-H₂ model, all other values in Table 4.14 are valid kH.9.CO₂ interpretations under the original and extended VDH11 approaches discussed above. It appears that the *less than ±25%* overall 2 σ uncertainty (S.S. Vasu, personal communication 2011) explicitly assumed in VDH11 for the kH.9.CO₂ determinations is not reasonable. This is particularly clear when considering that the present analysis is in many ways less complete than, for instance, that of Heyne (2014) for kH.1 rate coefficient determinations from similar experiments.

In light of the results of re-analysis of the VDH11 data, some judgment must be made as to which values of $k_{H.9.CO_2}$ in Table 4.14 are “best” representative of the experimental measurements as well as to what uncertainty should be associated with these values. The recommendation of this thesis is to use the LPL-adjusted nominal Consensus values from Table 4.12 as reasonable nominal values of $k_{H.9.CO_2,LPL}(T)$. However, due to the herein documented ambiguity associated with kinetic model interpretation as well as other factors not considered here that would also contribute to rate coefficient determination uncertainty, this thesis prescribes no definitive uncertainties for the VDH11-associated $k_{H.9.CO_2,LPL}$ determinations. It is worth noting, however, that, given the high quality of the VDH11 experimental measurements, future work such as pursued by Heyne may permit more robust quantification of $k_{H.9.CO_2}$ and its uncertainties.

4.3 Recommended $k_{H.9.CO_2,LPL}$ Expressions Based on HPLFR Measurements and Literature Reinterpretations

The preceding reassessments of apparent $k_{H.9.CO_2}$ values from the literature combined with the new HPLFR $k_{H.9.CO_2,LPL}$ determinations presented in Section 4.1 provide a basis for a final recommendation of $k_{H.9.CO_2,LPL}$ over an extended temperature range relevant to combustion applications. Figure 4.15 compiles recommended $k_{H.9.CO_2,LPL}(T)$ values and corresponding uncertainties from Tables 4.4, 4.5, 4.7, and 4.12. A line of best fit through $\log(k_{H.9.CO_2,LPL})$ versus inverse temperature data provides a slope and intercept with an activation energy and pre-exponential factor interpretation associated with the standard Arrhenius form. Assuming no weighting of any of the included data, standard linear least squares regression statistics also provide uncertainties for these parameters:

$$k_{H.9.CO_2,LPL} = (6.1 \pm 1.2 / -1.0) \times 10^{15} \exp((1164 \pm 306 \text{ kcal/mol})/RT) \text{ [cm}^6/\text{mol}^2/\text{s}] \text{ at 95\% CI,} \quad (4.10)$$

valid over the 633-1305 K range of the included data. The upper and lower uncertainty bounds are in very good agreement with the (independent) quadrature-derived 2σ uncertainties corresponding to the static reactor and flow reactor data and are consistent with maximum and minimal Consensus bounds for the shock tube measurements (Table 4.12). For these reasons, an uncertainty-weighted regression was not pursued. It is also worth noting that (1) the uncertainty bounds computed here also include many of

the nominal $k_{H.9.CO2_{LPL}}(T)$ values that were previously excluded for reasons explained earlier, and (2) the 95% CI applies individually to values of A-factor and activation energy. The 95% CI of the least squares *fit* lies somewhat inside of the extremal combinations of A-factor and activation energy give in the preceding equation.

Many instances of $k_{H.9.M}$ expressions in the literature – whether associated with elementary rate coefficient measurement or complex kinetic modeling – use a modified form of Arrhenius rate coefficient expression with zero activation energy. In this case, the temperature dependence of the rate coefficient is captured by the temperature exponent. Logarithmic transform of the included $k_{H.9.CO2_{LPL}}(T)$ data permits determination of the temperature exponent and pre-exponential factor:

$$k_{H.9.CO2_{LPL}} = 10^{17.86 \pm 0.68} T^{-0.605 \pm 0.179} [\text{cm}^6/\text{mol}^2/\text{s}] \text{ at 95\% CI.} \quad (4.11)$$

Here T is measured in kelvin; the uncertainty associated with the temperature exponent is based on the 95% CI for the slope of the best fit line through the log-transformed (T, $k_{H.9.CO2_{LPL}}$) data; and the uncertainty associated with the pre-exponential factor has been set so that maximum and minimum confidence interval bounds essentially coincide with those given by Equation 4.10. Note that the agreement between nominal expressions in Equations 4.10 and 4.11 is excellent.

Relatively few literature expressions for $k_{H.9.CO2_{LPL}}$ are available, and most depend on the same experimental measurements critically examined here. For this reason, comparison among present results and literature values is somewhat tautological. Nevertheless and notwithstanding criticisms discussed earlier in this chapter, Figure 4.15 includes the termolecular $k_{H.9.CO2}$ recommendations of Vasu *et al.* and Ashman & Haynes extrapolated across the entire 633-1305 K temperature range of present interest. Both of these nominal literature expressions are in excellent agreement with those presently offered.

It is notable that the Vasu *et al.* study uses an expression attributed therein to GRI-Mech 3.0. This expression is ultimately attributable to the rate coefficient compilation of Warnatz (1984), which predates all but the $M = \text{CO}_2$ static reactor experiments discussed in this thesis. So in a sense, Figure 4.15 indicates that all of these later experiments – including the new HPLFR experiments presented here – have served primarily to corroborate the earlier static reactor experiments, provide some quantitative

refinement to $k_{H.9.CO_2}$, reduce uncertainty in the rate coefficient, and/or extend the (T,P) space at which this rate coefficient has been examined.

Finally, it is worth noting that Equations 4.10 and 4.11 are expressed as absolute rate coefficients. This facilitates determination of the collisional efficiency ($\epsilon_{CO_2/M}$) of CO_2 relative to another gas M for which a reference $k_{H.9.M_{LPL}}$ expression is available. However, given the variation in $k_{H.9.M_{LPL}}(T)$ expressions across the Consensus constituents discussed earlier, no attempt has been made here in this chapter to recommend a single value of $\epsilon_{CO_2/M}$ for a particular reference gas M (e.g., Ar or N_2). The value of $\epsilon_{CO_2/M}$ remains entirely dependent on the reference $k_{H.9.M_{LPL}}(T)$. Chapter 5 discusses particular kinetic models that prescribe $k_{H.9.M_{LPL}}(T)$ expressions, so corresponding values of $\epsilon_{CO_2/M}$ are revisited there.

Table 4.1 – Nominal initial conditions for HPLFR kH.9.CO2 determination experiments

Experiment Reference	Pressure (atm)	Temperature (K)	H₂ (ppm)	O₂ (ppm)	NO (ppm)
4/I	8.0	820	7253	4533	98
4/II	6.0	828	9922	9641	97
4/III	2.1-6.1	796	19298	25564	100
4/IVa	2.5	802	19093	17589	94
4/IVb	2.1-4.9	798	19093	17589	94
4/Va	2.5	778	19280	21904	93
4/Vb	2.5	776	19280	21904	93

Table 4.2 – Measured profile-averaged ratio of O₂ and NO₂ mole fractions from HPLFR CO₂ bath gas experiments

Experiment Reference	Nominal Pressure (atm)	Nominal Temperature (K)	[O ₂]/[NO ₂] ^a	kN.1/kH.9.CO ₂ ^a	Estimated 2σ Uncertainty in kN.1/kH.9.CO ₂ ^b
4/I	8.0	820	84.0	83.6	16%
4/II	6.0	828	127.9	127.8	16%
4/III	varies	796	Table 4.3		18.5%
4/IVa	2.5	802	250.0	245.8	16%
4/IVb	varies	798	Table 4.3		16%
4/Va	2.5	778	252.5	246.2	16%
4/Vb	2.5	776	248.0	241.9	16%

^a Profile-averaged values of [O₂]/[NO₂] give kN.1/kH.9.CO₂ under Equation 3.1 QSSP assumptions, with correction by Equation 3.16 and assumed collisional efficiencies for M = H₂O, H₂, O₂, and CO₂ relative to N₂ (see Section 3.2). Use of collisional efficiencies relative to Ar presents negligible (<0.5%) uncertainty in kN.1/kH.9.CO₂. ^b Uncertainty estimated from contributions due to profile averaging, NO₂ and O₂ quantification, variations in absolute pressure and temperature, and plug-flow and QSSP idealizations.

Table 4.3 – Measured ratio of O₂ and NO₂ mole fractions from HPLFR pressure-varying M = CO₂ experiments

Experiment Reference	Nominal Temperature (K)	Measured Pressure (atm)	[O ₂]/[NO ₂] ^a	kN.1/kH.9.CO ₂ ^a	kN.1/kH.9.CO ₂ TER (10 ⁻³ mol/cm ³)
4/III	796	2.08	300.0	291.5	9.257
		2.47	273.6	265.8	10.04
4/IVb	798	2.14	287.2	283.4	9.161
		2.21	279.6	275.8	9.251
		2.42	258.3	254.7	9.308
		2.48	250.9	247.4	9.308
		2.49	248.9	245.5	9.274
		2.71	233.6	230.1	9.465
		2.80	228.0	224.6	9.585
		2.92	221.4	218.0	9.664
		2.97	215.6	212.2	9.582
		3.31	202.0	198.5	10.01
		3.37	199.0	195.6	10.02
		3.38	197.1	193.7	9.961

^a Values of [O₂]/[NO₂] give kN.1/kH.9.CO₂ under Equation 3.1 QSSP assumptions, with correction by Equation 3.16 and assumed collisional efficiencies for M = H₂O, H₂, O₂, and CO₂ relative to N₂ (see Section 3.2). Use of collisional efficiencies relative to Ar presents negligible (<0.5%) uncertainty in kN.1/kH.9.CO₂.

Table 4.4 – Summary of falloff corrections for HPLFR $k_{H.9.CO2_{LPL}}$ determinations

Experiment Reference	Avg. Consensus Falloff Depression ^a	$k_{H.9.CO2(T,P)}$ ($cm^6/mol^2/s$) ^b	$k_{H.9.CO2_{LPL}}$ ($cm^6/mol^2/s$)	Estimated 2σ Uncertainty in $k_{H.9.CO2_{LPL}}$ ^c
4/I	14.1%	1.08×10^{16}	1.26×10^{16}	39%
4/II	13.3%	0.96×10^{16}	1.11×10^{16}	39%
4/III	11.4%	1.11×10^{16}	1.26×10^{16}	40%
4/IVa	11.6%	1.15×10^{16}	1.30×10^{16}	39%
4/IVb	11.8%	1.12×10^{16}	1.27×10^{16}	39%
4/Va	11.7%	1.10×10^{16}	1.25×10^{16}	39%
4/Vb	11.7%	1.12×10^{16}	1.27×10^{16}	39%

^a Falloff depression = $1 - (k_{H.9.M(T,P)}/k_{H.9.M_{LPL}})$ based on Consensus falloff expressions for $M = N_2$ and Ar. ^b Based on values of $k_{N.1/kH.9.CO2}$ (species-resolved experiments) or average $k_{N.1/kH.9.CO2_{TER}}$ (pressure-resolved experiments) in Tables 4.2 and 4.3 and $k_{N.1_{VRC-FTST}}$ described in Section 3.2.2. ^c Quadrature-propagated uncertainty from experimentally-determined $k_{N.1/kH.9.CO2}$ values, reference $k_{N.1_{VRC-FTST}}$ expression, and falloff correction.

Table 4.5 – Summary of kH.9.CO2 reinterpretations of 633 K Ashmore & Tyler (1962) experiments

Interpretive Method	kN.1/ kH.9.CO2_{TER} (10⁻³ mol/cm³)	kH.9.CO2(T,P) (cm⁶/mol²/s)^b	kH.9.CO2_{LPL} (cm⁶/mol²/s)	Estimated 2σ Uncertainty in kH.9.CO2_{LPL}
Method 1 ^a	6.884	1.48 × 10 ¹⁶	1.64 × 10 ¹⁶	48%
Method 2 ^b	---	1.44 × 10 ¹⁶	1.61 × 10 ¹⁶	50%

^a Relative method based on absolute AT62 measured slope of P_S/P_{O₂} versus P_{CO₂}. ^b Relative method based on modern Consensus value for kH.9.N₂ and ratio of AT62 slopes for M = CO₂ and N₂.

Table 4.6 – Reinterpretation of Ashman & Haynes (1998) kH.9.CO2 experiments by apparent collisional efficiency

Temp. (K)	Original kH.9.CO2(T) ^{a,b}	Bromly <i>et al.</i> kH.9.N2(T) ^c	Consensus kH.9.N2(T) ^c	Revised kH.9.CO2(T) ^c	kH.9.CO2 _{LPL} (cm ⁶ /mol ² /s) ^d
800	1.22 × 10 ¹⁶	6.08 × 10 ¹⁵	4.22 × 10 ¹⁵	8.44 × 10 ¹⁵	9.37 × 10 ¹⁵
850	1.23 × 10 ¹⁶	5.78 × 10 ¹⁵	3.92 × 10 ¹⁵	8.31 × 10 ¹⁵	9.20 × 10 ¹⁵
900	1.15 × 10 ¹⁶	5.53 × 10 ¹⁵	3.65 × 10 ¹⁵	7.60 × 10 ¹⁵	8.40 × 10 ¹⁵

^a All rate coefficients in this table are for termolecular elementary reactions, in units of cm⁶/mol²/s. ^b Digitized values from Ashman & Haynes (1998), which agree to within 5% (2σ) of digitized values from Ashman (1999). ^c P = 1.0 atm. ^d Based on 9.5-9.9% falloff depressions computed from Consensus falloff expressions for M = N₂.

Table 4.7 – Reinterpretation of Ashman (1999) kH.9.CO2 experiments by QSSP analysis

Temp. (K)	[NO ₂] ^a	[O ₂]/[NO ₂] ^a	kN.1/kH.9.CO ₂ ^a	kH.9.CO ₂ (T,P) (cm ⁶ /mol ² /s)	kH.9.CO ₂ _{LPL} (cm ⁶ /mol ² /s)	Estimated 2σ Uncertainty in kH.9.CO ₂ _{LPL}
* 760	* 48.7	* 615	* 598	* 1.11 × 10 ¹⁶	* 1.23 × 10 ¹⁶	---
800	47.7	605	593	1.19 × 10 ¹⁶	1.32 × 10 ¹⁶	41%
850	40.5	650	649	1.17 × 10 ¹⁶	1.30 × 10 ¹⁶	41%
† 900	† 32.8	† 767	† 772	† 1.05 × 10 ¹⁶	† 1.16 × 10 ¹⁶	† +55%, -27%
* 950	* 28.9	* 862	* 869	* 1.00 × 10 ¹⁶	* 1.10 × 10 ¹⁶	---
* 1000	* 21.7	* 1152	* 1160	* 7.97 × 10 ¹⁵	* 8.77 × 10 ¹⁵	---

* Measurements may not be at near-QSSP conditions. Rate coefficient values are to be excluded from comparisons to other values of kH.9.CO₂ and formulation of present kH.9.CO₂ rate coefficient recommendation. † Extended QSSP conditions. Rate coefficient values subject to bias in uncertainty compared to QSSP values. ^a Digitized values of apparent, measured values reported by Ashman (1999). ^b Equation 3.1 QSSP assumptions with correction by Equation 3.16 and assumed collisional efficiencies for M = H₂O, H₂, O₂, and CO₂ relative to N₂ (see Section 3.2). ^c Uncertainty estimated from contributions due to profile averaging, NO₂ and O₂ quantification, variations in absolute pressure and temperature, and plug-flow and QSSP idealizations.

Table 4.8 – Reinterpretation of static reactor kH.9.CO₂ experiments by apparent relative collisional efficiency

Study	Temp. (K)	$\epsilon_{\text{CO}_2/\text{H}_2}$	$\epsilon_{\text{M}/\text{H}_2}$	$\epsilon_{\text{CO}_2/\text{M}}$	Effective Pressure (atm) ^c	Consensus kH.9.M _{LPL} (cm ⁶ /mol ² /s)	Nominal kH.9.CO ₂ _{LPL} (cm ⁶ /mol ² /s)
vEL42	803	1.467	0.433 ^a	3.39 ^a	0.165	4.67 × 10 ^{15 a}	1.58 × 10 ¹⁶
WH46	853	0.90	0.35 ^a	2.57 ^a	1.0	4.32 × 10 ^{15 a}	1.11 × 10 ¹⁶
LS63 ^d	803	1.53	0.43 ^a	3.56 ^a	0.132	4.67 × 10 ^{15 a}	1.66 × 10 ¹⁶
LS63 ^d	803	1.53	0.18 ^b	8.50 ^b	0.132	2.62 × 10 ^{15 b}	2.23 × 10 ¹⁶

^a M = N₂. ^b M = Ar. ^c All of these conditions appear to be at the low pressure limit; present results are essentially insensitive to assumed effective pressure. ^d LS63 also report CO₂ collisional efficiencies relative to O₂ and D₂, which are themselves referenced to $\epsilon_{\text{H}_2/\text{H}_2} \equiv 1.00$; the H₂-referenced data are therefore considered to be most reliable.

Table 4.9 – Reinterpretation of Dryer (1987) kH.9.CO2 experiments by apparent collisional efficiency

Temp. (K) ^a	Original kH.9.N2(T) ^{b,c}	Consensus kH.9.N2(T) ^{b,c}	$\epsilon_{\text{CO}_2/\text{N}_2}$	Consensus kH.9.CO2(T) ^{b,c}	Nominal kH.9.CO2 _{LPL} ^{b,d}
1010	3.99×10^{15}	3.17×10^{15}	2.7	8.55×10^{15}	$9.40 \times 10^{15} \pm 32\%$
1080	3.55×10^{15}	2.91×10^{15}	2.7	7.87×10^{15}	$8.63 \times 10^{15} \pm 32\%$
1150	2.47×10^{15}	2.70×10^{15}	2.7	7.28×10^{15}	$7.97 \times 10^{15} \pm 32\%$

^a Nominal temperature; reported range includes ± 30 K. ^b All rate coefficients in this table are for termolecular elementary reactions, in units of $\text{cm}^6/\text{mol}^2/\text{s}$. ^c $P = 1.0$ atm. ^d Low pressure limits based on 9.1-8.6% falloff depressions computed from Consensus falloff expression for $M = \text{N}_2$. Representative 32% uncertainties directly are propagated from Dryer (1987) and are not rigorously supported in the present work.

Table 4.10 – Low pressure limit corrections to nominal kH.9.CO2 values from Vasu *et al.* (2011)

Temp. (K)	Pres. (atm)	Vasu <i>et al.</i> (2011) Nominal kH.9.CO2 ^a	Hong <i>et al.</i> (2011) Basis		Bates <i>et al.</i> (2001) Basis	
			kH.9.CO2 _{LPL} ^{a,b,c}	difference	kH.9.CO2 _{LPL} ^{a,b}	difference
1277	8.41	8.43 × 10 ¹⁵	9.04 × 10 ¹⁵	+7.2%	9.48 × 10 ¹⁵	+12.5%
1291	7.59	8.5 × 10 ¹⁵	9.10 × 10 ¹⁵	+7.0%	9.52 × 10 ¹⁵	+12.0%
1305	8.16	9.8 × 10 ¹⁵	1.05 × 10 ¹⁶	+7.3%	1.11 × 10 ¹⁶	+13.0%

^a All rate coefficients in this table are for termolecular elementary reactions, in units of cm⁶/mol²/s. ^b Computed at nominal experimental temperature and pressure. ^c Preferred values consistent with and corresponding to the GRI-VDH model.

Table 4.11 – Alternative “swap” model kH.9.CO2 interpretations of Vasu *et al.* (2011) values

Temp. (K)	Pres. (atm)	GRI-VDH Vasu <i>et al.</i> (2011) ^{a,b}	GRI-Mech 3.0 (1999) ^{a,c}	Li <i>et al.</i> (2007) ^{a,d}	Burke <i>et al.</i> (2012) ^{a,d}	Kéromnès <i>et al.</i> (2013) ^a
At Falloff - kH.9.CO2(T,P)						
1277	8.41	8.43 × 10 ¹⁵	5.85 × 10 ¹⁵	7.88 × 10 ¹⁵	7.88 × 10 ¹⁵	8.35 × 10 ¹⁵
1291	7.59	8.50 × 10 ¹⁵	5.91 × 10 ¹⁵	7.97 × 10 ¹⁵	7.94 × 10 ¹⁵	8.43 × 10 ¹⁵
1305	8.16	9.80 × 10 ¹⁵	7.21 × 10 ¹⁵	9.23 × 10 ¹⁵	9.17 × 10 ¹⁵	9.67 × 10 ¹⁵
Low Pressure Limit - kH.9.CO2 _{LPL} (T)						
1277	---	9.04 × 10 ¹⁵	---	9.63 × 10 ¹⁵	9.63 × 10 ¹⁵	9.19 × 10 ¹⁵
1291	---	9.10 × 10 ¹⁵	---	9.69 × 10 ¹⁵	9.65 × 10 ¹⁵	9.26 × 10 ¹⁵
1305	---	1.05 × 10 ¹⁶	---	1.13 × 10 ¹⁶	1.13 × 10 ¹⁶	1.07 × 10 ¹⁶

^a All rate coefficients in this table are for termolecular elementary reactions, in units of cm⁶/mol²/s. ^b Table 4.10, Hong *et al.* basis at the LPL. ^c kH.9.M expressions are all LPL-referenced in GRI-Mech 3.0 regardless of actual pressure. ^d These models reference all kH.9.M expressions to either M = Ar or N₂. M = Ar expressions used in present determinations. Both models share same LPL, but differ in HPL and falloff behavior.

Table 4.12 – Vasu *et al.* (2011) kH.9.CO2 determinations based on Consensus kH.9.Ar expressions

Temp. (K)	Pres. (atm)	Vasu <i>et al.</i> (2011) ^{a,b}	Consensus (min. bound) ^{a,c,d}	Consensus ^{a,c}	Consensus (max. bound) ^{a,c,d}
At Falloff - kH.9.CO2(T,P)					
1277	8.41	8.43×10^{15}	7.38×10^{15}	8.14×10^{15}	8.92×10^{15}
1291	7.59	8.50×10^{15}	7.45×10^{15}	8.23×10^{15}	8.98×10^{15}
1305	8.16	9.80×10^{15}	8.75×10^{16}	9.52×10^{15}	1.03×10^{16}
Low Pressure Limit - kH.9.CO2 _{LPL} (T)					
1277	---	9.04×10^{15}	8.33×10^{15}	9.20×10^{15}	1.01×10^{16}
1291	---	9.10×10^{15}	8.42×10^{15}	9.29×10^{15}	1.01×10^{16}
1305	---	1.05×10^{16}	9.89×10^{16}	1.08×10^{16}	1.16×10^{16}

^a All rate coefficients in this table are for termolecular elementary reactions, in units of $\text{cm}^6/\text{mol}^2/\text{s}$. ^b Table 4.10, Hong *et al.* basis at the LPL. ^c Consensus falloff correction of 11.5% applied uniformly to kH.9.CO2(T,P) determinations to derive LPL values. ^d Minimal and maximal Consensus bounds are based on $\pm 25\%$ of nominal kH.9.Ar Consensus (see discussion of Equation 4.9).

Table 4.13 – Alternative whole-model determinations of kH.9.CO2 from the Vasu *et al.* (2011) 1277 K experiment

Temp. (K)	Pres. (atm)	GRI-VDH Vasu <i>et al.</i> (2011) ^{a,b}	GRI-Mech 3.0 (1999) ^{a,c}	Li <i>et al.</i> (2007) ^{a,d}	Burke <i>et al.</i> (2012) ^{a,d}	Kéromnès <i>et al.</i> (2013) ^a
At Falloff - kH.9.CO2(T,P)						
1277	8.41	8.43 × 10 ¹⁵	5.85 × 10 ^{15**}	7.75 × 10 ¹⁵	4.38 × 10 ¹⁵	9.04 × 10 ¹⁵
Low Pressure Limit - kH.9.CO2 _{LPL} (T)						
1277	---	9.04 × 10 ¹⁵	6.24 × 10 ^{15**}	9.47 × 10 ¹⁵	5.22 × 10 ¹⁵	9.98 × 10 ¹⁵

^a All rate coefficients in this table are for termolecular elementary reactions, in units of cm⁶/mol²/s. ^b Table 4.10, Hong *et al.* basis at the LPL. ^c kH.9.M expressions are all LPL-referenced in GRI-Mech 3.0 regardless of actual pressure. ^d These models reference all kH.9.M expressions to either M = Ar or N₂. M = Ar expressions used in present determinations. Both models share same LPL, but differ in HPL and falloff behavior. In addition, the Burke *et al.* model lacks reaction C.1. ^{**} An alternative interpretation treats the optimal GRI-Mech 3.0 determination as a falloff termolecular value for kH.9.CO2(T,P); then kH.9.CO2_{LPL} is found by falloff correction using the same Hong *et al.* LPL basis as applied to GRI-VDH kH.9.CO2(P) determinations.

Table 4.14 – Summary of kH.9.CO2 determinations for the Vasu *et al.* (2011) 1277 K experiment

At Falloff - kH.9.CO2(T,P) ^a	Low Pressure Limit - kH.9.CO2 _{LPL} (T) ^a
9.04 × 10 ¹⁵	1.01 × 10 ¹⁶
8.92 × 10 ¹⁵	9.98 × 10 ¹⁵
<u>8.43 × 10¹⁵</u>	9.63 × 10 ¹⁵
8.35 × 10 ¹⁵	9.63 × 10 ¹⁵
8.14 × 10¹⁵	9.48 × 10 ¹⁵
7.88 × 10 ¹⁵	9.47 × 10 ¹⁵
7.88 × 10 ¹⁵	9.20 × 10¹⁵
7.75 × 10 ¹⁵	9.19 × 10 ¹⁵
7.38 × 10 ¹⁵	<u>9.04 × 10¹⁵</u>
5.85 × 10 ¹⁵	8.33 × 10 ¹⁵
4.38 × 10 ¹⁵ **	6.24 × 10 ¹⁵
	5.22 × 10 ¹⁵ **

^a All rate coefficients in this table are for termolecular elementary reactions, in units of cm⁶/mol²/s. ** Model used for determination lacks secondary reaction C.1.

This table lists all unique kH.9.CO2 rate coefficient determinations appearing in Tables 4.10-4.13, derived from alternative interpretations of the 1277 K experiment. Italicized values are nominal values attributed to the original Vasu *et al.* interpretation; values in bold are recommended Consensus determinations. Entries in the same row do not necessarily correspond to a falloff-LPL pair.

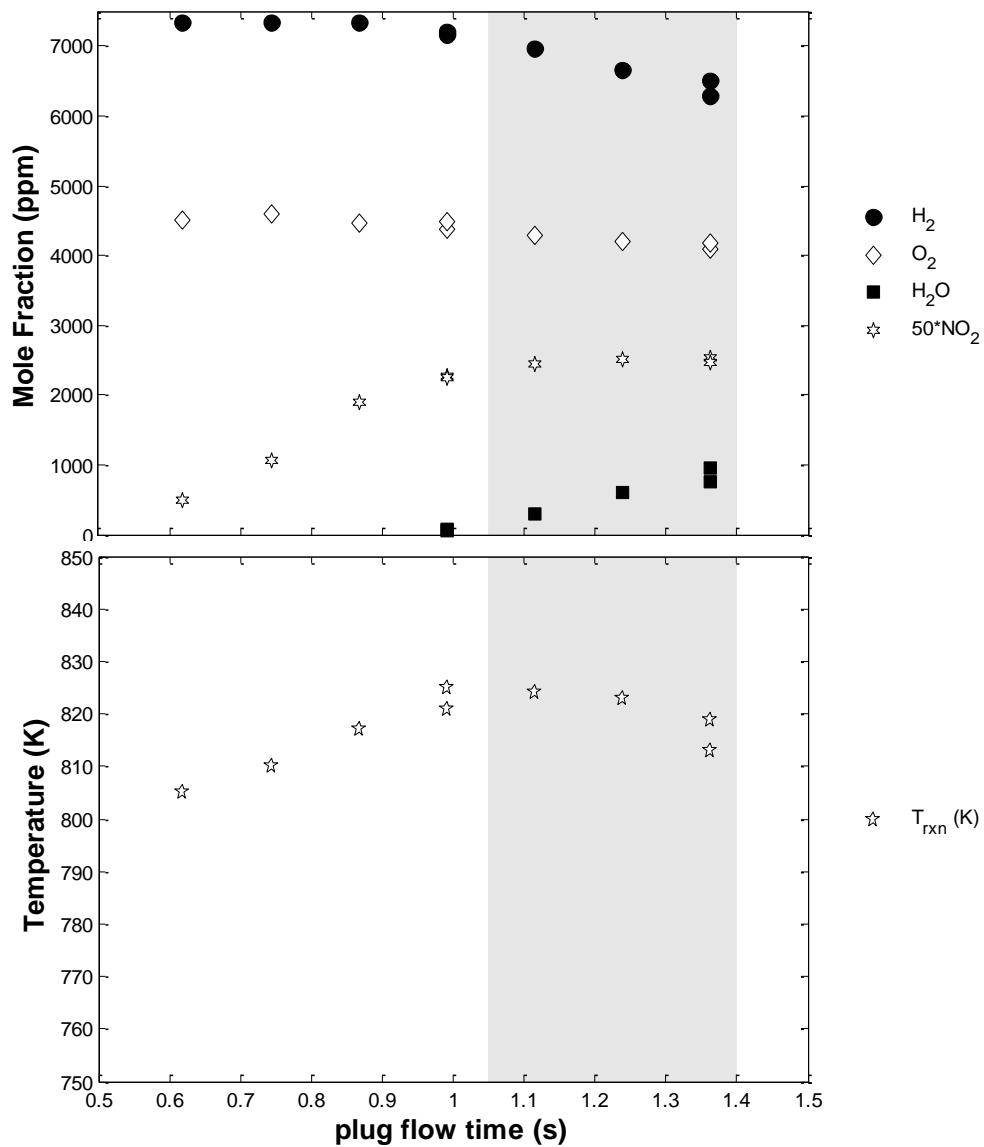


Figure 4.1 – Measured species and temperature profiles for HPLFR QSSP Experiment 4/I.

Nominal initial reaction conditions are 7253/4533/98 ppm H₂/O₂/NO in balance CO₂ bath gas at 8.0 atm. The water profile is computed based on the H atom balance. Temperature is nominally 820 K over the quasi-steady plateau indicated by shading, and the reaction proceeds essentially isothermally.

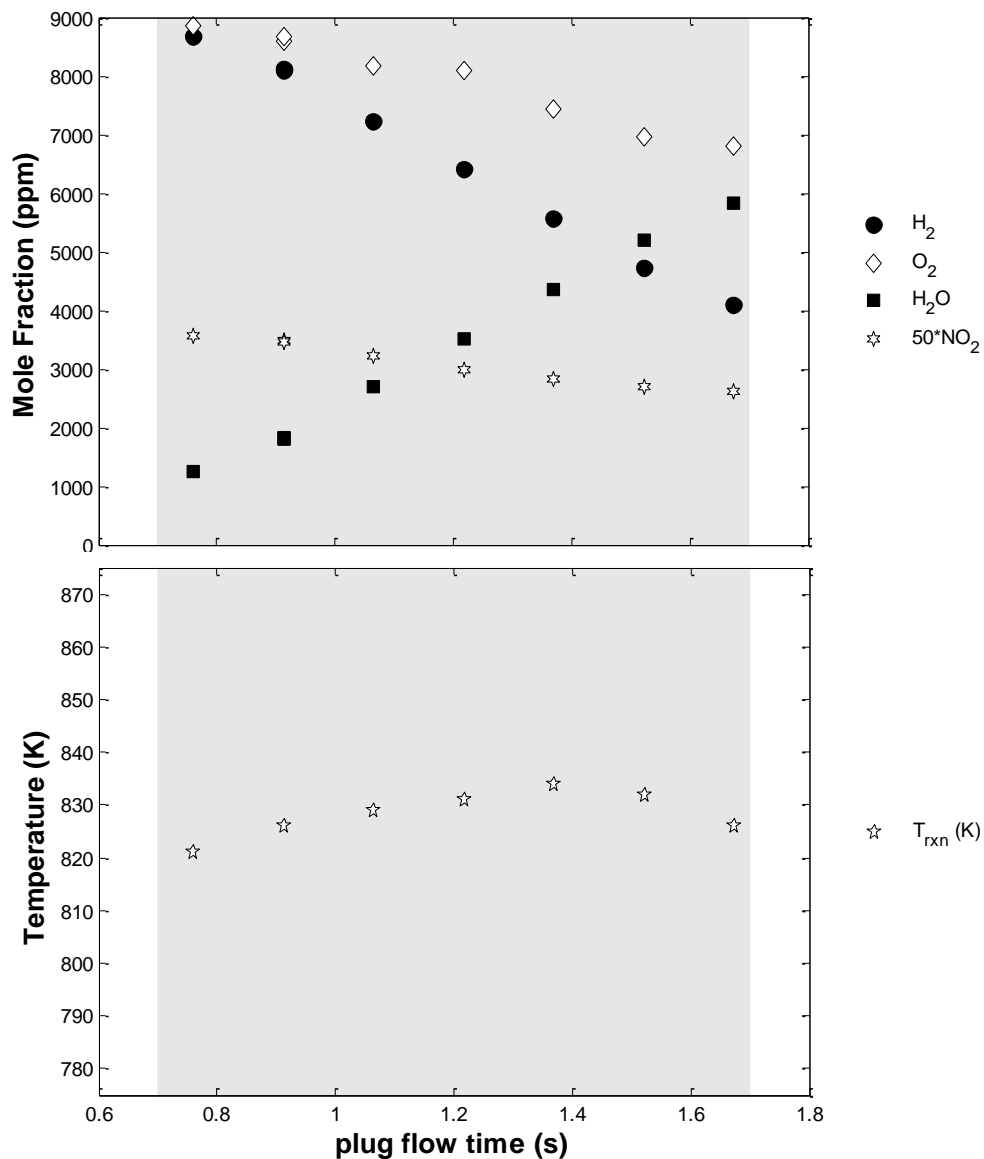


Figure 4.2 – Measured species and temperature profiles for HPLFR QSSP Experiment 4/II.

Nominal initial reaction conditions are 9922/9641/97 ppm H₂/O₂/NO in balance CO₂ bath gas at 6.0 atm. The water profile is computed based on the H atom balance. Temperature is nominally 828 K over the quasi-steady plateau indicated by shading, which in this case, includes the entire measurement set. The reaction proceeds essentially isothermally.

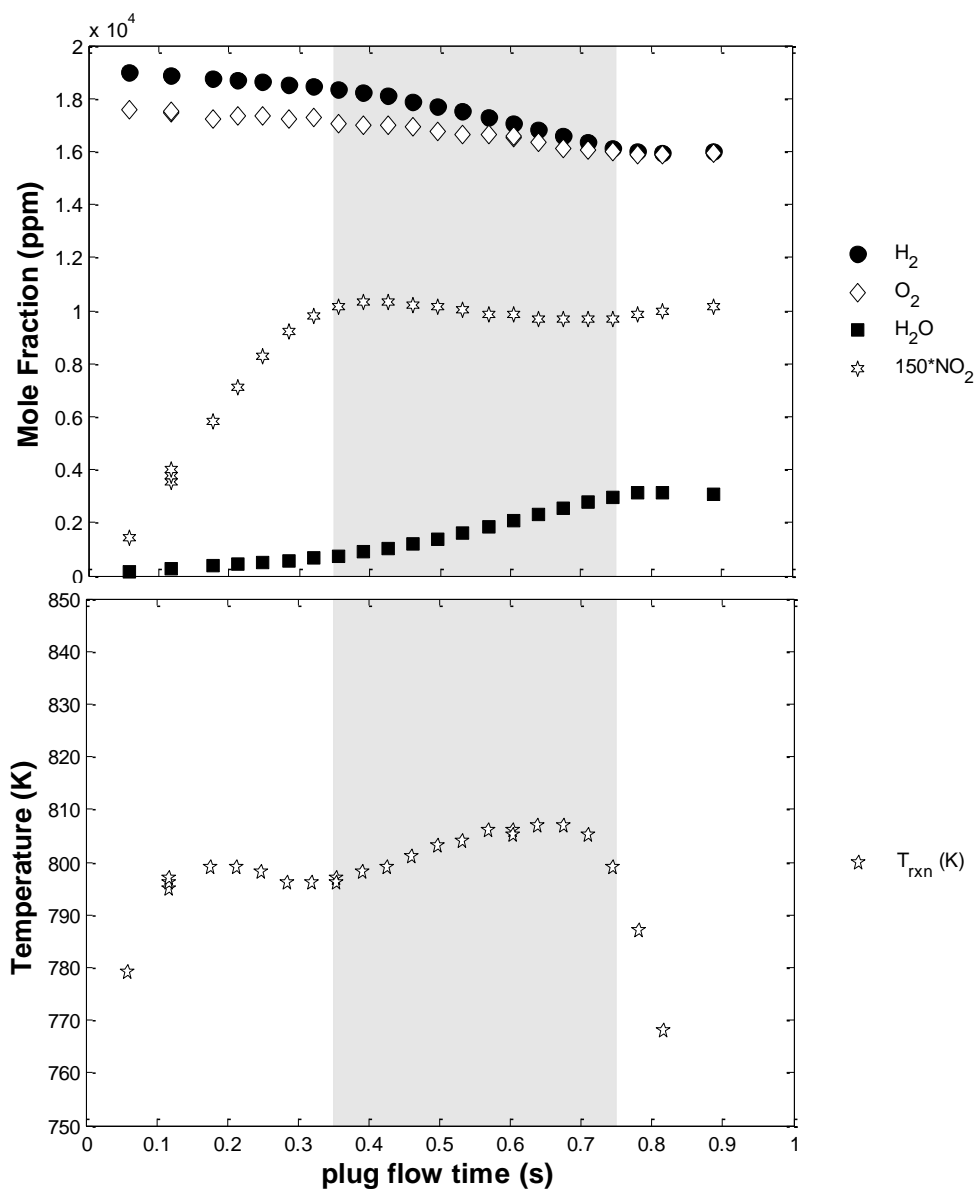


Figure 4.3 – Measured species and temperature profiles for HPLFR QSSP Experiment 4/IVa.

Nominal initial reaction conditions are 19093/17589/94 ppm H₂/O₂/NO in balance CO₂ bath gas at 2.5 atm. The water profile is computed based on the H atom balance. Temperature is nominally 802 K over the quasi-steady plateau indicated by shading, and the reaction proceeds essentially isothermally.

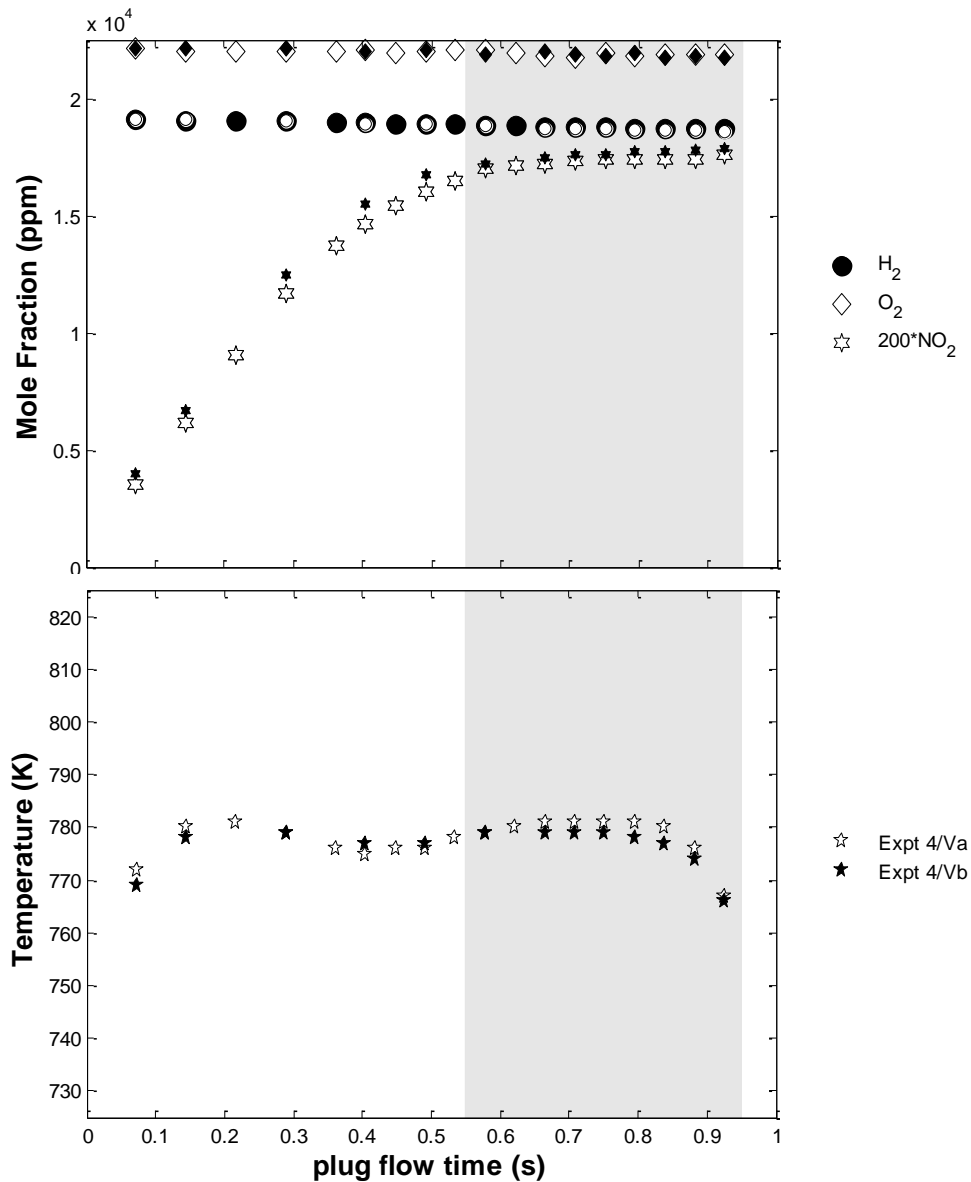


Figure 4.4 – Measured species and temperature profiles for HPLFR QSSP Experiments 4/Va and 4/Vb.

Nominal initial reaction conditions are 19280/21904/93 ppm H₂/O₂/NO in balance CO₂ bath gas at 2.5 atm. Temperature is nominally 777 K over the quasi-steady plateau indicated by shading, and the reaction proceeds essentially isothermally. Experiments 4/Va and 4/Vb were conducted back to back, and the present overlap of measured profiles requires no relative shifting. For species profiles, small markers correspond to Experiment 4/Va, and large markers correspond to Experiment 4/Vb. Marker shading has been inverted between 4/Va and 4/Vb for contrast.

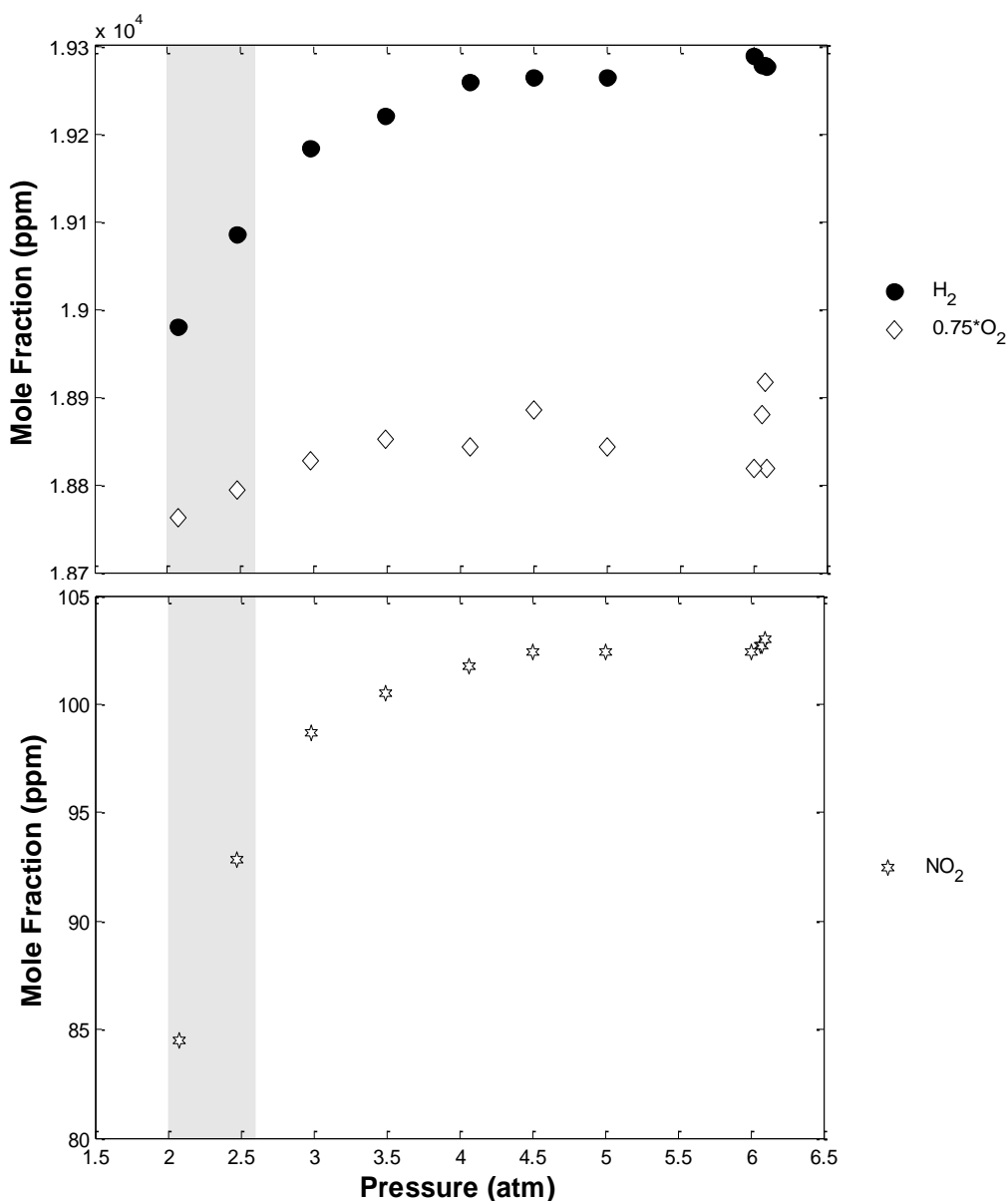


Figure 4.5 – Measured species profiles for HPLFR QSSP Experiment 4/III.

Nominal initial reaction conditions are 19298/25564/100 ppm H₂/O₂/NO in balance CO₂ bath gas for pressures ranging between 2.08 and 6.10 atm and a nominal temperature of 796 K. Measurements were acquired at a nominal axial reactor position of 55 cm except for those at P ~ 6 atm, which were taken over the range 40-55 cm to demonstrate relative invariance of the axial species profiles for these conditions.

Above ~3 atm, the QSSP NO_x cycle appears to be saturated (full conversion of NO→NO₂ and negligible H₂/O₂ consumption), as further demonstrated by plug flow modeling in Figure 4.7. Accordingly, the quasi-steady plateau region indicated by shading is limited to the points acquired at pressures less than 3 atm.

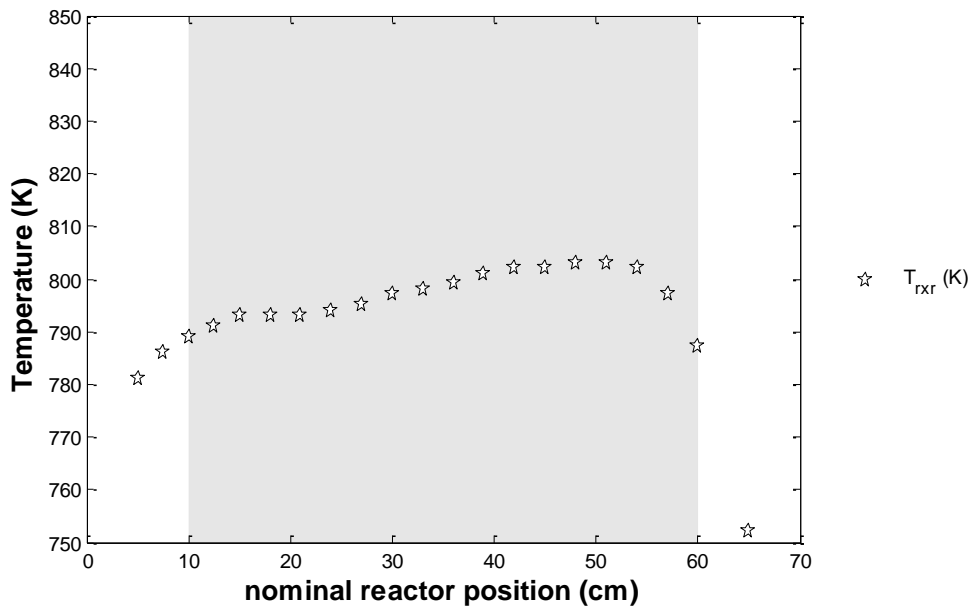


Figure 4.6 – Measured temperature profile for HPLFR QSSP Experiment 4/III.

Temperature is nominally 796 (± 7.5) K over the portion of the reactor test section indicated by shading. Diagnostic experiments indicate that this thermal profile is not sensitive to reactor pressure. The present temperature profile was acquired at 3.0 atm, and present species measurements (Figure 4.5) were acquired at 40-55 cm. Due to the minimal heat release associated with observed reactivity at the conditions of Experiment 4/III, the reaction may be considered to have occurred under essentially isothermal conditions.

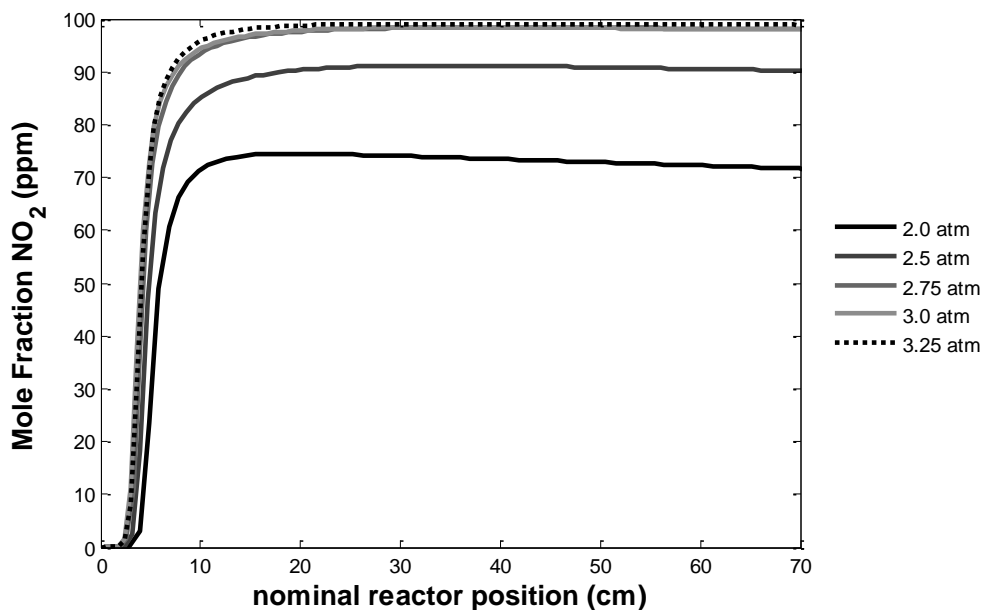


Figure 4.7 – Simulated NO₂ profiles for HPLFR QSSP Experiment 4/III.

Experiment 4/III seeks to demonstrate that the QSSP condition may permit kH.9.M rate coefficient determination even when the flow field is not experimentally well-characterized, such as in the experiments of Ashman (1999). Because the measurements of the present experiment are not spatially resolved (except partially at ~6 atm), both numerical simulation and kinetic intuition are required to deduce the behavior of the reacting flow at the unresolved locations in the HPLFR test section.

Present simulation results are based on a hybrid kinetic model using the H₂ chemistry of Li *et al.* (2004), the NO_x submodel of Mueller *et al.*, (1999b), the present kN.1_{VRC-FTST} recommendation (Section 3.2.2), and an assumed CO₂ collisional efficiency of 4.5 relative to Ar in the kH.9.M expression employed in the kinetic model. This collisional efficiency is roughly consistent with the final recommended value suggested elsewhere in this chapter. The QSSP saturation pressure threshold – roughly 2.75-3.0 atm at present reaction conditions – is insensitive to reasonable parametric variations in assumed kH.9.M CO₂ collisional efficiency, kN.1, and initial NO doping level.

These plug flow simulations corroborate saturation of the QSSP NO_x cycle evident in the experimental species data presented in Figure 4.5, and they support the decision to use only the data acquired at pressures significantly below 3 atm for QSSP rate coefficient determination. More computationally intensive two-dimensional simulations such as shown in Figure 3.13 appear to be unnecessary for present interpretation since the predicted NO→NO₂ induction length is short and well upstream of the sampling point.

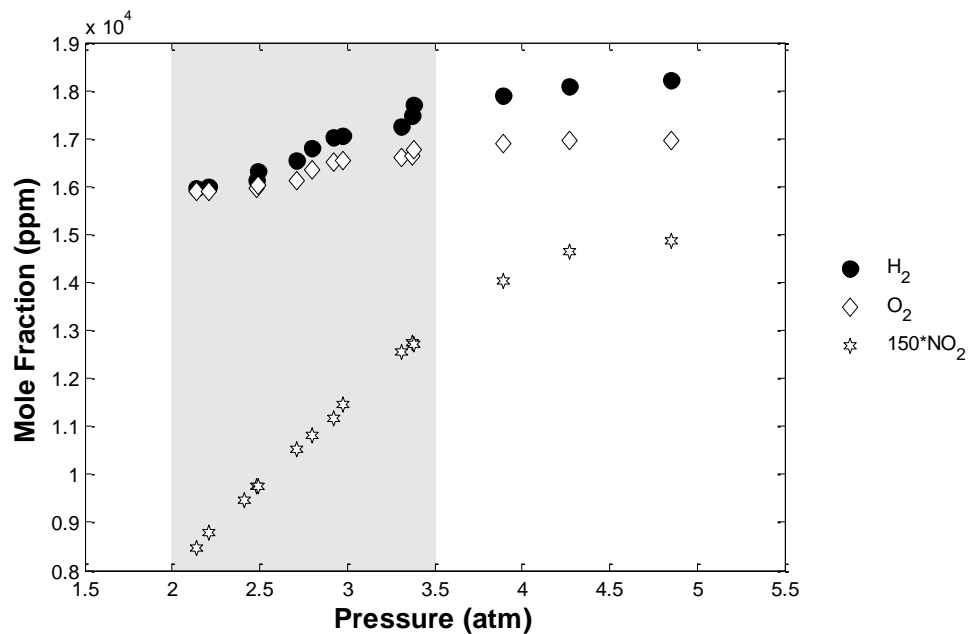


Figure 4.8 – Measured species profiles for HPLFR QSSP Experiment 4/IVb.

Nominal initial reaction conditions are 19093/17589/94 ppm H₂/O₂/NO in balance CO₂ bath gas. The essentially isothermal, pressure-independent temperature profile is 798 (±7.5) K in the reactor test section, which compares favorably with the temperature profile from Experiment 4/IVa, which was conducted immediately prior to Experiment 4/IVb. The present temperature profile was acquired at 2.51 atm, and present species measurements were acquired at a nominal axial reactor location of 57 cm, which should be well downstream of the NO→NO₂ induction length.

Above ~3.5 atm, the QSSP NO_x cycle appears to approach saturation. Accordingly, the quasi-steady plateau region indicated by shading is limited to the points acquired at pressures less than 3.5 atm.

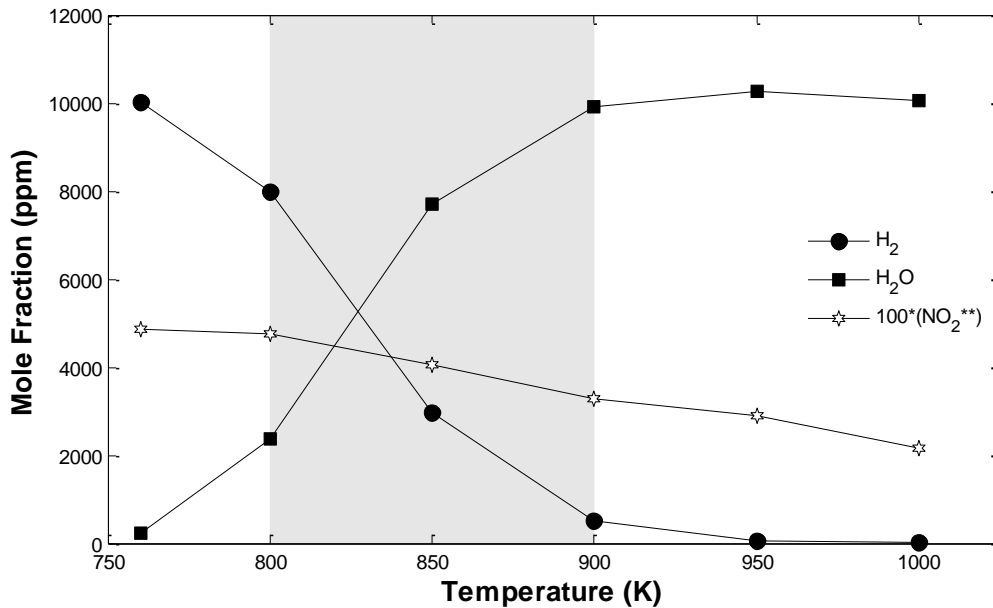


Figure 4.9 – Results from Ashman’s (1999) M = CO₂ laminar flow reactor experiments.

Nominal initial reaction conditions are 10000/30000/100 ppm H₂/O₂/NO in balance CO₂ bath gas at atmospheric pressure, and the reactor is effectively isothermal. Mass flow rate is fixed such that the plug flow residence time in the reactor is 1.0 second at 773 K. Oxygen was not directly quantified in these experiments, so O₂(T) can be computed by atom balance.

Lines have been added between the points in figure for clarity. The shaded region corresponds to experimental data that have been reinterpreted by (extended) QSSP analysis as described in the text and Table 4.7.

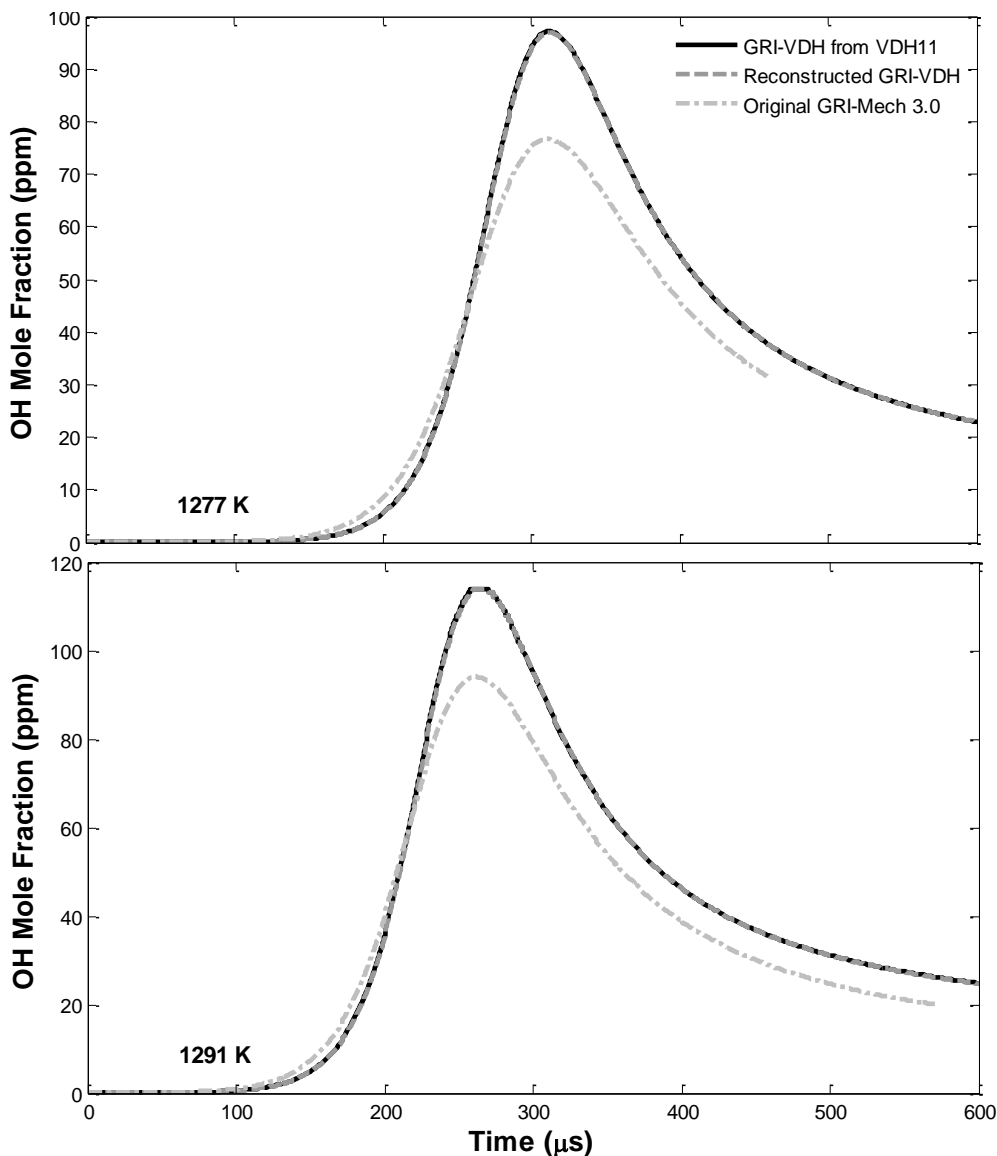


Figure 4.10 – Comparison of simulated OH profiles from GRI-VDH, present GRI-VDH reconstruction, and GRI-Mech 3.0 kinetic models

The root mean square deviation (RMSD) between the original GRI-VDH and reconstructed GRI-VDH curves is ~ 0.35 ppm for the 1277 K conditions of Vasu *et al.* (top) and ~ 0.23 ppm for the 1291 K conditions (bottom). For present purposes, these models are considered to match “exactly.”

Comparison of the GRI-Mech 3.0 and GRI-VDH curves serves to demonstrate the effect of the secondary chemistry changes adopted in transformation of GRI-Mech 3.0 into GRI-VDH. All simulations use the constant $k_{H.9.CO2}$ values of VDH11 for the nominal indicated temperature. Simulations for both GRI-VDH and its reconstruction are effectively time-shifted by the same experiment-specific $[H]_0$ doping levels indicated by Vasu *et al.*, while the GRI-Mech 3.0 curves are shifted to match the other curves at the point of 50% peak experimental OH at 257.5 μs and 219 μs for 1277 K and 1291 K conditions, respectively. Though not shown here, similar modeling results are evident for the 1305 K case. The GRI-VDH simulations were provided by S.S. Vasu (personal communication 2011).

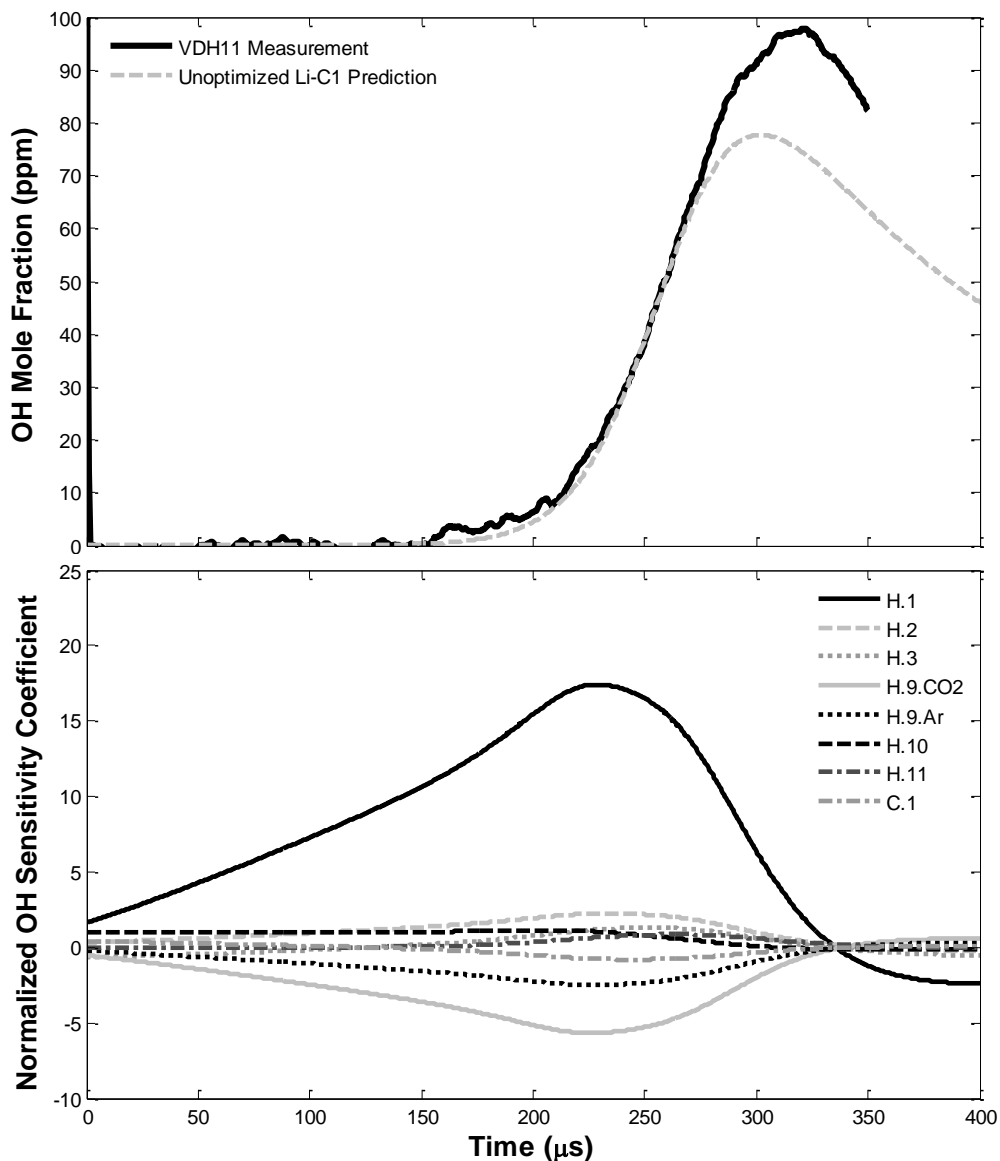


Figure 4.11 – Li-C₁ model-predicted OH profile and OH sensitivity for the 1277 K experiment of Vasu *et al.*

Simulations are shifted 63 μs to match the experimental measurements (top) at the point of 50% peak experimental OH (257.5 μs). Sensitivities to H.9.CO₂ and H.9.Ar are based on linear allocation of the computed H.9.M sensitivity according to the collisional efficiency of CO₂ relative to Ar ($\epsilon_{\text{CO}_2/\text{Ar}}$) used in the Li-C₁ model; therefore, the sum of the H.9.CO₂ and H.9.Ar curves gives overall sensitivity to H.9.M excluding a minor correction for gases other than CO₂ and Ar.

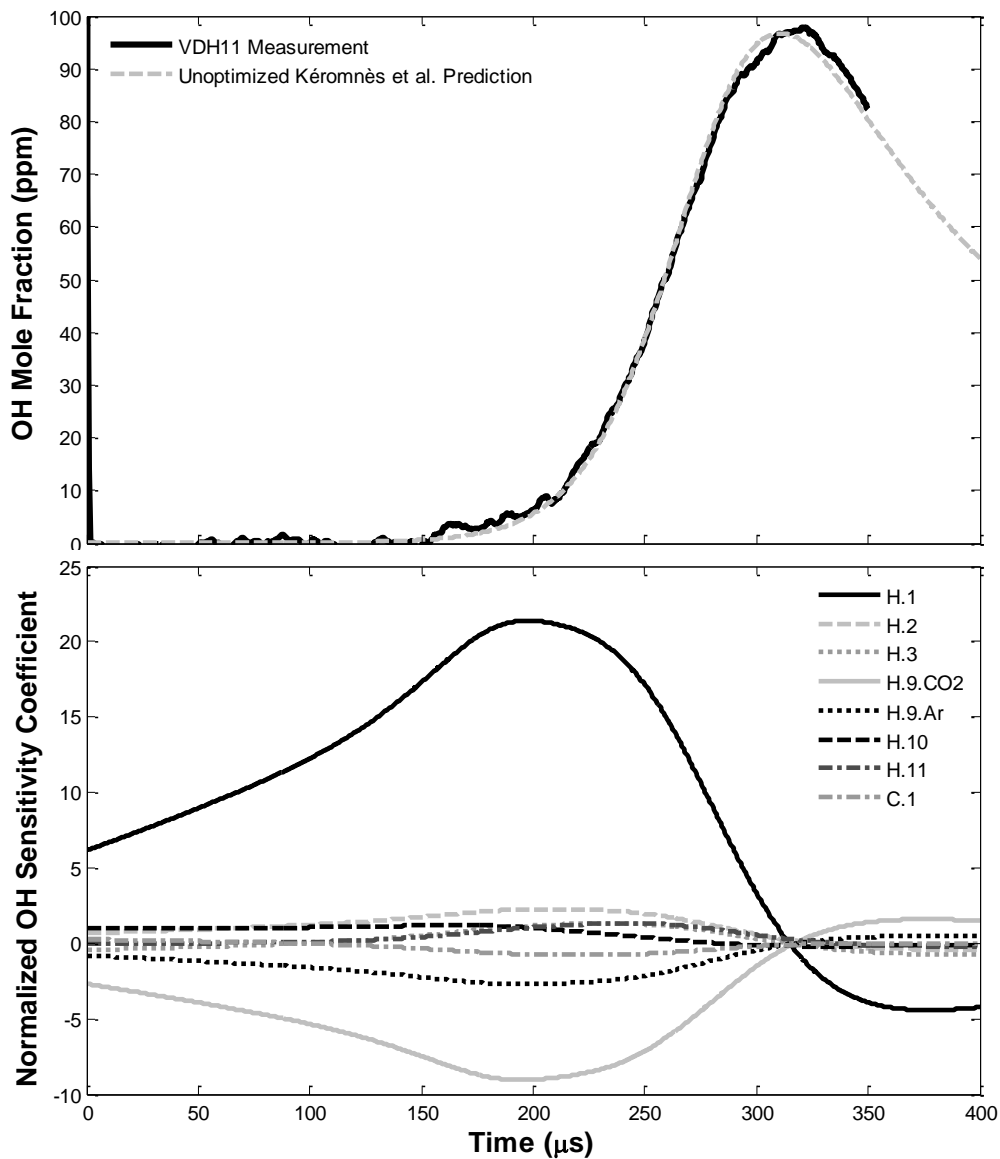


Figure 4.12 – Kéromnès *et al.* model-predicted OH profile and OH sensitivity for the 1277 K experiment of Vasu *et al.*

Simulations are shifted 131.5 μs to match the experimental measurements (top) at the point of 50% peak experimental OH (257.5 μs).

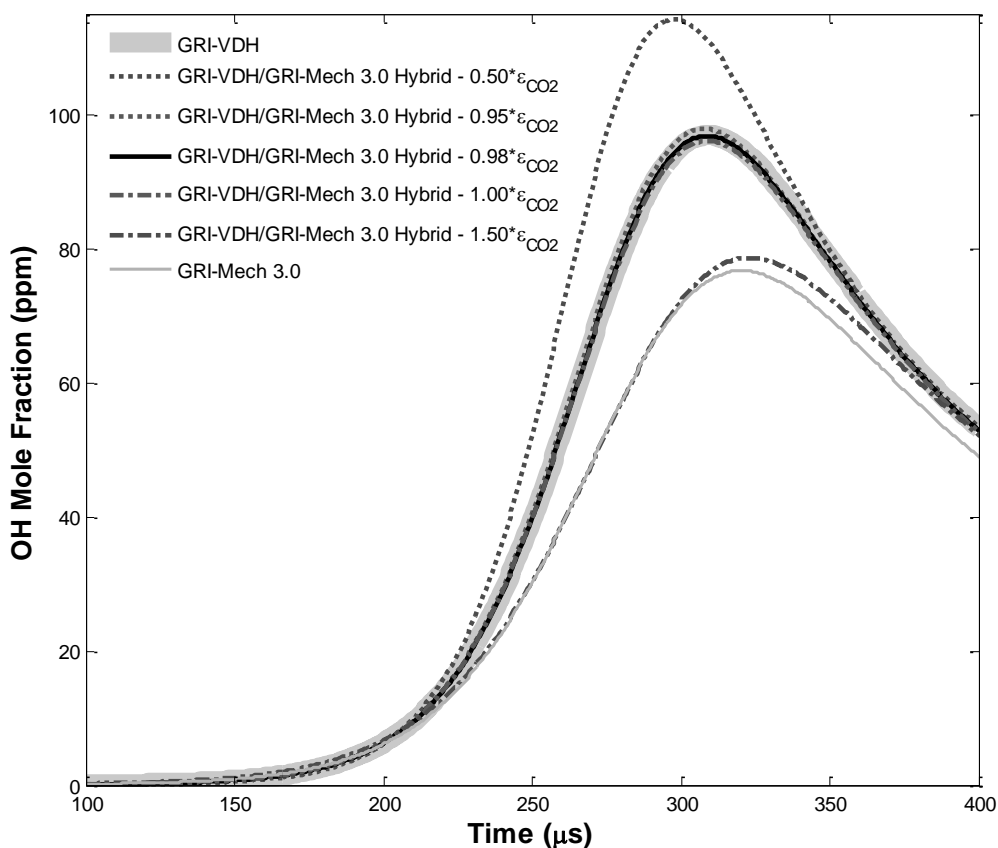


Figure 4.13 – Predicted OH profiles from iteration of $k_{H.9.CO2}$ values after $k_{H.9.M}$ swapping from GRI-Mech 3.0 into GRI-VDH, 1277 K experiment of Vasu *et al.*

The curve corresponding to the hybrid GRI-VDH/GRI-Mech 3.0 $0.98 \times \epsilon_{CO2}$ model has been shifted to match the GRI-VDH curve at the point of 50% peak experimental OH (257.5 μs). The other hybrid models have been shifted to indicate convergence to the same value of OH mole fraction at long times. The GRI-Mech 3.0 curve has been shifted such that it overlaps the GRI-VDH/GRI-Mech 3.0 - $1.50 \times \epsilon_{CO2}$ curve over the time domain of peak signal-to-noise ratio and rate coefficient sensitivity.

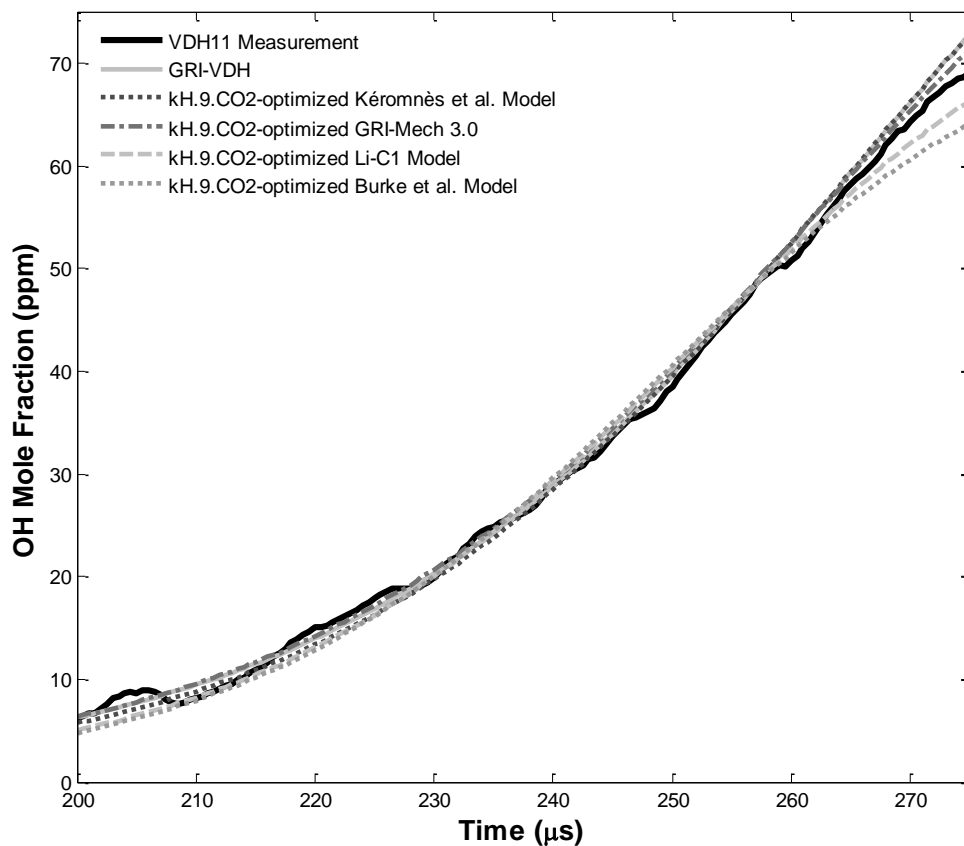


Figure 4.14 – Predicted OH profiles for several entire literature kinetic models with kH.9.CO₂-optimized to match the experimental OH profile from the 1277 K experiment of Vasu *et al.*

Simulations are shifted to match the experimental measurements (top) at the point of 50% peak experimental OH (257.5 μs). Corresponding kH.9.CO₂ values are listed in Table 4.13.

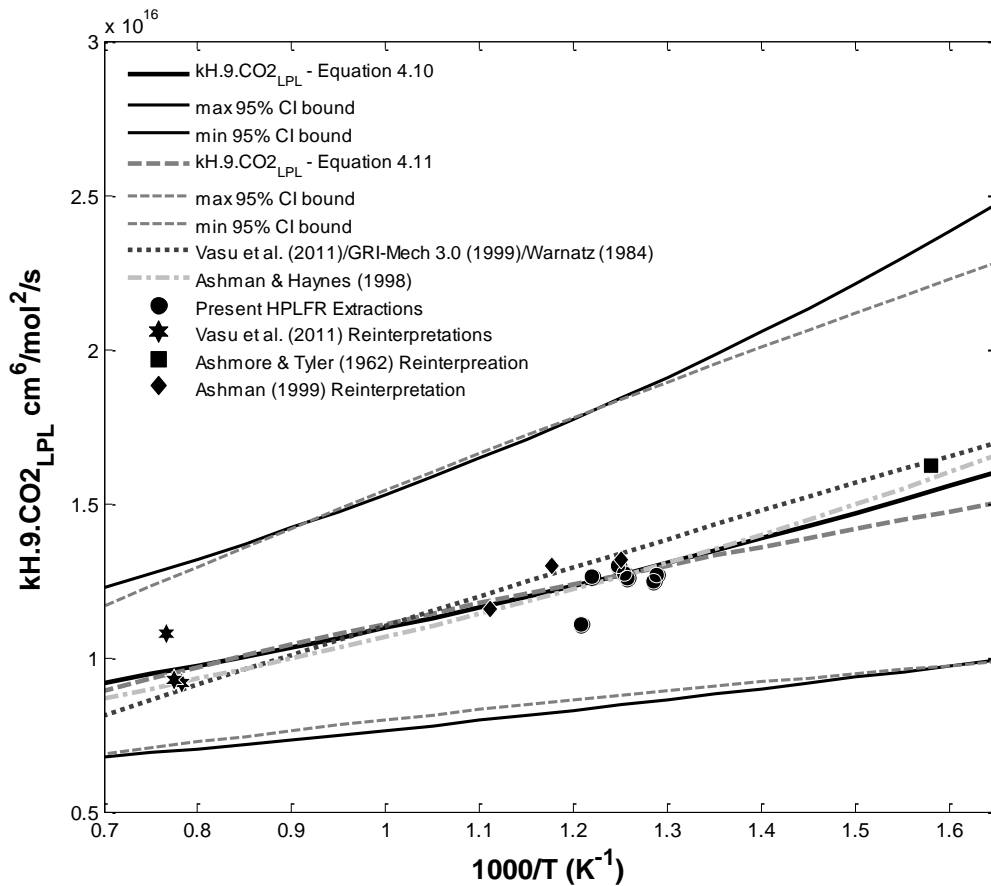


Figure 4.15 – Comparison of final $k_{H.9.CO2_{LPL}}$ rate coefficient expression recommendations with literature expressions and present determinations/reinterpretations of experimental measurements.

Part II

Chapter 5: An Updated Combustion Kinetic Model for Syngas Fuels Based on Recent Theory and Experiment

Synthesis gas (syngas) is a high H_2/CO content chemical product of the incomplete oxidation of traditional (natural gas, petroleum, coal) and bio/alternative energy feedstocks. As its name suggests, syngas can itself be used as a feedstock for synthesis of more complex chemicals, some of which are presently of interest as transportation fuels. There has also been recent and substantial interest in high H_2/CO content syngas as a fuel for next-generation stationary power production in Integrated Gasification Combined Cycle (IGCC) and bio/waste-derived energy applications.

Extensive fundamental, applied, and patent literature on syngas-related topics exists as part of an ever-increasing database, so, rather than presenting an exhaustive review of this voluminous literature, the following three observations serve to concisely motivate the present discussions:

- 1) Industry demands predictive kinetic-transport models for syngas combustion to aid in development of next-generation power generation schemes, particularly those operating at higher (tens of bar) pressures;
- 2) Comparison of recent laminar burning rate measurements to existing kinetic model predictions for systems of hydrogen and syngas mixtures reveals widespread inability for existing models to accurately predict burning rates at application-relevant higher pressures and lower flame temperatures (*e.g.*, Burke *et al.*, 2010; Santner *et al.*, 2013); and
- 3) The H_2/CO kinetic model provides a requisite hierarchical foundation, discussed in Chapter 1, for understanding and predicting nearly all aspects of the combustion behavior of larger hydrocarbon, oxygenate, and related species. Uncertainty in this core chemistry translates into significantly larger uncertainties at the subordinate levels of hierarchy corresponding to more complex fuels.

Towards addressing issues implicit in the preceding observations, the present focus is on updating the existing CO combustion kinetic submodel produced as part of the so-called C_1 model of Li *et al.* (2007, henceforth also called the Li- C_1 model), which also includes kinetics for the CH_2O and CH_3OH hierarchical ranks. The present model validation target set includes the Li- C_1 model validation subset relevant for CO oxidation but has also been augmented with targets at higher pressures or at conditions with significant H_2O , CO_2 , or O_2 concentrations. Practically, these extended validation cases consider

chemical aspects of syngas combustion sensitized by emission control strategies such as exhaust gas recirculation (EGR), steam injection, or oxy-fuel combustion. These additional validation cases extend the predictive performance of the new model to a more comprehensive set of conditions wherein the diverse chemical environments sensitize kinetic interactions in ways that those considered in the Li-C₁ model validation subset do not.

However, it is not the intention of this thesis to provide a comprehensive demonstration of the predictions of the kinetic model developed here against a very large number of validation cases or the predictions other kinetic models (unlike, for example, the relatively recently published kinetic models of Burke *et al.* (2012) for H₂ oxidation or Kéromnès *et al.* (2013) for syngas oxidation). This is in part due to the tight coupling between CO and H₂ combustion chemistry at conditions representative of most literature experimental observables used for validation, as well as at applications-relevant conditions. The apparent performance of the CO chemistry submodel depends significantly on the H₂ chemistry submodel; in particular, model assessment from the traditional complex kinetic model “validation” paradigm for CO combustion chemistry primarily reflects the ability for the H₂ submodel to properly populate the OH radical pool that then oxidizes CO via reaction C.1 ($\text{CO} + \text{OH} \leftrightarrow \text{CO}_2 + \text{H}$).

Instead, the purpose of the discussions below is to highlight and support updates to a more isolated CO chemistry submodel compiled as a product of this thesis. Within the hierarchical kinetic model paradigm discussed in Chapter 1 and below, such updates should be considered as improvements to the Li-C₁ CO chemistry submodel irrespective of its coupling to chemistry in the H₂ rank. While these updates are based on recent theory and/or experiment, it is important to note that continual contributions are being made to relevant aspects of CO combustion kinetics. Consequently, some advances in CO-related chemistry made contemporary to the writing of this thesis may not be reflected herein.

5.1 Kinetic Model Development Overview

Figure 5.1 depicts a conceptual scheme to complement the following overview of the present H₂/CO model development. The Li-C₁ model (2007) serves as the basis for the present kinetic model updates, although it may be viewed itself as an update and consolidation of previous kinetic models (*e.g.*, Li *et al.*, 2004; Held & Dryer, 1998). This C₁ model was developed to describe combustion chemistry of

H₂/CO/CH₂O/CH₃OH hierarchies and serve as submodel core for hierarchically subordinate species such as ethanol (Haas *et al.*, 2009), dimethyl ether (Zhao *et al.*, 2008), or jet fuel surrogate fuels (Dooley *et al.*, 2010). It can be essentially divided into chemistry submodels for H₂ assumed from Li *et al.* (2004) and CO/CH₂O/CH₃OH developed for the 2007 Li *et al.* C₁ study.

Recently Burke *et al.* (2012) have updated the Li *et al.* (2004) H₂/O₂ chemistry submodel to consider recent experimental and theoretical improvements in thermochemistry, transport, and rate coefficient parameters for the H₂/O₂ system. Models produced from these studies may also herein be referred to as the Burke-H₂ and Li-H₂ models, respectively. The Burke-H₂ model was developed, in part, to address widespread kinetic model deficiencies in the prediction of H₂ laminar burning rates at the higher pressures and lower flame temperatures relevant to energy conversion applications. It predicts well the targets utilized by the predecessor Li-H₂ model validation, as well as several more recently produced targets appearing in the literature.

According to the recent study of Zsély *et al.* (2013), the Burke-H₂ model demonstrates comparable, if not superior, predictive capabilities relative to several other recent and commonly used H₂/O₂ combustion kinetic submodels (*e.g.*, Hong *et al.*, 2011; Konnov, 2008; Smith *et al.*, 1999). Although there is little doubt that representations of the H₂/O₂ core chemistry will continue to evolve, the Burke-H₂ model has been selected as the representative foundational H₂ kinetic submodel for the present H₂/CO submodel update since it provides a static, robustly constructed, and validated parameter set on which to evaluate and update CO-rank chemistry parameters inherited from the Li-C₁ model. By hierarchical design, this choice of Burke-H₂ core chemistry limits the present scope of H₂/CO kinetic model development and validation primarily to the CO chemistry hierarchy – only minimal consideration for the isolated H₂ hierarchical rank will be subsequently considered at elementary reaction-level detail in the present work.

The present CO submodel update compiles a set of *essentially untuned* thermochemistry, transport, and rate coefficient parameters from available high-quality, critically evaluated experimental and theoretical studies. This approach minimizes dependence of the present CO chemistry parameters on the choice of base H₂ kinetic model. *The present CO submodel should be considered as an*

independent, unoptimized, fundamentally-based compilation of CO oxidation chemistry, as further elaborated upon in the following sections.

In the present work, the CO submodel remains intentionally unoptimized by collective adjustment of rate coefficient parameterizations since non-unique optima exist depending on assumed H₂ base model, optimization method, and assumptions employed – especially assumptions regarding application-specific cost functions (*i.e.*, models developed specifically for ignition, higher pressures, *etc.*). Instead, the present validation database and “untuned” CO submodel serve as fixed points to which advanced mathematical (*e.g.*, You *et al.*, 2011; Turányi *et al.*, 2012) or physics-based multi-scale informatics (Burke *et al.*, 2013) techniques for kinetic model optimization and uncertainty minimization may be applied. Sections 5.2, 5.3, and 5.4 below detail present kinetic model updates to the assumed base Li-C₁ and Burke-H₂ thermochemistry, transport, and reaction rate coefficient parameter sets respectively. Section 5.4.7 specifically discusses reactions involving the HOCO molecule.

5.2 Thermochemistry Parameters

Thermochemistry parameterizations for heat capacity, enthalpy of formation, and entropy for chemical species in complex kinetic models explicitly define equilibrium relationships among these species and the conditions of the simulation environment. In conjunction with forward reaction rate coefficients, thermochemistry also defines the reverse reaction rate coefficients through equilibrium constants. Moreover, thermochemistry controls the combustion environment through thermophysical properties such as heat capacity and standard reaction enthalpy change, which directly couple into important observables such as rate of heat release and peak flame temperature. Consequently, in the development of accurate, predictive kinetic models, it is important to include accurate thermochemistry parameterizations as a subset of the kinetic model parameters.

The thermochemistry parameterizations used in the present model derive exclusively from a recent update to the critically evaluated Third Millennium Thermodynamic Database (TMTD, Goos *et al.*, 2012; further discussed in Burcat & Ruscic, 2005), which is periodically informed and updated by the Active Thermochemical Tables (ATcT) (*e.g.*, Ruscic *et al.*, 2004), among many other independent other sources. These parameterizations are qualitatively rated by TMTD stewards for their associated

accuracy, and parameters adopted in this H₂/CO model update have been accorded “A” (most accurate) ratings, save for “B” ratings assigned to HO₂ and He.

Presently adopted thermochemistry parameters are generally in excellent agreement with thermochemistry parameters used in the predecessor Burke-H₂, Li-H₂, and Li-C₁ models, with the notable exception of HCO. Over the temperature range 298-3000K, maximum differences in TMTD and Burke/Li expressions for this species exceed 12%, 1.4 kcal/mol, and 0.9% respectively for heat capacity (c_p), enthalpy, and entropy.

Replacement of the original Burke-H₂ thermochemistry parameters with the presently adopted set does not discernibly affect model predictions at any of the validation conditions considered in the Burke *et al.* (2012) H₂ modeling study. Hence, the present treatment of H₂ submodel thermochemistry acts to retroactively update the Burke-H₂ model in addition to serving in the present model update. Likewise, the original Li-C₁ and presently adopted TMTD thermochemistry parameterizations lead to nearly indiscernible differences in predictions across the entire H₂/CO validation database compiled for this study.

For the H₂/CO kinetic system described in Tables 1.1 and 1.2, HCO forms in *trace amounts*, relative to the fuel, through the reactions



proceeding from right to left. Evidently, the present revisions to HCO thermochemistry do not modify the reverse rates of C.5.M-C.7 enough to significantly change predictions of observables at any of the validation conditions considered for H₂/CO. However, in more complex systems for which the *principal* fuel carbon flux to CO and subsequent CO₂ formation is through HCO (*i.e.*, CH₂O, CH₃OH, and hydrocarbons), this update of HCO thermochemistry is expected to have more than subtle effects on model predictions. In the near future, the present updates to HCO chemistry will likely be superseded by ongoing evaluation and description of the prompt HCO dissociation mechanism (Labbe *et al.*, 2016). Nevertheless, the simpler scheme embodied in reactions C.5.M-C.7 remains useful for present purposes.

However trivial the present thermochemistry updates may appear for H₂/CO chemistry, the preceding discussion calls to attention the ongoing need to update not only kinetic rate coefficient parameters but also parameters for thermochemistry and transport used in complex models of the combustion chemistry source term. To minimize propagated uncertainty, critically reviewed, consistent parameterizations such as provided by the TMTD/ATcT are to be preferred, when available. A recent comparison of commonly used thermochemical databases by Goldsmith *et al.* (2012) reveals discrepancies larger than ~1 kcal/mol in standard heats of formation (298 K) for several molecules in the C₁ system: CH₂O, CH₃O, CH₂OH. These species participate in the CH₂O and CH₃OH chemistry ranks immediately subordinate to the present H₂/CO focus hierarchies, and future extension of the present model to these ranks should consider available thermochemistry parameterizations for these molecules.

Finally, for examination of chemistry related to the hydroxyformyl (HOCO) radical discussed below in Section 5.4.7, the fit of Rasmussen *et al.* (2008) to the thermochemical properties of *trans*-HOCO computed by Fabian & Janoschek (2005) was used. This complements HOCO reactions and rate coefficients adopted from the Rasmussen *et al.* study, in which the specific *cis*- and *trans*-HOCO isomers were not treated as explicitly different species.

5.3 Transport Parameters

Flames have inherent spatial structure, and, in the present kinetic model development context, transport parameters are necessary to model the coupled chemistry and physics of simplified one dimensional (1-D) flame systems assumed as validation targets. Due to simplifying assumptions regarding physical models for shock tube ignition delay, flow reactor speciation, and related (assumed) homogeneous experiments, transport parameters do not impact model predictions for such 0-D targets. However, as reported in recent work on dimethyl ether oxidation in a flow tube (Guo *et al.*, 2013) or in previous discussion of HPLFR interpretation, transport parameters may also have utility in describing viscous, thermal, and mass diffusion processes in non-flame systems when 0-D assumptions are not reasonably justified.

The present treatment of transport properties generally follows Lennard-Jones(LJ)/Stockmayer-type parameterizations taken from the Li-C₁ model, which are also consistent with the database of Wang

et al. (2007) for all Li-C₁ model species (save C₂H₆, which is not further considered in this work). However, to be completely consistent with the Burke-H₂ submodel assumed herein, the present H₂/CO model also adopts the experimentally-informed *ab initio* transport parameterizations and modified transport model of Wang *et al.* for several binary pairs with high relative diffusivity (H-H₂, H-O₂, H₂-He, *etc.*). This modified treatment is based upon an apparent inadequacy for the repulsive branch of 6-12 LJ-type potentials to model intermolecular interactions among species at relatively higher temperatures important to flames (Paul & Warnatz, 1998). Relative to the traditional LJ/Stockmayer transport model, the updated modified transport leads to generally minor (order of experimental error) changes to H₂/CO model predictions for flame validation conditions. This change in the underlying transport model may increase or decrease model-predicted burning rate, depending on additional factors such as effective Lewis number. However, the effect of this change is uniformly more pronounced at higher predicted flame temperatures and for higher H₂ content fuels, which is consistent with observations of prior studies (*e.g.*, Burke *et al.*, 2012; Paul & Warnatz, 1998).

During the writing of this thesis, several additional transport parameters for binary systems of highly diffusive species (*e.g.*, H atom and H₂) with partners such as CO, CO₂, H₂O, O₂, He, and N₂ (among others) were published by Jasper *et al.* (2014a and 2014b) and Dagdigian (2015a and 2015b) based calculations using theory more advanced than Lennard-Jones theory. The effect of these parameterizations on the laminar burning rates predicted by the present model has not been evaluated here. However, the obvious relevance for syngas and high CO₂-, H₂O-, and O₂-content combustion coupled with the significant (up to ~10% burning rate decrease) effect of the H-CO/H-CO₂ parameters shown by Dagdigian (2015a) for 1 atm CH₄-air flames suggests that future improvements to the present model should consider the effects of parameterizations based on more advanced molecular transport theory.

5.4 Reaction Rate Coefficient Parameters

The remaining development of the present H₂/CO kinetic model centers on adoption of a specific set of reaction rate coefficient parameterizations for reactions of CO-rank species with other CO and H₂ rank species. This updated rate coefficient set is based on low-uncertainty experimental measurements

and/or high level *ab initio* theory without any tuning to the presently considered systems-type validation observables. Further, the validation observables used to assess the predictive fidelity of this model represent a comprehensive range of conditions for which the validation conditions of Burke *et al.* (2012) and Li *et al.* (2007) are a proper subset. The final assembly of kinetic, thermodynamic, and transport parameters provides the full chemical source term submodel for use in modeling practical combustion phenomena, whether in unmodified form or as a basis for further kinetic model optimization.

The present manner of assembling such rate coefficients follows hierarchical methods described earlier and rests upon the Burke-H₂ submodel and treatments of thermochemistry and transport as explained immediately above. A number of (relatively) recently conducted or ongoing experimental and *ab initio* computational studies have examined reactions relevant to the H.9.M and CO-rank reactions in Table 1.2 and yield results that suggest a need for the present review and holistic evaluation of rate coefficient expressions for these reaction systems.

In keeping with hierarchical structure, rate coefficient parameters for H.9.M for M = H₂O, CO₂, and O₂ are first considered since choice of parameters may retroactively affect predictive performance of the underlying Burke-H₂ submodel. Following selection of parameters for H.9.M, reactions of CO (C.1-C.4.M) are next considered as these reactions influence both homogeneous and flame targets in the present validation set. Finally, reactions of HCO (C.5.M-C.7) are considered as a distinct, lower influence subset of CO-rank chemistry as simulations for the entire present validation set show that HCO chemistry appears to be influential on prediction of experimental observables only for fuel-rich H₂/CO flames. Evidently, only in these rich flame systems are conditions favorable for reactions C.5.M-C.7 to form HCO in concentrations that lead to macroscopic changes in prediction of the target observable.

5.4.1 H.9.M: H + O₂ (+ M) ↔ HO₂ (+ M), M = H₂O, CO₂, O₂

The pressure-dependent HO₂-forming reaction H.9.M is among the most important in combustion chemistry. Due to its exceptional significance for H₂ oxidation, this reaction is reviewed in depth in the Burke-H₂ study for M = He, Ar, N₂, and H₂O. The Burke-H₂ model used herein adopts the low pressure limit (LPL) rate coefficient expressions for M = Ar and N₂ directly from the Li-H₂ model, which derived fits from ~300-3000 K to theoretical collision rate coefficient expressions developed by Michael *et al.* (2002) from their own experimental data for kH.9.M interpreted using advanced collision rate theory. However,

to better describe fundamental and applied results at higher pressures, Burke *et al.* (2012) recommended significant changes to Li-H₂ model expressions for H.9.M. These changes include 1) modification of the high pressure limit (HPL) rate coefficient; 2) altered falloff parameters for M = N₂; and 3) increased relative collisional efficiency of M = H₂O relative to He/Ar and N₂ based on both recent literature on the H.9.M reaction and improved kinetic model performance against a wide range of validation targets. The need for these changes suggests further scrutiny of H.9.M reactions may be necessary to improve predictions of high pressure combustion phenomena. Towards developing predictive models for application-relevant high H₂O, CO₂, or O₂ content combustion, parameters for kH.9.M for M = H₂O, CO₂, and O₂ have been re-examined as part of the present model development effort.

5.4.1.1 M = H₂O

The Burke-H₂ model collisional efficiencies for H₂O, relative to M = N₂ and Ar, are consistent within uncertainties of nominal rate coefficient values determined from a range of experimental determinations: high pressure, intermediate falloff data from Bates *et al.* (2001) near ~1170 K; atmospheric pressure data of Ashman & Haynes (1998) from 750-900 K; low pressure QSSP data of Ashmore & Tyler (1962) at 633 K (discussed in Section 4.2); and the 296 K average from Michael *et al.* (2002). The H₂O collisional efficiency is a sensitive parameter in the prediction of high pressure H₂ burning rates, and the present values predict well the targets used in the Burke-H₂ model validation. Present model predictions with $\pm 25\%$ parameter variation in the M = H₂O collisional efficiency depart significantly from validation measurements (*e.g.*, Figure 5.2), in addition to pushing kH.9.H₂O outside of the overlap of uncertainties of the aforementioned fundamental rate coefficient studies. Hence, no further modifications to collisional efficiency parameters for M = H₂O have been made in the present modeling effort.

5.4.1.2 M = CO₂, O₂

Treatment for M = CO₂ and O₂ is not explicitly discussed in the Burke *et al.* (2012) model development work, and the Burke-H₂ model adopts third body efficiency values of CO₂ and O₂ relative to N₂ and Ar directly from the Li-H₂ model. Consideration of H.9.CO₂ and H.9.O₂ in the Burke-H₂ model development can therefore be interpreted as essentially indirect, relying on goodness-of-fit of model predictions relative to experimental data as tacit validation of the inherited H.9.M rate

coefficients/collisional efficiencies for CO₂ and O₂. Since neither literature review nor model parameter variation was attempted for critical evaluation of these H.9.M reactions, the present work extends the Burke-H₂ consideration for M = CO₂ and O₂ through these means.

An absolute, model-independent rate coefficient recommendation for H.9.CO₂LPL has been discussed at length in Chapter 4. However, kinetic models often express pressure-dependent reactions in terms of a low pressure limit collisional efficiency relative to another collider M (e.g., $\epsilon_{\text{CO}_2/\text{M}}$). Under this framework, the pre-exponential term (“A-factor”) of the H.9.CO₂LPL rate coefficient expression results from pre-multiplication of the reference kH.9.M reference pre-exponential term by the given collisional efficiency; however, the temperature dependence of the reference kH.9.M expression is adopted. In the present case, this results in some interpretive ambiguity for $\epsilon_{\text{CO}_2/\text{M}}$ as the temperature dependence identified in Chapter 4 differs somewhat from the temperature dependencies of the M = N₂ and Ar expressions in the reference Burke-H₂ and Li-H₂ kinetic submodels. Present recommendations based on these kH.9.M expressions (for the temperature range 600-1400 K) seek to maintain $\epsilon_{\text{CO}_2/\text{M}}$ -referenced kH.9.CO₂ expressions within the 95% CI developed previously, while also informally weighting the expressions towards the larger body of kH.9.CO₂ experimental measurements between ~800-1000 K. Such a compromise yields a 25% reduction in collisional efficiency from the values adopted in the Burke-H₂ and Li-H₂ kinetic submodels, leading to recommended collision efficiency values relative to N₂/Ar of 3.04/4.32 (previously 3.8 and 5.4), respectively. It is worth noting that due to the relative nature of the collisional efficiency approach, *one of the absolute, model-independent rate coefficient expressions for kH.9.CO₂ (Equation 4.10 or 4.11) should be used as the reference rate coefficient for developing/comparing kinetic models which do not use these particular kH.9.N₂ and kH.9.Ar Burke/Li-H₂ expressions.*

Because the present kH.9.CO₂ change does not significantly impact the demonstrated predictive abilities of the Burke-H₂ kinetic model, it can be considered both to preserve hierarchical compatibility in the sense of the present H₂/CO model construction, as well as retroactively update the Burke-H₂ model. Indeed, only three validation target sets used for the Burke-H₂ model development include CO₂ chemistry. Figure 5.3 shows that model predictions for these three series of laminar flame speed measurements by Qiao *et al.* (2007) are not significantly impacted by the present change for kH.9.CO₂. The effects of this

change are more apparent at only a few other conditions across the entire H₂/CO validation set compiled in the present work. These cases, such as those included in Figure 5.4, tend to involve significant doping (tens of percent) of CO₂ in the reactant gas in order to sensitize H.9.CO₂.

For M = O₂, the only direct experimental rate coefficient measurements to date appear to be the LPL measurements of Michael *et al.* (2002) for temperatures from ~296-700 K. The Li-H₂ study derived a fit for M = O₂ from ~300-3000 K from the Michael *et al.* experimentally-informed theoretical collision rate coefficient expressions, following the same treatment as for M = Ar and N₂. From this fit, Li *et al.* (2004) took average ratios of kH.9.O₂ to both kH.9.N₂ and kH.9.Ar to yield the respective M = O₂ collisional efficiencies of 0.78 and 1.1. These relative efficiencies are adopted in the Burke-H₂ model and serve as the starting point for the present discussion.

The only other study to have explicitly examined H.9.O₂ appears to be the kinetic modeling study of Shimizu *et al.* (2011), which proposes a ~40% faster rate at 1100-1400 K for H.9.O₂ than the Michael *et al.* experimental extrapolation. The Shimizu *et al.* recommendation is based on fitting of a complex combustion model to ~9 atm ignition delay times of Hasegawa & Asaba (1972) in an undiluted 2/98 H₂/O₂ mixture, which provides conditions that considerably sensitize H.9.O₂ relative to most other experiments. Because this data must be fit to a complex combustion model and because there is some ambiguity in the induction period as defined in the original Hasegawa & Asaba study, the treatment of Shimizu *et al.* must be regarded both as minimally constrained and of high uncertainty. Towards increasing constraints on kH.9.O₂ and reducing associated uncertainty, the present modeling effort expands the H.9.O₂ parametric variation approach of Shimizu *et al.* to consider conditions of the full Burke-H₂ and presently expanded H₂/CO validation databases.

Initial kinetic model parametric variation using the Burke-H₂ model to predict the Hasegawa & Asaba induction time data reveals that a ~25% increase in the rate of H.9.O₂ is necessary for the Burke-H₂ model to achieve the same quality of prediction as Shimizu *et al.* for this single dataset; however, even after this change, the *absolute* adjusted Burke-H₂ model LPL rate coefficient for H.9.O₂ remains ~40% lower than the Shimizu *et al.* recommendation. This result suggests the non-uniqueness in predictive ability of kinetic models, particularly under limited constraint – the similar predictive performance of the Shimizu *et al.* and modified Burke-H₂ models masks the noted 40% discrepancy in kH.9.O₂.

The magnitude of this model-dependent discrepancy justifies both the *a priori* circumspection applied to the Shimizu *et al.* (2011) recommendation for kH.9.O2 based on a single isolated dataset as well as the present testing of model predictions against constraints of the *entire* validation target set. For the entire present validation database – which considers over 140 separate series of validation conditions covering significant ranges of temperature, pressure, dilution, and composition – model prediction results of the base H₂/CO kinetic model with $\pm 25\%$ variation in kH.9.O2 reveal that predictions are *remarkably insensitive* to the assumed collisional efficiency of M = O₂ in the examined 25% uncertainty band.

Given the lack of well-defined elementary kH.9.O2 studies beyond that of Michael *et al.* (2002) as well as a scarcity of well-defined, constraining systems-type validation data, there is no impetus at present to change the collisional efficiency of M = O₂ used by the Burke-H₂ study, which ultimately derives from the experimentally-informed theory of Michael *et al.* It appears that this parameter can be uncertain by at least a model-dependent $\pm 25\text{-}40\%$ without significantly impacting prediction results of complex combustion kinetic models for a very extensive range of validation conditions. Given the present scarcity of experimental or theoretical constraint for kH.9.O2, absolute rate coefficient uncertainties should be considered to be no less than $\pm 50\%$ over the entire range of combustion temperatures.

5.4.1.3 Summary for H.9.M

Consideration of the collisional efficiencies of M = H₂O, CO₂, and O₂ in reaction H.9.M, based on both fundamental rate coefficient determinations from the literature and the present work as well as extensive kinetic modeling, advances the following recommendations and conclusions to be adopted in the present H₂/CO kinetic model update:

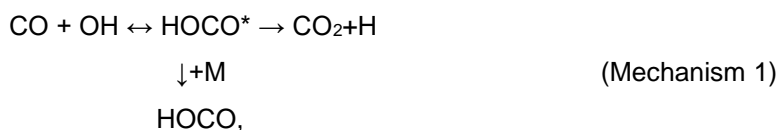
- a) Collisional efficiencies are herein discussed as a consequence of their pervasive use in combustion chemical source term modeling. Nevertheless, they represent (model-dependent) *relative* relationships between two rate coefficients. When developing or comparing kinetic models which do not use the presently adopted Burke/Li-H₂ expressions for kH.9.N2 and kH.9.Ar, the model-independent *absolute rate coefficient* expression for kH.9.M should be used.
- b) The collisional efficiency for M = H₂O is well constrained by both fundamental rate coefficient measurements detailed in the literature, as well as its goodness-of-fit verified by predictions of

parametrically-varied kinetic models to sensitive experimental measurements. Therefore, the present Burke-H₂ model parameterizations remain in use for the H₂/CO model update.

- c) The collisional efficiencies for M = CO₂ relative to N₂ and Ar have been constrained by fundamental rate coefficient measurements as described in Chapter 4 of the present work. Adoption of these collisional efficiencies preserves the predictive ability of the Burke-H₂ model against its limited CO₂ chemistry validation and therefore serves to retroactively update the Burke-H₂ model as well as the present base H₂/CO model. Model predictions appear sensitive to this parameter only in cases with significant CO₂ concentration and, particularly, near the H₂/O₂ second explosion limit or in high pressure flames.
- d) The collisional efficiency for M = O₂ is not well constrained by studies evident in the literature, but it is apparently also not a particularly sensitive parameter for modeling predictions across the present H₂/CO validation database. Limited direct kinetic rate coefficient measurements for H.9.O2 have been made, and sensitive validation experiments are scarce. The present consideration finds no reason to adjust to present Burke-H₂ model parameterizations for use in the H₂/CO model update.

5.4.2 C.1: CO + OH ↔ CO₂ + H

The chemically-activated reaction system



particularly the C.1 path from CO+OH to CO₂+H, is considered to be among the most important in combustion chemistry (Balakrishnan & Billing (1996), Miller *et al.* (1990)) since it represents both the predominant pathway for CO₂ production and a major source of heat release in virtually all H/C/O-based combustion systems. Predictions of kinetic models for most carbon-containing fuels are generally sensitive to the choice of C.1 rate coefficient expression, and, consequently, this reaction system continues to garner significant interest from the combustion and gas phase kinetics communities. While the present work does not intend to review decades' worth of literature on the CO+OH reaction, the interested reader may wish to consult papers by, *e.g.*, Dryer *et al.* (1971), Weston (1998), Baulch *et al.*

(2005), and Guo (2012) for supplementary discussion and historical context for a wide range of experimental and theoretical features of the CO+OH system.

The Mechanism 1 reaction scheme depicted above was originally proposed by Smith (1977) and involves an activated-complex reaction pathway representation for the CO+OH system. This scheme presents a simplification of more detailed descriptions of the CO+OH reaction but is appropriate for the present discussion. Reactants CO and OH combine to form a vibrationally excited HOCO* adduct, which may either (A) dissociate back to CO and OH, (B) collide with third body M and form a stabilized HOCO radical, or (C) decompose to CO₂ and H atom following the C.1 reaction pathway. The present focus for updating CO-rank combustion kinetics ($T > \sim 500$ K) is on rates of channels (B) and (C), which represent the high pressure limit and low pressure limit product-forming channels, respectively.

As shown in Figure 5.5, the pressures required for non-negligible flux of CO+OH to form HOCO radical at combustion-relevant temperatures are substantial and appear to increase dramatically with temperature, from lower limits of ~ 20 bar up to 200 bar as temperatures rise from 800 to 1200 K (Joshi & Wang, 2006). Consequently, the stabilization of HOCO* to HOCO by Channel (B) and any subsequent HOCO chemistry is typically assumed to be unimportant for the prediction of most combustion kinetics observables, which typically are measured below this pressure-temperature envelope or when the product of CO and OH concentrations is low. Description of HOCO chemistry is therefore omitted from most combustion chemistry models. In keeping with this paradigm, the immediate discussion temporarily assumes HOCO chemistry is not important. Present discussion of C.1 is limited to Channel (C) in Mechanism 1, which describes the low pressure limit reaction



However, discussion of HOCO chemistry is revisited in Section 5.4.7.

Rate coefficients for C.1 from several recent studies are in generally good agreement from 500-2500 K (Figure 5.6), especially considering the variety of empirical, theoretical, and model-constrained methods by which each was derived. Save for the recent purely theoretical result of Nguyen *et al.* (2012), values of $k_{\text{C.1}}$ differ by no more than about $\pm 20\%$ from the Li *et al.* (2007) rate coefficient used as a starting point for the present update of the Li-C₁ kinetic model. Given the sensitivity of predictions for

many syngas kinetics observables to kC.1, even 20% variation in this rate coefficient can lead to notable changes in predicted agreement for combustion kinetic models.

The kC.1 recommendation of Davis *et al.* (2005) was initially fit to experimental rate coefficient measurements of Wooldridge *et al.* (1994) and Golden *et al.* (1998)/Yu (1996) and then A-factor optimized against 13 syngas laminar burning rate, flow reactor species evolution, and shock tube ignition delay experiments using a complex kinetic model with ~30 optimization parameters. The resulting Davis *et al.* optimized kC.1 fit lies at the boundaries of its optimization constraint range, suggesting that true optimality for kC.1 using this approach may not have been achieved. Li *et al.* (2007) approached fitting of kC.1 through uncertainty-weighted least squares minimization against “the entire body of experimentally measured rate constants available in the literature,” which extends by several studies the experimental database employed for the Davis *et al.* fit. Based on stated or estimated uncertainties in the data used for their *empirical* kC.1 fit, Li *et al.* recommend a 95% confidence interval for kC.1 that suggests an experimental uncertainty in effective activation energy for C.1 of no greater than ~0.535 kcal/mol from 500-2500 K. This is an important figure of merit, for *chemical accuracy* of theoretical methods is generally held to be ~1.0 kcal/mol. It follows that theoretical computations of kC.1 may require a measure of empirical constraint in order meet the uncertainty limits imposed by high quality experiments.

Theoretical studies of the CO+OH system from Senosiain *et al.* (2005) and Joshi & Wang (2006) were published essentially contemporaneously to the work of Davis *et al.* and Li *et al.* Theory employed by these studies differs significantly in terms of assumed potential energy surfaces, variational and tunneling treatments, approximations related to *cis*↔*trans* isomerization of HOCO*, and master equation resolution for energy and rotation, among other specifics. However, both studies ultimately employed *experimentally-informed* adjustments to input parameters – Senosiain *et al.* limited consideration to 298 K, while Joshi & Wang fit their theory to experiments spanning 89-819 K. Recommended values of kC.1 from these studies agree to better than ±12% with the Li *et al.* weighted least squares kC.1 expression, while the Joshi & Wang expression also appears to overlap the Davis *et al.* fit particularly well from ~600-2000 K.

The study of Nguyen *et al.* (2012) (and related work of Weston *et al.* (2013)) appears among the most recent theoretical considerations for the reaction of CO with OH. This study, unlike the Senosiain

et al. and Joshi & Wang studies, does not adjust input parameters based on empirical inputs – it treats the CO+OH reaction system purely from an *ab initio* standpoint. While the Nguyen *et al.* recommendation for kC.1 agrees well with both experimental data and other parameterizations discussed above for temperatures up to ~1200 K, it begins to deviate sharply higher with increasing temperature to nearly 50% greater than the Li *et al.* empirical fit at 2500 K. Present work estimates of kC.1 uncertainty for the Nguyen *et al.* expression – derived based on joint ± 1.0 kJ/mol uncertainties in barrier heights for two key CO+OH transition states treated in their study – do not overlap beyond ~1600 K with the uncertainty-weighted 95% confidence interval for kC.1 developed by Li *et al.* The reason for this discrepancy appears to lie at least partly in the Nguyen *et al.* treatment of anharmonicity (S.J. Klippenstein, personal communication 2013), which becomes increasingly important at higher temperatures. On the basis of this discrepancy, the C.1 rate coefficient from Nguyen *et al.* is excluded from further consideration in this CO kinetic model update.

Given the general consensus in kC.1 values recommended by the approaches discussed above, particularly below ~1200K, as well as the departure from consensus of the *purely ab initio* rate coefficient at higher temperatures, concluding remarks from the Joshi & Wang study remain an insightful viewpoint for selecting the kC.1 parameterization to be used in the present kinetic model update: “given the current knowledge of the potential energy surface and the experimental data available, the treatment of the [CO+OH] reaction remains semi-theoretical, as...different [theoretical] models can satisfactorily reproduce the wide range of data.” Accordingly, adoption of either the experiment-advised theory kC.1 recommendation from Senosiain *et al.* or that of Joshi & Wang satisfies the overarching goal of the present CO kinetic model update, which seeks to compile untuned kinetic parameters from experimental and theoretical studies, while also remaining within the envelope of experimental uncertainties determined by Li *et al.* Moreover, their respective treatments of the full pressure dependence of the CO+OH reaction extends to HOCO chemistry considered subsequently in Section 5.4.7.

The present model update adopts the kC.1 recommendation of Joshi & Wang (2006) based on the more comprehensive experimental database and temperature range they considered when adjusting transition state barrier heights for their RRKM fit to experimental kC.1 measurements. Nevertheless, it is important to recognize that each of the Davis *et al.*, Li *et al.*, Senosiain *et al.*, and Joshi & Wang

expressions lie in overlapping uncertainty bands representing effective *sub-chemical accuracy* in determination of kC.1. Because CO and H₂ rank reactions are highly coupled, combinations of any of these kC.1 expressions with complimentary H₂ submodels can yield reasonably predictive model performance over a wide range of conditions. Future improvement in accuracy for kC.1 must come from significantly more constraining experimental or theoretical techniques than have been applied hitherto.

To further underscore this point, the very recent kC.1 measurements of Nasir & Farooq (2016) at conditions approaching the low pressure limit should be noted. The nominal experimental rate coefficient determinations and recommended expression for temperatures between 700-1230 K lie everywhere below the Joshi & Wang LPL expression and essentially at the lower limits of the Li *et al.* 95% confidence interval. Despite the relative bias, their kC.1 expression still remains within sub-chemical accuracy of the consensus described above.

5.4.3 C.2: $\text{CO} + \text{O}_2 \leftrightarrow \text{CO}_2 + \text{O}$

Kinetic modeling predictions are generally insensitive to choice of C.2 rate coefficient since reaction C.2 is exceptionally slow in comparison with most others in the H₂/CO ranks. This suggests C.2 may be unimportant in both fundamental and applied processes where the rate of convective/diffusive transport of reactive species and their subsequent reactions dominates over reaction flux through reaction C.2. Even so, this reaction appears to modestly affect prediction of induction/ignition behavior above ~1000 K in idealizing validation experiments with high [CO]x[O₂] content resulting from increased reaction pressure and/or selective fuel enrichment with CO. Thorough review of the literature for C.2 reveals recent theoretical treatment and reinterpretation of older experiments that warrants further consideration of this reaction.

Direct measurement of the elementary rate coefficient kC.2 is frustrated by the comparatively slow rate of C.2 relative to reactions of CO with radical species, particularly OH. A consequence of this is the well-known fact that minute traces of H atom-containing impurities (H₂, H₂O, CH₄, *etc.*) in otherwise pure CO/O₂/inert mixtures can significantly accelerate the overall rate of CO oxidation through reaction C.1 and subsequent H₂-rank chemistry. Modeling work of Sutherland *et al.* (1992) suggests that as little as 200 ppb of initial H atom impurity affects apparent kC.2 determination by factors of roughly 2, 10, and 70 at temperatures of 2000, 1700, and 1500 K, respectively. Other studies (*e.g.*, Bacskay & Mackie,

2005; Dean & Kistiakowsky 1970 and 1971) also appreciate that these impurities may lead to the *orders of magnitude* discrepancy for kC.2 observed among studies in the literature.

In addition to complications arising from impurities, determinations for kC.2 may also be confounded by ambiguities in defining ground and excited states for participating species in C.2. Consistent with most combustion applications, combustion kinetic models typically assume that ground state species $O_2(X^3\Sigma_g^-)$ and $O(^3P)$ participate as reactants/products in reactions and that excited species are excluded. However, the recent theoretical study of Sharipov & Starik (2011) extends consideration for reaction C.2 to include reactions of ground state and electronically excited O_2 species, which may form products including ground state $O(^3P)$ and electronically excited $O(^1D)$ atoms. Their analysis suggests that non-equilibrium effects among these species may additionally influence experimentally-derived kC.2 measurements and extrapolations.

Since interpretation of existing experimental kC.2 data may be muddled by both hydrogenous impurity and excited species issues, the present work prefers the theoretically-derived rate coefficient recommendation of Sharipov & Starik (2011) for the ground state reaction



Figure 5.7 presents a comparison of the adopted Sharipov & Starik kC.2 rate coefficient recommendation to several of the experimental, theoretical, and critically reviewed kC.2 expressions discussed herein. Over the temperature range 1000-2500 K, this computed rate coefficient agrees very well, by approximately a factor of two, with experimentally-derived kC.2 recommendations of Dean & Kistiakowsky (1971) and Thielen & Roth (1983), both of which explicitly consider effects of hydrogenous impurities. This presently-adopted recommendation for kC.2 ranges from a factor of ~2 to ~10 lower at 2500 and 1500 K, respectively, than the kC.2 expression adopted by the Li-C₁ kinetic model from the critical review of Tsang & Hampson (1986), itself from the earlier recommendation of Baulch *et al.* (1976), which critically considers over 20 studies published prior to 1974. Simulations reveal that, for kC.2 expressions considering only the ground state $O_2(X^3\Sigma_g^-)/O(^3P)$ species, model predictions differ negligibly when using either the rate coefficient recommendation of Sharipov & Starik or the earlier theory-based

recommendation of Bacskay & Mackie (2005). The latter is a factor of ~3-6 lower than the former from $1000 < T < 2500$ K.

5.4.4 C.3: $\text{CO} + \text{HO}_2 \leftrightarrow \text{CO}_2 + \text{OH}$

For combustion temperatures, essentially no direct experimental determinations for kC.3 exist in the literature. Indirect experimental determinations are subject to uncertainties of the interpretive model adopted for rate coefficient determination, and consequently, nominal kC.3 determinations shift in response to changes in kinetic model assumptions. The Baulch *et al.* (1976) kC.3 recommendation, based primarily on pre-1974 studies of relative rate and weakly constraining systems measurements, persists as the preferred kC.3 expression through the later rate coefficient compilation of Tsang & Hampson (1986). Despite its model-dependent derivation, the Baulch *et al.* expression appears essentially unaltered in kinetic models until at least 1999 (*e.g.*, Smith *et al.*).

However, in a predecessor study to the Li-C₁ kinetic model development, Mueller *et al.* (1999b) reconsider the underlying model-dependence of the Baulch *et al.* expression and its later interpretations. Based on reinterpretation of acetaldehyde oxidation results of Colket *et al.* (1977) and relative rate measurements of Atri *et al.* (1977) with a (then) more modern determination for kH.14, Mueller *et al.* recommend a factor of ~3 reduction in the Baulch *et al.* expression, with the caveat that additional study of kC.3 is warranted to further address model dependencies. The subsequent study of You *et al.* (2007) provides additional, comprehensive discussion of literature involving experimental kC.3 determinations and convincingly argues that theoretical treatment of reaction C.3 may reduce uncertainty in the rate coefficient, as well as extrapolate over a larger temperature range.

Choice of rate coefficient recommendation for C.3 is shown in several studies to be significant for the prediction of H₂/CO mixture ignition in a rapid compression machine (RCM) at the higher pressure (15-50 bar), intermediate temperature (950-1100K) conditions studied by Mittal *et al.* (2006). Moreover, Sivaramakrishnan *et al.* (2007) find their model-predicted reactivity for dilute H₂/CO mixtures reacting at high pressures (21-450 bar) and intermediate temperatures (1000-1500 K) is sensitive to C.3. Motivated in part by both of these studies, You *et al.* (2007) determined a pressure-independent kC.3 from high-level electronic structure theory, transition state theory, and master equation modeling, and found good

agreement with the empirically-adjusted model-fit rate coefficient expression suggested by the Mittal *et al.* experiments.

For several reasons discussed in depth in the study of Chaos & Dryer (2008) and above, the present model update initially replaced the Mueller *et al.* (1999b) kC.3 recommendation inherited from the Li-C₁ model with the newer computed rate coefficient from You *et al.* From 500-2000 K, this revision gives a kC.3 expression of about one quarter and one twelfth of the kC.3 expressions recommended by Mueller *et al.* and Baulch *et al.*, respectively. Use of the You *et al.* rate coefficient in present kinetic model variations improves agreement of predictions with the Mittal *et al.* (2006) ignition observables. However, this change reduced model-predicted reactivity for quite a few ignition delay and flow reactor validation targets to an extent that could not be compensated by other changes in the kinetic model or accounted for in the uncertainty of the experimental data.

Recent work-in-progress by S.J. Klippenstein (personal communication 2013) has examined the potential energy surface for the C.3 reaction system with higher accuracy *ab initio* methods than employed by You *et al.*, and finds that a transition state energy barrier for the trans-HOOCO channel in the C.3 system is ~ 0.65 kcal/mol lower than found by You *et al.* Applying simple Evans-Polanyi scaling for this energy barrier change to the apparent activation energy of the You *et al.* kC.3 recommendation permits a preliminary adjustment of kC.3 based on the more accurate theoretical treatment. At 1000 K, this energy barrier adjustment leads to a revised kC.3 that is a factor of 1.4 times higher than the You *et al.* recommendation. Figure 5.8 compares several kC.3 recommendations, including those from the predecessor Li-C₁ model, You *et al.*, and the present estimate. The present energy barrier-scaled estimate falls within uncertainty bands prescribed by You *et al.* and is close to the expression computed by Sun *et al.* (2007). Moreover, the higher rate slightly improves predicted model reactivity for cases adversely impacted by adoption of the You *et al.* rate coefficient.

The present scaled kC.3 expression is to be regarded as an estimate with uncertainties comparable to those given by You *et al.*, *i.e.*, factors of approximately 3, 2 and 1.75 at temperatures of 700, 1400, and 2000 K, respectively. The estimated uncertainty band of the present scaled kC.3 expression also overlaps the inferred factor of ~ 2 uncertainty band from the kC.3 reassessment of Mueller *et al.* for the temperatures considered in that study. Clearly, additional analysis of reaction C.3 is

warranted pending either more refined theoretical analysis by Klippenstein or other investigators, or more highly-constraining experimental $k_{C.3}$ measurements from modern elementary rate coefficient measurement techniques. At the time of writing of this thesis, such analysis appears to be imminently forthcoming (Klippenstein, 2017).

5.4.5 C.4.M: $\text{CO} + \text{O} (+ \text{M}) \leftrightarrow \text{CO}_2 (+ \text{M})$

Over a wide range of conditions, including those found in high pressure syngas flames, the spin-forbidden C.4 reaction system acts to reduce overall oxidative reactivity by terminating atomic O biradical into stable CO_2 , albeit with significant heat release. Oxygen atoms so terminated cannot participate in branching reactions such as



which control both the rate of radical pool growth during ignition/induction processes as well as the size and quality of the radical pool during flame propagation/extinction. Reaction H.4, acting in the right-to-left sense, is particularly important for steam-diluted systems such as those indicated in Figure 5.2.

For many conditions, H_2/CO kinetic model predictions are modestly sensitive to the choice of $k_{C.4.M}$ expression. However, uncertainty associated with $k_{C.4.M}$ at combustion temperatures remains surprisingly large. Experimentally, study of C.4.M suffers from the same impurity and slow relative rate problems as C.2 as well as added interpretive complexities due to pressure- and bath gas-dependencies. Consequently, few reliable measurements of the forward or reverse reaction rate coefficient have been made at combustion temperatures (~500-2500 K), and theoretical determinations of $k_{C.4.HPL}$ and $k_{C.4.M}$ are likewise scarce.

Higher temperature (> 2500 K) experimental rate coefficient information for C.4.M comes primarily from studies of the C.4.M reaction acting in reverse to dissociate CO_2 . The large dissociation energy for CO_2 (~530 kJ/mol) necessitates the high temperatures associated with these studies, which exceed those generally encountered in combustion. Nevertheless, these studies may provide asymptotic constraint for combustion-appropriate $k_{C.4.M}$ rate coefficient expressions.

A likely consequence of scarce reliable experimental and theoretical C.4 rate coefficient information, particularly in recent years, is that use of both the experiment-informed Troe (1975) high pressure limit (HPL) recommendation and the Westmoreland *et al.* (1986) bimolecular QRRK theory-derived low pressure limit (LPL) recommendation persists in many recent kinetic models. Notably, the Troe (1975) HPL expression is used as an input for the Westmoreland *et al.* LPL recommendation. The bimolecular QRRK theory used by Westmoreland *et al.* propagates uncertainty from the assumed Troe HPL one-to-one into uncertainty for the computed LPL. Accordingly, the following discussion first considers recent advances in quantifying kC.4.HPL.

5.4.5.1 High Pressure Limit (HPL) for C.4.HPL

The present study adopts the theory-based kC.4.HPL recommendation of Jasper & Dawes (2013a). This recommendation differs significantly from the Troe (1975) expression used as a basis for kC.4.HPL and kC.4.M expressions in the Li-C₁ model as well as more recent syngas kinetic models, *e.g.*, Saxena & Williams (2011) and Kéromnès *et al.* (2013). Considering (1) the persistence and pervasiveness of the Troe (1975) recommendation, (2) the relatively significant differences between Troe and Jasper & Dawes HPL expressions, and (3) the potential importance of the HPL rate coefficient for determining LPL rate coefficients, the following discussion provides a critical summary of relevant literature in further support of the present change in kC.4.HPL expression. Comparisons of kC.4.HPL determinations and expressions are presented in Figure 5.9 to accompany this discussion.

There appear to be no direct experimental investigations of kC.4.HPL appearing in the literature after the 1974 study of Wagner & Zabel, which appears to follow-up an earlier study from the Wagner group in which water or hydrocarbon impurities were suspected of influencing kC.4.HPL determinations (Olschewski, Troe & Wagner, 1966). The Wagner & Zabel study evidently supersedes that of Olschewski *et al.*, so details of the latter will not be considered further.

Wagner & Zabel extrapolate experimentally measured, high pressure, high temperature ($\geq \sim 3000$ K) CO₂ dissociation rate coefficients to the HPL using Lindemann theory and a LPL parameterization based on experiments from their companion study (Hardy *et al.*, 1974). Some interpretive uncertainty in their extrapolations may arise from assumptions about the form of falloff dependence, but later theoretical consideration of Yau & Pritchard (1978) finds that Lindemann theory is

adequate treatment for rate coefficient determination at the experimental conditions of Wagner & Zabel. Their extrapolated CO₂ dissociation rate coefficient determinations give CO + O recombination rate coefficients at the HPL upon conversion by equilibrium constant, and Wagner & Zabel imply that the resulting kC.4.HPL determinations have factor of ~3 uncertainty. They recommend a simple Arrhenius expression for HPL CO₂ dissociation for 3000 ≤ T ≤ 3700 K, based in part on fitting their own data and the kC.4.HPL determinations of Simonaitis & Heicklen (1972) for temperatures between 298-472 K. They also note the scarcity of data at temperatures between these two ranges as a possible source of uncertainty in their temperature-dependent recommendation.

The Wagner & Zabel experimental CO₂ dissociation-based CO + O recombination rate coefficient recommendation gives a kC.4.HPL expression which falls about a factor of 15 lower than the recent theory-based Jasper & Dawes recommendation for the high temperature range (≥ ~3000 K). Factors of ~2 or 3 uncertainty in theory notwithstanding, this significant discrepancy may reflect systematic experimental LPL uncertainties propagated from the Hardy *et al.* (1974) study into the Wagner & Zabel extrapolation to the HPL. The pressure-dependent Wagner & Zabel data used for HPL extrapolation lie only factors of ~2-5 below the pressure-dependent rate coefficients computed by Jasper & Dawes (2013b) for the same nominal pressure. This level of agreement is not unreasonable considering the significant difficulties inherent in experimental determination of this particular rate coefficient at any pressure.

Despite the (then) newer, contemporary kC.4.HPL determinations from Wagner & Zabel, the earlier Olschewski *et al.* experiments appear to be the sole high temperature data informing the frequently used kC.4.HPL recommendation of Troe (1975), which is a factor of ~2 lower than recommended by Wagner & Zabel and a factor of ~30 lower than recommended by Jasper & Dawes. Interestingly, the later rate coefficient compilation of Gardiner & Troe (1984) specifically limits the validity of the Troe expression to T ≤ 1500 K for reasons left unexplained in their review (though the suspected influence of impurities in the Olschewski *et al.* kC.4.HPL determinations may explain the restricted temperature range). Present interpretation of the interrelations among the several kC.4.HPL studies of Wagner, Troe, and coworkers, including Gaedtke *et al.* (1973) discussed below, is that the Olschewski *et al.* data remain highly uncertain. This uncertainty should propagate to the Troe (1975) kC.4.HPL recommendation, for which

the present retrospective consideration finds no strong quantitative experimental support at any temperature in the reported applicability range ($298 \leq T \leq 3500$ K).

As is the case at high temperature, instances of lower temperature, experiment-based kC.4.HPL recommendations are rare, and none are recent. Simonaitis & Heicklen (1972), DeMore (1972), and Gaedtke *et al.* (1973) all determined kC.4.HPL values as relative rate coefficient measurements, and they find agreement to a factor of ~3 at room temperature among their nominal kC.4.HPL values. Because Simonaitis & Heicklen extrapolated Hg-sensitized, near-atmospheric pressure rate coefficient measurements based on doubly relative reaction rates (CO + O relative to 2-trifluoromethylpropene + O relative to 1-C₄H₈ + O) to develop HPL expressions in their study, their kC.4.HPL determinations must be viewed as the most uncertain of these three studies. However, their study is the only one to provide kC.4.HPL temperature dependence. The DeMore and Gaedtke *et al.* studies measured kC.4.HPL at pressures well in excess of 10 atm and derive nominal kC.4.HPL values in very good agreement, although Gaedtke *et al.* set their value as an upper limit for the rate coefficient at 300 K. All of these lower temperature kC.4.HPL determinations lie somewhat higher than an extrapolation of the recommended Jasper & Dawes expression, which was developed for $1000 \leq T \leq 5000$ K.

However, quantitative comparison of theory and experiment at these lower temperatures is not presently advisable since use of the Jasper & Dawes HPL expression beyond its valid temperature range (particularly for lower temperatures) may be subject to significant extrapolation error. From a predictive combustion modeling standpoint, the reaction of CO with O may not be relevant at the ~300-500 K range considered in these lower temperature studies, so quantitative accuracy in kC.4.HPL would be unnecessary for such low temperatures. Moreover, characteristic temperatures for present syngas validation cases do not extend appreciably below 1000 K. Consequently, the published Jasper & Dawes (2013a) modified Arrhenius parameters for kC.4.HPL are presently adopted despite the potential for extrapolative extension to temperatures lower than 1000 K. It is worth noting that the only other study to have incorporated this kC.4.HPL expression into a combustion kinetic model appears to be that of Nilsson & Konnov (2016). However, this model differs from the present work in its treatment of the C.4 pressure dependence, which is described below.

5.4.5.2 Low Pressure Limit (LPL) for C.4.M

The preceding analysis of kC.4.HPL suggests that up to a factor of ~30 uncertainty may have been propagated from the Troe (1975) kC.4.HPL into the Westmoreland *et al.* (1986) kC.4.M recommendation, which is subject to further uncertainties associated with assumptions inherent in the bimolecular QRRK theory used to compute kC.4.M. Moreover, the Westmoreland *et al.* expression also departs significantly from reliable experimental rate coefficient determinations found in the literature, some of which are shown in Figure 5.10 and further discussed below. For these reasons, the Westmoreland *et al.* expression is not considered further.

The present study adopts a kC.4.M expression based on application of parameter-free (first principles) theory for $M = \text{Kr}$ and $1000 \leq T \leq 5000 \text{ K}$ (Jasper & Dawes, 2013a; Jasper & Dawes, 2013b; A.W. Jasper, personal communication 2013 and 2014; henceforth together referred to as Jasper, 2013). Jasper (2013) computed values of kC.4.Kr(T,P) from total energy (E) and total angular momentum (J) resolved classical trajectories of collisions of Kr bath gas with CO₂. Elements of this theory have been applied previously (*e.g.*, Jasper & Miller, 2009; Jasper & Miller, 2011). Under the reasonable assumption that Ar and Kr share similar collisional energy transfer behavior in unimolecular dissociation reactions, the presently recommended fit to Jasper (2013) trajectory ensemble-averaged kC.4.Kr-Ar(T) LPL values is given by

$$\text{kC.4.Ar} = 1.0 \times 10^{19} T^{-1.323} \exp(-3852/T) \text{ cm}^6/\text{mol}^2/\text{s}$$

for $1000 \leq T \leq 5000 \text{ K}$, subject to the same low temperature extrapolation caveats as discussed for the HPL. This expression is compared to other kC.4.M expressions and experimental rate coefficient determinations in Figure 5.10.

Adoption of a first principles-based rate coefficient for the C.4.M system avoids many of the often significant experimental and interpretive uncertainties resulting from impurity, collision partner, and pressure-dependent effects as well as dependencies resulting from complex kinetic models often used to determine rate coefficient data from experiments at combustion temperatures. In further support of the rationale in present choice of theory-based kC.4.Ar, the following discussion highlights the significant scatter in kC.4.M LPL expressions.

The review of Baulch *et al.* (1976) synthesizes *over 100 studies* of the C.4.M reaction, and comprehensive reevaluation of these pre-mid 1970s studies is beyond the scope of this thesis. The conclusion of Baulch *et al.* (1976), later reiterated by Tsang & Hampson (1986), is that the significant scatter in experimental kC.4.M rate coefficient determinations is largely attributable to impurity effects. From among the large number of studies they considered, Baulch *et al.* (1976) recommend an expression due to Slanger *et al.* (1972), restricted to $T \leq 500$ K. Notably, the Slanger *et al.* study serves to supersede the earlier Slanger & Black (1970) study in which reactant impurities were thought to have multiplied *apparent* kC.4.M values by a factor of ~ 7 . General awareness of impurity effects on experimental kC.4.M determinations appears to have emerged in the early 1970s, so the present discussion does not consider experimental kC.4.M studies prior to the mid-1970s nor does it consider critically evaluated kC.4.M recommendations based on these earlier experimental studies (*i.e.*, Baldwin *et al.*, 1972; Troe, 1975; Tsang & Hampson, 1986; Warnatz, 1984).

Present discussion centers on the relatively fewer studies of kC.4.M appearing in the literature after the mid-1970s and, in particular, those considering temperatures of 500-2500 K. Even the results of some of these later studies may have been impacted by impurity effects (*e.g.*, Fujii *et al.*, 1985; Fujii *et al.*, 1987). The studies of Dean & Steiner (1977) and Hardy *et al.* (1978) explicitly treat experimental impurity effects. These studies appear to be both reliable and overwhelmingly sensitive to kC.4.M.

Dean & Steiner (1977) find evidence of impurity effects in their own relatively low pressure ($< \sim 3$ atm), high temperature (2100-3200 K) N₂O/CO/Ar experimental results. However, they provide convincing model-based reassessment of *apparent* kC.4.M values determined from time-resolved species measurements of CO₂ and O at low extents of reaction. These measurements yield initial rate of reaction-type kC.4.M determinations, though these determinations are convolved with impurity effects. With increasing initial (and hence, post-reflected shock) pressures, the *apparent* kC.4.M determinations tend toward convergence, suggesting that at increasing pressures, any bimolecular, impurity-driven reactions such as C.1 ($\text{CO} + \text{OH} \leftrightarrow \text{CO}_2 + \text{H}$) diminish in importance compared to the termolecular C.4.M system reacting in the low pressure limit. Based on this observation, Dean & Steiner used kinetic modeling to correct *apparent* kC.4.M values to impurity-free kC.4.M values. They recommend a temperature-independent value of $5.8 \times 10^{13} \text{ cm}^6/\text{mol}^2/\text{s}$ ($\pm \sim 20\%$) for kC.4.Ar over 2100-3200 K, which is

in nominally excellent agreement (within ~20%) with the theoretical Jasper (2013) LPL for $M = \text{Ar}$ (Figure 5.10) as well as high temperature $k_{\text{C.4.M}}$ expressions derived from CO_2 dissociation experiments. The present review does not evaluate potential systematic uncertainties due to the $\text{H}_2/\text{CO}/\text{N}_2\text{O}$ kinetic scheme assumed by Dean & Steiner to correct *apparent* $k_{\text{C.4.M}}$ values to the recommended value. However, such uncertainties are not expected to exceed the ~15% differences between apparent and corrected values of $k_{\text{C.4.Ar}}$.

The contemporary study of Hardy *et al.* (1978) precludes aberrations due to uncontrolled impurities by deliberate doping of ~1000 ppm H_2 into the reactants. In their investigation, mixtures of 0.1/1.0/24/75 $\text{H}_2/\text{O}_2/\text{CO}/\text{Ar}$ are shock heated to between ~1250 and 2200 K (corresponding to post-reflected shock pressures of ~2 to 4 atm, respectively) to yield time-resolved 435 nm flame band (COxO) emission intensity profiles after passage of the reflected shock wave. The controlled introduction of H_2 “impurity” sensitizes production of O through cycling of reactions H.1 and C.1 while also preventing C.1 from overwhelming C.4 in the oxidation of CO to CO_2 .

Based on modeling results using a 27 reaction kinetic scheme, Hardy *et al.* determine that the characteristic decay time from $\frac{3}{4}$ maximum to $\frac{1}{4}$ maximum COxO emission intensity is an observable that is particularly sensitive to $k_{\text{C.4.M}}$, with limited competition from other reactions such as H.1 and C.1. This has also been confirmed with more recent kinetic modeling. Consequently, the (COxO) emission intensity decay serves as a quantitatively useful constraint for experimental validation of the Jasper (2013) $k_{\text{C.4.Ar}}(T,P)$ expression over a combustion-relevant temperature range. As shown in Figure 5.11, the *a priori* kinetic model prediction for a Lindemann fit to the Jasper (2013) $k_{\text{C.4.Ar}}^{\text{LPL}}$ and $k_{\text{C.4.HPL}}$ expressions appearing above is very good, while use of the frequently invoked Troe (1975) $k_{\text{C.4.HPL}}$ /Westmoreland *et al.* (1986) $k_{\text{C.4.M}}$ formulation leads to characteristically fast 435 nm emission decay times.

The paucity of reliable treatments of the $k_{\text{C.4}}$ system leaves little to say with regard to pressure dependency and bath gas effects. For this reason, the existing Li- C_1 collisional efficiencies for $M = \text{H}_2$, H_2O , CO , CO_2 , and N_2 (relative to Ar) are propagated into the present kinetic model.

5.4.6 C5.M-C7: Reactions of HCO

Formyl radical (HCO) is generated by syngas flames in reactions such as C.5.M



acting from right to left, particularly under rich, high pressure flame conditions favoring high [H] and [CO]. In these situations, reaction C.5.M effectively removes reactive species from the flame when HCO subsequently forms less reactive and stable products by, e.g., C.6 and C.7. Laminar burning rate predictions for these flames are acutely sensitive to changes in the size and quality of the radical pool, so the effective termination reactions included by C.5.M-C.7 HCO chemistry are necessary to adequately predict high pressure flame targets.

Syngas kinetic models lacking HCO chemistry require compensatory strategies to replace these termination effects. For example, Saxena & Williams (2011) increase the Troe (1975) rate coefficient for C.4.HPL by a factor of 10 in order to approximate the necessary radical termination in their HCO-absent model. This aids in prediction of 40 atm burning rates of 95/5% CO/H₂ mixtures (Sun *et al.*, 2007). However, considering the kC.4.M discussion in the preceding section, this tuning of kC.4.HPL represents a rate coefficient parameterization for which there is presently no experimental or theoretical basis.

While inclusion of HCO chemistry appears necessary to predict rich, high pressure syngas burning rates, the specific conditions accessed by these flames are insufficient to constrain HCO chemistry to a significant degree. The chemistry of these flames is highly coupled with H₂ rank and C.1-C.4.M reactions, leading to minimal constraint of HCO reactions imposed by the syngas-related validation database. Stronger constraint of HCO chemistry follows from detailed consideration of CH₂O rank chemistry, which is beyond the scope of the present work. However, as part of the present focus on updating H₂/CO rank chemistry, especially for high pressure flame applications, reactions C.5-C.7 are considered below in further detail.

5.4.6.1 C.5.M: $\text{HCO} + \text{M} \leftrightarrow \text{H} + \text{CO} + \text{M}$

Reaction C.5.M has been separately considered in recent experimental (Santner *et al.*, 2015) and theoretical (Yang *et al.*, 2013) efforts at Princeton, and rate coefficient parameters may benefit from revision pending final outcomes of either these investigations or recent study of prompt HCO dissociation conducted at Argonne National Laboratory (Labbe *et al.*, 2016). Nevertheless, the present work retains

the Li *et al.* kC.5.M expression based on least-squares fit to a broad database of experimental rate coefficient determinations. Notably, the preliminary pressure-dependent theoretical calculations of Yang *et al.* find kC.5.Ar and kC.5.N2 low pressure limits that lie within the uncertainty bounds prescribed by Li *et al.*

5.4.6.2 C.6: $\text{HCO} + \text{O}_2 \leftrightarrow \text{CO} + \text{HO}_2$

To first approximation, the net reaction C.5.M (in reverse and with $\text{M} = \text{O}_2$) + C.6 yields



which effectively removes reactive H to form less reactive HO_2 in loose analogy to H.9.CO. This net reaction suggests the role of C.6 as a step-wise radical sink for reducing the reactivity of HCO-sensitive syngas flames as discussed above. Another net reaction to consider is C.6 + C.3



which indicates a potential energy surface including HCO, O_2 , CO, HO_2 , CO_2 , and OH. Further, reaction C.X1 suggests that HCO and O_2 may be able to react directly to form CO_2 and OH, bypassing the CO and HO_2 intermediates that serve both as products for C.6 and reactants for C.3. However, theoretical studies (S.J. Klippenstein, personal communication 2013; You *et al.*, 2007; Hsu *et al.*, 1996) concur that a substantial energy barrier exists for the direct reaction C.X1, and Hsu *et al.* compute the rate coefficient of C.X1 to be orders of magnitude slower than kC.3 at combustion temperatures. For this reason, the present work considers the only products of reaction between HCO and O_2 to be CO and HO_2 . Furthermore, reactions C.6 and C.3 are treated as independent processes.

For the present work, rate coefficient parameters for kC.6 are taken directly from the recent theoretical recommendation of S.J. Klippenstein (personal communication 2013):

$$k_{\text{C.6}} = 7.83 \times 10^{10} T^{0.521} \exp(262/T) \text{ cm}^3/\text{mol/s}$$

for temperatures of 200-2000 K. This expression includes a constant factor of 1.3 upward shift to bring the initial theoretical prediction into quantitative agreement with experimental kC.6 determinations of DeSain *et al.* (2001) for $296 \leq T \leq 673$ K. For temperatures between 500 and 2000 K, the presently

adopted Klippenstein kC.6 expression is about 30-40% lower than that of Timonen *et al.* (1988), which is used in the Li-C₁ model.

5.4.6.3 C.7: $\text{HCO} + \text{H} \leftrightarrow \text{CO} + \text{H}_2$

Since HCO is generated from a large H atom pool by reaction C.5.M in certain syngas flames, the recombination of additional H with HCO generated by this process is, not surprisingly, a somewhat sensitive parameter for prediction of these conditions. In the forward direction, reaction C.7 proceeds at nearly collisional rates through both direct H abstraction and excited CH₂O* adduct channels. The CH₂O* molecule may either dissociate to reactants H and HCO or products CO + H₂, or collisionally stabilize to CH₂O. This mechanism implies that C.7 is a pressure-dependent reaction; however, recent theoretical work of Troe & Ushakov (2007) suggests that C.7 is adequately described by low pressure limit processes at pressures up to at least several atm. At present, literature experimental and theoretical determinations for kC.7 are not sufficiently resolved to ascribe pressure-dependence and bath gas collisional efficiencies for kC.7 with any level of confidence. Accordingly, the present work further considers only the LPL rate coefficient for C.7.

Below 1000 K, many of the experimental data for kC.7 agree to within a factor of ~2 with the measurements of Friedrichs *et al.* (2002) and the recent classical trajectory calculations of Troe & Ushakov (2007). Both of these studies are in excellent agreement and find that kC.7 is essentially temperature-independent up to 1000 K, but neither study considers higher temperatures relevant to flames. The earlier variational transition state theory calculations of Harding & Wagner (1988) also find that kC.7 is essentially temperature independent below 1000 K, but that it rises by a factor of ~2 at 3000 K.

The present work provides a modified Arrhenius fit to approximate the Harding & Wagner temperature dependence and scales it upward by a factor of ~2 to coincide with the temperature-independent Friedrichs *et al.* and Troe & Ushakov kC.7 recommendations below 1000 K:

$$k_{\text{C.7}} = 1.45 \times 10^{13} T^{0.30} \exp(125.8/T) \text{ cm}^3/\text{mol/s}$$

for temperatures of 300-3000 K. Relative to kC.7 recommendations from these three studies, the present fit improves agreement for kC.7 with the nominal high temperature recommendations of Cribb *et al.* (1992) and Hidaka *et al.* (1993), which are based on complex kinetic model fitting of experimental data.

5.4.7 Consideration of HOCO Chemistry

From the pressure-temperature boundary demarcated in Figure 5.5 and earlier discussion of the CO+OH reaction system in Section 5.4.2, it appears that the CO₂+H product channel C.1 may adequately describe all relevant Mechanism 1 chemistry for conditions commonly encountered during combustion. It seems reasonable to assume that for conditions that do not favor HOCO formation, any small quantity of HOCO that does form will react rapidly to donate H-atom in a subsequent bimolecular process (Rasmussen *et al.*, 2008), to similar net effect as C.1.

However, the sufficiency of this simplifying assumption for predicting combustion phenomena was tested for the entire database of homogeneous validation targets used herein, including observables from shock tube and rapid compression machine (RCM) ignition delays; and flow reactor, stirred reactor, and shock tube species evolution profiles. These observables correspond to pressure conditions from sub-atmospheric to 450 atm; temperatures from below 1000 K to in excess of 2800 K; fuel compositions from 0-99% CO; fuel dilutions spanning three decades; chemically-relevant bath gases including He, Ar, N₂, O₂, CO₂, and H₂O; stoichiometry from very lean to very rich; and timescales of approximately 10⁻⁵ to 10⁰ seconds. Flame targets were not used as characteristic temperatures imply extraordinary pressures for significant flux to HOCO formation. Briefly, the pressure-dependent HOCO chemistry submodel of Rasmussen *et al.*, was incorporated into initial variations of the present model, and HOCO was treated as an undistinguished “average” of *trans*- and *cis*- isomers. For almost all conditions, the additional HOCO chemistry appeared not to materially affect model predictions.

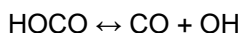
However, shock tube ignition delay time predictions at high pressure and low-to-intermediate temperature conditions studied by Petersen *et al.* (2007) were accelerated by factors (of nearly 10 at ~775 K, for example) as a result of including the Rasmussen *et al.* HOCO chemistry submodel. This is important because the Petersen *et al.* study shows that an orders of magnitude discrepancy exists between syngas ignition delay times predicted by homogeneous chemical kinetic models and those observed experimentally in a variety of facilities. Rasmussen *et al.* suggest that hitherto omitted HOCO chemistry may also be important in (partially) explaining the observed discrepancy at these conditions. Contemporary work of Chaos & Dryer (2008) suggests, however, that the homogeneous chemistry sensitivities to perturbations in the mild ignition transition to strong ignition are such that many factors

may contribute to significant ignition delay time perturbation (e.g., catalysis, inhomogeneous mixing, trace contamination of the reactants, or departures from physical model assumptions). Such perturbing effects, either singly or acting in unison, could satisfactorily explain the apparent orders of magnitude discrepancy in the mild ignition regime. There is now a significant body of literature (e.g., Pang *et al.*, 2009; Medvedev *et al.*, 2010; Urzay *et al.*, 2014) that supports the latter position - what had been thought to be homogenous kinetic experiments are perturbed by facility effects and heterogeneous initiation phenomena. Nevertheless, the results of such non-idealities do not preclude the concurrent effect of HOCO chemistry that was previously omitted from kinetic models.

The apparent impasse regarding the effect of HOCO chemistry seems to be resolved by updating the rate coefficient for the reaction



from the estimate used by Rasmussen *et al.* to the theory- and experiment-based rate coefficient expression developed by Glarborg & Marshall (2009). This updated rate coefficient is substantially slower (proceeding from left to right) than the initial estimate, leading to reduced flux of CO-“catalyzed” net H₂O₂ decomposition via CX.2 and



at the conditions considered by Petersen *et al.* (2007). The reduced production of OH formed by this sequence altogether suppresses the reactivity initially ascribed to including the Rasmussen *et al.* HOCO chemistry. In other words, *predictions of the Rasmussen et al. HOCO submodel updated with the Glarborg & Marshall rate coefficient for C.X2 are indiscernible from the base model altogether lacking HOCO chemistry.*

Finally, it is worth noting that the recent study of Nilsson & Konnov (2016) concurs with present overall conclusions regarding the relative unimportance of HOCO chemistry in describing syngas combustion, at least for conditions considered by the existing literature validation database. However, it is worthwhile to acknowledge that HOCO chemistry participates in the oxidation of small oxygenated species (e.g., formic acid, small esters), though in these cases, its principal formation mechanism is not via CO+OH.

5.5 Chapter Summary

The preceding sections have discussed general updates to the thermochemistry, transport, and elementary kinetic rate coefficient parameters of the CO submodel of the Li-C1 kinetic model (Li *et al.*, 2007). The most significant updates are to elementary rate coefficient parameters, and are listed below:

- The relative H.9.M collisional efficiencies for CO₂ relative to Ar and N₂ have each been reduced by 25% from the original Burke-H2 (Burke *et al.*, 2012) values. This is based on absolute rate coefficient expressions for kH.9.CO2_{LPL} developed in Part I of this thesis.
- A theory-based expression kC.3 has been provisionally updated to reflect improved theory since the study of You *et al.* (2007). Forthcoming work of Klippenstein will likely provide a more formal update to this rate coefficient, which is influential in syngas ignition at higher pressures and low/intermediate temperatures.
- Both the high pressure and low pressure limits of kC.4 have been updated to reflect recent theoretical treatment by Jasper (2013). The present pressure-dependent parameterization appears to be unique in the combustion modeling literature and updates decades-old treatment of kC.4 due to Troe (1975) and Westmoreland *et al.* (1986) for the HPL and LPL, respectively.

In addition, the relative H.9.M collisional efficiencies for H₂O and O₂, and the chemistry of the HOCO molecule have been considered. In the case of the former, no strong evidence was found suggesting a change from the values inherited from the Burke-H2 model. In the case of the latter, no strong evidence was found suggesting that including HOCO chemistry in the CO submodel meaningfully affects syngas model predictions at conditions relevant to the existing validation database.

The complete model, including Burke-H2 submodel, is provided in the Appendix in a format intended to be directly applied to the CHEMKIN II suite of codes (*e.g.*, Lutz *et al.* (1997); Kee *et al.*, 1985), as well as later versions of CHEMKIN (*e.g.*, Kee *et al.*, 2003). However, some re-formatting may be necessary, and, in particular, it is worth noting that the standard CHEMKIN interpreter must be told to ignore the modified transport parameters of Wang *et al.* (2007). It instead uses the provided Lennard-Jones parameters to compute transport coefficients for the binary systems that would otherwise be

considered by the modified transport treatment. As the time of completion of this thesis, the hyperlink provided in the transport submodel for the alternative Wang *et al.* transport interpreter was still active.

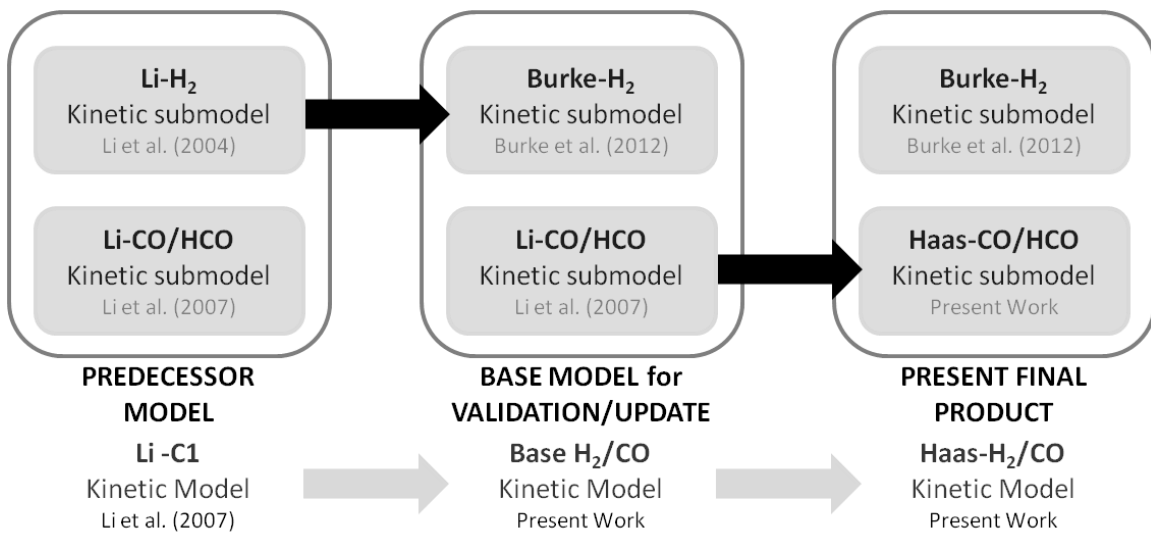


Figure 5.1 – Scheme for present H₂/CO kinetic model development.

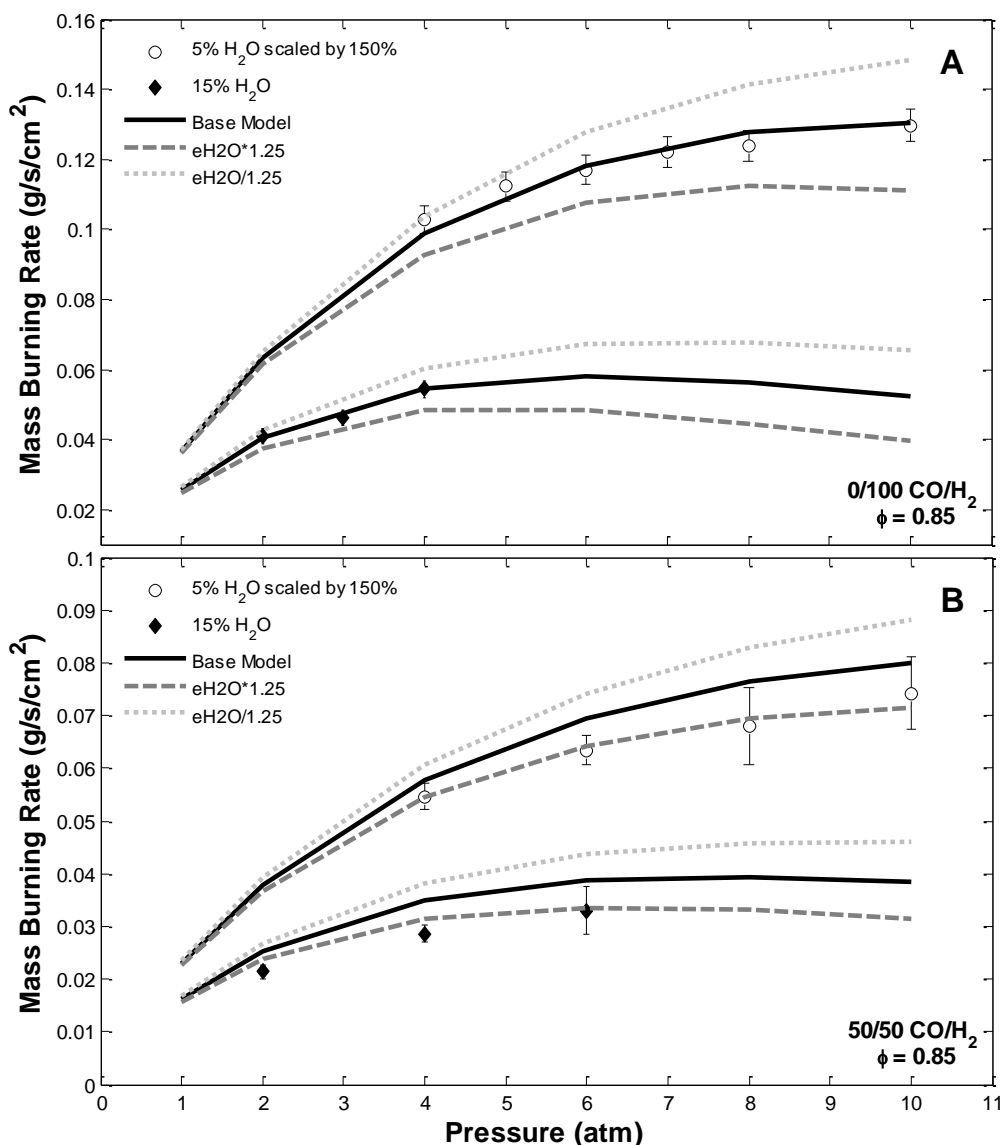


Figure 5.2 – Comparison of model predictions and Santner *et al.* (2013) experimental laminar mass burning rate measurements for H₂O-diluted a) H₂ flames and b) syngas flames.

Model predictions for these conditions display clear and significant sensitivity to $\epsilon_{\text{H}_2\text{O}/\text{Ar}}$, the collisional efficiency of $M = \text{H}_2\text{O}$ relative to Ar, in kH.9.M when this parameter is varied by 25% from the Burke-H₂ kinetic model value. In this figure, eH₂O has the same meaning as $\epsilon_{\text{H}_2\text{O}/M}$. The original Burke-H₂ model collisional efficiencies are kept in the present kinetic model update based on their agreement with a range of literature rate coefficient determinations, as well as the present quality of model predictions compared to experimental measurements.

For the present comparison purposes of this figure and Figures 5.3 and 5.4, “Base Model” refers to the hybridized Burke-H₂ + Li-CO/HCO model presented in Figure 5.1, with additional present updates to thermochemistry and transport as discussed in Sections 5.2 and 5.3 of the body text. This definition of “Base Model” serves to isolate effects on model predictions solely due to changes in assumed reaction rate coefficient values.

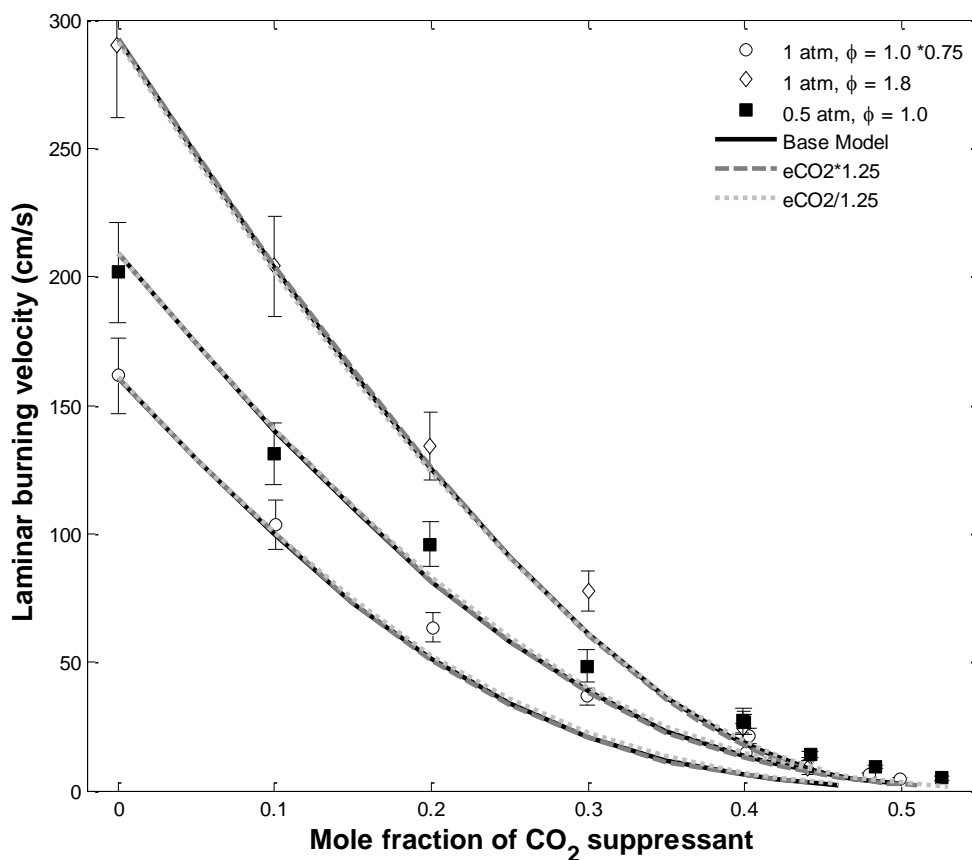


Figure 5.3 – Comparison of model predictions and Qiao *et al.* (2007) experimental laminar burning velocity measurements for CO₂-diluted H₂-air flames.

Predictions from three variants of the present base H₂/CO kinetic model are compared to assess the effect of modifying the original Burke-H₂ collisional efficiency for CO₂ by a factor of 25%. These predictions are clearly insensitive to this parameter. In this and the following figure, eCO₂ has the same meaning as $\epsilon_{CO_2/M}$.

The recommended ~25% reduction in $\epsilon_{CO_2/Ar}$ developed in the present work does not discernibly affect the predictive ability of the Burke-H₂ model against its validation target set, for which CO₂ chemistry validation considers only these three Qiao *et al.* laminar burning rate datasets. The present change, based on more direct rate coefficient measurements discussed in Chapter 4, as well as more extensive validation for H₂/CO rank targets, therefore retroactively updates the Burke-H₂ model while preserving its predictive abilities. The revised collisional efficiency for CO₂ is adopted as part of the updated kinetic model.

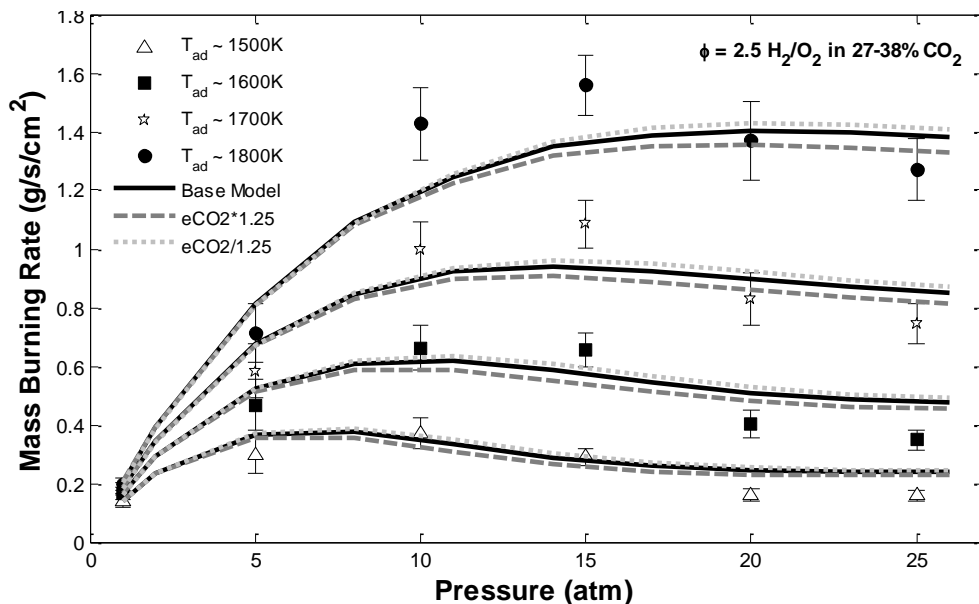
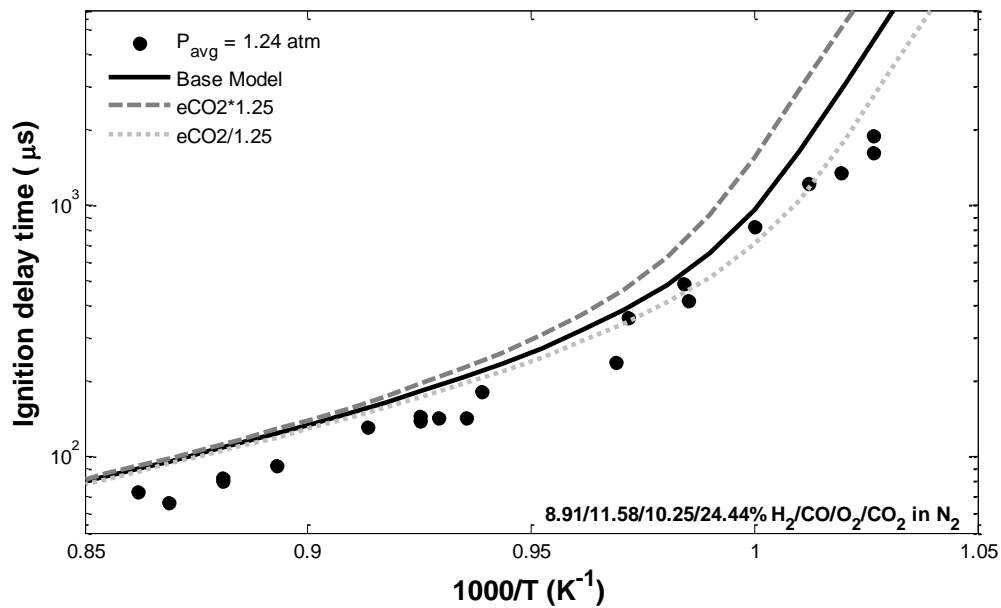


Figure 5.4 – Comparison of model predictions and experimental measurements for which high levels of CO_2 have been included in the reactants.

The presently recommended ~25% reduction in the CO_2 collisional efficiency for kH.9.M increases predicted reactivity of CO_2 -sensitized syngas ignition delay times near the explosion limit, such as those of Vasu *et al.* (2011) (top), and slightly increases the predicted reactivity of high pressure CO_2 -diluted H_2 flames such as those studied by Burke *et al.* (2010) (bottom).

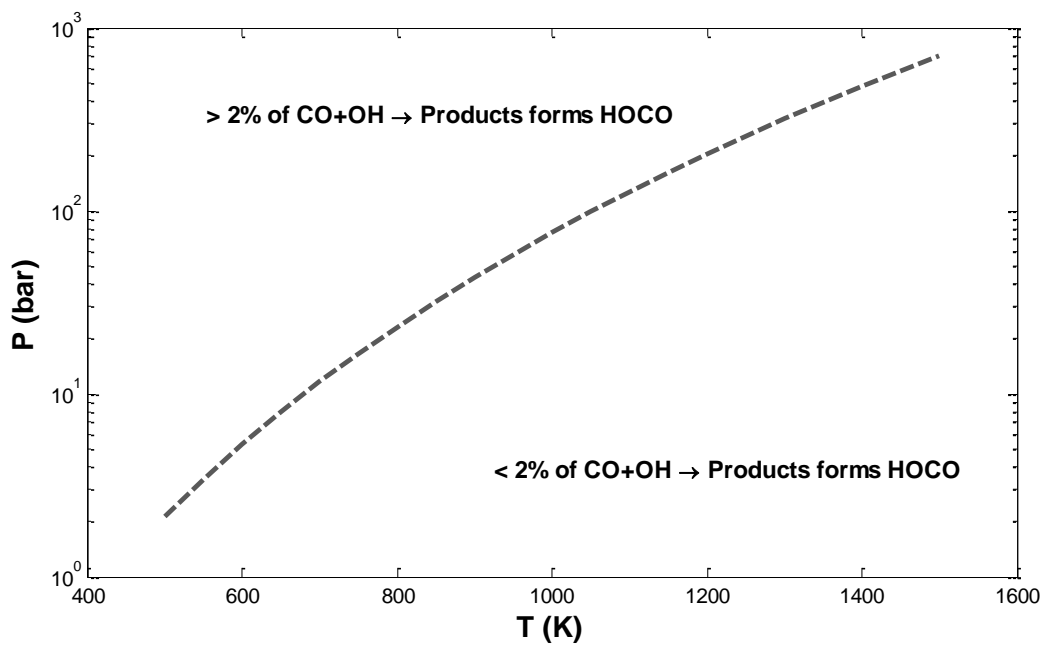


Figure 5.5 – Pressure-temperature relationship delineating conditions for which stabilized HOCO radical may form at non-negligible rates, based on Joshi & Wang (2006).

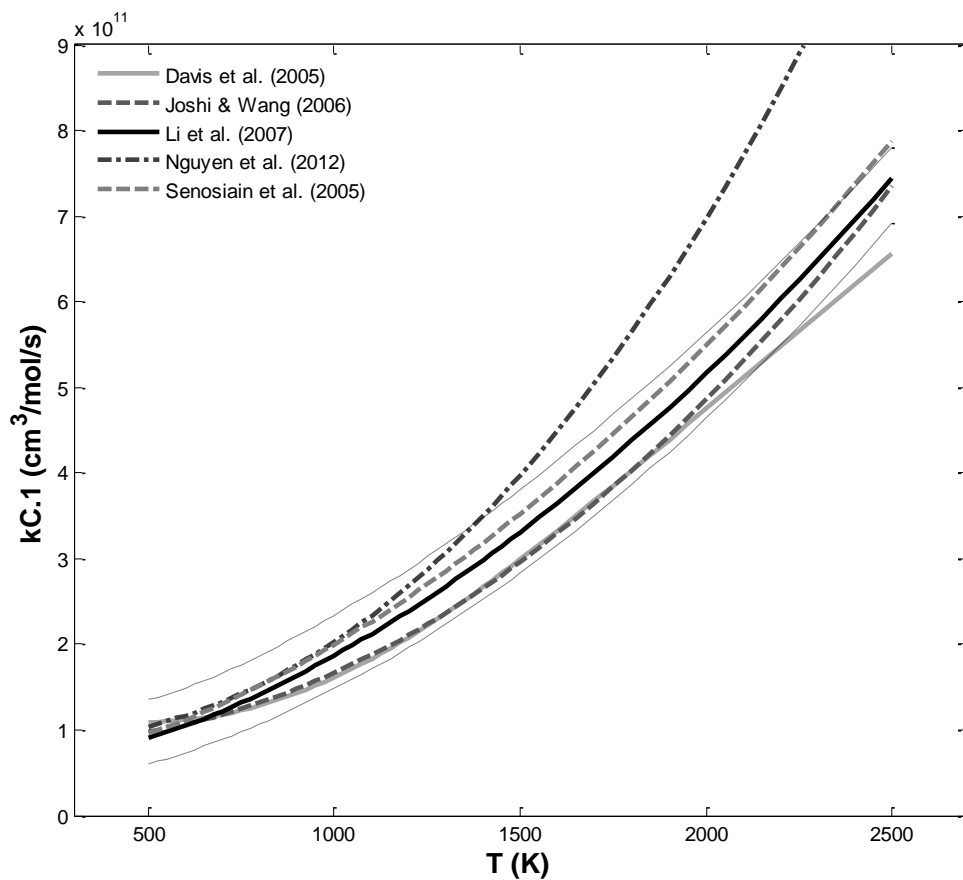


Figure 5.6 – Comparison of rate coefficient expressions for C.1 ($\text{CO} + \text{OH} \rightarrow \text{CO}_2 + \text{H}$) for temperatures between 500 and 2500 K.

The thin dashed lines represent upper and lower 95% confidence interval bounds for $k_{\text{C.1}}$ recommended by Li *et al.* (2007) based on extensive review of experimental literature – note the sign error apparent in the activation energies for these bounds initially reported by Li *et al.*

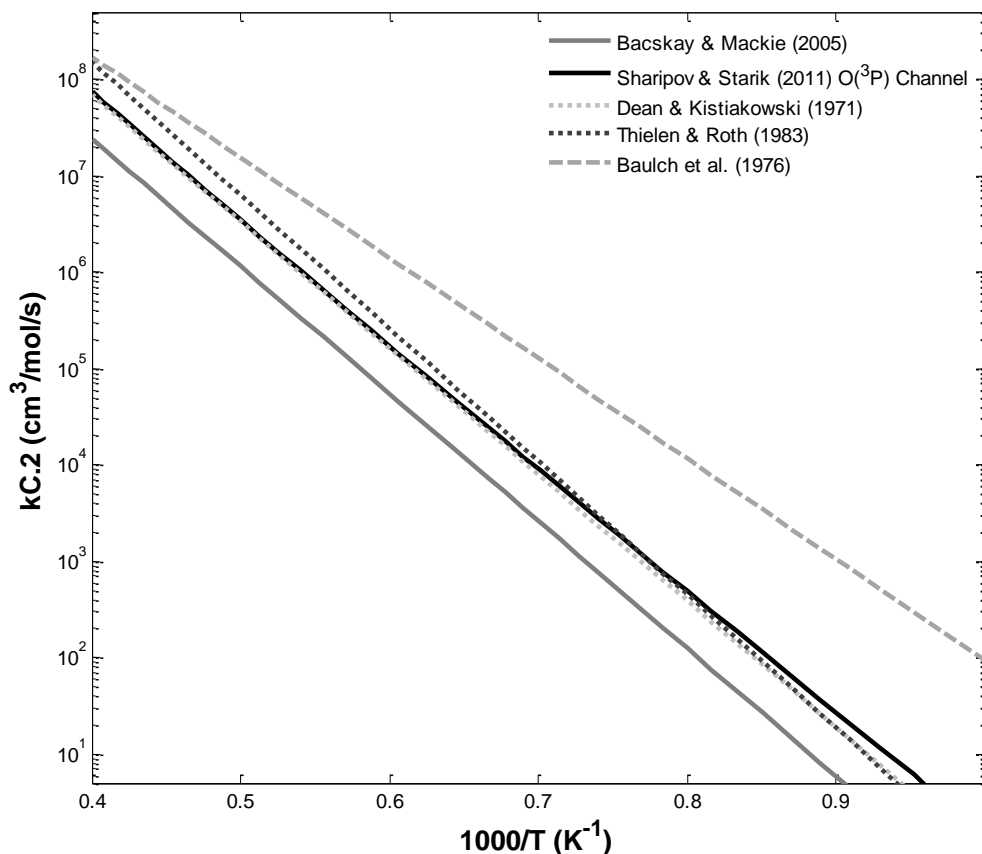


Figure 5.7 – Comparison of rate coefficient expressions for C.2 ($\text{CO} + \text{O}_2 \rightarrow \text{CO}_2 + \text{O}$) for temperatures between 1000 and 2500 K.

The Baulch *et al.* $k_{\text{C.2}}$ expression appears in the later compilation of Tsang & Hampson (1986), from which the Li-C₁ model derives its $k_{\text{C.2}}$ parameters. Note that rates of C.2 below 1000 K are exceptionally slow, regardless of choice of expression.

For sake of comparison, expressions plotted in the figure may extend beyond original authors' recommended temperature range; however, the present treatment is consistent with combustion kinetic models, which routinely employ extrapolation of rate coefficients to cover temperature and pressure ranges outside those specified by primary rate coefficient recommendations.

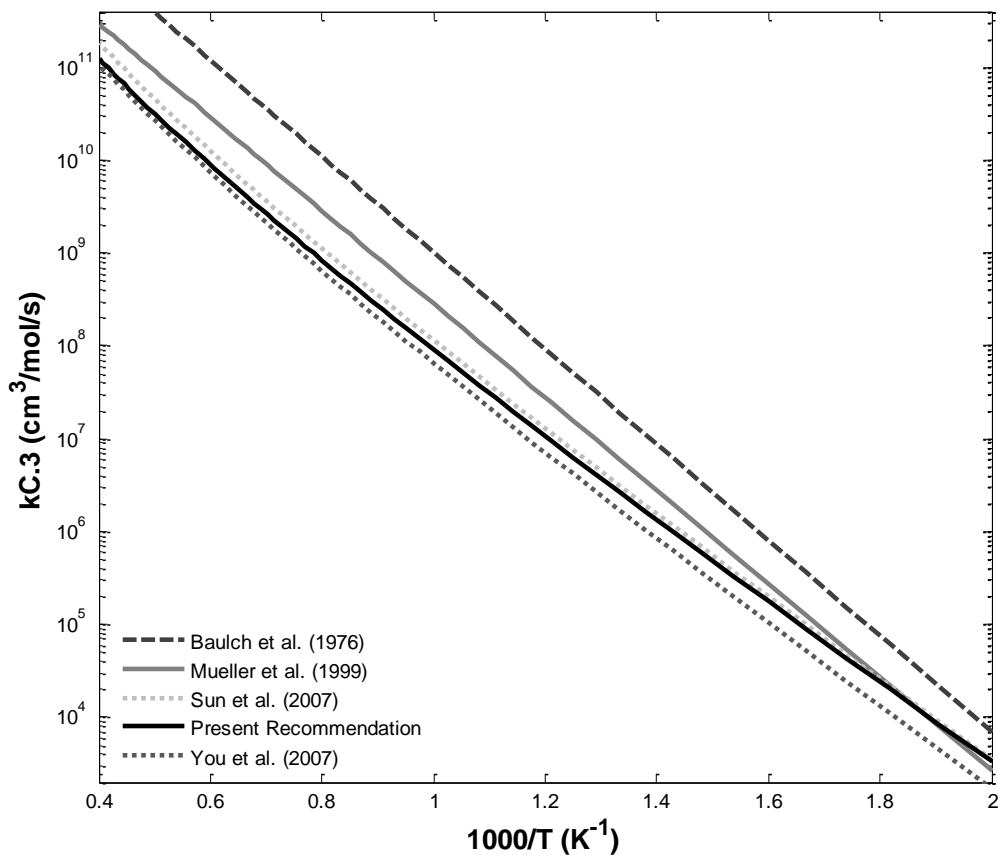


Figure 5.8 – Comparison of rate coefficient expressions for C.3 ($\text{CO} + \text{HO}_2 \rightarrow \text{CO}_2 + \text{OH}$) for temperatures between 500 and 2500 K.

For sake of comparison, expressions plotted in the figure may extend beyond original authors' recommended temperature range; however, the present treatment is consistent with combustion kinetic models, which routinely employ extrapolation of rate coefficients to cover temperature and pressure ranges outside those specified by primary rate coefficient recommendations.

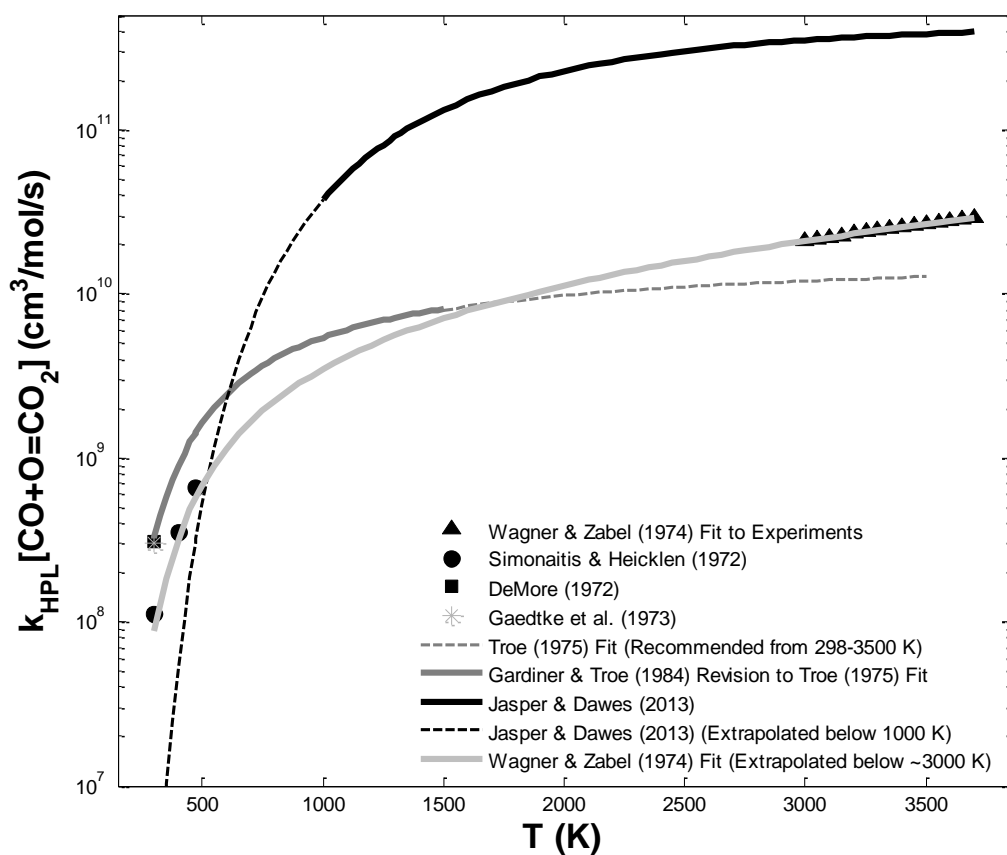


Figure 5.9 – Comparison of rate coefficient determinations for C.4.HPL ($\text{CO} + \text{O} \rightarrow \text{CO}_2$) for $300 \leq T \leq 3700$ K.

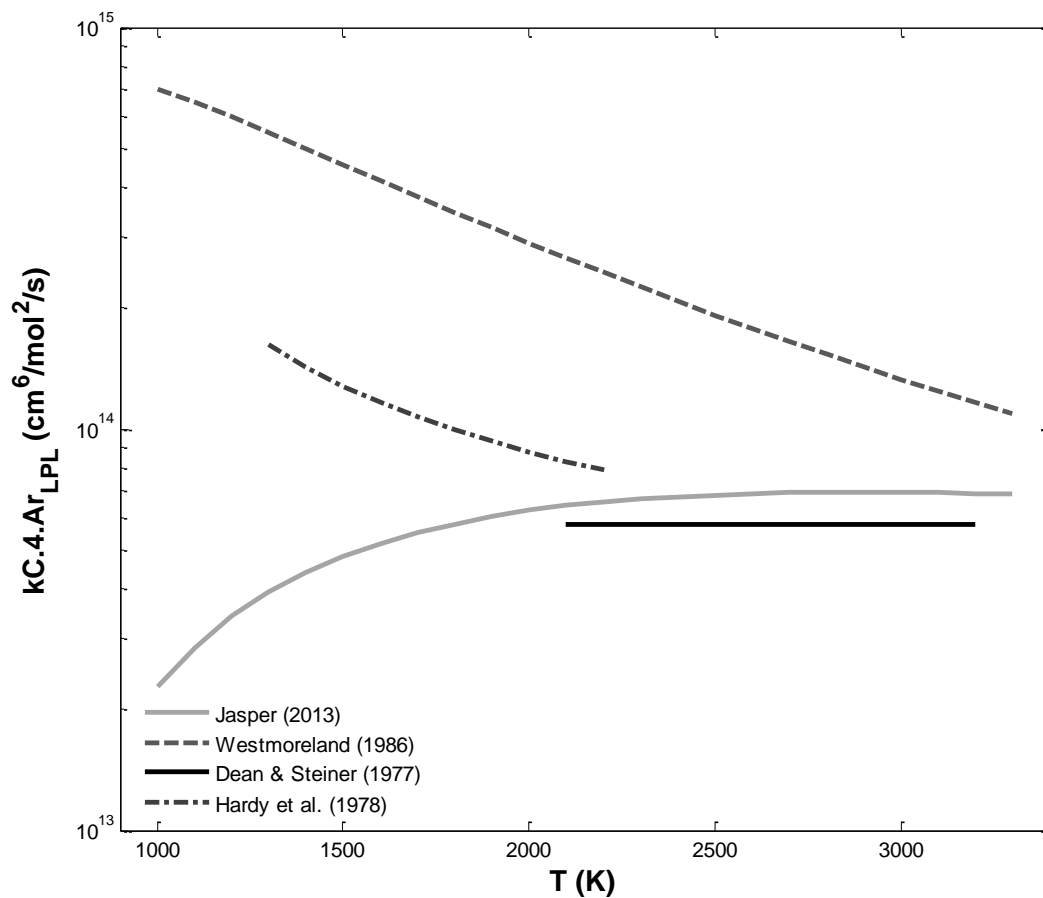


Figure 5.10 – Comparison of rate coefficient determinations for C.4.Ar_{LPL} for 1000 ≤ T ≤ 3300 K.

Experiment-based kC.4.Ar_{LPL} determinations of Dean & Steiner and Hardy *et al.* are presented as described in the respective studies (*i.e.*, without modern kinetic modeling reinterpretation). Present reinterpretation of the Hardy *et al.* results are presented in Figure 5.11.

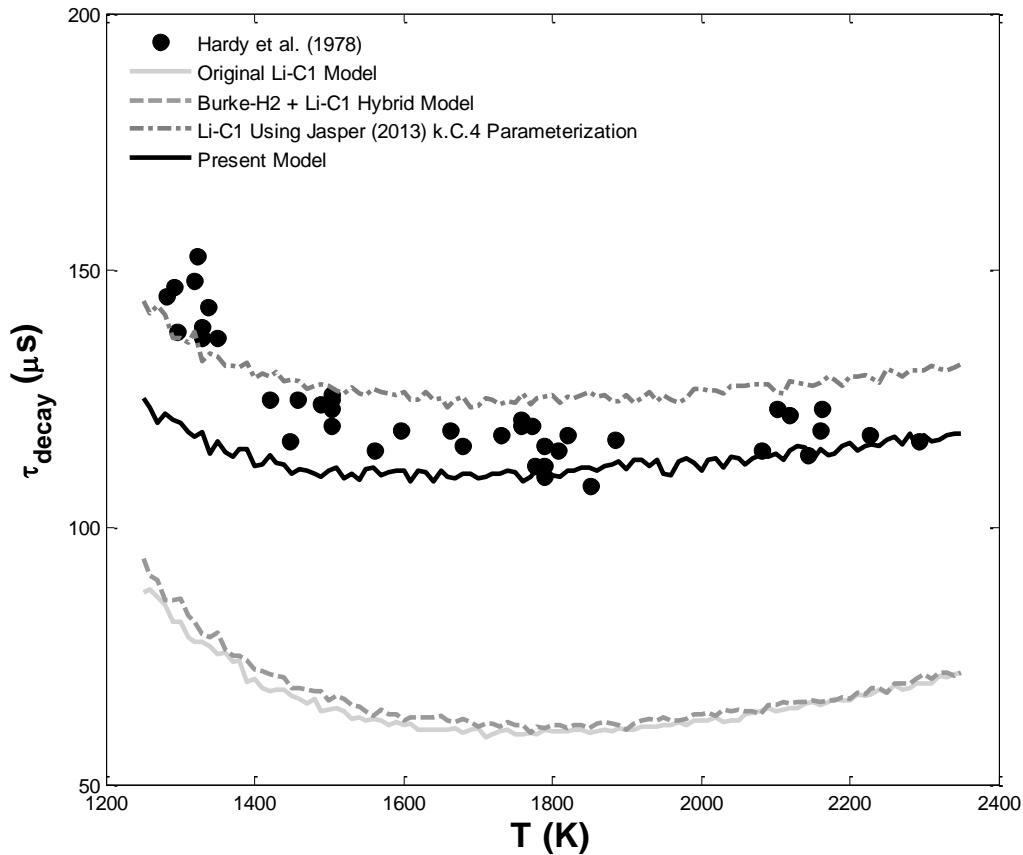


Figure 5.11 – Comparison among predictions of several kinetic model variants and experimental 435 nm CO flame band emission decay measurements of Hardy *et al.* (1978).

The original Li-C1 model uniformly under-predicts the emission decay observable by a factor of ~ 2 , and complete replacement of the Li-C1 H₂ submodel with the extensively updated Burke-H2 model negligibly changes this result despite updated expressions for reactions such as H.1 ($\text{H} + \text{O}_2 \leftrightarrow \text{O} + \text{OH}$). The demonstrated insensitivity to kH.1 is a particular feature of the experimental conditions and the $\frac{3}{4}$ - to $\frac{1}{4}$ -maximum post-peak emission decay time metric.

However, using the original Li-C1 model and replacing only the kC.4 expressions with those of Jasper (2013) shifts the predictions to within very good agreement with the measurements. The effect of all other CO-rank chemistry modifications discussed in this Chapter is a slight reduction in predicted decay time, though still in good agreement with the measurements over most of the temperature range. At higher temperatures, the observable is most sensitive to kC.4 by factors (~ 5 from 1800-2350 K) compared to the rate coefficient for H.7.M ($\text{O} + \text{H} + \text{M} \leftrightarrow \text{OH} + \text{M}$), which the second most influential reaction rate coefficient. At lower temperatures, kC.1 and kH.1 remain influential.

Chapter 6: Concluding Remarks and Perspectives on Related and Future Work

This thesis has examined the kinetics of several important small molecule species that participate in the foundational ranks of the combustion chemistry hierarchy. In particular, it describes a new high pressure laminar flow reactor (HPLFR) facility that was developed to study formation of HO₂ by the reaction H.9.M (H+O₂(+M) ↔ HO₂(+M)). This thesis further discusses a kinetic submodel addressing thermochemistry, transport, and reaction kinetics among species of the H₂ and CO ranks of the combustion chemistry hierarchy presented in Figure 1.1.

In order to provide confidence in the ability of the newly-built and hitherto untested HPLFR to provide accurate determinations of kH.9.CO₂, the facility was first tested using Ar and N₂ bath gases to determine values of kH.9.Ar and kH.9.N₂, respectively. These latter HPLFR rate coefficient determinations compared favorably with literature Consensus, suggesting that the experimental and interpretive methodology applied to CO₂ bath gas experiments provides reliable values of kH.9.CO₂(T,P).

In this context, the experimental efforts to measure kH.9.Ar and kH.9.N₂ yielded methodological confirmation for subsequent investigation of kH.9.CO₂. However, the relative rate approach used for determining kH.9.M from kN.1 and experimental HPLFR measurements also permitted re-purposing of the M = Ar and N₂ data to quantify kN.1 at significantly higher pressures than previously reported in the literature. This collateral study of kN.1 is reported in Haas & Dryer (2015) as an extension of analysis depicted in Figure 3.22. Notably, this kN.1 study also re-purposes the high pressure flow reactor experiments of Mueller *et al.* (1998), which also originally sought to determine kH.9.M (M = Ar, N₂) from relative rate experiments similar to those conducted in the HPLFR. Future work specific to the H.9.M/N.1 system could involve similarly re-purposing the H.9.M-motivated measurements of Ashman & Haynes (1998) and Bromly *et al.* (1995), for example. Nevertheless, this idea of data re-purposing is significantly more general than just the H.9.M/N.1 system (*cf.*, Scire *et al.*, 2001, for example) and may offer an avenue for further contributions to the experimental study of combustion kinetics that, somewhat counterintuitively, requires no new experimental measurements.

Another approach related to data re-purposing is the critical re-interpretation of existing literature data to offer new insights on or quantitative analysis of the chemistry initially intended for study by such

literature (*i.e.*, with the same purpose). This was employed extensively herein to extend the temperature range of $k_{H.9.CO_2_{LPL}}$ determinations significantly beyond the range accessed by the HPLFR experiments. Fusion of present HPLFR $k_{H.9.CO_2}$ values and re-interpreted $k_{H.9.CO_2}$ determinations from static reactor, shock tube, and other flow reactor facilities permitted development of uncertainty-bounded, absolute rate coefficient expressions $k_{H.9.CO_2_{LPL}}$ (Equations 4.10 and 4.11). Similarly, re-interpretation here of the Hardy *et al.* (1978) C.4.M-sensitive experiments using a significantly more accurate kinetic model enabled (a limited) experimental validation of the Jasper (2013) pressure-dependent $k_{C.4}$ expressions developed from *ab initio* theory and incorporated into the CO chemistry submodel discussed in Chapter 5.

One broad conclusion that can be drawn from this thesis work is that *a significant corpus of future progress in combustion chemical kinetics can (and should) rely on thoughtful stewardship, re-purposing, and/or re-interpretation of existing experimental data.* The value in reincarnating literature data is not a unique observation due to this thesis work; however, it merits the present reiteration. For areas of research (such as combustion chemistry) supported by relatively scarce (funding) resources, the best new experiment to conduct may be the experiment that was *not* conducted in deference to thoughtful interpretation of one already existing in the literature – the originality of such an experiment comes from the fresh perspective offered by novel elucidation of the experimental information content. Now more than ever, such retrospective-cum-prospective experiments are possible due to progress in *ab initio* theory, kinetic model accuracy, new modeling paradigms (*e.g.*, Burke *et al.*, 2013), and enlightened treatment of experimental non-idealities (*e.g.*, Dryer *et al.*, 2014; Santner *et al.*, 2014). Moreover, successful leverage of these tools against the existing experimental database can also serve to guide the design and execution of truly “novel” (Vinkers *et al.*, 2015) combustion experiments that may offer amplified constraint of the target chemistry rather than redundancy of existing information content resulting from a lack of retrospective awareness, among other issues.

The $k_{H.9.CO_2_{LPL}}$ expressions developed from Part I of this thesis contribute just one set of many kinetic parameters that together form the H_2/CO chemistry model discussed in Part II. The purpose in developing this kinetic model was to generally update the CO/syngas chemistry model of Li *et al.* (2007) with fitting- and optimization-free parameters for thermochemistry, transport, and elementary reaction

kinetics of CO-rank chemistry in particular. The final product of model parameters (Appendix A) based mostly on theory or high quality experimental measurements remains unoptimized to the relatively large set of relevant literature experimental “validation” measurements. This permits true validation of this particular model in the future; however, for present purposes, such validation has not been pursued due to the significant interaction of CO-rank chemistry with the H₂ oxidation chemistry submodel. Few if any validation experiments effectively isolate CO chemistry to an extent that the present CO submodel modifications can be independently evaluated against “systems”-type experiments that do not attempt to isolate and study single elementary reactions. Such CO chemistry-isolating measurements are desirable future additions to the experimental literature database.

Notwithstanding any potentially significant impacts of recent and forthcoming advances in the description of transport (*e.g.*, Dagdigian, 2015a and 2015b) and H₂- and CO-rank elementary reaction kinetics (*e.g.*, Burke *et al.*, 2013; Klippenstein, 2017) on model predictions, the present model development work provides some insight on syngas oxidation chemistry and suggests future lines of research. From a modeling perspective, the tremendous sensitivity of many validation observables to the rate of C.1 (CO+OH ↔ CO₂+H) is moderated by a rate coefficient with very low uncertainty of ~20% and generally insignificant competing flux to form HOCO over the range of applications-relevant combustion conditions. Despite the low uncertainty of kC.1, the choice of particular rate coefficient expression still considerably impacts predictions of common experimental observables (*e.g.*, ignition delay time, laminar burning rate, flow reactor species evolution). This poses a significant hurdle to future improvements in the accuracy of kC.1 since the narrow existing rate coefficient uncertainty challenges the uncertainties propagated through even the most carefully designed and operated kC.1 determination experiments.

Moreover, the strong coupling between the H₂ chemistry submodel and reaction C.1 generally overwhelms direct experimental study of the other CO oxidation reactions C.2-C.4.M to the point that hydrogenous impurities at few parts per million levels may skew quantitative determination of rate coefficients for these other reactions. Rate coefficient determination for these secondary reactions is best treated with theoretical approaches, as reflected here in choice of corresponding rate coefficients. However, it is worth noting that though present treatment of kC.4.M relies on rate coefficient expressions determined from the theoretical work of Jasper (2013), very particularly designed experiments such as

those conducted by Hardy *et al.* (1978) offer a degree of experimental constraint for the C.4.M reaction system at combustion temperatures and pressures. Future, similarly sensitive experiments extending to beyond the Hardy *et al.* temperature and pressure range are desirable as additional support for the Jasper (2013) kC.4.M theory result.

Finally, it is worth noting that a recent study promoting a prompt HCO dissociation mechanism (Labbe *et al.*, 2016) challenges the status quo framework – present model included – for description of HCO-related gas phase kinetics. For purposes of H₂/CO combustion chemistry, this may pose little problem given the limited range of conditions and extent of influence that HCO chemistry plays. Such mechanistic uncertainty propagated into model predictions of laminar burning rate is likely of the same second order importance in syngas combustion as the interpretive uncertainty due to radiative heat transfer in the target validation experiments (Santner *et al.*, 2014). However, this is likely not the case for chemical systems sensitive to kinetics at sub-CO ranks, as Labbe *et al.* suggest in modeling of the CH₂O (via 1,3,5-trioxane) burning rates of Santner *et al.* (2015). To preserve hierarchical kinetic model structure, the assumed sufficiency of C.5.M-C.7 in describing HCO-related chemistry of syngas oxidation will likely need re-examination if the present model is to be extended to the full C₁ (*i.e.*, CH₂O and CH₃OH) chemistry rank and beyond.

Considering the recommendations for future work set out in the preceding paragraphs, it is clear that the combustion chemistry of small molecules remains a fertile research topic for experimentalists, kinetic modelers, and theoretical chemists, among others. More work – and perhaps a paradigm shift in kinetic model formalism – is needed to mitigate uncertainty and improve predictive accuracy to meet demands on the predictive ability of combustion chemistry submodels in the context of the larger, more complex multi-physics models used to describe combustion applications. Perhaps the largest uncertainty to overcome, however, is in determining how much more work is necessary to achieve this threshold, though consideration of such a topic is certainly beyond the scope of *this* thesis.

References

1. Ashman, P.J. *Aspects of homogeneous and heterogeneous reactions leading to the emission of oxides of nitrogen from combustion processes* Ph.D. Thesis, University of Sydney, 1999.
2. Ashman, P.J.; Haynes, B.S. *Rate coefficient of $H+O_2+M\rightarrow HO_2+M$ ($M=H_2O, N_2, Ar, CO_2$)*. Symposium (International) on Combustion, 1998, 27 (1), 185-191. DOI: 10.1016/S0082-0784(98)80404-9.
3. Ashmore, P.G.; Tyler, B.J. *Reaction of hydrogen atoms with nitrogen dioxide*. Transactions of the Faraday Society, 1962, 58, 1108-1116. DOI: dx.doi.org/10.1039/tf9625801108.
4. ASME, 2007 Boiler and pressure vessel code. In *Section II – Part D*, American Society of Mechanical Engineers International: New York, NY, 2007.
5. Atri, G.M.; Baldwin, R.R.; Jackson, D.; Walker, R.W. *The reaction of OH radicals and HO₂ radicals with carbon monoxide*. Combustion and Flame, 1977, 30 (0), 1-12. DOI: 10.1016/0010-2180(77)90046-3.
6. Bacskay, G.B.; Mackie, J.C. *Oxidation of CO by SO₂: A theoretical study*. The Journal of Physical Chemistry A, 2005, 109 (9), 2019-2025. DOI: 10.1021/jp045086n.
7. Balakrishnan, N.; Billing, G.D. *A quantum-classical study of the reaction $CO(v_1, j_1)+OH(v_2, j_2) \rightarrow CO_2+H$* . The Journal of Chemical Physics, 1996, 104 (11), 4005-4011. DOI.
8. Baldwin, R.R.; Jackson, D.; Melvin, A.; Rossiter, B.N. *The second limit of hydrogen + carbon monoxide + oxygen mixtures*. International Journal of Chemical Kinetics, 1972, 4 (3), 277-292. DOI: 10.1002/kin.550040305.
9. Bates, R.W.; Golden, D.M.; Hanson, R.K.; Bowman, C.T. *Experimental study and modeling of the reaction $H+ O_2+ M \rightarrow HO_2+ M$ ($M= Ar, N_2, H_2O$) at elevated pressures and temperatures between 1050 and 1250 K*. Phys. Chem. Chem. Phys., 2001, 3 (12), 2337-2342. DOI.
10. Baulch, D.L.; Bowman, C.T.; Cobos, C.J.; Cox, R.A.; Just, T.; Kerr, J.A.; Pilling, M.J.; Stocker, D.; Troe, J.; Tsang, W.; Walker, R.W.; Warnatz, J. *Evaluated kinetic data for combustion modeling: Supplement II*. Journal of Physical and Chemical Reference Data, 2005, 34 (3), 757-1397. DOI.
11. Baulch, D.L.; Drysdale, D.D.; Duxbury, J.; Grant, S.J. *Evaluated kinetic data for high temperature reactions, Vol. 3: Homogeneous gas phase reaction of the O₂-O₃ system, the CO-O₂-H₂ systems and of sulphur-containing species*. Butterworths: London, 1976.
12. Brabbs, T.A.; Robertson, T.F. *The carbon dioxide chaperon efficiency for the reaction $H+O_2+M\rightarrow HO_2+M$ from ignition delay times behind reflected shock waves*. NASA Technical Memorandum 100125, NASA Lewis Research Center, 1987.
13. Bromly, J.H.; Barnes, F.J.; Nelson, P.F.; Haynes, B.S. *Kinetics and modeling of the H₂-O₂-NO_x system*. International Journal of Chemical Kinetics, 1995, 27 (12), 1165-1178. DOI: 10.1002/kin.550271204.
14. Burcat, A.; Ruscic, B. *Third millenium ideal gas and condensed phase thermochemical database for combustion with updates from Active Thermochemical Tables*. Report ANL-05/20 and Report TAE 960, Argonne National Laboratory and Technion-IIT, Aerospace Engineering, September 2005.

15. Burke, M.P.; Chaos, M.; Dryer, F.L.; Ju, Y. *Negative pressure dependence of mass burning rates of H₂/CO/O₂/diluent flames at low flame temperatures*. Combustion and Flame, 2010, 157 (4), 618-631. DOI: 10.1016/j.combustflame.2009.08.009.
16. Burke, M.P.; Chaos, M.; Ju, Y.; Dryer, F.L.; Klippenstein, S.J. *Comprehensive H₂/O₂ kinetic model for high-pressure combustion*. International Journal of Chemical Kinetics, 2012, 44 (7), 444-474. DOI: 10.1002/kin.20603.
17. Burke, M.P.; Klippenstein, S.J.; Harding, L.B. *A quantitative explanation for the apparent anomalous temperature dependence of OH + HO₂ = H₂O + O₂ through multi-scale modeling*. Proceedings of the Combustion Institute, 2013, 34 (1), 547-555. DOI: 10.1016/j.proci.2012.05.041.
18. Burke, S.M.; Metcalfe, W.K.; Herbinet, O.; Battin-Leclerc, F.; Haas, F.M.; Santner, J.; Dryer, F.L.; Curran, H.J. *An experimental and modeling study of propene oxidation: Part I: Speciation measurements in jet-stirred and flow reactors*. Combustion & Flame, 2014, 161 (11), 2765-2784. DOI: 10.1016/j.combustflame.2014.05.010.
19. Chaos, M.; Dryer, F.L. *Syngas combustion kinetics and applications*. Combustion Science and Technology, 2008, 180 (6), 1053-1096. DOI: 10.1080/00102200801963011.
20. Colket, M.B.; Naegeli, D.W.; Glassman, I. *High temperature oxidation of acetaldehyde*. Symposium (International) on Combustion, 1977, 16 (1), 1023-1039. DOI: 10.1016/S0082-0784(77)80393-7.
21. Committee on America's Energy Future; National Academy of Sciences; National Academy of Engineering; National Research Council of the National Academies. *America's energy future: technology and transformation*. The National Academies Press: 2009.
22. Cribb, P.H.; Dove, J.E.; Yamazaki, S. *A kinetic study of the pyrolysis of methanol using shock tube and computer simulation techniques*. Combustion and Flame, 1992, 88 (2), 169-185. DOI: 10.1016/0010-2180(92)90050-Y.
23. Crocco, L.; Glassman, I.; Smith, I.E. *Kinetics and mechanism of ethylene oxide decomposition at high temperatures*. The Journal of Chemical Physics, 1959, 31 (2), 506-510. DOI.
24. Curran, H.J.; Bourque, G.; Petersen, E.L.; Healy, D.; Donato, N.S.; Aul, C.J.; Zinner, C.M.; Kopp, M.M.; Polley, N.L.; Kalitan, D.M. Natural Gas III. Version c5_49. Available at: <http://c3.nuigalway.ie/mechanisms.html>, 2010. (Accessed July 2013).
25. Dagaut, P.; Cathonnet, M.; Rouan, J.P.; Foulatier, R.; Quilgars, A.; Boettner, J.C.; Gaillard, F.; James, H. *A jet-stirred reactor for kinetic studies of homogeneous gas-phase reactions at pressures up to ten atmospheres (≈1 MPa)*. Journal of Physics E: Scientific Instruments, 1986, 19 (3), 207. DOI.
26. Dagdigian, P.J. *Accurate transport properties for H-CO and H-CO₂*. The Journal of Chemical Physics, 2015a, 143 (5), 054303. DOI: 10.1063/1.4927711.
27. Dagdigian, P.J. *Combustion simulations with accurate transport properties for reactive intermediates*. Combustion and Flame, 2015b, 162 (6), 2480-2486. DOI: 10.1016/j.combustflame.2015.02.016.
28. Davidson, D.F.; Petersen, E.L.; Röhrig, M.; Hanson, R.K.; Bowman, C.T. *Measurement of the rate coefficient of H+O₂+M→HO₂+M for M=Ar and N₂ at high pressures*. Symposium (International) on Combustion, 1996, 26 (1), 481-488. DOI: 10.1016/S0082-0784(96)80250-5.

29. Davis, S.C.; Diegel, S.W.; Boundy, R.G. *Transportation energy data book: Edition 31, Table 4-1*. Report ORNL-6987, Oak Ridge National Laboratory, 2012.
30. Davis, S.G.; Joshi, A.V.; Wang, H.; Egolfopoulos, F. *An optimized kinetic model of H₂/CO combustion*. Proceedings of the Combustion Institute, 2005, 30 (1), 1283-1292. DOI: 10.1016/j.proci.2004.08.252.
31. Dean, A.M.; Kistiakowsky, G.B. *Oxidation of carbon monoxide by oxygen in shock waves*. The Journal of Chemical Physics, 1970, 53 (2), 830-838. DOI.
32. Dean, A.M.; Kistiakowsky, G.B. *Oxidation of carbon monoxide/methane mixtures in shock waves*. The Journal of Chemical Physics, 1971, 54 (4), 1718-1725. DOI.
33. Dean, A.M.; Steiner, D.C. *A shock tube study of the recombination of carbon monoxide and oxygen atoms*. The Journal of Chemical Physics, 1977, 66 (2), 598-604. DOI.
34. DeMore, W.B. *Pressure dependence and mechanism of the reaction of atomic oxygen and carbon monoxide*. The Journal of Physical Chemistry, 1972, 76 (24), 3527-3532. DOI: 10.1021/j100668a003.
35. DeSain, J.D.; Jusinski, L.E.; Ho, A.D.; Taatjes, C.A. *Temperature dependence and deuterium kinetic isotope effects in the HCO (DCO) + O₂ reaction between 296 and 673 K*. Chemical Physics Letters, 2001, 347 (1-3), 79-86. DOI: 10.1016/S0009-2614(01)01016-8.
36. Dooley, S.; Won, S.H.; Chaos, M.; Heyne, J.; Ju, Y.; Dryer, F.L.; Kumar, K.; Sung, C.-J.; Wang, H.; Oehlschlaeger, M.A.; Santoro, R.J.; Litzinger, T.A. *A jet fuel surrogate formulated by real fuel properties*. Combustion and Flame, 2010, 157 (12), 2333-2339. DOI: 10.1016/j.combustflame.2010.07.001.
37. Dryer, F.L. *High temperature oxidation of carbon monoxide and methane in a turbulent flow reactor*. Ph.D. Thesis, Princeton University, 1972.
38. Dryer, F.L. *Comprehensive mechanisms for combustion chemistry: An experimental and numerical study with emphasis on applied sensitivity analysis*. Annual report to US Department of Energy, Office of Science, Office of Basic Energy Sciences for grant number FG0286ER13503 A001, 1987.
39. Dryer, F.L.; Haas, F.M.; Santner, J.; Farouk, T.; Chaos, M. *Interpreting chemical kinetics from complex reaction-advection-diffusion systems: Modeling of flow reactors and related kinetics experiments*. Progress in Energy and Combustion Science, 2014, 44, 19-39. DOI: 10.1016/j.pecs.2014.04.002.
40. Dryer, F.L.; Naegeli, D.; Glassman, I. *Temperature dependence of the reaction CO + OH = CO₂ + H*. Combustion & Flame, 1971, 17, 270-272. DOI.
41. EPA; NHTSA. *Joint technical support document: Final rulemaking for 2017-2025 light-duty vehicle greenhouse gas emission standards and corporate average fuel economy standards, Chapter 3*. Report EPA-420-R-12-901, United States Environmental Protection Agency and National Highway Traffic Safety Administration, August 2012.
42. ExxonMobil. *The outlook for energy: A view to 2040*. Report SP-131, Exxon Mobil Corporation, 2013.
43. Fabian, W.M.F.; Janoschek, R. *Thermochemical properties of the hydroxy-formyl radical, HO-CO, and the formyloxy radical, HC(O)O, and their role in the reaction OH+CO→H+CO₂. Computational G3MP2B3 and CCSD(T)-CBS studies*. Journal of Molecular Structure: THEOCHEM, 2005, 713 (1-3), 227-234. DOI: 10.1016/j.theochem.2004.08.065.

44. Federal Register. *2017 and later model year light-duty vehicle greenhouse gas emissions and corporate average fuel economy standards; Final rule*. 77 FR 62623. (2012-10-15).
45. Fernandes, R.X.; Luther, K.; Troe, J.; Ushakov, V.G. *Experimental and modelling study of the recombination reaction $H + O_2 (+M) \rightarrow HO_2 (+M)$ between 300 and 900 K, 1.5 and 950 bar, and in the bath gases $M = He, Ar, \text{ and } N_2$* . Physical Chemistry Chemical Physics, 2008, 10 (29), 4313-4321. DOI: 10.1039/b804553d.
46. Friedrichs, G.; Herbon, J.T.; Davidson, D.F.; Hanson, R.K. *Quantitative detection of HCO behind shock waves: The thermal decomposition of HCO*. Physical Chemistry Chemical Physics, 2002, 4 (23), 5778-5788. DOI.
47. Fujii, N.; Kakuda, T.; Sugiyama, T.; Miyama, H. *Direct determination of the rate constant for the reaction $CO + N_2O \rightarrow CO_2 + N_2$* . Chemical Physics Letters, 1985, 122 (5), 489-492. DOI: 10.1016/0009-2614(85)87251-1.
48. Fujii, N.; Kakuda, T.; Takeishi, N.; Miyama, H. *Kinetics of the high temperature reaction of carbon monoxide with nitrous oxide*. The Journal of Physical Chemistry, 1987, 91 (8), 2144-2148. DOI: 10.1021/j100292a033.
49. Gaedtke, H.; Glänzer, K.; Hippler, H.; Luther, K.; Troe, J. *Addition reactions of oxygen atoms at high pressures*. Symposium (International) on Combustion, 1973, 14 (1), 295-303. DOI: 10.1016/S0082-0784(73)80030-X.
50. Gardiner, W.C.; Troe, J., Rate coefficients of thermal dissociation, isomerization, and recombination reactions. In *Combustion Chemistry*, Gardiner, W.C., Ed. Springer-Verlag: New York, 1984.
51. Glarborg, P.; Marshall, P. *The rate constant for the $CO+H_2O_2$ reaction*. Chemical Physics Letters, 2009, 475 (1-3), 40-43. DOI: 10.1016/j.cplett.2009.05.028.
52. Golden, D.M.; Smith, G.P.; McEwen, A.B.; Yu, C.L.; Eiteneer, B.; Frenklach, M.; Vaghjiani, G.L.; Ravishankara, A.R.; Tully, F.P. *OH(OD) + CO: Measurements and an optimized RRKM fit*. The Journal of Physical Chemistry A, 1998, 102 (44), 8598-8606. DOI: 10.1021/jp982110m.
53. Goldsmith, C.F.; Magoon, G.R.; Green, W.H. *Database of small molecule thermochemistry for combustion*. The Journal of Physical Chemistry A, 2012, 116 (36), 9033-9057. DOI: 10.1021/jp303819e.
54. Goos, E.; Burcat, A.; Ruscic, B., Ideal gas thermochemical database with updates from Active Thermochemical Tables <<ftp://ftp.technion.ac.il/pub/supported/aetdd/thermodynamics>> mirrored at <<http://garfield.chem.elte.hu/Burcat/burcat.html>>; 4 December 2012 update.
55. Guo, H. *Quantum dynamics of complex-forming bimolecular reactions*. International Reviews in Physical Chemistry, 2012, 31 (1), 1-68. DOI: 10.1080/0144235x.2011.649999.
56. Guo, H.; Sun, W.; Haas, F.M.; Farouk, T.; Dryer, F.L.; Ju, Y. *Measurements of H_2O_2 in low temperature dimethyl ether oxidation*. Proceedings of the Combustion Institute, 2013, 34 (1), 573-581. DOI: 10.1016/j.proci.2012.05.056.
57. Haas, F.M.; Chaos, M.; Dryer, F.L. *Low and intermediate temperature oxidation of ethanol and ethanol-PRF blends: An experimental and modeling study*. Combustion and Flame, 2009, 156 (12), 2346-2350. DOI: 10.1016/j.combustflame.2009.08.012.

58. Haas, F.M.; Dryer, F.L. *Rate coefficient determinations for $H + NO_2 \rightarrow OH + NO$ from high pressure flow reactor measurements*. The Journal of Physical Chemistry A, 2015, 119 (28), 7792-7801. DOI: 10.1021/acs.jpca.5b01231.
59. Harding, L.B.; Wagner, A.F. *The reaction of atomic hydrogen with the formyl radical*. Symposium (International) on Combustion, 1986, 21 (1), 721-728. DOI: 10.1016/S0082-0784(88)80304-7.
60. Hardy, J.E.; Gardiner, W.C.; Burcat, A. *Recombination of carbon monoxide and oxygen atoms*. International Journal of Chemical Kinetics, 1978, 10 (5), 503-517. DOI: 10.1002/kin.550100508.
61. Hardy, W.A.; Vasatko, H.; Wagner, H.G.; Zabel, F. *Neuere Untersuchungen zum thermischen Zerfall von CO_2 1. Teil*. Berichte der Bunsengesellschaft für physikalische Chemie, 1974, 78 (1), 76-82. DOI: 10.1002/bbpc.19740780113.
62. Hasegawa, K.; Asaba, T. *Study of the ignition reaction in a mixture of oxygen with hydrogen at relatively high pressures and low temperatures in a shock tube*. Combustion, Explosion, and Shock Waves, 1972, 8 (3), 317-324. DOI: 10.1007/bf00742308.
63. Held, T.J. *The oxidation of methanol, isobutene and methyl tertiary-butyl ether*. Ph.D. Thesis, Princeton University, 1993.
64. Held, T.J.; Dryer, F.L. *A comprehensive mechanism for methanol oxidation*. International Journal of Chemical Kinetics, 1998, 30 (11), 805-830. DOI: 10.1002/(sici)1097-4601(1998)30:11<805::aid-kin4>3.0.co;2-z.
65. Herrmann, F.; Jochim, B.; Oßwald, P.; Cai, L.; Pitsch, H.; Kohse-Höinghaus, K. *Experimental and numerical low-temperature oxidation study of ethanol and dimethyl ether*. Combustion and Flame, 2014, 161 (2), 384-397. DOI: 10.1016/j.combustflame.2013.09.014.
66. Heyne, J.S. *Direct and indirect determinations of elementary rate constants*. Ph.D. Thesis, Princeton University, 2014.
67. Heyne, J.S.; Dryer, F.L. *Uncertainty analysis in the use of chemical thermometry: A case study with cyclohexene*. The Journal of Physical Chemistry A, 2013, 117 (26), 5401-5406. DOI: 10.1021/jp402982y.
68. Hidaka, Y.; Taniguchi, T.; Kamesawa, T.; Masaoka, H.; Inami, K.; Kawano, H. *High temperature pyrolysis of formaldehyde in shock waves*. International Journal of Chemical Kinetics, 1993, 25 (4), 305-322. DOI: 10.1002/kin.550250409.
69. Hoare, D.E.; Walsh, A.D. *The reaction of methyl radicals with oxygen and comparison with other third-order reactions*. Transactions of the Faraday Society, 1957, 53, 1102-1110. DOI.
70. Hong, Z.; Davidson, D.F.; Barbour, E.A.; Hanson, R.K. *A new shock tube study of the $H+O_2 \rightarrow OH+O$ reaction rate using tunable diode laser absorption of H_2O near $2.5 \mu m$* . Proceedings of the Combustion Institute, 2011, 33 (1), 309-316. DOI: 10.1016/j.proci.2010.05.101.
71. Hong, Z.; Davidson, D.F.; Hanson, R.K. *An improved H_2/O_2 mechanism based on recent shock tube/laser absorption measurements*. Combustion and Flame, 2011, 158 (4), 633-644. DOI: 10.1016/j.combustflame.2010.10.002.
72. Hsu, C.C.; Mebel, A.M.; Lin, M.C. *Ab initio molecular orbital study of the $HCO+O_2$ reaction: Direct versus indirect abstraction channels*. The Journal of Chemical Physics, 1996, 105 (6), 2346-2352. DOI.
73. International Energy Agency. *World energy outlook 2011*. OECD Publishing: 2011.

74. Jasper, A.W.; Dawes, R. *Non-Born–Oppenheimer molecular dynamics of the spin-forbidden reaction $O(^3P) + CO(X^1\Sigma^+) \rightarrow CO_2(\tilde{X}^1\Sigma_g^+)$* . The Journal of Chemical Physics, 2013, 139 (15), -. DOI: 10.1063/1.4825204.
75. Jasper, A.W.; Dawes, R., Predictive theoretical kinetics of the pressure-dependent spin-forbidden reaction $O + CO \rightarrow CO_2$. In *8th US National Combustion Meeting*, 2013.
76. Jasper, A.W.; Kamarchik, E.; Miller, J.A.; Klippenstein, S.J. *First-principles binary diffusion coefficients for H, H₂, and four normal alkanes + N₂*. The Journal of Chemical Physics, 2014a, 141 (12), 124313. DOI: 10.1063/1.4896368.
77. Jasper, A.W.; Miller, J.A. *Collisional energy transfer in unimolecular reactions: Direct classical trajectories for $CH_4 \rightleftharpoons CH_3 + H$ in helium*. The Journal of Physical Chemistry A, 2009, 113 (19), 5612-5619. DOI: 10.1021/jp900802f.
78. Jasper, A.W.; Miller, J.A. *Theoretical unimolecular kinetics for $CH_4 + M \rightleftharpoons CH_3 + H + M$ in eight baths, $M = He, Ne, Ar, Kr, H_2, N_2, CO,$ and CH_4* . The Journal of Physical Chemistry A, 2011, 115 (24), 6438-6455. DOI: 10.1021/jp200048n.
79. Jasper, A.W.; Miller, J.A. *Lennard–Jones parameters for combustion and chemical kinetics modeling from full-dimensional intermolecular potentials*. Combustion and Flame, 2014b, 161 (1), 101-110. DOI: 10.1016/j.combustflame.2013.08.004.
80. Joshi, A.V.; Wang, H. *Master equation modeling of wide range temperature and pressure dependence of $CO + OH \rightarrow$ products*. International Journal of Chemical Kinetics, 2006, 38 (1), 57-73. DOI: 10.1002/kin.20137.
81. Kee, R.; Rupley, F.; Miller, J.; Coltrin, M.; Grcar, J.; Meeks, E. *Chemkin Collection, Release 3.7.1. Chemkin Collection, Release 371*. San Diego, CA Reaction Design Inc, 2003.
82. Kee, R.J.; Grcar, J.F.; Smooke, M.D.; Miller, J.A. *PREMIX: A FORTRAN Program for Modeling Steady Laminar One-dimensional Premixed Flames*, SAND85-8240 (Reprinted 1991); Sandia National Laboratories: 1985.
83. K romn s, A.; Metcalfe, W.K.; Heufer, K.A.; Donohoe, N.; Das, A.K.; Sung, C.-J.; Herzler, J.; Naumann, C.; Griebel, P.; Mathieu, O.; Krejci, M.C.; Petersen, E.L.; Pitz, W.J.; Curran, H.J. *An experimental and detailed chemical kinetic modeling study of hydrogen and syngas mixture oxidation at elevated pressures*. Combustion and Flame, 2013, 160 (6), 995-1011. DOI: 10.1016/j.combustflame.2013.01.001.
84. Klippenstein, S.J. *From Theoretical Reaction Dynamics to Chemical Modeling of Combustion*. Proceedings of the Combustion Institute, 2017, 36, (submitted). DOI.
85. Klippenstein, S.J.; Harding, L.B.; Glarborg, P.; Miller, J.A. *The role of NNH in NO formation and control*. Combustion and Flame, 2011, 158 (4), 774-789. DOI: 10.1016/j.combustflame.2010.12.013.
86. Ko, T.; Fontijn, A. *High-temperature photochemistry kinetics study of the reaction hydrogen atom + nitrogen dioxide \rightarrow hydroxyl + nitric oxide from 296 to 760 K*. The Journal of Physical Chemistry, 1991, 95 (10), 3984-3987. DOI: 10.1021/j100163a019.
87. Konnov, A.A. *Remaining uncertainties in the kinetic mechanism of hydrogen combustion*. Combustion and Flame, 2008, 152 (4), 507-528. DOI: 10.1016/j.combustflame.2007.10.024.

88. Labbe, N.J.; Sivaramakrishnan, R.; Goldsmith, C.F.; Georgievskii, Y.; Miller, J.A.; Klippenstein, S.J. *Weakly Bound Free Radicals in Combustion: "Prompt" Dissociation of Formyl Radicals and Its Effect on Laminar Flame Speeds*. The Journal of Physical Chemistry Letters, 2016, 7 (1), 85-89. DOI: 10.1021/acs.jpcclett.5b02418.
89. Lee, J.C.Y. *Simulations of two-dimensional chemically reactive flows*. Ph.D. Thesis, Princeton University, 1996.
90. Lefkowitz, J.K.; Heyne, J.S.; Won, S.H.; Dooley, S.; Kim, H.H.; Haas, F.M.; Jahangirian, S.; Dryer, F.L.; Ju, Y. *A chemical kinetic study of tertiary-butanol in a flow reactor and a counterflow diffusion flame*. Combustion and Flame, 2012, 159 (3), 968-978. DOI: 10.1016/j.combustflame.2011.10.004.
91. Li, J.; Zhao, Z.; Kazakov, A.; Chaos, M.; Dryer, F.L.; Scire, J.J. *A comprehensive kinetic mechanism for CO, CH₂O, and CH₃OH combustion*. International Journal of Chemical Kinetics, 2007, 39 (3), 109-136. DOI: 10.1002/kin.20218.
92. Li, J.; Zhao, Z.; Kazakov, A.; Dryer, F.L. *An updated comprehensive kinetic model of hydrogen combustion*. International Journal of Chemical Kinetics, 2004, 36 (10), 566-575. DOI: 10.1002/kin.20026.
93. Linnett, J.W.; Selley, N.J. *The stabilization of HO₂ and DO₂ by inert molecules*. Z. Physik. Chem. (NF), 1963, 37, 402-13. DOI.
94. Lutz, A.E.; Kee, R.J.; Miller, J.A. *SENKIN: A FORTRAN Program for Predicting Homogeneous Gas Phase Chemical Kinetics with Sensitivity Analysis*, SAND87-8248 (Revised); Sandia National Laboratories: 1997.
95. Medvedev, S.P.; Agafonov, G.L.; Khomik, S.V.; Gelfand, B.E. *Ignition delay in hydrogen-air and syngas-air mixtures: Experimental data interpretation via flame propagation*. Combustion and Flame, 2010, 157 (7), 1436-1438. DOI: 10.1016/j.combustflame.2010.03.003.
96. Michael, J.V.; Nava, D.F.; Payne, W.A.; Lee, J.H.; Stief, L.J. *Rate constant for the reaction atomic hydrogen + nitrogen dioxide from 195 to 400 K with FP-RF and DF-RF techniques*. The Journal of Physical Chemistry, 1979, 83 (22), 2818-2823. DOI: 10.1021/j100485a003.
97. Michael, J.V.; Su, M.C.; Sutherland, J.W.; Carroll, J.J.; Wagner, A.F. *Rate constants for H + O₂ + M → HO₂ + M in seven bath gases*. The Journal of Physical Chemistry A, 2002, 106 (21), 5297-5313. DOI: 10.1021/jp020229w.
98. Miller, J.A.; Kee, R.J.; Westbrook, C.K. *Chemical kinetics and combustion modeling*. Annual Review of Physical Chemistry, 1990, 41 (1), 345-387. DOI: doi:10.1146/annurev.pc.41.100190.002021.
99. Mittal, G.; Sung, C.-J.; Yetter, R.A. *Autoignition of H₂/CO at elevated pressures in a rapid compression machine*. International Journal of Chemical Kinetics, 2006, 38 (8), 516-529. DOI: 10.1002/kin.20180.
100. Mueller, M.A.; Kim, T.J.; Yetter, R.A.; Dryer, F.L. *Flow reactor studies and kinetic modeling of the H₂/O₂ reaction*. International Journal of Chemical Kinetics, 1999a, 31 (2), 113-125. DOI: 10.1002/(sici)1097-4601(1999)31:2<113::aid-kin5>3.0.co;2-0.
101. Mueller, M.A.; Yetter, R.A.; Dryer, F.L. *Measurement of the rate constant for H+O₂+M→HO₂+M (M=N₂, Ar) using kinetic modeling of the high-pressure H₂/O₂/NO_x reaction*. Symposium (International) on Combustion, 1998, 27 (1), 177-184. DOI: 10.1016/S0082-0784(98)80403-7.

102. Mueller, M.A.; Yetter, R.A.; Dryer, F.L. *Flow reactor studies and kinetic modeling of the H₂/O₂/NO_x and CO/H₂O/O₂/NO_x reactions*. International Journal of Chemical Kinetics, 1999b, 31 (10), 705-724. DOI: 10.1002/(sici)1097-4601(1999)31:10<705::aid-jck4>3.0.co;2-#.
103. Mueller, M.E.; Iaccarino, G.; Pitsch, H. *Chemical kinetic uncertainty quantification for Large Eddy Simulation of turbulent nonpremixed combustion*. Proceedings of the Combustion Institute, 2013, 34 (1), 1299-1306. DOI: 10.1016/j.proci.2012.07.054.
104. Nasir, E.F.; Farooq, A. *A Shock-Tube Study of the CO + OH Reaction Near the Low-Pressure Limit*. The Journal of Physical Chemistry A, 2016, 120 (22), 3924-3928. DOI: 10.1021/acs.jpca.6b01322.
105. Nguyen, T.L.; Xue, B.C.; Weston, R.E.; Barker, J.R.; Stanton, J.F. *Reaction of HO with CO: Tunneling is indeed important*. The Journal of Physical Chemistry Letters, 2012, 3 (11), 1549-1553. DOI: 10.1021/jz300443a.
106. Nilsson, E.J.K.; Konnov, A.A. *Role of HOCO Chemistry in Syngas Combustion*. Energy & Fuels, 2016, 30 (3), 2443-2457. DOI: 10.1021/acs.energyfuels.5b02778.
107. Ó Conaire, M.; Curran, H.J.; Simmie, J.M.; Pitz, W.J.; Westbrook, C.K. *A comprehensive modeling study of hydrogen oxidation*. International Journal of Chemical Kinetics, 2004, 36 (11), 603-622. DOI: 10.1002/kin.20036.
108. Olschewski, H.A.; Troe, J.; Wagner, H.G. *Untersuchung unimolekularer Reaktionen bei hohen Drucken in Stoßwellen: Zerfall von CS₂ und CO₂*. Berichte der Bunsengesellschaft für physikalische Chemie, 1966, 70 (9-10), 1060-1064. DOI: 10.1002/bbpc.19660700926.
109. Olsen, L.O. *Catalytic effects of thermocouple materials*. SAE-620414, Society of Automotive Engineers, 1962.
110. Pang, G.A.; Davidson, D.F.; Hanson, R.K. *Experimental study and modeling of shock tube ignition delay times for hydrogen–oxygen–argon mixtures at low temperatures*. Proceedings of the Combustion Institute, 2009, 32 (1), 181-188. DOI: 10.1016/j.proci.2008.06.014.
111. Paul, P.; Warnatz, J. *A re-evaluation of the means used to calculate transport properties of reacting flows*. Symposium (International) on Combustion, 1998, 27 (1), 495-504. DOI: 10.1016/s0082-0784(98)80439-6.
112. Petersen, E.L.; Kalitan, D.M.; Barrett, A.B.; Reehal, S.C.; Mertens, J.D.; Beerer, D.J.; Hack, R.L.; McDonell, V.G. *New syngas/air ignition data at lower temperature and elevated pressure and comparison to current kinetics models*. Combustion and Flame, 2007, 149 (1–2), 244-247. DOI: 10.1016/j.combustflame.2006.12.007.
113. Qiao, L.; Gu, Y.; Dahm, W.J.A.; Oran, E.S.; Faeth, G.M. *A study of the effects of diluents on near-limit H₂–air flames in microgravity at normal and reduced pressures*. Combustion and Flame, 2007, 151 (1–2), 196-208. DOI: 10.1016/j.combustflame.2007.06.013.
114. Ranzi, E.; Frassoldati, A.; Faravelli, T.; Cuoci, A.; Buzzi Ferraris, G. CRECK (Chemical Reaction Engineering and Chemical Kinetics) Model (H₂/CO Mechanism) Version 1212. Available at: <http://creckmodeling.chem.polimi.it/>, 2012. (Accessed July 2013).
115. Rasmussen, C.L.; Hansen, J.; Marshall, P.; Glarborg, P. *Experimental measurements and kinetic modeling of CO/H₂/O₂/NO_x conversion at high pressure*. International Journal of Chemical Kinetics, 2008, 40 (8), 454-480. DOI: 10.1002/kin.20327.
116. Reaction Design CHEMKIN-PRO, San Diego, 2011.

117. Ruscic, B.; Pinzon, R.E.; Morton, M.L.; von Laszewski, G.; Bittner, S.J.; Nijssure, S.G.; Amin, K.A.; Minkoff, M.; Wagner, A.F. *Introduction to Active Thermochemical Tables: Several "key" enthalpies of formation revisited*. The Journal of Physical Chemistry A, 2004, 108 (45), 9979-9997. DOI: 10.1021/jp047912y.
118. Santner, J.; Dryer, F.L.; Ju, Y. *The effects of water dilution on hydrogen, syngas, and ethylene flames at elevated pressure*. Proceedings of the Combustion Institute, 2013, 34 (1), 719-726. DOI: 10.1016/j.proci.2012.06.065.
119. Santner, J.; Haas, F.M.; Dryer, F.L.; Ju, Y. *High temperature oxidation of formaldehyde and formyl radical: A study of 1,3,5-trioxane laminar burning velocities*. Proceedings of the Combustion Institute, 2015, 35 (1), 687-694. DOI: 10.1016/j.proci.2014.05.014.
120. Santner, J.; Haas, F.M.; Ju, Y.; Dryer, F.L. *Uncertainties in interpretation of high pressure spherical flame propagation rates due to thermal radiation*. Combustion and Flame, 2014, 161 (1), 147-153. DOI: 10.1016/j.combustflame.2013.08.008.
121. Saxena, P.; Williams, F.A. *Testing a small detailed chemical-kinetic mechanism for the combustion of hydrogen and carbon monoxide*. Combustion and Flame, 2006, 145 (1-2), 316-323. DOI: 10.1016/j.combustflame.2005.10.004.
122. Saxena, P.; Williams, F.A., Detailed and short mechanisms for syngas combustion. Paper RK75. In *7th US National Combustion Meeting*, Georgia Institute of Technology, Atlanta, GA, 2011.
123. Schofield, K. *Large scale chemical kinetic models of fossil fuel combustion: Adequate as engineering models—no more, no less*. Energy & Fuels, 2012, in press. DOI: 10.1021/ef300858s.
124. Scire, J.J.; Klotz, S.D.; Dryer, F.L. *Initial observations of ketene in flow reactor kinetic studies*. Zeitschrift für Physikalische Chemie International journal of research in physical chemistry and chemical physics, 2001, 215 (8/2001), 1011. DOI.
125. Sellevåg, S.R.; Georgievskii, Y.; Miller, J.A. *The temperature and pressure dependence of the reactions $H+O_2(+M) \rightarrow HO_2(+M)$ and $H+OH(+M) \rightarrow H_2O(+M)$* . The Journal of Physical Chemistry A, 2008, 112 (23), 5085-5095. DOI: 10.1021/jp711800z.
126. Senosiain, J.P.; Klippenstein, S.J.; Miller, J.A. *A complete statistical analysis of the reaction between OH and CO*. Proceedings of the Combustion Institute, 2005, 30 (1), 945-953. DOI: 10.1016/j.proci.2004.07.009.
127. Sharipov, A.; Starik, A. *Theoretical study of the reaction of carbon monoxide with oxygen molecules in the ground triplet and singlet delta states*. The Journal of Physical Chemistry A, 2011, 115 (10), 1795-1803. DOI: 10.1021/jp110345s.
128. Sheen, D.A.; You, X.; Wang, H.; Løvås, T. *Spectral uncertainty quantification, propagation and optimization of a detailed kinetic model for ethylene combustion*. Proceedings of the Combustion Institute, 2009, 32 (1), 535-542. DOI: 10.1016/j.proci.2008.05.042.
129. Shimizu, K.; Hibi, A.; Koshi, M.; Morii, Y.; Tsuboi, N. *Updated kinetic mechanism for high-pressure hydrogen combustion*. Journal of Propulsion and Power, 2011, 27 (2), 383-395. DOI.
130. Simonaitis, R.; Heicklen, J. *Kinetics and mechanism of the reaction of $O(^3P)$ with carbon monoxide*. The Journal of Chemical Physics, 1972, 56 (5), 2004-2011. DOI.

131. Sivaramakrishnan, R.; Comandini, A.; Tranter, R.S.; Brezinsky, K.; Davis, S.G.; Wang, H. *Combustion of CO/H₂ mixtures at elevated pressures*. Proceedings of the Combustion Institute, 2007, 31 (1), 429-437. DOI: 10.1016/j.proci.2006.08.057.
132. Slanger, T.G.; Black, G. *Reaction rate measurements of O(³P) atoms by resonance fluorescence. II O(³P)+CO+M → CO₂+M; M = He, Ar, N₂*. The Journal of Chemical Physics, 1970, 53 (9), 3722-3725. DOI.
133. Slanger, T.G.; Wood, B.J.; Black, G. *Kinetics of O(³P)+CO+M recombination*. The Journal of Chemical Physics, 1972, 57 (1), 233-238. DOI.
134. Smith, G.P.; Golden, D.M.; Frenklach, M.; Moriarty, N.W.; Eiteneer, B.; Goldenberg, M.; Bowman, C.T.; Hanson, R.K.; Song, S.; Gardiner, W.C., Jr.; Lissianski, V.V.; Qin, Z. GRI-MECH 3.0. Available at: http://www.me.berkeley.edu/gri_mech/, 1999. (Accessed October 2012).
135. Smith, I.W.M. *The mechanism of the OH + CO reaction and the stability of the HOCO radical*. Chemical Physics Letters, 1977, 49 (1), 112-115. DOI: 10.1016/0009-2614(77)80453-3.
136. Stein, Y.; Yetter, R.A.; Dryer, F.L., Flow reactor studies of the reaction H+O₂+M → HO₂+M. In *Eastern Sectional Meeting of the Combustion Institute*, San Juan, PR, 1986.
137. Su, M.C.; Kumaran, S.S.; Lim, K.P.; Michael, J.V.; Wagner, A.F.; Harding, L.B.; Fang, D.C. *Rate constants, 1100 ≤ T ≤ 2000 K, for H + NO₂ → OH + NO using two shock tube techniques: Comparison of theory to experiment*. The Journal of Physical Chemistry A, 2002, 106 (36), 8261-8270. DOI: 10.1021/jp0141023.
138. Sun, H.; Yang, S.I.; Jomaas, G.; Law, C.K. *High-pressure laminar flame speeds and kinetic modeling of carbon monoxide/hydrogen combustion*. Proceedings of the Combustion Institute, 2007, 31 (1), 439-446. DOI: 10.1016/j.proci.2006.07.193.
139. Sutherland, J.W.; Patterson, P.M.; Klemm, R.B. *Direct studies of the thermal decomposition of N₂O and CO₂ and of the reaction of CO with O₂*. BNL-46985, Brookhaven National Laboratory, 1992.
140. Thielen, K.; Roth, P. *Stoßwellenuntersuchungen zum Start der Reaktion CO + O₂*. Berichte der Bunsengesellschaft für physikalische Chemie, 1983, 87 (10), 920-925. DOI: 10.1002/bbpc.19830871017.
141. Timonen, R.S.; Ratajczak, E.; Gutman, D. *Kinetics of the reactions of the formyl radical with oxygen, nitrogen dioxide, chlorine, and bromine*. The Journal of Physical Chemistry, 1988, 92 (3), 651-655. DOI: 10.1021/j100314a017.
142. Tomlin, A.S. *The role of sensitivity and uncertainty analysis in combustion modelling*. Proceedings of the Combustion Institute, 2013, 34 (1), 159-176. DOI: 10.1016/j.proci.2012.07.043.
143. Troe, J. *Thermal dissociation and recombination of polyatomic molecules*. Symposium (International) on Combustion, 1975, 15 (1), 667-680. DOI: 10.1016/S0082-0784(75)80337-7.
144. Troe, J.; Ushakov, V. *Classical trajectory study of the reaction between H and HCO*. The Journal of Physical Chemistry A, 2007, 111 (29), 6610-6614. DOI: 10.1021/jp0674017.
145. Tsang, W.; Hampson, R.F. *Chemical kinetic data base for combustion chemistry. Part I. Methane and related compounds*. Journal of Physical and Chemical Reference Data, 1986, 15 (3), 1087-1279. DOI.
146. Turányi, T.; Nagy, T.; Zsély, I.G.; Cserháti, M.; Varga, T.; Szabó, B.T.; Sedyó, I.; Kiss, P.T.; Zempléni, A.; Curran, H.J. *Determination of rate parameters based on both direct and indirect*

measurements. *International Journal of Chemical Kinetics*, 2012, **44** (5), 284-302. DOI: 10.1002/kin.20717.

147. Urzay, J.; Kseib, N.; Davidson, D.F.; Iaccarino, G.; Hanson, R.K. *Uncertainty-quantification analysis of the effects of residual impurities on hydrogen–oxygen ignition in shock tubes*. *Combustion and Flame*, 2014, **161** (1), 1-15. DOI: 10.1016/j.combustflame.2013.08.012.

148. Vasu, S.S.; Davidson, D.F.; Hanson, R.K. *Shock tube study of syngas ignition in rich CO₂ mixtures and determination of the rate of H+O₂+CO₂ → HO₂+CO₂*. *Energy & Fuels*, 2011, **25** (3), 990-997. DOI: 10.1021/ef1015928.

149. Vermeersch, M.L. *A variable pressure flow reactor for chemical kinetic studies: Hydrogen, methane, and butane oxidation at 1 to 10 atmospheres and 880 to 1,040 K*. Ph.D. Thesis, Princeton University, 1991.

150. Vinkers, C.H.; Tijdink, J.K.; Otte, W.M. *Use of positive and negative words in scientific PubMed abstracts between 1974 and 2014: retrospective analysis*. *BMJ*, 2015, 351. DOI: 10.1136/bmj.h6467.

151. Voevodsky, V.V.; Kondratiev, V.N., Determination of rate constants for elementary steps in branched-chain reactions. In *Progress in Reaction Kinetics*, Porter, G., Ed. Pergamon Press: Oxford, 1961; Vol. 1, pp 43-65.

152. von Elbe, G.; Lewis, B. *Mechanism of the thermal reaction between hydrogen and oxygen*. *The Journal of Chemical Physics*, 1942, **10** (6), 366-393. DOI.

153. Wagner, H.G.; Zabel, F. *Neuere Untersuchungen zum thermischen Zerfall von CO₂. Teil II*. *Berichte der Bunsengesellschaft für physikalische Chemie*, 1974, **78** (7), 705-712. DOI: 10.1002/bbpc.19740780717.

154. Wang, H.; You, X.; Joshi, A.V.; Davis, S.G.; Laskin, A.; Egolfopoulos, F.; Law, C.K. USC Mech Version II. High-temperature combustion reaction model of H₂/CO/C₁-C₄ compounds. Available at: http://ignis.usc.edu/USC_Mech_II.htm, May 2007. (Accessed October 2012).

155. Warnatz, J., Rate coefficients in the C/H/O system. In *Combustion Chemistry*, Gardiner, W.C., Ed. Springer-Verlag: New York, 1984.

156. Westbrook, C.K.; Dryer, F.L. *Chemical kinetics and modeling of combustion processes*. Symposium (International) on Combustion, 1981, **18** (1), 749-767. DOI: 10.1016/s0082-0784(81)80079-3.

157. Westmoreland, P.R.; Howard, J.B.; Longwell, J.P.; Dean, A.M. *Prediction of rate constants for combustion and pyrolysis reactions by bimolecular QRRK*. *AIChE Journal*, 1986, **32** (12), 1971-1979. DOI: 10.1002/aic.690321206.

158. Weston, R.E. *A case study in chemical kinetics: The OH + CO reaction*. *Journal of Chemical Education*, 1988, **65** (12), 1062. DOI: 10.1021/ed065p1062.

159. Weston, R.E.; Nguyen, T.L.; Stanton, J.F.; Barker, J.R. *HO + CO reaction rates and H/D kinetic isotope effects: Master equation models with ab Initio SCTST rate constants*. *The Journal of Physical Chemistry A*, 2013, **117** (5), 821-835. DOI: 10.1021/jp311928w.

160. Willbourn, A.H.; Hinshelwood, C.N. *The mechanism of the hydrogen-oxygen reaction. I. The third explosion limit*. *Proceedings of the Royal Society of London. Series A. Mathematical and Physical Sciences*, 1946, **185** (1003), 353-369. DOI: 10.1098/rspa.1946.0023.

161. Wooldridge, M.S.; Hanson, R.K.; Bowman, C.T. *A shock tube study of the CO+OH→CO₂+H reaction*. Symposium (International) on Combustion, 1994, 25 (1), 741-748. DOI: 10.1016/S0082-0784(06)80706-X.
162. Yang, X.; Tan, T.; Dievart, P.; Carter, E.A.; Ju, Y., Theoretical assessment on reaction kinetics HCO and CH₂OH unimolecular decomposition. Paper # 070RK-0163. In *8th US National Combustion Meeting*, 2013.
163. Yau, A.W.; Pritchard, H.O. *Lindemann unimolecular fall-off in weak-collision systems at high temperature*. Chemical Physics Letters, 1978, 60 (1), 140-144. DOI: 10.1016/0009-2614(78)85729-7.
164. You, X.; Wang, H.; Goos, E.; Sung, C.-J.; Klippenstein, S.J. *Reaction kinetics of CO + HO₂ → products: Ab initio transition state theory study with master equation modeling*. The Journal of Physical Chemistry A, 2007, 111 (19), 4031-4042. DOI: 10.1021/jp067597a.
165. Yu, C.-L. *Chemical kinetics of reaction systems CO + OH and CH₃ + O₂*. Ph.D. Thesis, The Pennsylvania State University, 1996.
166. Zhao, Z.; Chaos, M.; Kazakov, A.; Dryer, F.L. *Thermal decomposition reaction and a comprehensive kinetic model of dimethyl ether*. International Journal of Chemical Kinetics, 2008, 40 (1), 1-18. DOI: 10.1002/kin.20285.
167. Zsély, I.G.; Olm, C.; Pálvölgyi, R.; Varga, T.; Nagy, T.; Turányi, T., Comparison of the performance of several recent hydrogen combustion mechanisms. Paper P4-13. In *6th European Combustion Meeting*, Lund University, Lund, Sweden, 2013.


```

DUPLICATE

H2+OH = H2O+H          0.216E+09  1.51  0.343E+04
OH+OH = O+H2O          3.34E+04   2.42 -1.93E+03

!=====
!H2-O2 Dissociation Reactions
!=====

H2+M = H+H+M           4.577E+19 -1.40  1.0438E+05
  H2/2.5/ H2O/12/
  CO/1.9/ CO2/3.8/
  AR/0.0/ HE/0.0/

H2+AR = H+H+AR         5.840E+18 -1.10  1.0438E+05
H2+HE = H+H+HE         5.840E+18 -1.10  1.0438E+05

O+O+M = O2+M           6.165E+15 -0.50  0.000E+00
  H2/2.5/ H2O/12/
  AR/0.0/ HE/0.0/
  CO/1.9/ CO2/3.8/

O+O+AR = O2+AR         1.886E+13  0.00 -1.788E+03
O+O+HE = O2+HE         1.886E+13  0.00 -1.788E+03

O+H+M = OH+M           4.714E+18 -1.00  0.000E+00
  H2/2.5/ H2O/12/
  AR/0.75/ HE/0.75/
  CO/1.9/ CO2/3.8/

H2O+M = H+OH+M         6.064E+27 -3.322 1.2079E+05
  H2/3.0/ H2O/0.0/
  HE/1.10/ N2/2.00/
  O2/1.5/
  CO/1.9/ CO2/3.8/

H2O+H2O = H+OH+H2O     1.006E+26 -2.44  1.2018E+05

!=====
! Formation and consumption of HO2
!=====
! MAIN BATH GAS IS N2 (comment this reaction otherwise)
!
!H+O2(+M) = HO2(+M)     4.65084E+12  0.44  0.000E+00
!  LOW/6.366E+20 -1.72  5.248E+02/
!  TROE/0.5 1E-30 1E+30/
!  H2/2.0/ H2O/14/ O2/0.78/ CO/1.9/ CO2/3.04/ AR/0.67/ HE/0.8/
!=====
! MAIN BATH GAS IS AR OR HE (comment this reaction otherwise)
!
!H+O2(+M) = HO2(+M)     4.65084E+12  0.44  0.000E+00
!  LOW/9.042E+19 -1.50  4.922E+02/
!  TROE/0.5 1E-30 1E+30/
!  H2/3.0/ H2O/21/ O2/1.1/ CO/2.7/ CO2/4.32/ HE/1.2/ N2/1.5/
!=====

HO2+H = H2+O2          2.750E+06  2.09 -1.451E+03
HO2+H = OH+OH          7.079E+13  0.00  2.950E+02
HO2+O = O2+OH          2.850E+10  1.00 -7.2393E+02
HO2+OH = H2O+O2       2.890E+13  0.00 -4.970E+02

!=====
!Formation and Consumption of H2O2
!=====

```

```

HO2+HO2 = H2O2+O2          4.200E+14  0.00  1.1982E+04
  DUPLICATE
HO2+HO2 = H2O2+O2          1.300E+11  0.00 -1.6293E+03
  DUPLICATE

H2O2(+M) = OH+OH(+M)        2.00E+12  0.90  4.8749E+04
  LOW/2.49E+24 -2.30 4.8749E+04/
  TROE/0.43 1E-30 1E+30/
  H2O/7.5/ CO2/1.6/
  N2/1.5/ O2/1.2/
  HE/0.65/ H2O2/7.7/
  H2/3.7/ CO/2.8/

H2O2+H = H2O+OH            2.410E+13  0.00  3.970E+03
H2O2+H = HO2+H2            4.820E+13  0.00  7.950E+03
H2O2+O = OH+HO2            9.550E+06  2.00  3.970E+03

H2O2+OH = HO2+H2O          1.740E+12  0.00  3.180E+02
  DUPLICATE
H2O2+OH = HO2+H2O          7.590E+13  0.00  7.270E+03
  DUPLICATE

```

```

!*****
! CO SUBMODEL
! from thesis of Haas (2016)
!*****
!=====
!CO Reactions
!=====

```

```

!C.1
CO+OH<=>CO2+H              7.046e+04  2.053  -276.221
  DUPLICATE
CO+OH<=>CO2+H              5.757e+12  -0.664  331.8624
  DUPLICATE

!C.2
CO+O2 = CO2+O              7.625E+06  1.67  5.356E+04

!C.3
CO+HO2 = CO2+OH            1.570E+05  2.18  1.729E+04

!C.4
CO+O(+M) = CO2(+M)         4.001E+15 -0.96  9.836E+03
  LOW/1.000E+19 -1.323 7.655E+03/
  H2/2.87/ H2O/13.8/ CO/2.18/ CO2/4.37/ N2/1.15/

```

```

!=====
!HCO Reactions
!=====

```

```

!C.5.M
HCO+M = H+CO+M             4.7485E+11  0.659  1.4874E+04
  H2/2.5/ H2O/6/ CO/1.9/ CO2/3.8/

!C.6
HCO+O2 = CO+HO2            7.829E+12  0.521 -5.203E+02

!C.7
HCO+H = CO+H2              1.450E+13  0.30 -2.500E+02

```

END

Transport Parameters (tran.dat)

!Transport used by Burke et al. (2012)
 !includes highly diffusive species treatment of Wang et al. (see bottom section)

AR	0	136.500	3.330	0.000	0.000	0.000
CO	1	98.100	3.650	0.000	1.950	1.800
CO2	1	244.000	3.763	0.000	2.650	2.100
HCO	2	498.000	3.590	0.000	0.000	0.000
HE	0	10.200	2.576	0.000	0.000	0.000
H	0	145.000	2.050	0.000	0.000	0.000
H2	1	38.000	2.920	0.000	0.790	280.000
H2O	2	572.400	2.605	1.844	0.000	4.000
H2O2	2	107.400	3.458	0.000	0.000	3.800
HO2	2	107.400	3.458	0.000	0.000	1.000
N2	1	97.530	3.621	0.000	1.760	4.000
O	0	80.000	2.750	0.000	0.000	0.000
O2	1	107.400	3.458	0.000	1.600	3.800
OH	1	80.000	2.750	0.000	0.000	0.000

! 1-15: Species name
 ! 16-80: Molecular parameters
 ! molecule index: 0 = atom, 1= linear molec.
 ! 2 = nonlinear molec.
 ! L-J potential well depth, e/kb (K)
 ! L-J collision diameter, s, _
 ! Dipole moment, f, Debye
 ! Polarizability, ` , _2
 ! Rotational relaxation number, Zrot at 298K
 ! Comments
 END

!*****
 !Highly diffusive species treatment of Wang et al.
 !Comment all lines below if special interpreter (http://ignis.usc.edu/Mechanisms/USC-Mech%20II/USC_Mech%20II.htm) is not installed

! Middha et al, Proc. Comb. Inst., Vol. 29

H HE	-9.66994265100	2.10026266000	-0.07705964500	0.00546112600	0.93003284006
	0.08015000695	-0.00947327267	0.00063458775		
	0.87637862374	0.10238278295	-0.01480299828	0.00098803605	
	1.06001553391	-0.05992751365	0.01026504945	-0.00073450868	
H H2	-11.74984983000	3.15068443400	-0.25747189600	0.01589155500	
	0.68564849197	0.15339038119	-0.01367350360	0.00032210353	
	0.67794933764	0.13747070299	-0.01105868963	0.00016576525	
	0.65119387990	0.08215979427	-0.00438944167	-0.00027358319	
H2 HE	-12.75127347000	3.42444798700	-0.28472577300	0.01593170100	
	0.59534394712	0.20780905298	-0.02484767627	0.00100127755	
	0.67714740207	0.13579177260	-0.01142533631	0.00018885880	
	0.65191818266	0.08365135783	-0.00445010155	-0.00025986744	

! AIChE 2002

H AR	-9.05107284400	1.61614185700	-0.00287779500	0.00130541500	
	0.68819287418	0.15342306998	-0.01769949486	0.00088795976	
	0.69683113086	0.17157988788	-0.02435683182	0.00136547873	
	0.67026727852	0.11433417790	-0.01504070012	0.00051875848	

! Stallcop et al, Phys. Rev. A, 64, Art. 042722

N H2	-11.06296595000	2.35003553100	-0.10371499000	0.00580309100	
	1.31576376016	-0.13458345098	0.02492533153	-0.00119098283	
	6.99070003974	-2.59649971924	0.37720200602	-0.01788555212	
	1.28549476326	-0.20526851249	0.03796449261	-0.00230740895	
N N2	-14.50976666000	3.27038987700	-0.22411274000	0.01070436600	
	1.28549476326	-0.20526851249	0.03796449261	-0.00230740895	
	1.31470940230	-0.12581573177	0.02093874922	-0.00091239288	
	1.18530004024	-0.00109904512	-0.00679031552	0.00082436382	
H O2	-11.04103178000	2.40427694900	-0.10279690200	0.00532644300	

	1.29254489763	-0.18498887975	0.04271031056	-0.00260823132
	1.99269990199	-0.27220069165	0.02059506743	0.00016444098
	1.27566027457	-0.22786150854	0.04449949355	-0.00274619496
O O2	-14.60250025000	3.29049804400	-0.22351565500	0.01068641100
	1.29827044958	-0.17304622424	0.03635310801	-0.00206726443
	9.96160341198	-3.95288550918	0.58275322682	-0.02828930035
	1.26594984746	-0.24767207966	0.04946972829	-0.00300929402
! Stallcop et al, J. Chem. Phys., 97, 3431 (1992)				
H N2	-13.27028844000	3.51865269300	-0.29664901800	0.01643138100
	1.33864596568	-0.08545398502	0.00922905086	0.00004406488
	-2.20299987672	1.59160087079	-0.25339378410	0.01364477086
	1.27615648812	-0.22593374251	0.04641828877	-0.00310151225
! Stallcop et al, Phys. Rev. A, 62, Art. 062709				
H2 N2	-10.99943193000	2.20257995900	-0.08115516500	0.00440608700
	1.31648435027	-0.13202102692	0.02416204045	-0.00120258929
	1.94229781522	-0.41910587564	0.06711915359	-0.00336850295
	1.29072759648	-0.19301215992	0.03398993578	-0.00196835629
N2 N2	-16.51750614000	4.05271572500	-0.34593622800	0.01671006600
	1.35301607939	-0.05405097875	-0.00113356164	0.00059799157
	3.61489786826	-1.08630677454	0.15481851859	-0.00723438967
	1.25620046061	-0.26881554497	0.05577645068	-0.00340833729
! Stallcop et al, J. Thermophys. Heat Tra., 12, 514 (1998)				
H2 H2	-9.96095484000	2.05602189500	-0.06497689600	0.00413678100
	1.32208755845	-0.12074925804	0.02204710917	-0.00105955055
	3.63140155962	-1.13979323643	0.16942078618	-0.00812678015
	1.29811062932	-0.17814060954	0.02956707397	-0.00170200851

ENDDIFF